Performance-Based Seismic Design of structural walls using a hysteretic multilinear model

Juan Pablo Herrera Castaño

Universidad Nacional de Colombia
Faculty of Engineering and Architecture
Department of Civil Engineering
Manizales, Colombia
2019

Diseño Sísmico Basado en Desempeño de muros estructurales usando un modelo histerético multilineal

Juan Pablo Herrera Castaño

Universidad Nacional de Colombia
Facultad de Ingeniería y Arquitectura
Departamento de Ingeniería Civil
Manizales, Colombia
2019

Performance-Based Seismic Design of structural walls using a hysteretic multilinear model

Juan Pablo Herrera Castaño

Dissertation submitted in partial fulfillment of the requirements for the degree of:
Master in Engineering - Structures

Advisor:
Ph.D. Daniel Alveiro Bedoya Ruiz
Co-Advisor:
Ph.D. Jorge Eduardo Hurtado Gómez

Research lines:
Performance-Based Earthquake Engineering
Identification of hysteretic systems
Research group:
Earthquake Engineering and Seismology Group

Universidad Nacional de Colombia
Faculty of Engineering and Architecture
Department of Civil Engineering
Manizales, Colombia
2019

GLORY TO GOD!

To my beloved mother, my beautiful grandmother and my gorgeous Mariana for their love and their support in all this time. You are the loves of my life, forever.

Acknowledgements

Firstly, I would like to express my eternal gratitude to my advisor, Ph.D. Daniel Alveiro Bedoya Ruiz, for his continuous support, guidance, and assistance, not only in the professional and academic field but also in my private life. His friendship, fraternity, empathy, and his valuable knowledge, among others, have been very important to me. Thanks for believing in me, in my abilities, for seeing my potential and helping me to develop it, for instilling in me the enthusiasm for the structural engineering, and for encouraging me to not give up at the difficult moments of this process. I am also very grateful to my co-advisor, Ph.D. Jorge Eduardo Hurtado Gómez, for his admirable and extraordinary view to address issues; his incalculable knowledge, suitable ideas, and opportune suggestions were a fundamental pillar in this research.

I would like to thank my mom for her support in each stage of my life, for her dedication, patience, and love. She has always given everything for me, her lessons and words have given me the strength and the encouragement to reach my purposes; I am who I am thanks to God and to her. I also show my grandma gratitude for all her advice, admiration and love. Additionally, I thank Mariana for her love, patience, support, and confidence; thanks for being there, for listening to me and cheering me.

Of course, I also want to especially thank to:

- my family for its support and admiration through the years. They are part of my inspiration. I will continue reaching goals, and being a good example for them, especially for my sisters and for the other younger family members: If I was able to do it, they can do it too!
- Professor Diego Andrés Alvarez Marín for his teachings, kindness and timely helps.
- Bryan Chalarca for his advice and appropriate suggestions and, especially, for sharing his knowledge.
- the *Earthquake Engineering and Seismology Group* from Universidad Nacional de Colombia at Manizales. The experimental information needed to this study was obtained thanks to the research and extension projects about the seismic behavior of structural walls, specially the project: “Estudio y comportamiento sísmico de estructuras de materiales económicos de

construcción, tales como el ferrocemento y otros materiales, por medio del análisis experimental y el análisis numérico determinista y estocástico", DIMA project, code HERMES No.12870.

- the Sustainable Building Company Econciencia S.A.S. for its support in this research.
- the Laboratorio de Estructuras and Laboratorio de Materiales of Universidad Nacional de Colombia at Manizales, especially to the operators Wilson Cardona, Juan David Cardona y Jahir Cardona.
- the Department of Civil Engineering of Universidad Nacional de Colombia at Manizales for allowing me to develop my teaching skills by the time I was in this process.
- Universidad Nacional de Colombia for being my "Alma Mater".
- all the researchers and institutions that have contribute to the development of the structural and seismic engineering:

"If I have seen farther, it is by standing upon the shoulders of giants"
- Isaac Newton (1642 - 1727)

JUAN PABLO HERRERA CASTAÑO
Manizales, Colombia
April 2019

Abstract

In recent years, innovative structural systems based on Recycled Plastic Lumber walls (RPLW), precast ferrocement walls (PFW), and hollow reinforced concrete walls (HRCW) have been proposed for one and two-story housing so as to lessen the housing deficiency. This thesis presents the results drawn from cycling loading tests carried out over these three types of structural walls, in order to determine their strength, hysteretic behavior, ductility, energy dissipation capacity, equivalent viscous damping, and damage limit states. With the aim to assess their performances for the Design Basic Earthquake (DBE) and the Maximum Considered Earthquake (MCE), it was developed a nonlinear dynamic analysis methodology focused on the Performance-Based Seismic Design philosophy, which uses the Mostaghel's multilinear hysteretic model to represent and describe accurately the actual inelastic behavior and energy dissipation capacity of the structural walls; for the parameter identification of this hysteretic model, a novel procedure that uses the simple Particle Swarm Optimization (PSO) algorithm was proposed, which estimated in a good way the experimental hysteretic behavior of the walls, so the models were good enough for simulation purposes. Additionally, the IO, LS, and CP structural performance levels were related to the damage limit states and several assumptions were made to obtain performance-based seismic assessments as realistic as possible. Also, sets of actual recorded and artificial ground motions were employed to validate the use of the methodology, which were scaled to achieve the spectral matching with the NSR-10 target spectrum. Using the median of the Incremental Dynamic Analysis (IDA) results, the performance points of the RPLW fell within the LS and CP ranges for the DBE and the MCE, respectively, which evidences that this structural system meets exactly the basic safety performance objective established in the design philosophy of the NSR-10 building code. On the other hand, the performance points of the PFW and HRCW fell within the IO range for both earthquake hazard levels, which demonstrates their excellent seismic behavior. The obtained results approve the use of these structural systems for one and two-story housing.

Keywords: Performance-Based Seismic Design, Mostaghel's multilinear hysteretic model, Particle Swarm Optimization, fragility, Incremental Dynamic Analysis, hysteresis, ferrocement wall, Recycled Plastic Lumber wall, hollow reinforced concrete wall, cyclic loading tests.

Resumen

En los últimos años, sistemas estructurales basados en muros de madera plástico reciclado (RPLW), muros prefabricados de ferrocemento (PFW) y muros huecos de concreto reforzado (HRCW) han sido propuestos para viviendas de uno y dos pisos con el fin de disminuir la deficiencia de vivienda. Esta tesis presenta los resultados obtenidos de las pruebas de carga cíclica realizadas sobre estos tres tipos de muros estructurales, a fin de determinar su resistencia, comportamiento histérico, ductilidad, capacidad de disipación de energía, amortiguamiento viscoso equivalente y estados límite de daño. Con el objetivo de evaluar sus desempeños para el terremoto básico de diseño (DBE) y el terremoto máximo considerado (MCE), se desarrolló una metodología de análisis dinámico no lineal enfocada en la filosofía de diseño sísmico basado en desempeño, la cual utiliza el modelo histerético multilineal de Mostaghel para representar y describir con precisión el comportamiento inelástico real y la capacidad de disipación de energía de los muros estructurales; para la identificación de los parámetros de este modelo histerético, fue propuesto un novedoso procedimiento que usa el algoritmo simple de la Optimización por Enjambre de Partículas (PSO), el cual estimó de buena manera el comportamiento histerético experimental de los muros, por lo que los modelos fueron lo suficientemente buenos para propósitos de simulación. Adicionalmente, los niveles de desempeño estructural IO, LS y CP fueron relacionados con los estados límite de daño y varias suposiciones fueron hechas para obtener evaluaciones sísmicas basadas en el desempeño lo más realistas posible. También se emplearon conjuntos de sismos reales y sismos artificiales para validar el uso de la metodología, los cuales fueron escalados para lograr la coincidencia espectral con el espectro objetivo de la NSR-10. Usando la mediana de los resultados del Análisis Dinámico Incremental (IDA), los puntos de desempeño del RPLW cayeron dentro de los rangos LS y CP para el DBE y el MCE, respectivamente, lo que evidencia que este sistema estructural cumple exactamente con el objetivo de desempeño de seguridad básico establecido en la filosofía de diseño de la NSR-10. Por otro lado, los puntos de desempeño del PFW y HRCW cayeron dentro del rango de IO para ambos niveles de amenaza sísmica, lo que demuestra sus excelentes comportamientos sísmicos. Los resultados obtenidos aprueban el uso de estos sistemas estructurales para viviendas de uno y dos pisos.

Palabras clave: Diseño Sísmico Basado en Desempeño, modelo histerético multilineal de Mostaghel, Optimización por Enjambre de Particulas, fragilidad, Análisis Dinámico Incremental, histéresis, muro de ferrocemento, muro de Madera Plástico Reciclado, muro hueco de concreto reforzado, pruebas de carga cíclica.

Contents

List of Figures

List of Tables

List of acronyms

Acronym	Meaning
ADRS	Acceleration-Displacement Response Spectra
ASCE	American Society of Civil Engineers
ASTM	American Society for Testing and Materials
ATC	Applied Technology Council
CDF	Cumulative Distribution Function
CP	Collapse Prevention
CSM	Capacity Spectrum Method
DBE	Design Basic Earthquake
DCM	Displacement Coefficient Method
DM	Damage Measure
DS	Damage State
EDP	Engineering Demand Parameter
FBD	Force-Based Design
FEMA	Federal Emergency Management Agency
GA	Genetic Algorithm
HRCW	Hollow Reinforced Concrete Wall
IDA	Incremental Dynamic Analysis
IM	Intensity Measure
IO	Immediate Occupancy
LVDT	Linear Variable Differential Transformer
LS	Life Safety
MCE	Maximum Considered Earthquake
MCS	Monte Carlo Simulation
MDoF	Multiple Degree of Freedom
ME	Maximum Earthquake
NDA	Nonlinear Dynamic Analysis
NGA	Next-Generation Attenuation
NRHA	Nonlinear Response History Analysis
NSP	Nonlinear Static Procedures
NSR-10	Reglamento Colombiano de Diseño y Construcción Sismo Resistente

Acronym	Meaning
PBBE	Performance-Based Earthquake Engineering
PBE	Performance-Based Engineering
PBSD	Performance-Based Seismic Design
PEER	Pacific Earthquake Engineering Research Center
PFW	Precast Ferrocement Wall
PGA	Peak Ground Acceleration
PGV	Peak Ground Velocity
PHM	Polygonal Hysteretic Models
PSDF	Power Spectral Density Function
PSO	Particle Swarm Optimization
RC	Reinforced Concrete
RPL	Recycled Plastic Lumber
RPLW	Recycled Plastic Lumber Wall
SDoF	Single Degree of Freedom
SE	Serviceability Earthquake
SEAOC	Structural Engineers Association of California
SHM	Smooth Hysteretic Models
SPL	Structural Performance Level

1 Introduction

1.1 Motivation

The occurrence of strong and destructive earthquakes, housing deficiency and sustainable development, have inspired the need to create and to research innovative structural materials and systems that have satisfactory seismic performance and are environmentally friendly. Some of the innovations that have emerged in the field of structural engineering with these purposes are the structural systems based on ferrocement walls, prestressed and reinforced concrete walls, and recycled plastic lumber walls, which have been proposed initially for one and two-story housing.

Due to that analytical modeling alone is not adequate for predicting nonlinear seismic response of structural systems that have not been subjected to past earthquakes (FEMA, 2009a), experimental studies have been carried out in recent years so as to determine the structural parameters, properties and experimental hysteretic behavior of these structural walls, to calibrate hysteretic models and identification techniques, and to develop design criteria.

It has been evinced that under the action of dynamic loads, such as seismic loads, these structural systems present a nonlinear behavior known as hysteresis which appears when the structural response of the system begins to be inelastic. This nonlinear behavior is represented by several physical phenomena, such as stiffness degradation, strength deterioration and pinching effect. The structural walls exhibit these phenomena either alone or in combination, so it is essential to have a powerful mathematical hysteretic model capable of representing and describing completely their nonlinear behavior in order to design them and to assess their actual performances for different earthquake hazard levels in such a way that the actual inelastic behavior and energy dissipation capacity can be considered. However, the conventional linear elastic analysis and design approach does not include any methodology that allows reaching these purposes.

In that sense, the need for more realistic and reliable seismic design criteria has encouraged the ongoing development of new seismic design approaches that consider the uncertainties associated with the determination of the actual response and capacity of structures for specific seismic hazard levels. For instance, trends in seismic structural design move away from the conventional seismic design approaches which present several shortcomings (see e.g. Liu et al., 2004) and are based on the Force-Based Design (FBD) approach in which the structural response is calculated within the elastic behavior range and, subsequently, the inelastic responses are obtained applying the

well-known response reduction factor (R), which causes a misconception of the actual response. Another important limitation of the FBD approach is related to the design philosophy: the traditional seismic design codes are principally based on life safety, which implicitly is related to the fulfillment of only one performance objective, controlling the damage via drift limits. This philosophy does not necessarily ensure that the structure will be operational after frequent, occasional or rare earthquakes; in fact, significant damage can occur even when buildings are compliant with the building code. For instance, although the 1989 Loma Prieta, 1994 Northridge, and 1995 Kobe earthquakes did not cause large life loss, the level of damage of buildings, economic loss due to loss of use, and cost of repair were unexpectedly high (Ghobarah, 2001); therefore, it is indispensable to know what the structural performance will be at determined earthquake hazard levels and what the consequences of that performance will be in terms of damage, casualties, downtime, or economic losses.

Nowadays, the structural design has been focusing on the Performance-Based Seismic Design (PBSD) philosophy that assesses how structures can perform at specific seismic hazard levels, taking into account their actual inelastic behavior and energy dissipation capacity. In this design philosophy, the design criteria and the performance are expressed in terms of achieving stated performance objectives when the structures are subjected to specific levels of seismic hazard and in quantitative measurements of the acceptable risk of incurring levels of damage, respectively.

As the performance objective of structures usually implies large inelastic demands, PBSD requires nonlinear static or dynamic procedures in order to facilitate a better perception of the actual inelastic behavior and failure modes of structures, which resolves many uncertainties associated with elastic procedures and leads to more reliable and efficient solutions (FEMA, 2009a). In fact, the Nonlinear Dynamic Analysis (NDA) is the most reliable technique because provides a realistic estimation of the seismic response and performance of a structure subjected to sets of strong ground motions which are selected and scaled according to the objectives of the analysis, and takes into account hysteretic models that describe the inelastic behavior of the elements when are under cyclic loads (earthquake ground motions), which produces an explicit simulation of the energy dissipation capacity in the nonlinear range.

In this regard, PBSD together with NDA would allow designing and assessing the structural walls that form the earthquake-resistant systems of one and two-story housing, in order to know their actual seismic performances when they are subjected to different earthquake hazard levels.

1.2 Problem statement

Few studies have investigated the application of PBSD to innovative structural systems, and almost all have been focused on reinforced concrete walls using nonlinear static procedures. This is largely due to the fact that most of the published literature concerned with the experimental behavior

of different types of structural walls have not achieved to be extended to the nonlinear dynamic analysis procedures used in the PBSD approach, because of the lack of application of mathematical hysteretic models with suitable parameter identification techniques that allow simulating essential parameters in the seismic performance assessment, such as the actual inelastic behavior and energy capacity dissipation.

1.3 Objectives

The main objective of this dissertation is to develop a methodology based on nonlinear dynamic analysis for the performance-based seismic design and assessment of structural walls that form the earthquake-resistant system of one and two-story housings, such as recycled plastic lumber walls, precast ferrocement walls, and hollow reinforced concrete walls, using the Mostaghel's multilinear hysteretic model. In this document, the methodology will apply to these types of structural walls for sets of actual recorded and artificial ground motions.

According to this main idea, the following specific objectives are proposed:

- Present a whole literature review about the fundamentals and the development of PBSD, as well as the procedures for the performance-based seismic assessment of structures.
- Develop a novel procedure for the parameter identification of the Mostaghel's multilinear hysteretic model using the simple PSO algorithm.
- Experimentally obtain the hysteretic behavior, structural parameters and damage limit states of the structural walls.
- Test and evaluate the appropriateness and the efficiency of the Mostaghel's multilinear hysteretic model together with the proposed identification procedure for the simulation of the hysteretic behavior of the structural walls.
- Define the structural performance levels of the structural walls and the earthquake hazard levels, as well as the sets of actual recorded and artificial ground motions.
- Calculate the performance points and the seismic fragility functions of the structural walls subjected to the two sets of ground motions using the IDA procedure for the nonlinear dynamic analysis.
- Correct the obtained fragility functions by the FEMA P695 methodology so as to consider the total system damage uncertainty.
- Assess the probability of damage and collapse of the structural walls.

1.4 Outline of the thesis

After the previous introduction, this dissertation continues in Chapter 2 which is devoted to present the fundamentals of PBSD. This chapter includes a complete literature review of the state of development of PBSD and of the methodologies that have been proposed to estimate and to assess the seismic performance capability of structures. Then, Chapter 3 expounds the theory of structural dynamics related to linear and nonlinear behavior of SDoF systems, in which hysteresis is described in detail. Here, the Mostaghel's hysteretic model is explained and a novel procedure for the parameter identification of this model is developed using the PSO algorithm. Chapter 4 shows the experimental results of the cyclic loading tests, which are used to estimate the structural parameters and properties of each structural wall. In this sense, the chapter also summarizes the analytical modeling of the hysteretic behavior of each system, applying some variants of the Mostaghel's multilinear hysteretic model together with the proposed identification procedure. Subsequently, Chapter 5 presents the performance-based seismic assessment of the structural walls, which includes the estimation of performance points and fragility curves both for actual recorded and artificial ground motions. The document ends in Chapter 6 with a summary of the main results of the research, some concluding remarks and various suggestions that could inspire future research and work.

2 Fundamentals of Performance-Based Seismic Design

2.1 Basic concepts

Performance-based engineering (PBE) is relatively a new design philosophy that evaluates how buildings can perform when at specified levels of the excitations that can act on them. For the case that seismic hazard controls the design, the philosophy is known as Performance-based Earthquake Engineering (PBEE), which involves the complete design stage, construction and monitoring of the maintenance and function of the building during its lifespan, in order to assure that it will resist the effects of earthquake ground motions of different severities within specified limiting levels of damage (Bertero and Bertero, 2002). To achieve this, PBEE defines a procedure that consists of four important tasks: the definition of the seismic hazard, the structural analysis, the determination of damage and the loss analysis. In this regard, Performance-based seismic design (PBSD) can be defined as a subset of PBEE that refers a methodology focused on the design process, in which the design criteria are expressed in terms of achieving stated performance objectives when the structure is subjected to stated levels of seismic hazard (Ghobarah, 2001). PBSD considers uncertainties associated with the quantification of seismic hazard and actual building response, which allows obtaining a more realistic and reliable probable performance expressed in quantitative measurements of the acceptable risk of incurring levels of damage, life losses, downtime and economic losses caused by future earthquakes (Hamburger et al., 2004).

In general, PBSD is considered as an iterative process that initiates with the proper selection of performance objectives (which may be a limit state, a displacement, a drift, or a target damage state), followed by the development of a preliminary design, the performance capability determination, the assessment as to whether or not the design meets the performance objectives, and finally redesign and reassessment, if required, until the desired performance level is achieved (FEMA, 2006). Fig. **2-1** presents the key steps in this process. The performance assessment is considered as an indispensable step of the PBSD methodology, which consists of a structural analysis to predict building response to earthquake hazards, an assessment the likely amount of damage, and a determination the probable consequences related to that damage (see e.g. Fig. **2-2**).

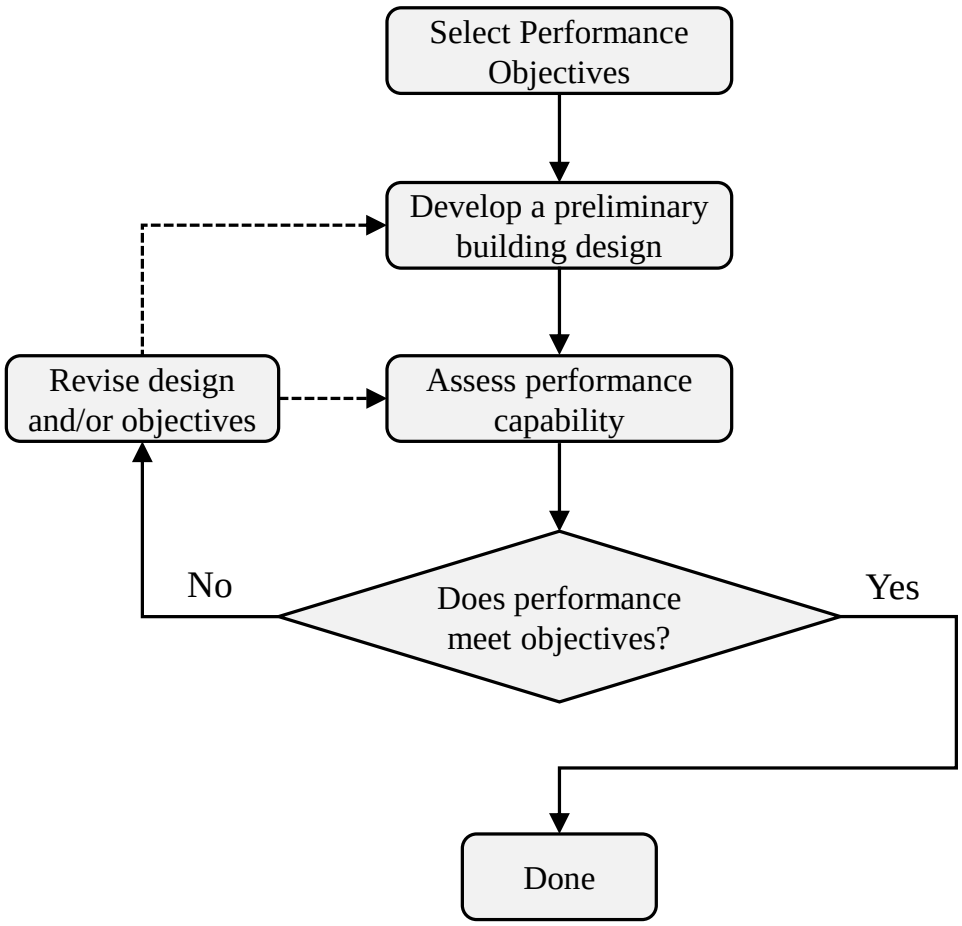

Figure 2-1: General flowchart of the PBSD process. (Adapted from FEMA (2006))

PBSD presents several advantages in contrast to prescriptive design approaches, such as the force-based design (FBD). For instance, the PBSD approach takes into account a systematic methodology to assess the performance capability of a building, system or component; this methodology provides a framework to determine the levels of safety and property protection, and the acceptable cost to stakeholders based on the specific needs of a project. Also, PBSD establishes a vocabulary that facilitates the communication between stakeholders and design professionals on the development and selection of design options. In addition, this new design philosophy can be used for (FEMA, 2006):

- Designing individual buildings with a higher level of confidence so that the intended performance by present seismic design codes will be achieved.
- Designing individual buildings that are capable of meeting the intended performance by present seismic design codes, but with lower construction costs.
- Designing individual buildings to achieve higher performance (and lower potential losses) than intended by present seismic design codes.

- Designing individual buildings that are beyond of code-prescribed limits with regard to configuration, materials, and systems, to meet the intended performance by present seismic codes.
- Assessing the potential seismic performance of existing structures and estimating potential losses in the event of a seismic hazard.
- Assessing the potential performance of current prescriptive code requirements for new buildings and serving as the basis for improvements to code-based seismic design criteria so that future buildings can perform more consistently and reliably.

2.2 State of development

The evolution of PBSD can be tracked against the occurrence of damaging earthquakes. For instance, in the latter part of the last century, earthquakes encouraged the development of design criteria that demanded minimum levels of lateral strength and ductility of structures, in order to avoid the collapse and to guarantee the life safety, which can be understood as the fulfillment of a unique performance objective. However, although the 1989 Loma Prieta, 1994 Northridge, and 1995 Kobe earthquakes did not cause large life loss, the level of damage of buildings, economic loss due to loss of use, and cost of repair were unexpectedly high (Ghobarah, 2001). For all of these reasons, it was generated a special interest and a great need to develop improved procedures and new building code requirements focused on a more formal performance-based seismic approach to estimate performances objectives for specific levels of seismic hazard, achieving in this way a more realistic conception of the expected structural response.

Another source of interest in PBSD was encountered in seismic retrofit of existing buildings. According to Hamburger et al. (2004), owners of existing buildings would not commit to investment in the retrofit process unless they knew what the probable performance of their buildings in future earthquakes was. As the codes did not provide this information, engineers began to develop basic procedures to assess the likely seismic performance of existing buildings so that they could evaluate the possible damage levels and their consequences. Due to the needs generated by the above reasons, the idea that seismic design can be based on achieving multiple performance objectives and their correct implementation led toward the development of the first generation procedure of PBSD. The bases of this approach are credited in three documents: SEAOC (1995), ATC (1996), and FEMA (1997).

In 1995, the Structural Engineer Association of California (SEAOC) developed a document know as *Vision 2000*, which provided a framework for procedures that lead to the design of structures of predictable seismic performance and is able to consider multiple performance objectives. This document is considered as the root of PBSD, which expounded and addressed the concepts related to performance levels for structural and nonstructural systems, described them in terms of

specified limits of transient and permanent drift. Also, SEAOC (1995) suggested that the capacity design principles should be applied to guide the inelastic response analysis of the structure and to designate the ductile links or forces in the lateral force resisting system. Possible design approaches presented include various elastic and inelastic analysis procedures (Ghobarah, 2001) such as conventional force and strength methods, displacement-based design, energy approaches, and prescriptive design approaches.

Subsequently in 1996, the Applied Technology Council (ATC) presented the ATC 40 document, *Seismic Evaluation and retrofit of concrete buildings* (ATC, 1996), which considers the PBSD as a methodology in which structural design criteria are expressed in terms of achieving a set of predefined performance objectives that are the desired levels of building performances defined in terms of acceptable structural and nonstructural damages for specified levels of seismic hazard (Zameeruddin and Sangle, 2016). The ATC 40 highlights the use of procedures based on the Capacity Spectrum Method (CSM) that involves determining the capacity of the structure using a nonlinear static analysis, e.g. pushover analysis, and obtaining the seismic demand via elastic spectra for different earthquakes which have specific probabilities of occurrence related to possible damage states. The performance point is defined as the intersection point between the capacity curve and the demand spectrum.

In 1997, the Federal Emergency Management Agency (FEMA) sponsored a study focused on rehabilitation design guidelines, known as the FEMA 273 report, *NEHRP guidelines for the seismic rehabilitation of buildings* (FEMA, 1997). This document presented a set of performance objectives related to probabilistic ground motions and also considered different types of analyses, ranging from linear static analysis to non-linear dynamic analysis, to obtain the structural response in terms of multi-level performance. The different performance levels were defined for non-structural systems and lateral load resisting structural systems, being the latter evaluated via drift limits. FEMA (1997) provided a direct method to calculate the displacement demand (performance point) of a nonlinear system, by multiplying the structural response of the elastic linear system by several coefficients; this procedure is widely known as the Displacement Coefficient Method (DCM).

These documents described the initial concepts of performance levels related to damage and to seismic hazard levels, and also provided a comprehensive set of guidelines on nonlinear analysis techniques and acceptance criteria. The first-generation procedures represented an important improvement over then-current building code procedures in the sense that they provided a systematic means of designing buildings to achieve the desired level of performance (FEMA, 2006).

The origin of the second generation of PBSD is traced to the FEMA 356 document, *Prestandard and Commentary for the Seismic Rehabilitation of Buildings* (FEMA, 2000), which was elaborated by FEMA in association with the American Society of Civil Engineers (ASCE). The document was presented as an update in the form of a preliminary design standard of the FEMA 273 report and represented an incremental improvement to the first-generation procedures with respect to tech-

nical updates of the analytical requirements and acceptance criteria according to the information gained from using the procedure in engineering practice and in study cases given in others FEMA reports. Later, ASCE (2007) presented a standard developed from the FEMA 356 document that provided an improved generation of the performance-based seismic rehabilitation methodology based on the selection of rehabilitation objectives which involved building performance and hazard levels. This standard recommended four analysis procedures to estimate seismic demands: the first two were linear static and dynamic force-based procedures, whereas the third and the fourth were nonlinear static and dynamic displacement-based procedures. In recent years, it was updated and replaced by the ASCE 41-13 standard, *Seismic Evaluation and Retrofit of Existing Buildings* (ASCE, 2014), which defines the present generation and the current state of PBSD.

Thanks to the second generation procedures, the PBSD concepts have become widely known in the field of structural and earthquake engineering, and they have encouraged the use of improved nonlinear analysis techniques. Nevertheless, the ongoing advances and researches allowed identifying the following limitations in these procedures (Hamburger et al., 2004; Zameeruddin and Sangle, 2016):

- The accuracy and reliability of available analytical procedures in predicting actual building response was questionable because of the second generation procedures evaluated the performance on the basis of the demands and capacities of individual components, rather than global building behavior.
- The level of conservatism in most of the acceptance criteria contained in the documents was questionable because they were based on judgment from the engineers' experience, rather than experimental test results data or other scientific evidence.
- The limitation to reliably and economically apply the PBSD procedures for the design of new buildings.
- The need for alternative ways of communicating the performance to stakeholders that be more meaningful and useful in order to make a decision.

With the purpose of addressing these issues, FEMA began planning the development of the next-generation PBSD procedures for new and existing buildings, initiating a series of projects which would become known as the ATC 58 projects (ATC, 2003). These projects considered relating discrete performance levels to the primary concerns of the stakeholders; in fact, the ATC 58 recommended performance metrics based on direct and indirect losses, cost of damage and repairs, downtime of the building, life losses and casualties. The ATC 58 program led to the FEMA 445 publication, *Next-Generation Performance-Based Seismic Design Guidelines, Program Plan for New and Existing Buildings* (FEMA, 2006), which would afford a task-oriented program for improving the PBSD procedures.

Subsequently, the ATC 58 developed the first in a series of the next-generation PBSD criteria and guidelines, known as FEMA P58 report, *Seismic Performance Assessment of Buildings* (FEMA,

2012), which included a methodology and an implementation guide applicable to the assessment of new or existing buildings. This methodology expresses the consequences as probability distributions and defines performance objectives based on an acceptable risk of incurring casualties, direct economic loss (repair cost), and occupancy interruption (downtime) associated with the repair or replacement of damaged structural and nonstructural elements at a specified level of seismic hazard (Zameeruddin and Sangle, 2016). Fig. **2-2** shows the corresponding key steps of the FEMA P58 methodology.

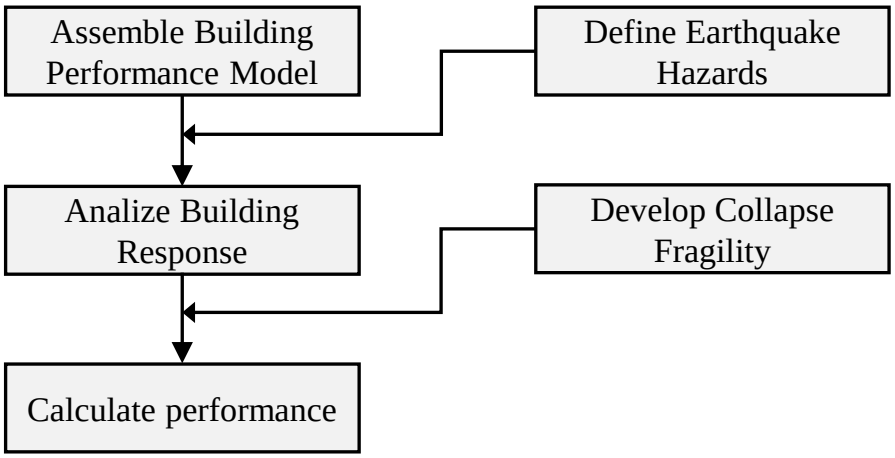

Figure 2-2: Performance assessment process. (Adapted from FEMA (2012))

The FEMA P58 methodology for PBSD allows three different types of performance assessments (FEMA, 2012):

1. Intensity-based assessment, which evaluates the probable performance of a building assuming that it is subjected to a specified earthquake shaking intensity, e.g. a response spectrum of a design code;

2. Scenario-based assessment, which evaluates the probable performance of a building assuming that it is subjected to an earthquake scenario consisting of a specific magnitude earthquake occurring at a specific location relative to the building site;

3. Time-based assessment, which evaluates the probable performance of a building over a specified period of time considering all earthquakes that could occur in that time period, and the probability of occurrence associated with each earthquake.

The continuous development of the PBSD generations procedures has created the need for developing simplified and useful tools that assist the engineers in the PBSD process, in order to make it more practical. In this way, it has been necessary to research on applications of the PBSD approach to different structural systems, optimal simulation techniques, experimental and hysteretic behavior of structural systems, nonlinear dynamical models, seismic hazard determination, risk communication, among others.

2.3 Performance Objectives

Performance objectives specify the desired seismic performance of structures, which are defined by selecting the expected performance levels for specific earthquake hazard levels. These objectives can be assigned using structural, functional, preservation, or economic considerations which principally depend on the use of structures. Selecting the performance objectives is the first step in the PBSD process (see Fig. **2-1**), in which each performance objective is intended as the admissible risk of incurring specific levels of damage at a specified level of seismic hazard. In the present PBSD generation, the consequential losses that occur as a result of that damage can be associated with both structural and nonstructural damage; however, the FEMA P58 methodology allows expressing them in the form of casualties, direct economic costs, and downtime (see e.g. FEMA, 2012).

A seismic design using the PBSD approach could consider many possible singles, dual or multiple performance objectives, which helps to owners and stakeholders to understand, in a realistic and reliable way, the seismic performance of their structures and to make decisions about it. In this way, the building owner sets performance objectives and the engineer identifies both the seismic demand to be used in the analysis and the acceptability criteria to be used for the assessment and design of the structural and nonstructural systems.

2.3.1 Performance Levels

A performance level is defined as a limiting damage state or condition represented by the physical damage of the building components, the risk to life safety of the occupants due to the damage, and the post-earthquake serviceability of the building facilities. In general, building performance levels are a combination of structural and nonstructural performance levels. The first and second generation procedures of PBSD introduced the concept of performance in terms of discretely defined performance levels with names intended to connote the expected level of damage: Operational, Immediate Occupancy, Collapse Prevention, and Collapse.

2.3.1.1 Proposal of the Vision 2000 report

In the Vision 2000 report, SEAOC (1995) defined four general performance levels which include both structural and nonstructural considerations, in qualitative terms of public acceptability and in engineering technical terms for the evaluation and design of existing and new buildings. Table **2-1** shows a description of the Vision 2000 performance levels.

Table 2-1: Building performance levels defined by SEAOC (1995)

Performance level	Damage state	Description
Fully Operational	Negligible	Structural and non-structural negligible damages. The building remains completely safe for its occupants. All the facilities and services of the building remain functional and available for use. In general, repairs are not required.
Operational	Light	The structural damage is light and the non-structural elements present moderate damage. The building remains safe for its occupants. Most services and functions are resumed immediately. Some repairs are required.
Life Safety	Moderate	Structural and non-structural damages are moderate. The structure exhibits a diminution in its lateral strength and stiffness; however, it remains stable and functional. Life safety is protected and the building may be evacuated after the earthquake. Repair is possible.
Near Collapse	Severe	Structural damage is severe and the non-structural elements fail; however, the collapse is prevented. The safe of occupants is at risk. Repair is probably not practical so it can be more feasible to demolish the building.
Collapse	Complete	Structural collapse. Repair is not possible.

2.3.1.2 Proposal of the present-generation of PBSD

ATC (1996) and FEMA (1997, 2000) defined a set of structural and nonstructural performance levels which are very similar in terminology and concepts each other; later, ASCE (2007, 2014) improved these proposed performance levels. According to this, the performance levels of theses reports are grouped together in the present document in order to avoid the redundant text.

The structural and nonstructural performance levels are defined independently: structural performance levels are given names and number designations, whereas nonstructural performance levels are given names and letter designations. The structural performance levels Immediate Occupancy (IO), Life Safety (LS), and Collapse Prevention (CP), are defined as discrete damage states and they can be used directly in evaluation and retrofit procedures to define technical criteria. These descriptions are conceptually similar to those proposed in the Vision 2000 report (SEAOC, 1995) and they have been selected to allow combinations that will correspond to single performance levels also proposed by SEAOC (1995), providing the flexibility to formalize the combined performance levels commonly used in practice.

Building performance levels are formed of combinations of structural and nonstructural performance levels in order to completely describe the desired limiting damage state for a building. Fig. **2-3** depicts possible combinations of performance levels. The four more common building performance levels of the present-generation of PBSD are shown in Table **2-2** with their respective description.

Nonstructural Performance Levels	**Structural Performance Levels**					
	Immediate Occupancy (S-1)	Damage Control Range (S-2)	**Life Safety (S-3)**	Limited Safety Range (S-4)	**Collapse Prevention (S-5)**	Not Considered (S-6)
Operational (N-A)	**Operational (1-A)**	2-A	Not Recommended	Not Recommended	Not Recommended	Not Recommended
Immediate Occupancy (N-B)	**Immediate Occupancy (1-B)**	2-B	3-B	Not Recommended	Not Recommended	Not Recommended
Life Safety (N-C)	1-C	2-C	**Life Safety (3-C)**	4-C	5-C	6-C
Hazards Reduced (N-D)	Not Recommended	2-D	3-D	4-D	5-D	6-D
Not Considered (N-E)	Not Recommended	Not Recommended	Not Recommended	4-E	**Collapse Prevention (5-E)**	No evaluation or retrofit

Figure 2-3: Combinations of structural and nonstructural seismic performance levels (see ATC, 1996; FEMA, 1997, 2000; ASCE, 2007, 2014)

2.3.2 Earthquake Hazard Levels

Earthquake hazard levels are expressed either by a probabilistic approach, i.e. specifying a level of ground motion associated with a given probability of occurrence, or in terms of the maximum ground motion expected from a single event of a specified magnitude on a specified source fault, which is known as a deterministic approach. In both cases, the level of earthquake hazard is expressed in terms of either response spectra or an equivalent series of simulated recordings of earthquake motions to be used subsequently in the seismic analysis and design.

2.3.2.1 Proposal of the Vision 2000 report

SEAOC (1995) established the parameters to define the seismic hazard studies aimed at obtaining four earthquake hazard levels, defined as Frequent, Occasional, Rare, and Very Rare, which would allow analyzing the structure considering the possible seismic events that could occur during its lifetime. Table **2-3** shows the earthquake hazard levels proposed in the Vision 2000 report with their respective return period and probability of occurrence.

Table 2-2: Building performance levels of the present-generation of PBSD (ATC, 1996; FEMA, 1997, 2000; ASCE, 2007, 2014)

Performance level	Damage state	Description
Operational (1-A)	Very light	No permanent drift. Structure substantially retains original strength and stiffness. Minor cracking of facades, partitions, and ceilings as well as structural elements. All important systems for the normal operation are functional. Continued occupancy and use highly likely. Negligible damage occurs in non-structural components. This is the performance level related to functionality
Immediate Occupancy (1-B)	Light	No permanent drift. Structure substantially retains original strength and stiffness. Continued occupancy likely. Equipment and contents are generally secure but perhaps some secondary services present small interruptions of easy and immediate repair. Some cracking of facades, partitions, and ceilings as well as structural elements. This level corresponds to the most widely used criteria for essential facilities.
Life Safety (3-C)	Moderate	Some permanent drift. Some residual strength and stiffness left in all stories. Gravity-load-bearing elements function. No out-of-plane failure of walls. Damage to partitions. Continued occupancy might not be likely before repair. The building might not be economical to repair. Falling hazards, such as parapets, mitigated, but many architectural, mechanical, and electrical systems are damaged. This corresponds to the obtained performance level by the application of the conventional seismic design codes
Collapse Prevention (5-E)	Severe	Large permanent drifts. Little residual stiffness and strength to resist lateral loads, but gravity load-bearing columns and walls function. Some exits blocked. The building is near collapse in aftershocks and should not continue to be occupied. Extensive damage. It is very likely that the damage will not be technically or economically repairable.

Table 2-3: Earthquake hazard levels according to SEAOC (1995)

Earthquake level	Return Period	Probability of occurrence
Frequent	43 years	50% in 30 years
Ocassional	72 years	50% in 50 years
Rare	475 years	10% in 50 years
Very Rare	975 years	5% in 50 years

2.3.2.2 Proposal of the ATC 40 report

The ATC 40 report defined three levels of earthquake hazard: 1) the Serviceability Earthquake (SE), which is 0.5 times the Design Earthquake, represents a frequent seismic event that likely could occur during the life of the building; 2) the Design Basic Earthquake (DBE), which represents a rare seismic event that can occur during the life of the building; and (3) the Maximum Earthquake (ME)[1], which is typically about 1.5 times the Design Earthquake, is defined deterministically as the maximum level of earthquake ground motion which may ever be expected at the building site so it represents a very rare seismic event. The return period and the probability of occurrence associated with these earthquake hazard levels are summarized in Table **2-4**.

Table 2-4: Earthquake hazard levels according to ATC (1996)

Earthquake level	Return Period	Probability of occurrence
Serviceability Earthquake (SE)	72 years	50% in 50 years
Design Basic Earthquake (DBE)	475 years	10% in 50 years
Maximum Earthquake (ME)	975 years	5% in 50 years

2.3.2.3 Proposal of the ASCE 41-13 standard

ASCE (2007, 2014) improved the earthquake hazard levels initially proposed by FEMA (1997, 2000). The ASCE 41-13 standard uses several probabilistic earthquake hazard levels to describe earthquake ground motions for which performance evaluations are made. Such ground motions are often referred to either as a probability of occurrence in a specified time period or as a return period of the specified ground motion (see Table **2-5**). This standard defines explicitly the Maximum Considered Earthquake (MCE) and suggests that once MCE is obtained, the Design Basic Earthquake(DBE) is taken as 2/3 times the MCE.

[1]The definition of the ME hazard level is different from the definition of the Maximum Considered Earthquake (MCE) proposed by FEMA (1997, 2000) and ASCE (2007, 2014). In probabilistic terms, the ME has a return period of 975 years, whereas the MCE has a return period of 2475 years.

Table 2-5: Earthquake hazard levels according to ASCE (2007, 2014)

Earthquake level	Return Period	Probability of occurrence
Frequent	43 years	50% in 30 years
Ocassional	72 years	50% in 50 years
Basic Safety Earthquake (BSE)	225 years	20% in 50 years
Design Basic Earthquake (DBE)	475 years	10% in 50 years
Very Rare	975 years	5% in 50 years
Maximum Considered Earthquake (MCE)	2475 years	2% in 50 years

2.3.3 Examples of Performance Objectives proposals

The selection of performance objectives is not the same for all building projects because this depends in large part on the specific performance that the owners choose and expect. Nevertheless, some standards and technical reports have defined several proposals of performance objectives for different acceptability criteria and risk categories of structures; these proposals can be used as a model to set the performance objectives of any structural design project. The first proposal of performance objectives in PBSD was made by SEAOC (1995) and it has been widely used as a reference for others proposals (see e.g. ATC, 1996; FEMA, 1997, 2000; ASCE, 2007, 2014).

Fig. **2-4** shows three multi-performance objectives of the Vision 2000 report, which are defined according to the occupancy or use of the structure: the *Safety Critical Objectives*, associated with facilities that contain large quantities of hazardous materials (toxins, radioactive materials, explosives) with significant external effects of damage to the building; the *Essential Objectives*, related to critical post-earthquake facilities (hospitals, communications centers, police, fire stations, etc.); and the *Basic Objectives* that include all other structures. On the other hand, Fig. **2-5** shows a dual performance objective known as the Basic Safety Performance Objective which is commonly related to the seismic design goal of the conventional codes (ATC, 1996; AIS, 2010).

2.4 Performance-based seismic assessment

Performance-based seismic assessment is the process used to determine the performance capability of a given building design, in which structural analyses are conducted to predict building response to earthquake hazards and to assess the likely amount of damage. Subsequently, this predicted performance is compared with the desired performance objectives for the building: if the assessed performance meets the defined performance objectives, the building design is suitable; otherwise, the building design must be revised or the performance objectives modified until the performance and the desired objectives match (FEMA, 2009a).

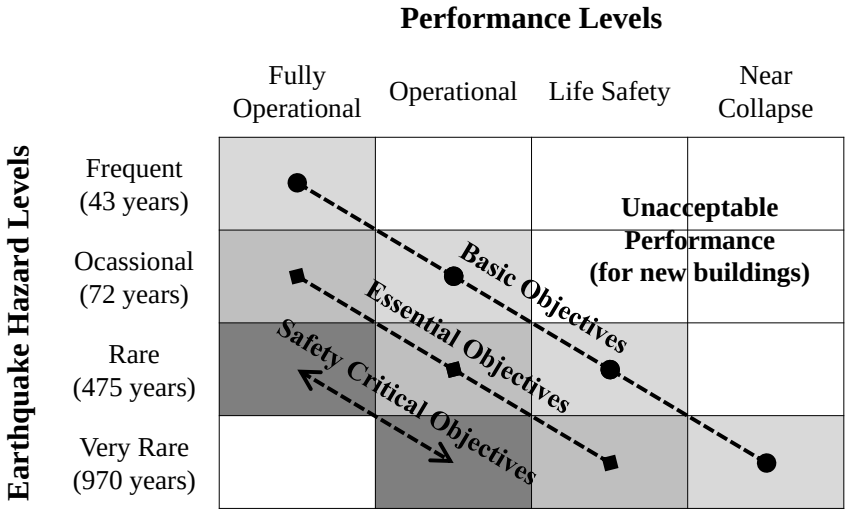

Figure 2-4: Recommended performance objectives in the Vision 2000 report (SEAOC, 1995)

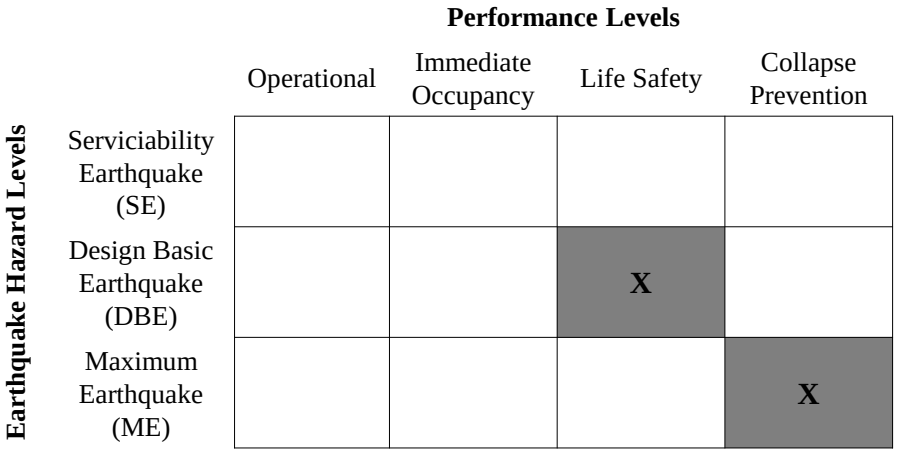

Figure 2-5: The Basic Safety Performance Objective of the ATC 40 report and the NSR-10 building code (ATC, 1996; AIS, 2010)

In this process, there are two fundamental elements: Capacity, which is a representation of the ability that the structure has to resist seismic loads; and Demand, which represents the seismic hazard. Nonlinear structural analysis has been widely employed to determine these elements. Despite the fact that linear elastic analysis gives satisfactory results of the elastic capacity of structures and it has an uncertainty relatively low when structures are expected to behave within the elastic range, it can predict neither inelastic demands nor failure mechanisms that structures would experience at the performance objective. Due to that, nonlinear analysis procedures are used to determine the actual performance of structures, which also help to understand the behavior of them beyond of their elastic range when they are subjected to high levels of seismic hazard. This choice diminishes the uncertainties and leads to a design that focuses on the critical aspects of the building, leading to more reliable and efficient solutions (NIST, 2017a).

There are two types of procedures within nonlinear structural analysis to model the seismic effects and to assess the performance of structures: Nonlinear Static Analysis, which uses response spectra and equivalent Single Degree of Freedom (SDoF) models; and Nonlinear Dynamic Analysis, which employs ground motion records with a detailed structural model. In recent years, both have been applied in researches, building codes and standards for seismic design and assessment of structures (see e.g. ASCE, 2014, 2017b,a; FEMA, 2009a,b, 2012). However, Nonlinear Dynamic Analysis has become more reliable because nonlinear static procedures imply greater uncertainty due to the empirical procedures used to estimate the maximum response displacement (FEMA, 2009a). The nonlinear static and nonlinear dynamic procedures used in performance-based seismic assessment are presented and explained in the following sections.

2.4.1 Nonlinear Static Analysis

Nonlinear static analysis involves a set of Nonlinear Static Procedures (NSPs) which allow estimating the maximum displacement demand of equivalent SDoF structural models subjected to specific seismic ground motions that are represented by response spectra. The central focus of this type of procedures is the generation of the capacity curve by nonlinear static analysis (pushover analysis) which represents the lateral displacement as a function of the force applied to the structure. The capacity curve is generally constructed to represent the first mode response of the structure based on the assumption that the fundamental mode of vibration is the predominant response of the structure.

NSPs are used in the performance assessment of structures given their simplicity. The predominant methods of NSPs include the Capacity Spectrum Method that uses the intersection of the capacity (pushover) curve and a reduced response spectrum to estimate maximum displacement; and the Displacement Coefficient Method that uses pushover analysis and a modified version of the equal displacement approximation to estimate the maximum displacement.

2.4.1.1 Capacity Spectrum Method

Capacity Spectrum Method (CSM) is a nonlinear static method that provides a useful graphical representation of the estimation of the performance point which represents the condition for which the seismic capacity of the structure is equal to a specified seismic demand imposed on it. In general, CSM defines this point by the intersection of the capacity curve with a specified reduced demand spectrum that represents the nonlinear demand. The determination of the performance point is achieved by an iterative process because essential parameters of CSM are based on unknown values related to the ductility. In this sense, several procedures have been proposed in order to address and to simplify that process.

The initial methodology was developed by Freeman et al. (1975) and Freeman (1978) and subsequently modified, improved and corrected, giving rise to two different approaches of CSM: the first one is known as Equivalent Linearization which was proposed in the ATC 40 report (ATC, 1996) and improved later in the FEMA 440 report (FEMA, 2009a); and the second one is the CSM based on Inelastic Spectra that was proposed by Reinhorn (1997), developed by Chopra and Goel (1999a,b) and Fajfar (1999, 2000), and extended as a mathematical procedure known as the N2 method (Fajfar, 2000).

CSM based on Equivalent Linearization: Proposal of the ATC 40 report

The inelastic response of systems subjected to seismic loads can be estimated by approximate analytical methods in which the nonlinear system is replaced by an equivalent linear system. The basic assumption in this equivalent system is that the maximum displacement of a nonlinear SDOF system can be estimated from the maximum displacement of a linear elastic SDOF system that has a period and a damping ratio that are larger than those of the initial values for the nonlinear system (FEMA, 2009a). Such elastic SDOF system is usually referred to as the equivalent or substitute system. Similarly, the period of vibration and damping ratio of the elastic system are commonly referred to as equivalent period and equivalent damping ratio, respectively; this equivalent damping is approximated by analysis procedures to avoid the dynamic analysis of the inelastic system.

The simplified inelastic analysis procedure in ATC 40 is a version of CSM which is based on equivalent linearization. This CSM technique proposed by ATC (1996) needs that both the demand response spectrum and the structural capacity curve (pushover curve) be converted to the Acceleration-Displacement Response Spectra format (ADRS), i.e. S_a *vs* S_d, and be plotted in the same graph. The conversion of the response spectrum curve, initially in the standard format (S_a *vs* T), to the ADRS format is made by applying the following equation for each ith point of the curve:

$$S_{d_i} = \frac{T_i^2}{4\pi^2} S_{a_i} g \tag{2-1}$$

where S_{a_i} is the spectral acceleration corresponding to the fundamental period T_i. The capacity curve is initially in terms of base shear V and roof displacement Δ_r. In order to develop the capacity spectrum, it is necessary to do a point by point conversion to the first mode. In this way, each ith point on the capacity curve is converted using the following equations:

$$S_{a_i} = \frac{V_i/W}{\alpha_i} \tag{2-2}$$

$$S_{d_i} = \frac{\Delta_r}{PF_1 \Phi_{1r}} \tag{2-3}$$

where W is the effective seismic weight; α_1 and PF_1 are respectively the modal mass coefficient and participation factors for the first natural mode of the structure; and Φ_{1r} is the roof level amplitude of the first mode.

Subsequently, a bilinear representation of the capacity spectrum is needed to estimate the equivalent damping and appropriate spectral reductions factors. The construction of this representation requires the definition of the trial performance point (a_{pi}, d_{pi}) that is estimated by the engineer. In this sense, the first choice of this point might be the end point of the capacity spectrum, or it might be any other point chosen on the basis of engineering judgment or could be determined by the Equal Displacement Approximation technique which is a useful tool to estimate this initial trial point in the iterative capacity spectrum procedures; this technique estimates that the inelastic spectral displacement is the same as that which would occur if the structure remained perfectly elastic, as shown in Fig. **2-6**. In the bilinear curve, the first line segment is drawn from the origin, with a slope equal to the initial stiffness of the structure. Then, the second line segment is traced from the trial performance point (a_{pi}, d_{pi}) such that when intersect the first line, at the yield point (a_{py}, d_{py}), the areas above and below the capacity curve are approximately equals (see Fig. **2-7**).

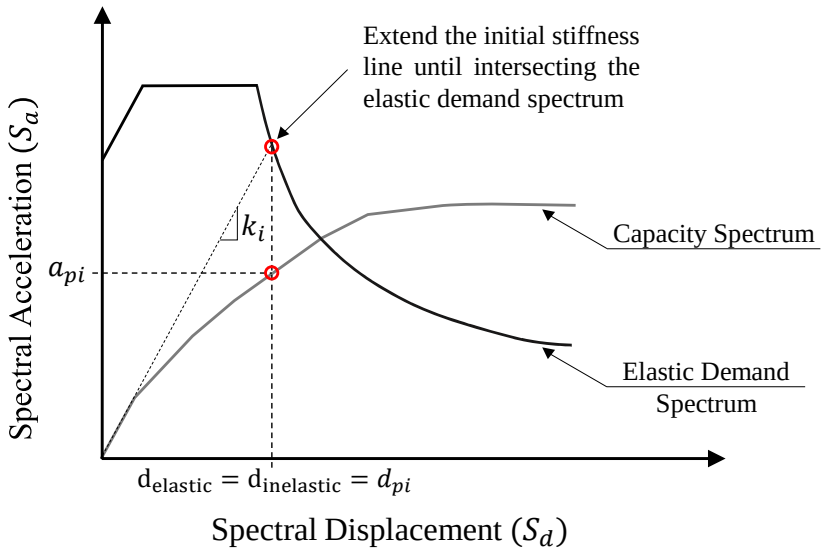

Figure 2-6: Estimation of the initial trial performance point (a_{pi}, d_{pi}) by the Equal Displacement Approximation technique (Adapted from ATC (1996))

Spectral reduction factors, which are given in terms of the equivalent damping, are defined as SR_A and SR_V; this factors are applied in the constant acceleration range of spectrum and in the constant velocity range of the spectrum, respectively. In this sense, the damping that occurs when earthquake ground motion leads to a structure into the inelastic range can be viewed as a combination of viscous damping that is inherent in the structure and hysteretic damping, which can be represented as equivalent viscous damping. The equivalent viscous damping β_{eq} associated with a maximum displacement of d_{pi} can be estimated from the following equation:

$$\beta_{eq} = 5 + \frac{63.7k(\alpha_y d_{pi} - \alpha_{pi} d_y)}{\alpha_{pi} d_{pi}}$$

where $0.33 \leq k \leq 1$ depends on the structural behavior of the building, which in turn depends on the quality of the seismic resisting system and the duration of ground shaking (see e.g. ATC, 1996).

In this way, the equations for the spectral reduction factors are given by:

$$SR_A = \frac{3.21 - 0.68\ln(\beta_{eq})}{2.12}$$

$$SR_V = \frac{2.31 - 0.41\ln(\beta_{eq})}{1.65}$$

The performance point, which represents the maximum structural displacement expected for the demand earthquake ground motion, is defined by the intersection of the capacity spectrum and the reduced demand spectrum (Bermúdez et al., 2008). If the displacement corresponding to this intersection (d_i) is within 5% of the displacement of the trial performance point d_{pi}, i.e. $0.95d_{pi} \leq d_i \leq 1.05d_{pi}$, then (a_{pi}, d_{pi}) becomes the performance point; otherwise a new (a_{pi}, d_{pi}) point is selected and the process is repeated. Fig. **2-7** illustrates the concept.

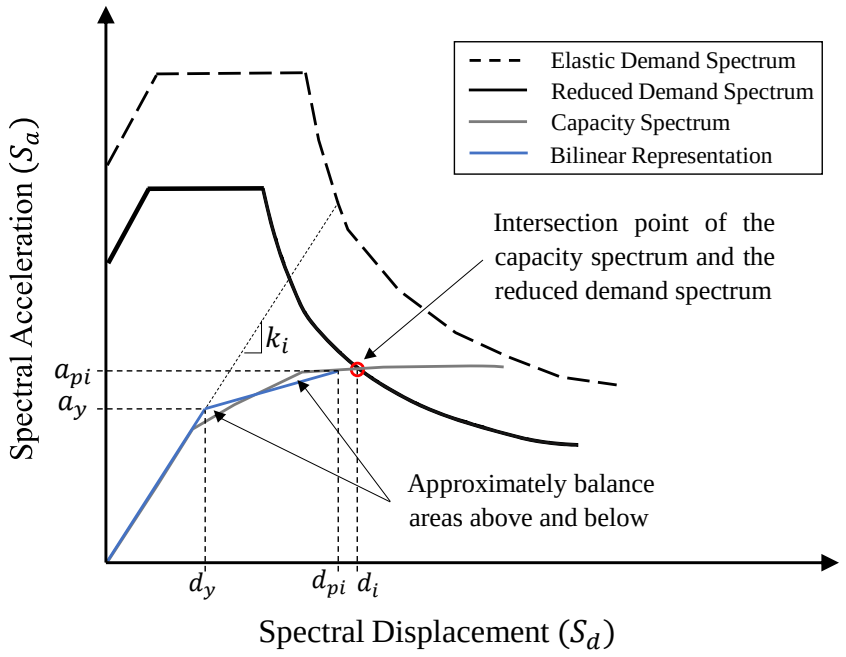

Figure 2-7: Determination of the performance point using the CSM Procedure A of the ATC 40 report (Adapted from ATC (1996))

The ATC 40 report considers three different procedures that standardize and simplify the iterative process of the determination of the performance point. It is important to highlight that these alternate procedures are based on the same concepts and mathematical relationships but they vary in their implementation. The main features of these pocedures are (ATC, 1996):

- Procedure A, which is shown in Fig. **2-7**, is the most straightforward application of CSM and consequently is the easiest procedure to understand. In addition, it is more an analytical method than a graphical method so it easily can be programmed;

- Procedure B introduces a simplification in the bilinear representation that enables a relatively direct solution for the performance point with little iteration. Also, it is more an analytical method than a graphical method, and it is probably the most convenient for spreadsheet programming. However, it may be less transparent application of the methodology than procedure A;
- Procedure C is a pure graphical method convenient for hand analysis, so it is not particularly convenient for programming. It is the least transparent application of CSM.

CSM based on Equivalent Linearization: Proposal of the FEMA 440 report

The FEMA 440 report (FEMA, 2009a) presents the improvements of equivalent linearization procedures of CSM developed by ATC 40. Such improvements, which are focused on the estimation of the equivalent period and damping, were determined on an optimization process in which the error between the displacements predicted using the equivalent linear system and the nonlinear response history analysis was minimized. Since these parameters are both dependent on ductility, the performance point must be found using iterative or graphical techniques; therefore, the FEMA 440 report expounds three procedures that have been developed to this aim and that are similar to those of the ATC 40 report. The first essential step of the improved techniques of CSM is selecting a spectral representation of the ground motion of interest with initial damping, β_i (normally 5%), which may be an elastic demand spectrum from design codes. This spectrum, which is initially in the standard format (S_a *vs* T), is subsequently converted to the ADRS format (S_a *vs* S_d) applying Eq. (2-1). After that, a capacity curve for the structure to be analyzed is generated by pushover analysis. This curve, which is in the format (V *vs* Δ_r), is converted to the ADRS format applying Eqs. (2-2) and (2-3).

In the same way, as in the ATC 40 methodology, the improved CSM also requires a bilinear representation to define the initial period T_o and the yield point (a_{py}, d_{py}). This representation needs the definition of an initial trial performance point (a_{pi}, d_{pi}) which may be based on the Equal Displacement Approximation, as shown in Fig. **2-6**, or any other point based on engineering judgment. The bilinear curve, which is made by the same technique used in the ATC 40 procedures defined above, allows determining the ductility demand μ that is defined as the ratio of maximum displacement d_{pi} to yield displacement d_y and the post-elastic stiffness that is given by:

$$\alpha = \frac{\left(\frac{a_{pi} - a_y}{d_{pi} - d_y}\right)}{\left(\frac{a_y}{d_y}\right)}$$

Using the calculated value of the ductility, the following approximate equations for the effective damping β_{eff} and for the effective period T_{eff}, which have been optimized for application to any

capacity, are respectively:

$$\beta_{eff} = \begin{cases} 4.9(\mu-1)^2 + 1.1(\mu-1)^3 + \beta_o, & 1 < \mu < 4 \\ 14 + 0.32(\mu-1) + \beta_o, & 4 \leq \mu \leq 6.5 \\ 19\left[\dfrac{0.64(\mu-1)-1}{[0.64(\mu-1)]^2}\right]\left(\dfrac{T_{eff}}{T_o}\right) + \beta_o, & \mu > 6.5 \end{cases}$$

$$T_{eff} = \begin{cases} T_o[0.20(\mu-1)^2 - 0.038(\mu-1)^3 + 1], & 1 < \mu < 4 \\ T_o[0.28 + 0.13(\mu-1) + 1], & 4 \leq \mu \leq 6.5 \\ T_o\left\{0.89\left[\sqrt{\dfrac{(\mu-1)}{1+0.05(\mu-2)}} - 1\right] + 1\right\}, & \mu > 6.5 \end{cases}$$

where β_o is the equivalent hysteretic viscous damping for an idealized bilinear system (typically $\beta_o = \beta_i$); and $0.2 \leq T_o \leq 2$ is the initial period of vibration of the nonlinear system ($T_o = T_i$).

According to (FEMA, 2009a), the spectral reduction for the improved equivalent linearization procedures normally requires spectral reduction factors to adjust the initial response spectrum to the appropriate level of effective damping. In this regard, the spectral reduction to the elastic demand spectrum is given by:

$$S_{a_B} = \frac{S_{a_o}}{B}$$

where S_{a_o} is the spectral acceleration ordinates of the elastic demand spectrum (S_{a_o}) in ADRS format; and B is the spectral reduction factor defined by the following equation:

$$B = \frac{4}{5.6 - \ln(\beta_{eff})}, \qquad with\ \beta_{eff}[\%]$$

On the other hand, FEMA (2009a) developed a technique to modify the reduced demand spectrum in order to keep the original CSM approach in which the performance point is defined as the intersection of a demand curve with a capacity curve. The modified reduced spectrum (MS_{a_B}), which is used in two FEMA 440 procedures, is computing by multiplying the ordinates of the reduced demand spectrum by the modification factor defined as:

$$M = \left(\frac{T_{eff}}{T_o}\right)^2 \left[\frac{1 + \alpha(\mu-1)}{\mu}\right]$$

Subsequently, three possible procedures are proposed by FEMA (2009a) in order to address the iterative process in the estimation of the performance point:

- Procedure A, which is known as Direct Iteration, allows that the iteration converges directly on the estimated performance point d_i which is determined using the intersection of the T_{eff}

radial line with the reduced demand spectrum (S_{a_B}), as shown in Fig. **2-8a**. If $0.95d_{pi} \leq d_i \leq 1.05d_{pi}$, then (a_{pi}, d_{pi}) becomes the performance point; otherwise a new (a_{pi}, d_{pi}) point is selected and the process is repeated since the step corresponding to the bilinear curve construction.

- Procedure B defines the estimated performance point d_i as the intersection of the capacity spectrum with the modified reduced spectrum (MS_{a_B}), as shown in Fig. **2-8b**. If $0.95d_{pi} \leq d_i \leq 1.05d_{pi}$, so (a_{pi}, d_{pi}) becomes the performance point; else a new (a_{pi}, d_{pi}) point is selected and the process is repeated since the step corresponding to the bilinear curve construction. This procedure is useful because it provides a visualization tool by facilitating a direct graphical comparison of capacity and demand.

- Procedure C uses the modified reduced spectrum (MS_{a_B}) for multiple assumed solutions (a_{pi}, d_{pi}) and the corresponding ductilities to generate a locus of possible performance points. The actual performance point is located at the intersection of this locus and the capacity spectrum.

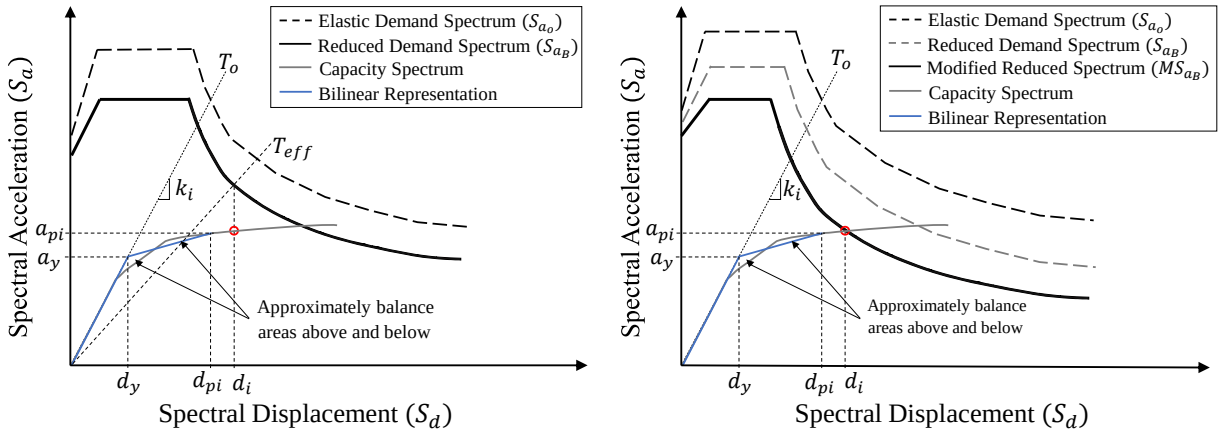

a) Procedure A (Direct Iteration)

b) Procedure B (Intersection with Modified Reduced Spectrum)

Figure 2-8: Determination of the performance point using the improved CSM (Adapted from FEMA (2009a))

CSM based on inelastic spectra: The N2 method

Several deficiencies have been found in the original proposal of CSM (Krawinkler, 1994; Reinhorn, 1997; Chopra and Goel, 1999b; Fajfar, 1999), among which the most controversial is the use of equivalent linear systems with highly damped elastic spectra for the determination of seismic demand. For instance, Krawinkler (1994) found that the original CSM was questionable due to two relevant deficiencies: first, there is no physical principle that justifies the existence of a stable

relationship between the hysteretic energy dissipation and equivalent viscous damping, particularly for highly inelastic systems; and second, the period associated with the intersection of the capacity curve with the highly damped spectrum may have little to do with the dynamic response of the inelastic system. Consequently, Reinhorn (1997) proposed an alternative to the use of elastic spectra with equivalent damping, in order to eliminate the controversial deficiencies of the original CSM. Reinhorn's proposal neither equivalent viscous damping nor the period associated with the intersection of the capacity curve with the highly damped spectrum did consider. In fact, this idea was based on using the inelastic demand spectra in the ADRS format within the original CSM, which would allow combining the visual representation of CSM with the superior physical basis of inelastic demand spectra. Chopra and Goel (1999a,b) and Fajfar (1999, 2000) employed this alternative in the development of improved procedures of CSM that used the ductility design spectrum for the demand diagram which was established by reducing the elastic design spectrum by appropriate ductility-dependent factors.

The idea of considering the use of inelastic demand spectra in the CSM procedures was extended as a simple nonlinear method as known the N2 method (Fajfar, 1999, 2000) which combines the pushover analysis of an MDoF model with the response spectrum analysis of an equivalent SDoF system. This method is based on inelastic spectra rather than elastic spectra with equivalent damping and period, which represents the major difference regarding those presented in the ATC 40 and FEMA 440 reports. In addition, the N2 method is formulated in the ADRS format which enables the visual interpretation both the capacity spectrum and the inelastic demand spectra in the performance point estimation, keeping the graphical implementation of the original approach of CSM.

The first step of the N2 method is the determination of the data of the MDoF system, in order to define the nonlinear behavior of structural elements under monotonic loading. The more common element model is the beam element with concentrated plasticity at both ends. After that and in the same way as in the aforementioned ATC 40 and FEMA 440 reports, seismic demand is defined by an elastic design spectrum which is given in the standard format (S_{ae} *vs* T) and is converted to the ADRS format (S_{ae} *vs* S_{de}) applying Eq. (2-1). Subsequently, a pushover analysis is performed by subjecting the structure to a monotonically increasing pattern of lateral forces that represent the inertial forces which would be experienced by the structure under seismic loads. According to Fajfar (1999, 2000), the selection of appropriate lateral load distribution is an important step within the pushover analysis because a unique solution does not exist. In this regard, the N2 method sets a vector of lateral loads $\mathbf{P}$ to be used in the pushover analysis, given by:

$$\mathbf{P} = p\,\mathbf{M}\,\boldsymbol{\Phi}$$

where p controls the magnitude of the lateral loads; $\mathbf{M}$ is the diagonal mass matrix; and $\boldsymbol{\Phi}$ is an assumed vector of displacements shape, which is given in the normalized form. Defined the lateral load pattern, the structure is analyzed to calculate the capacity curve of the MDoF systems in terms of the base shear V and the roof displacement D_t.

The N2 method considers transforming base shears and roof displacements of the MDoF system into those of an equivalent SDoF system. The initial stiffness of the SDoF system remains the same as that of the MDoF system, whereas the force F^* and the displacement D^* of this equivalent system are given by the following expressions, respectively:

$$F^* = \frac{V}{\Gamma}; \qquad D^* = \frac{D_t}{\Gamma} \tag{2-4}$$

where Γ is usually known as the modal participation factor which is equivalent to the PF_1 factor in CSM, and to the coefficient C_0 in DCM. This parameter is calculated according to:

$$\Gamma = \frac{m^*}{\sum m_i \Phi_i^2}$$

where $m^* := \sum m_i \Phi_i$ is the equivalent mass of the SDoF system. The force-displacement relationship of the equivalent SDoF system requires to be idealized into an elastic-perfectly plastic representation because the graphical procedure of the N2 approach requires the post-yield stiffness equal to zero (see Fig. **2-9**). In order to do this, it can be used either engineering judgment or some criteria of guidelines such as the FEMA 273 report (FEMA, 1997) which establishes that the effective lateral stiffness can be taken as the secant stiffness calculated at a force equal to 60% of the yield strength. The elastic-perfectly plastic curve defines the parameters F_y^* and D_y^* which are the yield strength and displacement, respectively. With these parameters, it is possible to estimate the elastic period of this idealized bilinear system by the following equation:

$$T^* = 2\pi \sqrt{\frac{m^* D_y^*}{F_y^*}}$$

Subsequently, the elastic-perfectly plastic curve is required in the ADRS format in order to be plotted with the seismic demand curves at the same graph. Therefore, the forces of the bilinear curve F^* are divided by the equivalent mass m^*. The following step of the N2 procedure is to obtain the inelastic demand spectrum from the elastic demand spectrum which has already been defined above. The inelastic acceleration spectrum S_a and the displacement spectrum S_d can be determined by the following expressions, respectively (Vidic et al., 1994):

$$S_a = \frac{S_{ae}}{R_\mu}; \qquad S_d = \frac{\mu}{R_\mu} S_{de}$$

where μ is the ductiliy factor defined as the ratio between the maximum displacement and the yield displacement; however, it also can be determined as (Vidic et al., 1994):

$$\mu = \begin{cases} 1 + (R_\mu - 1)\dfrac{T_C}{T^*}, & T^* < T_C \\ R_\mu, & T^* \geq T_C \end{cases}$$

where T_C is transition period in which the constant acceleration segment of the response spectrum passes to the constant velocity segment of the spectrum (see Fig. **2-9**). R_μ is the reduction factor due to the hysteretic energy dissipation of ductile structures, which is not equivalent to the

reduction factor R used widely is seismic codes for the traditional design approach. In the N2 method, R_μ can be determined as the ratio between the accelerations corresponding to the elastic and inelastic systems:

$$R_\mu = \frac{S_{ae_{T^*}}}{S_{ay}}$$

where $S_{ay} := F_y^*/m^*$ is the yield acceleration that represents both the acceleration demand and the capacity of the inelastic system; and $(S_{ae_{T^*}}, S_{de_{T^*}})$ is the intersection point of the radial line corresponding to the elastic period of the idealized bilinear system T^* with the elastic demand spectrum (see Fig. **2-9**). In the last step, the maximum expected displacement D_p^* of the equivalent system is estimated using the following expression:

$$S_d = D_p^* = \begin{cases} \dfrac{S_{de_{T^*}}}{R_\mu}\left[1 + (R_\mu - 1)\dfrac{T_C}{T^*}\right], & T^* < T_C \\ S_{de_{T^*}}, & T^* \geq T_C \end{cases}$$

Fig. **2-9a** shows the graphical estimation of D_p^* for the case $T^* < T_C$, whereas Fig. **2-9b** illustrates the graphical estimation of D_p^* for the case $T^* \geq T_C$. In both cases, the inelastic demand in terms of accelerations and displacements corresponds to the intersection point of the bilinear capacity diagram with the inelastic demand spectrum corresponding to the ductility demand μ. Consequently, the displacement demand for the SDoF model D_p^* is transformed into the maximum top displacement D_t of the MDoF system (target displacement) by using Eq. (2-4) in order to determine the global and local seismic demands by a pushover analysis in which the structure is pushed to that target displacement. The performance of the structure is subsequently assessed by comparing with the performance objectives.

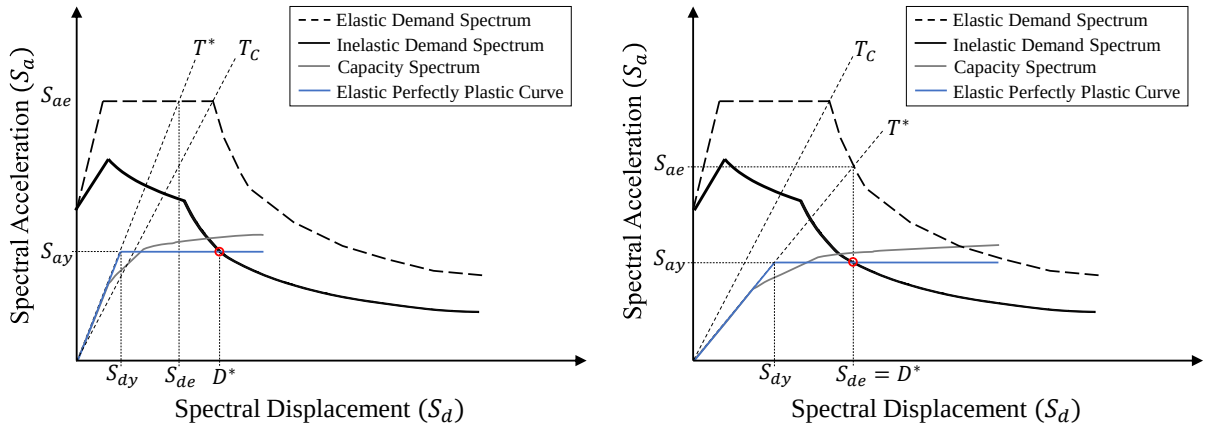

Figure 2-9: Determination of the performance point using the N2 method (Adapted from Fajfar (1999, 2000))

All steps the N2 method involves can be performed numerically, however, the visual interpretation of the procedure allows having a better comprehension of the seismic performance of the structure under seismic loads.

2.4.1.2 Displacement Coefficient Method

Displacement Coefficient Method (DCM) is a mathematical model which directly incorporates the nonlinear load-deformation characteristics of individual elements of the structure; this model is subjected to monotonically increasing lateral loads (pushover analysis) which represent inertia forces in an earthquake until a target displacement is exceeded. DCM provides a direct numerical process to calculate the target displacement δ_t which is intended to represent the maximum displacement that will probably experience a characteristic node on the top of a structure during a seismic event.

The DCM procedure does not require converting the capacity curve to spectral coordinates; however, this nonlinear relationship between base shear and displacement of the control node is replaced with an idealized force-displacement curve, in order to calculate the effective lateral stiffness, k_e, and effective yield strength, V_y, of the structure. The effective lateral stiffness k_e is taken as the secant stiffness calculated at a base shear force equal to 60% of the effective yield strength of the structure V_y which cannot be taken as greater than the maximum base shear force at any point along the actual capacity curve. The previous methodology of DCM was initially proposed in the FEMA 273 report (FEMA, 1997) and extended by the FEMA 356 report (FEMA, 2000). Subsequently, the FEMA 440 report improved the procedure which was adopted later in the ASCE 41 standards (ASCE, 2007, 2014, 2017b).

Previous methodology

In the FEMA 356 procedure, the first step is to obtain the capacity curve of the structure via pushover analysis. Then, an idealized force-displacement curve is constructed as a bilinear representation with an initial slope k_e and post-yield slope αk_e. The line segments of this bilinear curve are located using an iterative graphical procedure that approximately balances the area above and below the curve. The post-yield slope αk_e is determined by a line segment that passes through the actual curve at the calculated target displacement. Fig. **2-10** shows the idealized bilinear curve for the DCM procedure.

The effective fundamental period T_e in the direction under consideration is based on the idealized force displacement curve, calculated accordance with the following equation:

$$T_e = T_i \sqrt{\frac{k_i}{k_e}} \tag{2-5}$$

where T_i is the elastic fundamental period (in seconds) calculated by elastic dynamic analysis, k_i is the elastic lateral stiffness of the building, and k_e is the effective lateral stiffness of the building obtained by the idealized bilinear curve.

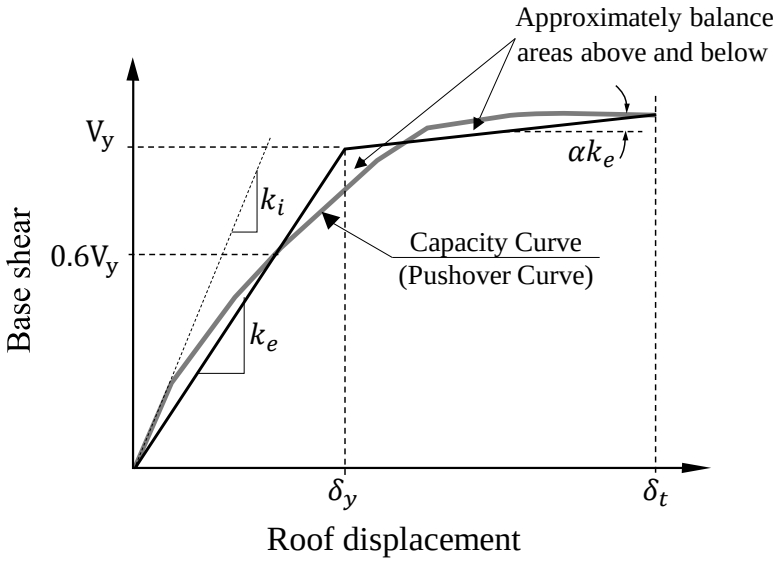

Figure 2-10: Bilinear representation of Capacity Curve for DCM (Adapted from FEMA (2000))

The target displacement δ_t, which is the same as the performance point, is calculated by the following equation:

$$\delta_t = C_0 C_1 C_2 C_3 S_a \frac{T_e^2}{4\pi^2} g$$

where T_e is as defined above; S_a is the response spectrum acceleration at the effective fundamental period T_e of the building in the direction under consideration; and g is the acceleration of gravity.

The coefficient C_0 relates the spectral displacement of an equivalent single degree of freedom system to the roof displacement of multi degree of freedom system. The coefficient C_1, which relates expected maximum inelastic displacements to displacements calculated for linear elastic response, is given by:

$$C_1 = \begin{cases} 1, & T_e \geq T_0 \\ \dfrac{1+(R-1)(T_0/T_e)}{R}, & T_e < T_0 \end{cases}$$

where T_0 is a characteristic period of the response spectrum, defined as the period associated with the transition from the constant acceleration segment of the spectrum to the constant velocity segment of the spectrum; and R is the ratio of elastic strength demand to yield strength coefficient considering the effective seismic weight W, given by the following equation:

$$R = \frac{S_a}{V_y/W} \cdot \frac{1}{C_0}$$

The coefficient C_2, which represents the effect of pinching, stiffness degradation and strength deterioration at the maximum displacement response, is obtained from FEMA 356 tables for different framing systems and structural performance levels. On the other hand, the coefficient C_3, which represents increased displacements due to dynamic P-Δ effects, is calculated according to the post-yield stiffness α by the equation:

$$C_3 = \begin{cases} 1, & \alpha \geq 0 \\ 1 + \dfrac{|\alpha|(R-1)^{3/2}}{T_e}, & \alpha < 0 \end{cases}$$

Current methodology

The improvement of DCM includes revisions of the coefficients used to calculate the target displacement, in order to expound the actual understanding of the building's behavior during seismic events. The recommendations proposed by FEMA (2009a) include several improved alternatives for the basic ratio of the maximum displacement (elastic plus inelastic) for an elastic-perfectly plastic SDoF oscillator to the maximum displacement for a completely linear elastic oscillator that is designated as the coefficient C_1 in the original DCM. In addition, a distinction is recognized between two different types of strength degradation that have different effects on the system response and performance; this distinction leads to recommendations for the coefficient C_2 to account for cyclic degradation in strength and stiffness. Also, FEMA (2009a) suggested eliminating the coefficient C_3 and replacing it by a limit on minimum strength (maximum value of R) required to avoid the dynamic instability.

Fig. **2-11** displays the idealized force-displacement curve of the current DCM. The first line segment of this curve begins at the origin and has a slope equal to the effective lateral stiffness k_e. The second line segment represents the positive post-yield slope $\alpha_1 k_e$ determined by a point (V_d, Δ_d) and a point at the intersection with the first line segment such that the areas above and below the capacity curve are approximately balanced; the point (V_d, Δ_d) is a point on the capacity curve either at the calculated target displacement or at the displacement corresponding to the maximum base shear, whichever is least. For models that exhibit negative post-elastic stiffness, a third line segment represents the negative post-yield slope $\alpha_2 k_e$, determined by the point at the end of the positive post-yield slope (V_d, Δ_d) and the point at which base shear degrades to 60% of the effective yield strength; such negative slope approximates the effects of cyclic and in-cycle degradation of strength.

The target displacement δ_t, which is the same as the performance point, is calculated by the following equation:

$$\delta_t = C_0 C_1 C_2 S_a \frac{T_e^2}{4\pi^2} g$$

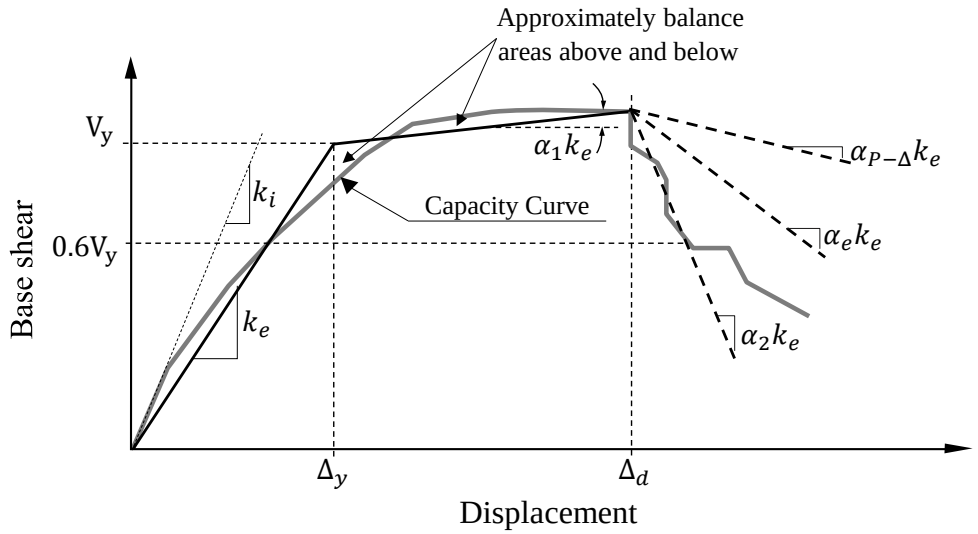

Figure 2-11: Idealized force-displacement curve according to ASCE 41 standards (Adapted from ASCE (2007, 2014, 2017b))

where T_e is defined by Eq. (2-5); S_a is the response spectrum acceleration at the effective fundamental period T_e of the building in the direction under consideration; g is the acceleration of gravity; and the coefficient C_0 has the same definition of the previous methodology.

The coefficient C_1, which relates expected maximum inelastic displacements to displacements calculated for linear elastic response, is given by the following improved equation:

$$C_1 = \begin{cases} 1, & T_e > 1 \\ 1 + \dfrac{R-1}{aT_e^2}, & 0.2 < T_e \leq 1 \\ 1 + \dfrac{R-1}{0.04a}, & T_e \leq 0.2 \end{cases}$$

where a represents the influence of different soil site classes: 130 for soil site classes A and B, 90 for soil site class C, and 60 for soil site classes D, E, and F; and R is the ratio of elastic strength demand to yield strength coefficient computed by:

$$R = \frac{S_a}{V_y/W} \cdot C_m$$

where W is the effective seismic weight; and C_m represents the effective mass factor to account for higher mode mass participation effects obtained from the structural configuration, which is obtained from tables of the ASCE 41 standards but it can be taken as 1.0 if the fundamental period is greater than 1.0 s. For buildings with negative post-yield stiffness, the maximum strength ratio R_{max} is calculated in accordance with the following equation:

$$R_{max} = \frac{\Delta_d}{\Delta_y} + \frac{|\alpha_e|^{-h}}{4}$$

where $h := 1 + 0.15\ln(T_e)$; Δ_d is the lesser of the target displacement δ_t or the displacement corresponding to the maximum base shear (see Fig. **2-11**); Δ_y is the displacement at effective yield strength V_y; and α_e is the effective negative post-yield slope ratio defined as:

$$\alpha_e = \alpha_{P-\Delta} + \lambda(\alpha_2 - \alpha_{P-\Delta})$$

where $\alpha_{P-\Delta}$ is the negative slope ratio caused by P-Δ effects; and λ is the near-field effect factor which is related to the 1-second spectral acceleration S_1 for the MCE (see e.g. ASCE, 2014), given as 0.8 for $S_1 \geq 0.6$, and 0.2 for $S_1 \leq 0.6$.

The coefficient C_2, which represents the effect of pinching, stiffness degradation and strength deterioration on maximum the displacement response, is given by:

$$C_2 = \begin{cases} 1, & T_e > 0.7 \\ 1 + \dfrac{1}{800}\left(\dfrac{R-1}{T_e}\right)^2, & T_e \leq 0.7 \end{cases}$$

2.4.2 Nonlinear Dynamic Analysis

Nonlinear dynamic analysis (NDA), which is frequently known as Nonlinear Response History Analysis (NRHA), is a sophisticated technique that provides a more realistic estimation of the seismic response of a structure subjected to strong ground motions which are selected and scaled according to the objectives of the analysis. In contrast to NSPs, NDA overcomes most limitations due to its ability to accurately represent multi-mode behavior and other time or history dependent behaviors. In fact, the approximations associated with the selection of loading pattern and solution for target displacements are avoided and higher mode effects and cyclic degradation can be directly accounted for in the analysis (NIST, 2017a). Consequently, NDA is gaining in popularity significantly relative to nonlinear static analysis, due to the perceived enhanced accuracy of the results obtained as well as the greater availability of the software and computing power necessary to make practical this type of analysis (NIST, 2017b).

NDA takes into account the inelastic behavior of the elements when are under cyclic loads (earthquake ground motions), which produces an explicit simulation of energy dissipation in the nonlinear range. As a consequence of this, NDA is commonly used to assess the seismic behavior of any structure subjected to any ground motion in order to obtain demands parameters such as story drift ratios, displacements, floor accelerations, among others, which allow predicting the performance of the structure. However, due to the inherent variability in earthquake ground motions, it is necessary to perform multiple dynamic analyses for a set of ground motions, in order to calculate statistically robust values of the demand parameters for a given ground motion intensity (NIST, 2010). In fact, a powerful emerging method known as Incremental Dynamic Analysis (IDA) is commonly applied in NDA to perform this task. This method is presented in the following sections. Additionally, NDA is capable of producing results with low uncertainty, provided that the

nonlinear inelastic properties of the structure in the analytical model are accurate and reliable. In this regard, NDA requires appropriate definitions both the input ground motion and the hysteretic behavior of elements. The definition of input ground motions is presented in the following section, whereas different hysteretic models used to represent the nonlinear cyclic behaviors are presented and discussed in Chapter 3.

2.4.2.1 Characterization of Earthquake Hazard

The most common type of performance assessment used in NDA to define earthquake hazards and to compute the response of a structure (in terms of forces, deformations, story drifts, or global estimates of losses) for a specified level of ground motion is the aforementioned Intensity-based assessment in which the ground motion intensity is defined by 5%-damped elastic acceleration response spectra. Intensity-based assessments require a target acceleration response spectrum, e.g. a building code response spectrum, and suites of n ground motion records that should be selected and scaled for consistency and compatibility with the target spectrum (FEMA, 2012). In this sense, it is important to emphasize that the input ground motions should represent accurately the specific seismic hazard of interest in order to obtain meaningful results of the structural response. With the purpose of achieving this, Intensity-based assessments define a general procedure that involves the development of an appropriate target acceleration response spectrum, the selection of an appropriate suite of earthquake ground motions, and the scaling of the ground motions selected to match the target spectrum.

Target Acceleration Response Spectrum

For Intensity-based assessments, any 5%-damped elastic acceleration response spectrum can be used as the target response spectrum. However, in PBSD practice, it is common to define the target response spectrum as the building code response spectrum in order to keep the consistency in the geologic characteristics of the site and in the seismic design criteria established. In general, the seismic hazard is defined in terms of response spectral accelerations with a specified mean annual frequency of exceedance. For the case of this research, the target spectrum is defined according to the Colombian building code, NSR-10 (AIS, 2010), which defines the 5%-damped elastic acceleration design spectrum as a function of a set of parameters that represent the seismic characteristics of a specific site. This design spectrum is defined for a return period of 475 years and a probability of occurrence of 10% in 50 years, which allows associated it with the *Rare* seismic event and with the DBE level of the earthquake hazard levels proposal in PBSD (see Section 2.3.2).

NSR-10 defines the ground motions as a function of the parameters A_a and A_v which represent the peak ground acceleration (PGA) and the peak ground velocity (PGV) of the construction site, respectively. These parameters can be obtained either by a seismic microzonation study or by pre-

defined values in NSR-10 according to the seismic hazard zone wherein will be built the structure, this is, high, medium, or low seismic hazard zone. Additionally, NSR-10 evaluates the local effects according to site classes and site coefficients by the proper definition of the amplification factors F_a and F_v and it also takes into account the seismic design category (risk category) of buildings by the definition of the Seismic Importance Factor I. Fig. **2-12** illustrates the NSR-10 design spectrum which is defined by simple analytical functions that depend on the fundamental period of the structure T.

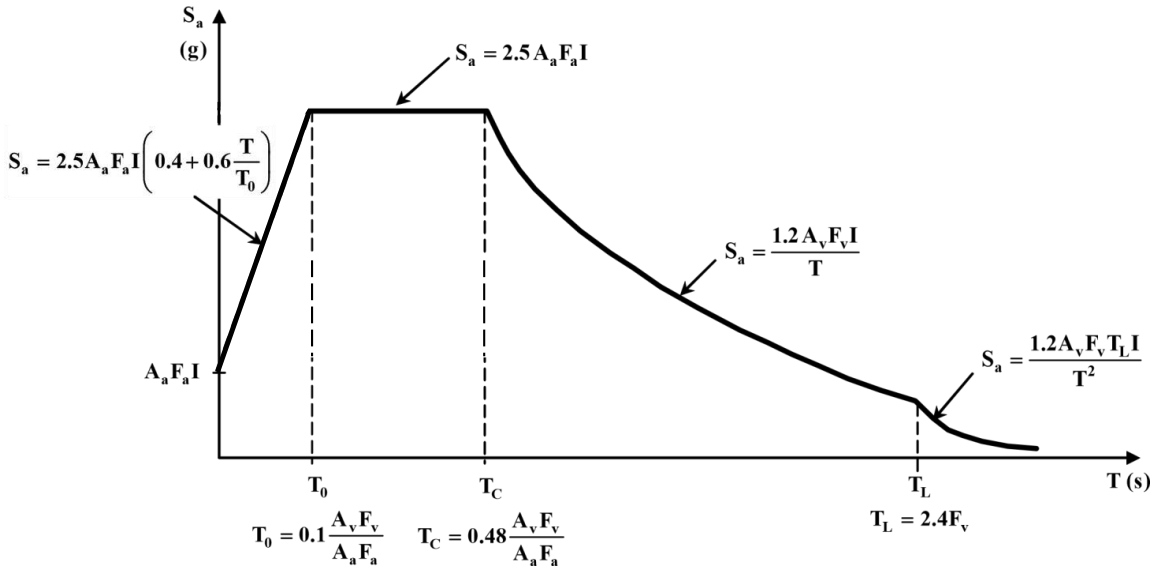

Figure 2-12: The 5%-damped elastic acceleration design spectrum of NSR-10 (AIS, 2010)

Ground Motion Selection and Scaling

The purpose of the selection and scaling of ground motions is to define a suitable set of them that allow obtaining estimations of median structural response when NDA is employed. Ground motions are selected such that, on average, they reasonably match the target response spectrum at the fundamental period or over the period range that includes the fundamental period of the structure. Given the inherent variability in earthquake ground motions, design standards typically require analyses for multiple ground motions to provide statistically robust measures of the demands and the structural behavior (NIST, 2010). For instance, the number of input ground motions needed for NDA is proposed by the ASCE/SEI 7-16 standard (ASCE, 2017a) which recommends: at least seven ground motions if the fit with the target spectrum is good; eleven ground motions if the fit is poor, in order to produce reasonable estimates of median response (this is the most recommended number of ground motions); or more than thirty ground motions if both the mean response estimate and the accurate prediction of response variability are required (NIST, 2017a).

The ground motions needed for NDA can come either from actual records from past earthquakes or an artificial generation method. Although actual recorded ground motions are usually preferred because they represent the actual seismic hazard expected at the site of interest, not many actual records of different seismic intensities are available for many regions, in order to characterize the seismic hazard of a specific site. Therefore, actual recorded ground motions from a standard or artificial ground motions could be used in NDA as an ideal solution for this issue.

2.4.2.2 Incremental Dynamic Analysis

Incremental Dynamic Analysis (IDA) is a powerful method used in NDA to estimate the structural response under seismic loads. This method was initially proposed by Luco and Cornell (1998) to determine the capacity of structures in the form of a dynamic pushover, but later, it was restructured and formalized by Vamvatsikos and Cornell (2002a) as a comprehensive procedure that provides a thorough estimation of the probabilistic distribution of structural response in terms of an Engineering Demand Parameter (EDP) given the seismic hazard level represented by an Intensity Measure (IM) as well as the required IM to achieve given values of EDP at any level of structural behavior. According to Vamvatsikos and Cornell (2002a), this estimation is achieved by performing nonlinear dynamic analyses of the structural model under a suite of ground motion records, each one scaled to several intensity levels designed to force the structure all the way from elasticity to final global dynamic instability. In this way, IDA supplies structural response curves of an EDP that represents a Damage Measure (DM) such as the maximum peak interstory drift, against an IM represented usually by the Peak Ground Acceleration (PGA) or the 5%-damped spectral acceleration $Sa(T;5\%)$. Furthermore, performance levels associated with limit states can be defined on each IDA curve and summarized to calculate the probability of exceeding of each one given a specified IM level (Vamvatsikos and Cornell, 2002b).

The IDA procedure requires the following essentials steps (Vamvatsikos and Cornell, 2002a; Vamvatsikos, 2015):

1. **Selection of ground motion records and intensity measures:** Select a suite of ground motion records and an efficient IM which is generally defined by the PGA or the $Sa(T;5\%)$. Usually, the input ground motions for IDA are generated taking into account the aforementioned definitions of the characterization of earthquake hazards.

2. **Definition of the structural model:** Define an appropriate structural model that considers the total elastic and inelastic behavior of the structure under investigation, including higher mode effects and hysteretic phenomena.

3. **Execution of the analysis:** For each ground motion record, incrementally scale it at constant or variable IM steps, and run a nonlinear dynamic analysis each time. Start from a low IM value where the structure behaves elastically, and stop when global collapse or numerical non-convergence is first encountered. In each nonlinear dynamical analysis, save the results

of the EDPs of interest which are selected depending on the desired application, for example, the peak floor accelerations are correlated with contents and non-structural damage, whereas the maximum interstory drift ratio is commonly related to global dynamic instability and with the structural performance levels.

4. **Postprocessing:** The graphical representation of the results of IDA, which is given in the EDP vs IM format, is initially compound of distinct points that represent the nonlinear dynamical analyses, as shown in Fig. **2-13a**. The postprocessing of this results comprises the following steps:

   i. Generate IDA curves by linear or spline interpolation of the points (EDP, IM), one for each individual ground motion record as illustrated in Fig. **2-13b**;

   ii. Define limit-states or performance levels and estimate the corresponding capacities on each IDA curve in order to be able to do the performance calculations needed for PBEE;

   iii. Summarize the IDA curves by appropriate techniques that will reduce this data to the distribution of EDP given IM and to the probability of exceeding any specific limit-state or performance level given the IM level. The IDA curves can be summarized into some central value, e.g. the mean or the median, and a measure of dispersion such as the standard deviation or the difference between two fractiles. Fig. **2-13b** shows an example of the summarized IDA curves into the 16%, 50%, and 84% fractiles.

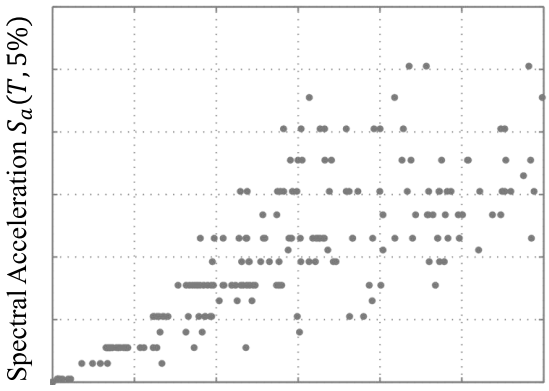

a) The resulting (EDP, IM) points for a suite of ground motion records obtained from the IDA procedure.

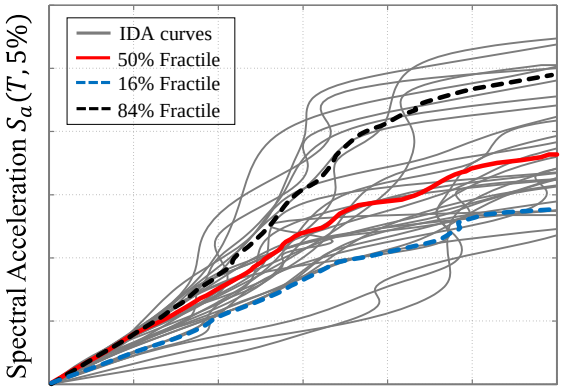

b) Individual IDA curves derived from a spline interpolation of the resulting points and the 16%, 84%, and 50% fractile IDA curves obtained by the summarizing process.

Figure 2-13: Example of the graphical representation of the IDA results in the EDP vs IM format. (Adapted from Vamvatsikos (2015))

IDA has been applied in many researches as the predominant method to perform NDA in order to assess the seismic performance of structures such as reinforced concrete buildings (Vamvatsikos

et al., 2003; Wang et al., 2010; Zarfam and Mofid, 2011; Vargas et al., 2013, 2014; Brunesi et al., 2015; Sengupta and Li, 2016; Kostinakis and Athanatopoulou, 2016), wood frames (Christovasilis et al., 2009; Goda and Yoshikawa, 2013), steel frames (Asgarian et al., 2010, 2012; Hariri-Ardebili et al., 2013; Nazri and Ken, 2014; Moradi et al., 2014; Silwal et al., 2016), bridges (Mander et al., 2007; Tehrani and Mitchell, 2013; Chomchuen and Boonyapinyo, 2017), among others. Indeed, there are three main applications of IDA in structural engineering (Vamvatsikos, 2015):

1. IDA has been adopted as the method of choice for determining strength reduction R-factors in the FEMA P695 report (FEMA, 2009b), which are commonly used to reduce the required design strength of a structure to take advantage of its ductility;

2. IDA yields a distribution of results at varying intensities that can be used to develop fragility functions through a cumulative distribution function (CDF) which represents the probability of exceeding a limit state given the IM level;

3. IDA has been applied to determine the probability distribution of EDP demand given the IM, i.e. $P(EDP|IM)$, in the seismic performance assessment methodology of the next-generation procedures of PBSD presented in the FEMA P58 report (FEMA, 2012). The results of IDA are used together with the seismic hazard to obtain the mean annual frequency of exceeding any specified level of repair cost, time to repair, or number of casualties.

According to the above, it can conclude that IDA is a powerful tool for performance-based assessment of structures. Therefore, IDA will be used for the NDA required in the seismic performance assessment and in the development of the fragility functions for the structural walls in this research. Chapter 5 presents the required definitions to perform IDA and the results obtained. On the other hand, the following section explains how to develop seismic fragility analyses using the IDA approach.

2.4.3 Seismic Fragility Analysis

Seismic fragility is defined as the probability that the response of structural or nonstructural systems exceeds a critical value under seismic ground motions of specified intensities (Kafali and Grigoriu, 2007). Seismic fragility analysis is portrayed by fragility curves which represent the probability of exceeding a prescribed damage state or performance level as a function of an intensity measure of seismic hazard. The estimation of fragility curves requires a large number of nonlinear dynamic analyses under seismic excitations that can be actual recorded ground motions from a strong motion database, which provide the most suitable form of seismic fragility analyses, artificial ground motions that match the target response spectra, and synthetic accelerograms from theoretical modeling of fault rupture (Ghosh et al., 2017).

Probabilistically, fragility curves are defined by the following expression (Kafali and Grigoriu, 2007; Uribe et al., 2014):

$F_{rg}(\mathbf{DS}, IM) = P(EDP \geq \mathbf{DS} \mid IM)$

where **DS** is the Damage State or the prescribed admissible limit state for the predefined EDP, which defines a threshold level of damage sustained by the structure under seismic loads and is characterized by direct indicators of damage such as initiation of cracking, extent of concrete crushing, sliding shear displacement, reinforcement yielding, buckling, fracture, among others (Gulec and Whittaker, 2009). Regarding the IM, the PGA and the $Sa(T_o;5\%)$ are commonly used in the calculation process; the $Sa(T_o;5\%)$ is related to the fundamental period of the structure T_o and provides a better correlation with the structural response variable (Ghosh et al., 2017). However, fragility curves also can be expressed as function of other EDP, such as the floor aceleration, story drift ratio, etc.

Fragility points that compound the curves are defined as observed fractions of damage and are extracted from the IDA results. These points can be computed as the conditional probability of failure, given by:

$$\widetilde{F_{rg}}(\mathbf{DS}, IM) = \frac{N_f}{N} \tag{2-6}$$

where N_f is the number of ground motions at the IM for which the **DS** is exceeded, i.e. $EDP \geq \mathbf{DS}$, and N is the total number of ground motions performed at the IM. Subsequently, the fragility curves can be built using two widely-known approaches: the nonparametric and the parametric.

2.4.3.1 Nonparametric simulation-based approach

This approach is based on the Monte Carlo Simulation (MCS) method which establishes fragility curves without assuming any shape for them. Delving into the nonparametric approach, the estimation of fragility curves with the MCS method requires a random sample of ground motions and the IDA methodology in order to obtain the number of analyses that produce damage predictions. As a result of this, the fragility curves are computed by Eq. (2-6). This simulation approach requires a large number of replications to obtain acceptable confidence in probabilities of damage.

2.4.3.2 Parametric approach

The parametric approach assumes that the fragility curves are represented usually by a lognormal cumulative distribution function (CDF) that provides a continuous estimation of the probability of damage as a function of IM, and in which its parameters are fitted through an optimization technique. The lognormal CDF is given by the equation (Baker, 2015a):

$$P(\mathbf{DS}|IM = x) = \Phi\left(\frac{\ln(x/\theta)}{\beta}\right) \tag{2-7}$$

where $P(\mathbf{DS}|IM = x)$ is the probability that a ground motion with $IM = x$ will cause the **DS** damage in the structure, $\Phi()$ is the standard normal cumulative distribution function (CDF), θ is the median of the fragility function and β is the standard deviation of $\ln IM$ (i.e. the dispersion of IM).

The generation of analytical fragility functions has motivated the development of methodologies for the estimation of the fragility parameters (θ, β). Some of the most common in literature are (Ghosh et al., 2017): the Method of Moments (Porter et al., 2007), in which the fragility parameters are obtained such that the moments, i.e. θ and β, of the resulting distribution match with the moments of observed fragility points; the Least Squares Regression, in which the fragility parameters are estimated by minimizing the sum of squared error between the predicted probabilities of damage and the observed fractions of damage obtained from structural analysis; and the Maximum Likelihood Estimation (MLE) (Shinozuka et al., 2000), in which the fragility parameters are associated with the highest probability of observing damage data obtained from structural analysis corresponding to a particular limit state.

Based on the MLE methodology, Baker (2015b) presented an efficient approach to estimate the fragility functions using NDA. Even though this approach was initially applied with Multiple Stripes Analysis in which different ground motions are used at each IM level, analyses have indicated that this approach produces effective fragility estimates even with IDA results, where the same ground motions are used at all IM levels (Baker, 2015b). Additionally, this approach was developed for the evaluation of collapse, but it can be extended to determine fragility functions for a set of **DS**s, among which the collapse state is included.

The Baker's approach considers that the probability of observing z_j damages out of n_j ground motions with $IM = x_j$ is given by the binomial distribution defined as (Baker, 2015b):

$$P(z_j \textit{ damages in } n_j \textit{ ground motions}) = \binom{n_j}{z_j} p_j^{z_j} (1 - p_j)^{n_j - z_j}$$

where p_j is the probability that a ground motion with $IM = x_j$ will cause the damage **DS** in the structure (i.e. $p_j = P(\mathbf{DS}|IM = x_j)$). The goal is to determine the fragility function that will provide p_j using the MLE. With the analysis data at multiple IM levels, the product of the binomial probabilities at each IM level is computed to get the likelihood function for the whole data set:

$$\text{Likelihood} = \prod_{j=1}^{m} \binom{n_j}{z_j} p_j^{z_j} (1 - p_j)^{n_j - z_j}$$

where m is the number of IM levels and Π means a product over all levels. Substituting pj for Eq. (2-7) in the above expression, the fragility parameters are explicit in the likelihood function which is given by the following equation:

$$\text{Likelihood} = \prod_{j=1}^{m} \binom{n_j}{z_j} \Phi\left(\frac{\ln(x_j/\theta)}{\beta}\right)^{z_j} \left(1 - \Phi\left(\frac{\ln(x_j/\theta)}{\beta}\right)\right)^{n_j - z_j}$$

The parameters of the fragility function are estimated by maximizing the above likelihood function. According to Baker (2015b), it is equivalent and numerically easier to maximize the logarithm of this likelihood function, so:

$$\{\hat{\theta},\hat{\beta}\} = \arg\max_{\theta,\beta} \sum_{j=1}^{m} \left\{ \ln \binom{n_j}{z_j} + z_j \ln \Phi\left(\frac{\ln(x_j/\theta)}{\beta}\right) + (n_j - z_j) \ln\left(1 - \Phi\left(\frac{\ln(x_j/\theta)}{\beta}\right)\right) \right\} \tag{2-8}$$

The data on the right side of this expression are easily extracted from the IDA results. Then, any optimization technique can be applied using computational software, in order to obtain the fragility function parameters that maximize the above equation. Fig. **2-14** illustrates an example of the application of the above method to fit observed fragility points.

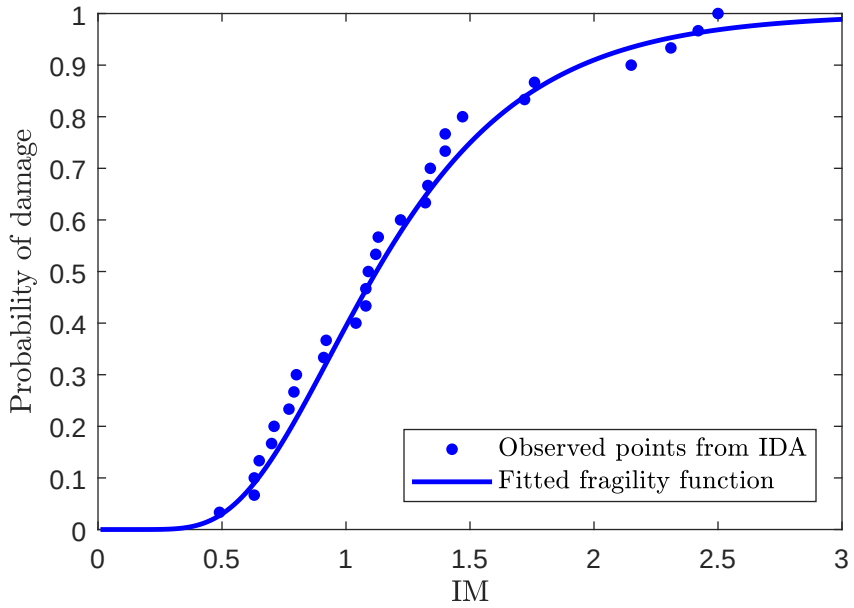

Figure 2-14: Observed fractions of damage and a lognormal fragility function fitted using the approach proposed by Baker (2015b)

Given its simplicity and practicality, the parametric approach explained by Baker (2015b) will be used in Chapter 5 to develop the fragility curves for the performance assessment of the walls.

2.4.3.3 FEMA P695 sources of uncertainty

In order to consider the total system damage uncertainty in the seismic performance assessment of structures, the FEMA P695 report developed a methodology that presents four sources of uncertainty which should be applied to the seismic fragility functions to obtain more accurate, realistic and reliable probabilities of damage. The descriptions of these sources of uncertainty are presented below (FEMA, 2009b):

- Record-to-Record (β_{RTR}): This rating implies the uncertainty associated with the variability in the response of structure when is subjected to different ground motion records. This variability is implicitly given in the IDA results, due to the variations in the dynamic characteristics of the ground motion records, as well as to the differences in the hazard characterization.
- Design Requirements (β_{DR}): This source of uncertainty is related to the completeness and robustness of the design requirements to address unexpected failure modes and their implementation in the construction process, and to the confidence in the basis for the design equations.
- Test Data (β_{TD}): This rating considers the completeness and robustness of the testing program to address testing issues and to quantify important behavior and failure modes, as well as the confidence in test results.
- Modeling (β_{MDL}): This uncertainty is associated with the quality, accuracy and robustness of the nonlinear mathematical model to simulate and to capture nonlinear behaviors and structural damages.

The sources of uncertainty are rated and represented by numerical values that are determined using the above qualitative descriptions. These values are defined as *Superior* (0.1), *Good* (0.20), *Fair* (0.35), and *Poor* (0.50). The reader is refereed to FEMA (2009b) to obtain more information. On the other hand, special attention is given to the numerical value of β_{RTR} that is taken to be equal to the standard deviation of the fragility function, given by Eq. (2-7), which is fitted from the IDA results.

The total system damage uncertainty (β_{Tot}) is subsequently compute combining the four sources of uncertainty. As these sources are assumed to be statistically independent, the β_{Tot} is given by the following expression (FEMA, 2009b):

$$\beta_{Tot} = \sqrt{\beta_{RTR}^2 + \beta_{DR}^2 + \beta_{TD}^2 + \beta_{MDL}^2}$$

Finally, β_{Tot} replaces the standard deviation of the fitted lognormal fragility function defined by Eq. (2-7), in order to generate a corrected fragility function that considers the four sources of uncertainty, which will improve the seismic performance assessment process of the structural walls. In Fig. **2-15**, a graphical comparison between a fitted fragility curve and its corrected version is illustrated.

The above sources of uncertainty will be considered in Chapter 5, for each structural wall, in order to correct the fragility functions obtained from the IDA results by the application of the Baker's approach.

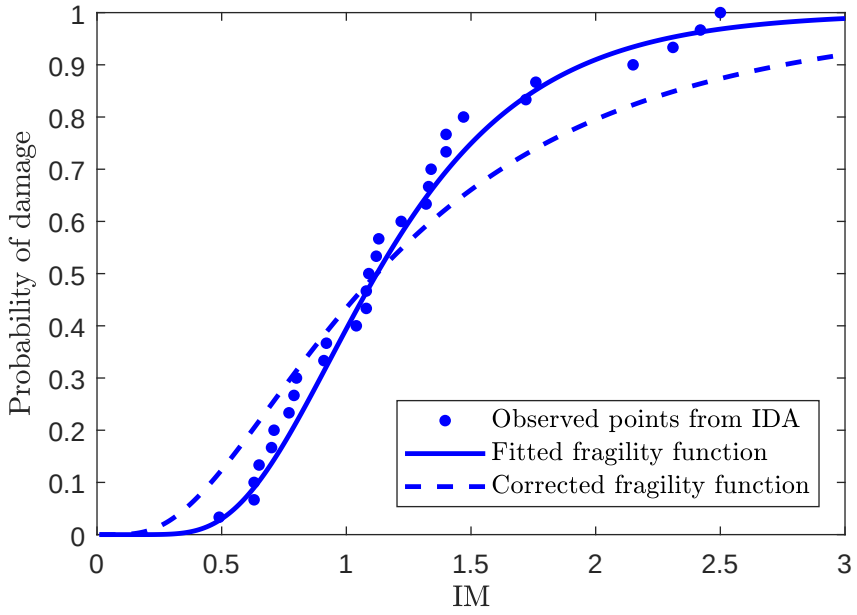

Figure 2-15: Comparison between a fitted lognormal fragility function and its corrected version obtained from the FEMAP695 methodology

3 Hysteretic response of structural systems

The analysis of the linear and nonlinear behavior of structural systems subjected to dynamic loads is the main objective in structural dynamics. To achieve this purpose, mathematical and physical concepts have been constantly developed in the literature, which initially have been applied in Single Degree of Freedom (SDoF) systems to afford a better understanding of structural dynamic problems, and subsequently, have been extended to Multiple Degree of Freedom (MDoF) systems. This chapter explains the theory of linear and nonlinear SDoF systems. First, an overview of the dynamic behavior of linear SDoF systems is presented. The concepts are later extended to nonlinear SDoF systems. Hysteresis, which is part of nonlinear systems, is studied in detail in Section 3.3, where the physical phenomena related to the nonlinear behavior of structures subjected to cyclic loads are explained. In Section 3.4, a brief overview of the types of mathematical hysteretic models are conducted, from which the Mostaghel's hysteretic model is subsequently studied in the next section. To apply that hysteretic model, the parameter identification issue is addressed in Section 3.6. The chapter ends with the development of an identification procedure using the Particle Swarm Optimization technique.

3.1 An overview of linear single degree of freedom systems

A simple idealization of a linear SDoF system subjected to an external dynamic loading is shown in Fig. **3-1a**. This system is composed of a rigid body with mass m, in which the single displacement coordinate $x(t)$ defines its position, a viscous damping constant c, and a spring of stiffness k. Fig. **3-1b** shows the free body diagram of the system.

Using the principle of D'Alembert, the equation of motion for the system is defined by the following equilibrium equation:

$$f_I(t) + f_D(t) + f_R(t) = p(t) \tag{3-1}$$

where $p(t)$ is the external dynamic excitation acting on the body, $f_I(t) := m\ddot{x}(t)$ is the inertial force, $f_D(t) := c\dot{x}(t)$ is the damping force, and $f_S(t) := kx(t)$ is the restoring force; here, $\ddot{x}(t)$, $\dot{x}(t)$ and

$x(t)$ are the acceleration, velocity and displacement of the system respectively. Substituting these expressions into the Eq. (3-1), the equation of motion for a linear SDOF system is given by:

$$m\ddot{x}(t) + c\dot{x}(t) + kx(t) = p(t) \tag{3-2}$$

The solution of Eq. (3-2) allows obtaining the response of a linear SDoF system when is subjected to an external dynamic loading, in terms of displacement and acceleration records.

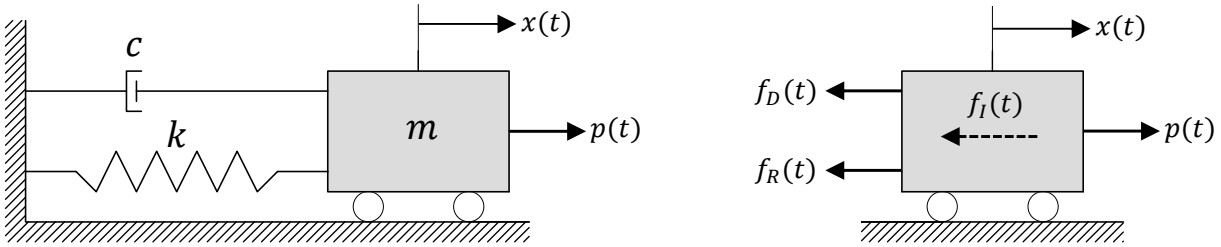

a) Components b) Free body diagram

Figure 3-1: Idealization of a linear single degree of freedom system

In structural and earthquake engineering, it is essential to analyze and to design structures having their behaviors in mind when are subjected to seismic ground motions on their supports. A simplified linear SDoF system that includes the earthquake excitation is shown in Fig. **3-2**, in which the total displacement of the structure from the fixed reference axis is represented by $x_T(t)$. This displacement is expressed as the sum of the horizontal ground motion caused by the earthquake, $x_g(t)$, and the displacement of the components of the structure, $x(t)$. In this way, the total acceleration of the system is defined as (see e.g. Clough and Penzien (1975)):

$$\ddot{x}_T(t) = \ddot{x}_g(t) + \ddot{x}(t) \tag{3-3}$$

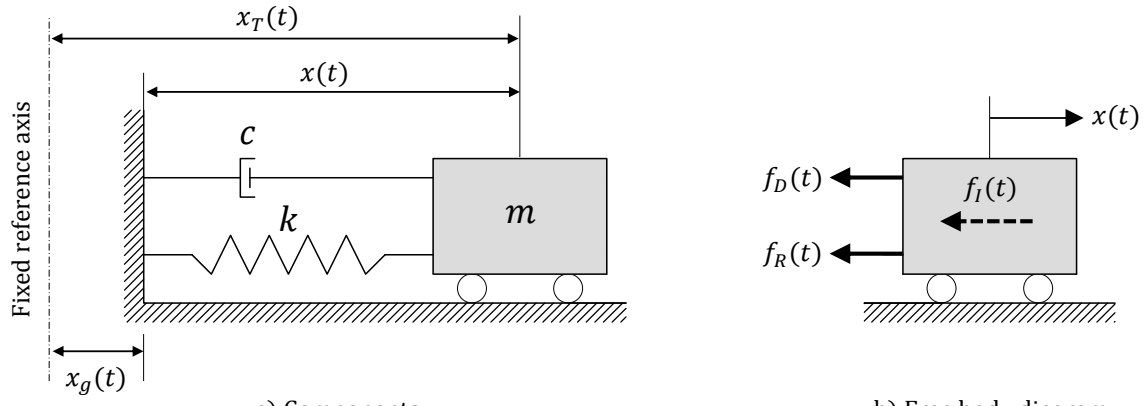

a) Components b) Free body diagram

Figure 3-2: Linear single degree of freedom system subjected to an earthquake excitation

Following a similar procedure as above, the equilibrium equation for the system is:

$$f_I(t) + f_D(t) + f_R(t) = 0 \tag{3-4}$$

where the damping force and the restoring force are defined as in Eq. (3-2); however, the inertial force is now defined having the total acceleration of the mass in mind, so $f_I(t) := m\ddot{x}_T(t)$. Substituting the force expressions and Eq. (3-3) into the Eq. (3-4), the equation of motion for a linear SDoF system subjected to an earthquake excitation is given by the following differential equation:

$$m\ddot{x}(t) + c\dot{x}(t) + kx(t) = -m\ddot{x}_g(t) \tag{3-5}$$

dividing by the mass m, Eq. (3-5) is typically represented by:

$$\ddot{x}(t) + 2\xi\omega_o\dot{x}(t) + {\omega_o}^2 x(t) = -\ddot{x}_g(t) \tag{3-6}$$

where $\xi := c/2m\omega_o$ is the viscous damping ratio of the system, and $\omega_o := \sqrt{k/m}$ is the pseudo-natural frecuency of the system.

Eq. (3-6) models completely the behavior of a linear SDoF system, and allows computing the displacements and the accelerations of the structure from which the internal forces of the elements that make up the structure are calculated, and afterward, are used in many fields of structural engineering, e.g., in the seismic-resistant design.

3.2 Nonlinear single degree of freedom systems

Structures subjected to external dynamic loads experiences cyclic deformations in which the force-displacement relation is not only linear but also includes a nonlinear relation. For instance, structures during a strong earthquake event develop a linear force-displacement relation at small deformations, but this relation becomes nonlinear at larger deformations for which the material enters to the inelastic range (Chopra, 2012); therefore, it is essential to consider both types of behaviors in the analysis and seismic design of structures. According to this, an idealized nonlinear SDoF system subjected to earthquake excitations is sketched in Fig. **3-3**, in order to have a more realistic approach to the structural response expected.

The governing differential equation of the nonlinear system shown in Fig. **3-3** is given by:

$$m\ddot{x}(t) + c\dot{x}(t) + f_R(\dot{x}(t), x(t)) = -m\ddot{x}_g(t)$$

where the restoring force f_R is now an implicit function of the velocity and displacement of the mass m, which is formed of a linear behavior represented by the spring and a nonlinear phenomenon known as *hysteresis*. The response for this kind of systems can be determined experimentally by cycling tests or analytically by nonlinear dynamic models that include the hysteretic behavior.

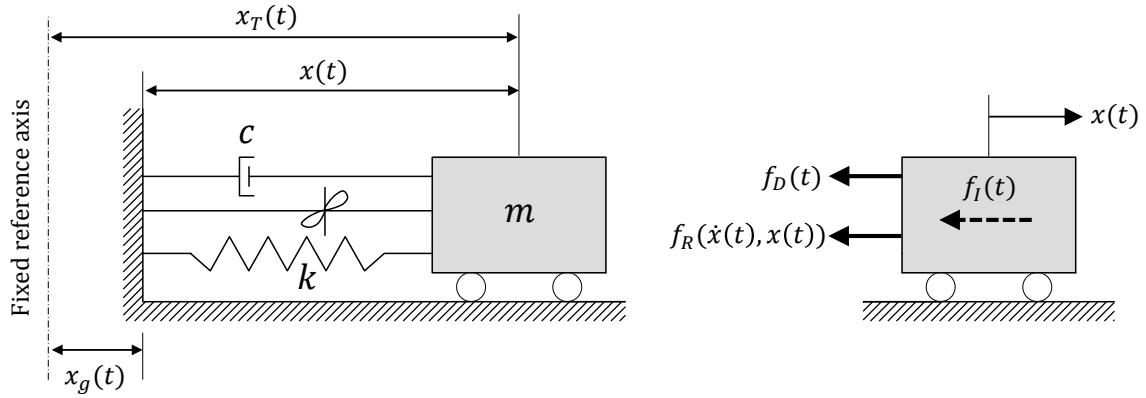

Figure 3-3: Nonlinear single degree of freedom system subjected to an earthquake excitation

3.3 Hysteresis

Hysteresis is a nonlinear behavior exhibited by structures under dynamic loadings, such as strong earthquake excitations. This phenomenon is an inherent property of the structural materials that appears when the structural response is governed by the inelastic behavior, and it is seen as a natural mechanism developed by the materials to dissipate energy (Ikhouane and Rodellar, 2007). According to this, in the seismic-resistant design, structures under seismic loads must dissipate energy, therefore, this characteristic has a great importance; in fact, by proper selection of materials and details for structural members and their connections, appropriate hysteretic characteristics can be incorporated into structural elements as well as into structural systems, in order to increase their safety margin against collapse (Mostaghel, 1999).

The hysteretic behavior in a structure depends on the material and structural system properties to a great extent, and besides, it depends not only on the immediate deformation of elements but also on the past history of the deformations because it represents the energy dissipated by the structure. (Zeynalian et al., 2012). This nonlinear behavior is typically represented by a force vs displacement curve formed by cycles that completely define the behavior of the system.

The shape of the hysteretic cycles is governed by both changes in material properties and changes in the structural geometry of the system (Zeynalian et al., 2012). In this way, structural systems can experience either stable hysteresis cycles or a deterioration in its properties due to the progressive damage in each repeated cyclic loading or deformation; this type of hysteretic behavior is represented by several physical phenomena, such as *stiffness degradation*, *strength deterioration* and *pinching effect*, which must be considered in the analysis and seismic design of structures.

3.3.1 Stiffness degradation

Under reverse cyclic loading, many structural systems usually exhibit some level of stiffness degradation after each load cycle, which becomes stronger with large deformations. Some structural materials have evinced stiffness degradation due to fatigue (see e.g. Whitworth (1997)), cracking, loss of bond or interaction with high shear or axial stresses (FEMA, 2009a). Fig. **3-4** shows a typical hysteresis curve with stiffness degradation represented by a progressive loss of stiffness.

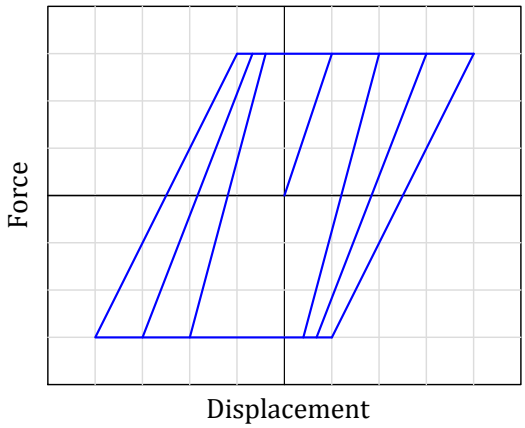

Figure 3-4: Stiffness degradation in a hysteresis curve. (Adapted from FEMA (2009a))

3.3.2 Strength degradation

Strength degradation, also known as *load deterioration*, appears when structural systems subjected to reverse cyclic loading experience reductions in their capacity to resist lateral loads. In hysteretic systems, these reductions can occur by two mechanisms: after the end of each cycle, called *cyclic strength degradation*; and in the same cycle, known as *in-cycle strength degradation*. At the first one, reductions in lateral strength increase with the number of cycles and occur after the loading has been reversed and during subsequent loading cycles (FEMA, 2009a); Fig. **3-5a** illustrates this behavior. On the other hand, *in-cycle strength degradation* occurs when the system experiences a reduction of strength during the same cycle (see Fig. **3-5b**), in combination with the stiffness degradation phenomenon. Most structural systems experience the strength deterioration as a combination of the aforementioned mechanisms (Bougioukos, 2017).

3.3.3 Pinching

Pinching is another hysteretic phenomenon observed in structural systems under dynamic cyclic loading, which is characterized by a sudden large reduction of stiffness during the reloading after

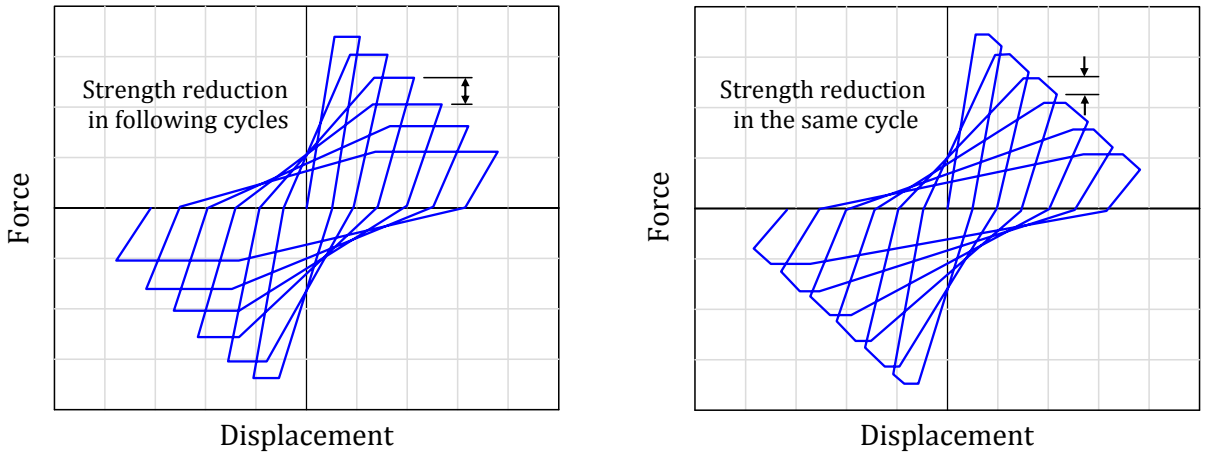

a) Cyclic strength degradation b) In-cycle strength degradation

Figure 3-5: Types of strength degradation in a hysteresis curve. (Adapted from FEMA (2009a))

unloading, followed by a rapid recovery and increase of it when a displacement has been imposed in the opposite direction. This phenomenon causes a reduction of the area under hysteresis loops close to the point of origin after unloading (see Fig. **3-6**), so it leads to a reduction of the amount of dissipated energy (Bougioukos, 2017).

Physically, the pinching phenomenon is encountered in reinforced concrete elements, certain types of masonry components, wood elements, and some connections in steel structures (FEMA, 2009a), which is caused by different mechanisms that depend on the material behavior. For instance, in concrete and masonry, pinching occurs as a result of an opening and closing cracks process; in steel connections, the phenomenon is induced by an opening and closing gaps process between the connection plates; and in wood elements, pinching is caused by a slipping and a softening at connections joints as a result of an opening and closing gaps process.

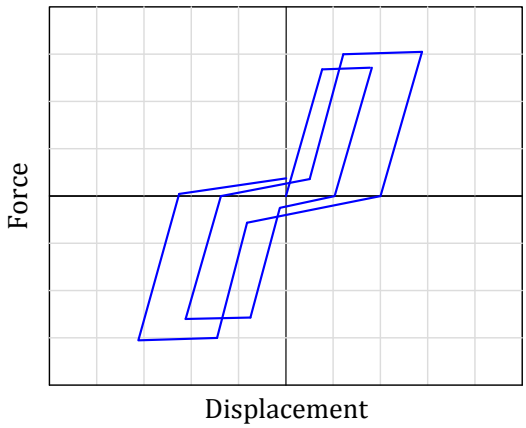

Figure 3-6: Example of pinching behavior in hysteresis cycles

According to FEMA (2009a), all of those phenomena depends in a great extent both on the characteristics of the structure (e.g., material properties, geometry, level of ductile detailing, connection type) and on the loading history (e.g., the intensity in each cycle, number of cycles, sequence of loading cycles). Some structural systems can exhibit those phenomena either alone or in combination, as shown in Fig. **3-7**, so it is essential to have a powerful nonlinear dynamical model capable of representing completely the hysteretic behavior of the system.

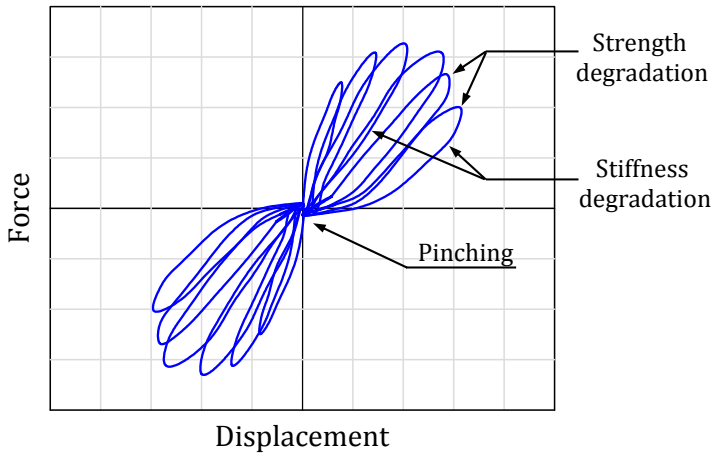

Figure 3-7: A typical hysteresis curve of a structural system with phenomena combination

3.4 Overview of hysteretic models

The assumption of structural systems have a linear behavior under cyclic load together with the non-inclusion of the nonlinear hysteretic phenomena has conducted to unrealistic structural analysis and designs, creating the need for finding a powerful and useful nonlinear dynamical model for all different types of hysteretic behavior exhibited by structural systems. Many studies have been carried out in order to develop hysteretic models capable to capture effectively the cyclic hysteretic responses of structural systems, achieving to improve and to increment the literature related to hysteretic models and their correct application in the structural analysis and design. In general, the hysteretic models can be classified into *Smooth Hysteretic Models* (SHM) and *Polygonal Hysteretic Models* (PHM) (see e.g. Sivaselvan and Reinhorn (2000, 1999)). Fig. **3-8** illustrates these two types of models.

3.4.1 Smooth Hysteretic Models

The Smooth Hysteretic Models (SHMs) use nonlinear formulations to model the response of a system, representing in a good way the continuous changes in the material during the cyclic load-

ing. According to Ray and Reinhorn (2014), the total stiffness of SHMs can be represented by an appropriate combination of component springs (reciprocal structures) with phenomenological meaning so that this decomposition of the whole model into sub-models can result to the easier construction of algorithms for its implementation (Bougioukos, 2017).

The initial formulation of a SHM was developed by Bouc (1967) and later modified by Wen (1976), which is known as *the Bouc-Wen hysteretic model*. Subsequently, Baber and Wen (1981), Baber and Noori (1985), Baber et al. (1986), Foliente (1995), and Foliente et al. (1996) expanded the model to include degradation and pinching effects. This model has set the basis for the development of many others smooth hysteretic models in spite of that Charalampakis (2009) found some deficiencies. Sivaselvan and Reinhorn (2000) developed a more versatile model that can address the stiffness and strength degradation as well as track bond slip and gap opening and closing in cross sections of structural members, usually represented by pinched hysteretic models by changing the properties of component springs. Rodgers et al. (2012) formulated a model through rational mechanics, that simulate yielding, pinching, and flag-shaped hysteresis, achieving to model various rate-dependent dampers. Recently, Ray and Reinhorn (2014) proposed a enhanced SMH capable to simulate a rate independent hysteretic behaviour, which can capture quite accurately the behaviour of ductile and brittle materials, and include stiffnes degradation, strength degradation and pinching effects.

3.4.2 Polygonal Hysteretic Models

Polygonal Hysteretic Models are represented with piecewise linear relationships that describe each stage of the structural response of a system. The simplest model of this kind of models is the bilinear hysteretic model proposed initially by Clough and Johnston (1966), which includes the stiffness degradation effect. Iwan (1966) proposed a distributed-element PHM composed of n number of spring sets considered in parallel for elastic-perfectly plastic elements, where the elastic branch is piecewise linear; later, Iwan and Cifuentes (1986) improved the distributed-element model to take into account the stiffness degradation phenomenon. Thyagarajan (1989) modified the Iwan's model by using an infinite number of springs, thus obtaining a curvilinear hysteretic behavior. Takeda et al. (1970) proposed a PHM considering cracking and yielding with a number of load-displacement conditions and branch stiffness rules, which is a complicated PHM that considers both the effect of stiffness degradation and strength deterioration. Park et al. (1987) developed a PHM known as *the three parameter model* in which the parameters are associated with stiffness degradation, strength deterioration and pinching effect; in fact, the model presents a novel formulation because the stiffness degradation of the unloading branch is encountered through a vertex point. A few years later, Sivaselvan and Reinhorn (1999) presented a thorough study of a general framework for PHMs, wherein also developed a hysteretic model in which the stiffness degradation and the strength deterioration are defined by a backbone curve.

On his behalf, Mostaghel (1999) proposed an physically-based analytical description of structural hysteretic systems based on a SDoF system composed of a mass, springs and sliders, similar to the distributed-element model proposed by Iwan (1966); the analytical models were formulated for bilinear and multilinear hysteretic systems. This model presents a differential equation description of PHMs that takes into account the pinching, stiffness degradation, and load deterioration effects. Ibarra et al. (2005) also suggested a PHM capable of representing the aforementioned hysteretic phenomena. In recent years, Zeynalian et al. (2012) improved the Mostaghel's bilinear model including the sliding effect, and besides, they corrected an original equation of the model to satisfy some of the boundary conditions of the first cycle.

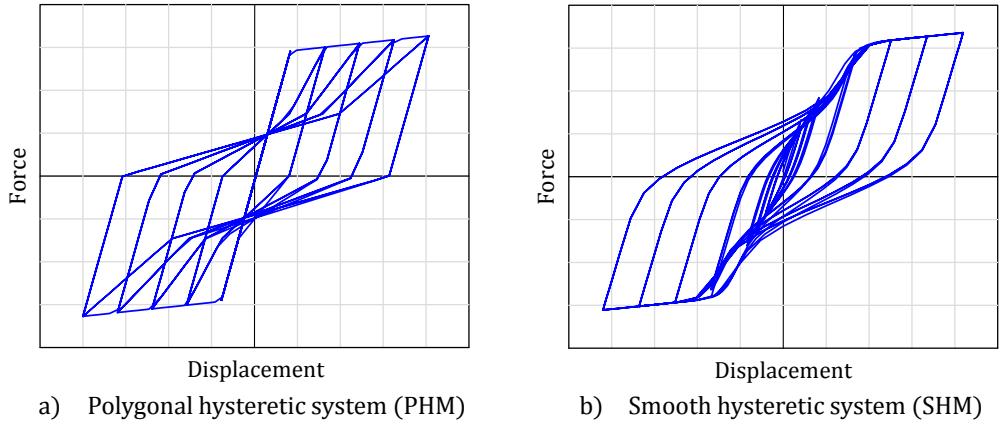

Figure 3-8: Comparison between PHM and SHM. (Adapted from Ray and Reinhorn (2014))

In this study, the original PHM proposed by Mostaghel (1999) with the essential corrections made by Zeynalian et al. (2012) is employed for the investigation and the simulation of the nonlinear response of the structural walls, because those systems experimentally have presented pinching, stiffness degradation and load deterioration effects, and this model compared with some of the analytical models currently yields more precise responses (Zeynalian and Mokhtari, 2017a).

3.5 The Mostaghel's model of hysteresis

The hysteretic model proposed by Mostaghel (1999) is a PHM physically-based analytical model capable of describing the behavior of general hysteretic systems, including stiffness degradation, load deterioration, and pinching effect. One of the principal advantages of the Mostaghel's formulation is that all of the system parameters are in terms of definite physical quantities or system properties that can be measured through tests. According to the examples presented by Mostaghel (1999), Zeynalian et al. (2012), and Zeynalian and Mokhtari (2017a,b), it is possible to conclude that this formulation can effectively model the behavior of SDoF hysteretic systems, and to be expanded to model the hysteretic behavior of the structural walls.

Initially, the formulation for bilinear hysteretic systems is presented; subsequently, the formulation is expanded to multilinear hysteretic systems. In all cases, to develop the equations that govern the Mostaghel's formulation, it is necessary to consider the following complementary functions:

$$N(x) = 0.5[1+\text{sgn}(x)]\{1+[1-\text{sgn}(x)]\} = \begin{cases} 1, & x \geq 0 \\ 0, & x < 0 \end{cases}$$

$$M(x) = 0.5[1-\text{sgn}(x)]\{1-[1+\text{sgn}(x)]\} = \begin{cases} 0, & x \geq 0 \\ 1, & x < 0 \end{cases}$$

$$\bar{N}(x) = 0.5[1+\text{sgn}(x)]\{1-[1-\text{sgn}(x)]\} = \begin{cases} 1, & x > 0 \\ 0, & x \leq 0 \end{cases}$$

$$\bar{M}(x) = 0.5[1-\text{sgn}(x)]\{1+[1+\text{sgn}(x)]\} = \begin{cases} 0, & x > 0 \\ 1, & x \leq 0 \end{cases}$$

where $N(x)$ is the *unit step function*; $M(x)$, $\bar{N}(x)$, and $\bar{M}(x)$ are functions derived from the unit step function; and $sgn(x)$ is the *signum function* defined as:

$$sgn(x) = \begin{cases} -1, & x \geq 0 \\ 0, & x = 0 \\ 1, & x > 0 \end{cases}$$

3.5.1 Bilinear hysteretic system

The SDoF bilinear hysteretic system proposed by Mostaghel (1999) is composed of a mass m, two springs and a viscous damping coefficient (c), which is excited by an external force $P_o(t)$ (see Fig. **3-9**). The spring of stiffness αk is directly connected to the mass and its deformation is represented by x; the other spring, which is connected to the mass through a slider with friction coefficient μ, has a stiffness $(1-\alpha)k$ and its deformation is denoted by u. The parameter k represents the overall stiffness of the bilinear system, and $0 < \alpha \leq 1$ is the stiffness ratio.

The maximum force in the slider connected to the second spring is given by:

$$\mu mg = (1-\alpha)k\delta$$

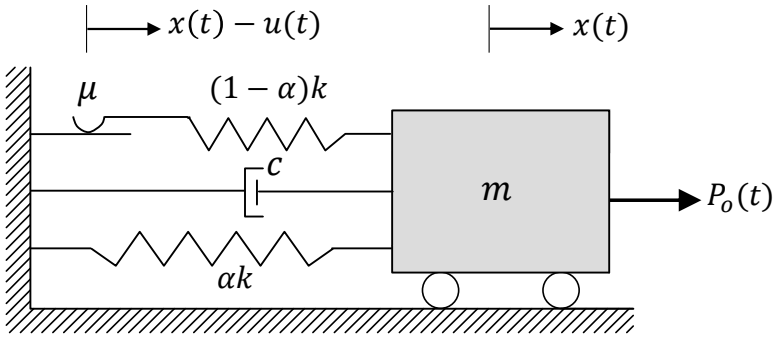

Figure 3-9: SDoF bilinear system of the Mostaghel's hysteretic model

where δ is the limiting deformation of the spring connected to the slider. Therefore, $-\delta \leq u \leq \delta$ which means that the slider starts to slide after the spring reaches the maximum elongation (Zeynalian et al., 2012).

The motion equation of the bilinear system shown in Fig. **3-9** is given by the following differential equation which represents the behavior of a non-degenerating system:

$$m\ddot{x}(t) + c\dot{x}(t) + \alpha kx(t)(1-\alpha)ku = P_o(t) \tag{3-7}$$

According to Mostaghel (1999), pinching effect is included due to two sources. One source is known as *strength pinching* which is caused by the unequal strengths for loading in opposite directions (see Fig. **3-10**); this source is introduced in the model by the strength ratio λ_p, with the condition $0 \leq \lambda_p \leq 1$. The other source is attributed to *stiffness hardening*, this is, an additional stiffness encountered when the system yields at higher levels of response; this source is taken into account in the model by the insertion of two springs of stiffness k_s and initial gap δ_s, symmetrically located on both sides of the mass, as shown in Fig. **3-11**.

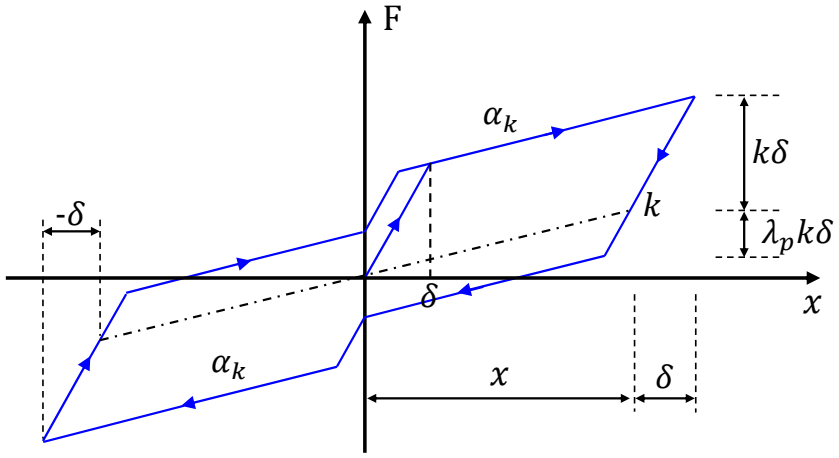

Figure 3-10: Hysteresis loop for a bilinear system with strength pinching

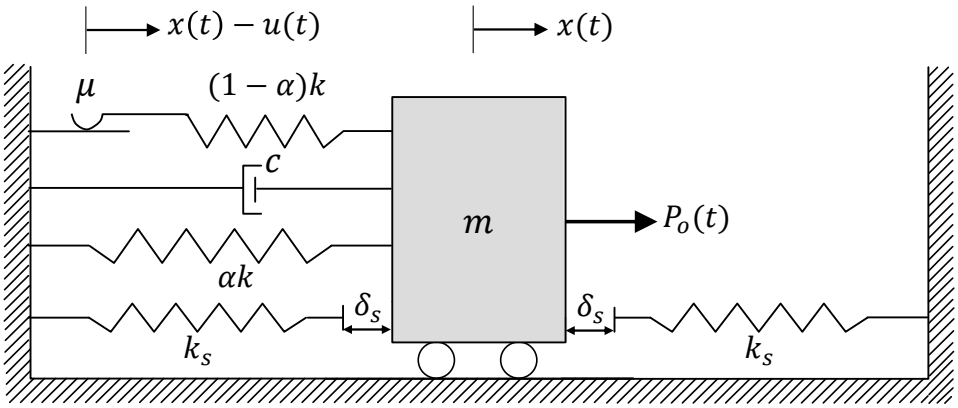

Figure 3-11: SDoF bilinear system of the Mostaghel's hysteretic model with stiffness hardening

Mostaghel (1999) also expanded the formulation to include stiffness degradation and load deterioration (strength degradation) phenomena via two functions defined in terms of the *total non-dimensional hysteretic energy* $h(\tau)$. In this way, the stiffness-degradation function $\Phi_k(\tau)$ and the load-deterioration function $\Phi_l(\tau)$ are given by the following expressions, respectively:

$$\Phi_k(\tau) = \frac{1}{1+\lambda_k h(\tau)}$$

$$\Phi_l(\tau) = \frac{1}{1+\lambda_l h(\tau)}$$

where $\lambda_k \geq 0$ and $\lambda_l \geq 0$ are stiffness-degradation and load-deterioration factors, respectively.

Due to the insertion of those hysteretic phenomena, Eq. (3-7) need to be expanded. Thus, the new equilibrium equation for the bilinear system is defined as:

$$m\ddot{x}(t) + c\dot{x}(t) + \alpha k x(t) + k_s(|x(t)| - \delta_s)\,\mathrm{sgn}(x(t))\bar{N}(|x(t)| - \delta_s) + (1-\alpha)ku = P_o(t) \tag{3-8}$$

The above equation includes two unknowns, x and u, so an additional equation is needed for computing the response of the system; this additional equation is obtained from the system behavior shown in Fig. **3-10**, by taking a close look at the denoted paths. Mostaghel (1999) developed the original formulation, however, Zeynalian et al. (2012) concluded that the equation did not satisfy some boundary conditions of the first cycle, therefore, they applied the necessary corrections on the original equation. In this way, according to Zeynalian et al. (2012), the additional equation is given by:

$$\begin{aligned}\dot{u}(t) = \; & \dot{x}(t)\{N(\dot{x}(t))[M(u(t)-\lambda_p\delta)\bar{M}(x(t)) + M(u(t)-\delta)\bar{N}(x(t))] \\ & + M(\dot{x}(t))[\bar{N}(u(t)+\lambda_p\delta)N(x(t)) + \bar{N}(u(t)+\delta)M(x(t))]\}\end{aligned}$$

The response force of the bilinear system $F(t)$ is given by:

$$F(t) = \alpha k x(t) + k_s(|x(t)| - \delta_s)\,\mathrm{sgn}(x(t))\bar{N}(|x(t)| - \delta_s) + (1-\alpha)ku(t) \tag{3-9}$$

The following expressions are used in order to nondimensionalize these equations:

$$\tau = t\omega; \qquad \omega = \sqrt{k/m}; \qquad \xi = c/2m\omega; \qquad \delta_s = \gamma_s\delta;$$
$$x(t) = \delta y(\tau); \qquad u(t) = \delta z(\tau); \qquad P_o(t) = k\delta p(\tau); \qquad F(t) = k\delta f(\tau);$$

As a result, the nondimensionalized differential equation of the system corresponding to Eq. (3-8) is given by:

$$\ddot{y}(\tau) + 2\xi\dot{y}(\tau) + \alpha y(\tau) + \alpha_s(|y(\tau)| - \gamma_s)\,\mathrm{sgn}(y(\tau))\bar{N}(|y(\tau)| - \gamma_s) + (1-\alpha)z(\tau) = p(\tau) \tag{3-11}$$

where $\alpha_{si} := k_s/k$ is the stiffness-hardening ratio and $\gamma_s := \delta_s/\delta$ is the stiffness-hardening gap ratio.

The non-dimensional force of the system corresponding to Eq. (3-9) is represented by:

$$f(\tau) = \alpha y(\tau) + \alpha_s(|y(\tau)| - \gamma_s)\,\mathrm{sgn}(y(\tau))\bar{N}(|y(\tau)| - \gamma_s) + (1-\alpha)z(\tau)$$

where $z(\tau)$ is the non-dimensional hysteretic displacement of the system, defined by the following differential equation::

$$\begin{aligned}\dot{z}(\tau) = \; & \dot{y}(\tau)\Phi_k(\tau)\{N(\dot{y}(\tau))[M(z(\tau) - \lambda_p\Phi_l(\tau))\bar{M}(y(\tau)) + M(z(\tau) - \Phi_l(\tau))\bar{N}(y(\tau))] \\ & + M(\dot{y}(\tau))[\bar{N}(z(\tau) + \lambda_p\Phi_l(\tau))N(y(\tau)) + \bar{N}(z(\tau) + \Phi_l(\tau))M(y(\tau))]\}\end{aligned} \tag{3-12}$$

with the initial condition $z(0) = 0$. The total non-dimensional hysteretic energy $h(\tau)$ absorbed by the system is represented by the differential equation:

$$\begin{aligned}\dot{h}(\tau) = \; & \Phi_l(\tau)(1-\alpha)|\dot{y}(\tau)|[N(\dot{y}(\tau))N(y(\tau) - \gamma_p) + \bar{M}(\dot{y}(\tau))M(y(\tau) + \gamma_p) \\ & + \lambda_p\bar{N}(\dot{y}(\tau))M(y(\tau)) + \lambda_p M(\dot{y}(\tau))N(y(\tau))] \cdot |1 - \{\bar{N}(\dot{y}(\tau))[\bar{M}(z(\tau) \\ & - \lambda_p\Phi_l(\tau))\bar{M}(y(\tau)) + \bar{M}(z(\tau) - \Phi_l(\tau))\bar{N}(y(\tau))] + M(\dot{y}(\tau))[N(z(\tau) \\ & + \lambda_p\Phi_l(\tau))N(y(\tau)) + N(z(\tau) + \Phi_l(\tau))M(y(\tau))]\}|\end{aligned} \tag{3-13}$$

with the initial condition $h(0) = 0$. Here, $\gamma_p := (1 - \lambda_p)$ is the pinched complementary strength ratio.

The simultaneous solution of the differential Eqs. (3-11), (3-12) and (3-13) allows obtaining the response of the Mostaghel's bilinear hysteretic system with pinching, stiffness degradation and load deterioration, for given physical values of stiffness ratio α, stiffness hardening ratio α_s, stiffness hardening gap ratio γ_s, strength ratio λ_p, stiffness degradation factor λ_k, load deterioration factor λ, and any applied external load $p(\tau)$; these equations can be solved using numerical methods for solving differential equations, for example, the Runge-Kutta method. Fig. **3-12** shows two examples that demonstrates the applicability of the model.

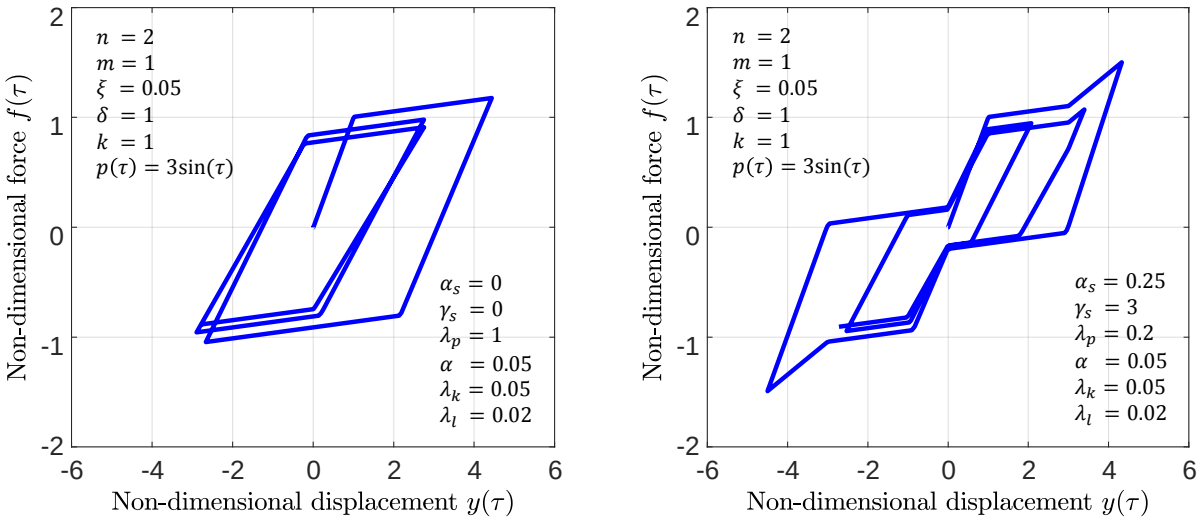

a) Response of a bilinear hysteretic system with stiffness degrading and load deterioration.

b) Response of a bilinear hysteretic system with stiffness degrading, load deterioration, pinching and stiffness hardening.

Figure 3-12: Two examples of the Mostaghel's bilinear hysteretic systems with different set of parameters

3.5.2 Multilinear hysteretic system

The Mostaghel's multilinear hysteretic system with n linear segments would need a total of $(2n-1)$ equations to correctly model the system. The necessity for the additional equations arises from the fact that the stiffness degradation and load deterioration are caused by the deterioration of the properties of the system, which starts at the inception of plastic deformation.

To develop the equations that govern the behavior of the multilinear hysteretic system proposed by Mostaghel (1999), it is necessary to consider the SDoF shown in Fig. **3-13**. As can be seen there, the system is composed of a mass m, $(n+j)$ number of springs, and a viscous damping coefficient (c), and it is excited by an external force $P_o(t)$. The system has a set of $(n-1)$ springs in parallel connection that are directly connected both to the mass and to a set of sliders; the stiffness and the deformation of the ith spring of this set are $\alpha_i k$ and u_i, respectively. The parameter $\alpha_i = k_i/k_{init}$ is the stiffness ratio, where k_i is the stiffness for the i-th spring and k_{init} is the elastic initial stiffness of the system. It is important to emphasize that k is the sum of the stiffnesses $\alpha_i k$ of all springs that are directly connected to the mass; therefore, the sum of all α_i is always equal to unity.

In addition to the above, the system also includes a spring of stiffness $\alpha_n k$ which is directly connected to the mass and its deformation is represented by x, and j other springs located on both sides of the mass, each one with stiffness k_{si} and initial gap δ_{si}. (To illustrate clearly the system, only these springs on one side are shown in Fig. **3-13**).

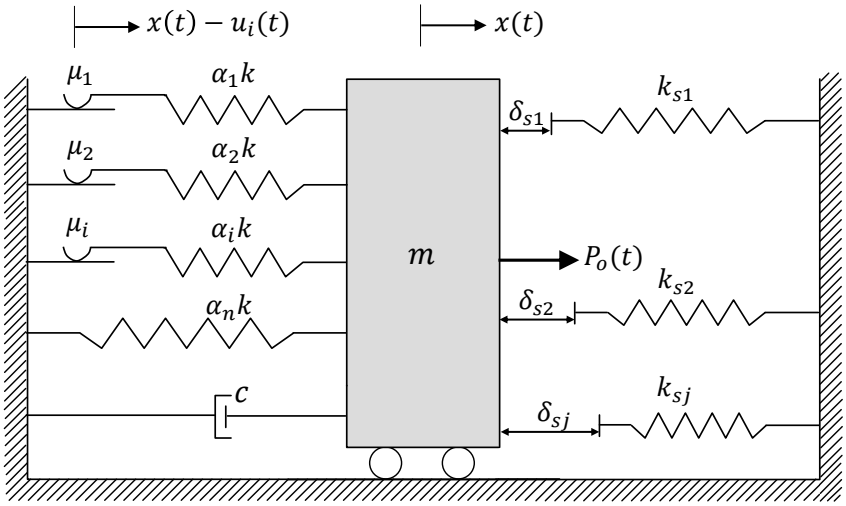

Figure 3-13: Representation of a SDoF multilinear system of the Mostaghel's hysteretic model

The equilibrium equation for the multilinear system is defined as (Mostaghel, 1999):

$$m\ddot{x}(t) + c\dot{x}(t) + \alpha_n k x(t) + k\sum_{i=1}^{n-1} \alpha_i \cdot u_i(t) + \sum_{i=1}^{m} \alpha_{si} k(|x(t)| - \gamma_{si}\delta)\,\mathrm{sgn}(x(t))\bar{N}(|x(t)| - \gamma_{si}\delta) = P_o(t) \tag{3-14}$$

The response force of the multilinear system $F(t)$ is given by:

$$F(t) = \alpha_n k x(t) + k\sum_{i=1}^{n-1} \alpha_i \cdot u_i(t) + \sum_{i=1}^{m} \alpha_{si} k(|x(t)| - \gamma_{si}\delta)\,\mathrm{sgn}(x(t))\bar{N}(|x(t)| - \gamma_{si}\delta) \tag{3-15}$$

where $\alpha_{si} := k_{si}/k_{init}$ is the stiffness-hardening ratio for the spring of stiffness k_{si}, and $\gamma_{si} := \delta_{si}/\delta_1$ is the stiffness-hardening gap ratio for the i-th spring (δ_{si}) to the limiting deformation of the first spring δ_1.

Similarly, as in the bilinear formulation, the equations are nondimensionalized by the following expressions:

$$\begin{array}{llll} \tau = t\omega; & \omega = \sqrt{k_{init}/m}; & \xi = c/2m\omega; & \delta_{si} = \gamma_{si}\delta_1; \\ x(t) = \delta_1 y(\tau); & u_i(t) = \delta_1 z_i(\tau); & P_o(t) = k_{init}\delta_1 p(\tau); & F(t) = k_{init}\delta_1 f(\tau); \end{array} \tag{3-16a-f}$$

As a result of applying those expressions, the nondimensionalized differential equations that govern the multilinear system are obtained. Thus, the corresponding equation to Eq. (3-14) is given by:

$$\ddot{y}(\tau) + 2\xi\dot{y}(\tau) + \alpha_n y(\tau) + \sum_{i=1}^{n-1} \alpha_i \cdot z_i(\tau) + \sum_{i=1}^{m} \alpha_{si}(|y(\tau)| - \gamma_{si})\,\mathrm{sgn}(y(\tau))\bar{N}(|y(\tau)| - \gamma_{si}) = p(\tau) \tag{3-17}$$

and the nondimensional force of the system corresponding to Eq. (3-15) is represented by:

$$f(\tau) = \alpha_n y(\tau) + \sum_{i=1}^{n-1} \alpha_i \cdot z_i(\tau) + \sum_{i=1}^{m} \alpha_{si}(|y(\tau)| - \gamma_{si})\,\mathrm{sgn}(y(\tau))\bar{N}(|y(\tau)| - \gamma_{si})$$

where $z_i(\tau)$ is the nondimensional hysteretic displacement of the i-th spring, defined by the following differential equation which includes the essential corrections made by Zeynalian et al. (2012):

$$\begin{aligned}\dot{z}_i(\tau) = \; & \dot{y}(\tau)\Phi_{ki}(\tau)\{N(\dot{y}(\tau))[M(z_i(\tau) - \lambda_{pi}\gamma_i\Phi_{li}(\tau))\bar{M}(y(\tau)) + M(z_i(\tau) - \gamma_i\Phi_{li}(\tau))\bar{N}(y(\tau))] \\ & + M(\dot{y}(\tau))[\bar{N}(z_i(\tau) + \lambda_{pi}\gamma_i\Phi_{li}(\tau))N(y(\tau)) + \bar{N}(z_i(\tau) + \gamma_i\Phi_{li}(\tau))M(y(\tau))]\}\end{aligned} \tag{3-18}$$

for $i = 1,2,3,...,n-1$, with the initial condition $z(0) = 0$.

The total nondimensional hysteretic energy $h_i(\tau)$ absorbed by a slider attached to the i-th spring is governed by the following differential equation:

$$\begin{aligned}\dot{h}_i(\tau) = \; & \Phi_{li}(\tau)\alpha_i\gamma_i|\dot{y}(\tau)|[N(\dot{y}(\tau))N(y(\tau) - \gamma_{pi}) + \bar{M}(\dot{y}(\tau))M(y(\tau) + \gamma_{pi}) \\ & + \lambda_{pi}\bar{N}(\dot{y}(\tau))M(y(\tau)) + \lambda_{pi}M(\dot{y}(\tau))N(y(\tau))] \cdot |1 - \{\bar{N}(\dot{y}(\tau))[\bar{M}(z(\tau) \\ & - \lambda_{pi}\gamma_i\Phi_{li}(\tau))\bar{M}(y(\tau)) + \bar{M}(z(\tau) - \gamma_i\Phi_{li}(\tau))\bar{N}(y(\tau))] + M(\dot{y}(\tau))[N(z(\tau) \\ & + \lambda_{pi}\gamma_i\Phi_{li}(\tau))N(y(\tau)) + N(z(\tau) + \gamma_i\Phi_{li}(\tau))M(y(\tau))]\}|\end{aligned} \tag{3-19}$$

for $i = 1,2,3,...,n-1$, where $0 \leq \lambda_{pi} \leq 1$ represents the pinching effects in function of the strength ratio for the i-th spring; $\gamma_{pi} := (1 - \lambda_{pi})$ is the pinched complementary strength ratio; $\gamma_i := \delta_i/\delta_1$ is the ratio of the limiting deformation for the i-th spring (δ_i) to limiting deformation of the first spring (δ_1), with the condition $\delta_1 \leq \delta_2 \leq \delta_3 ... \leq \delta_{n-1}$. The stiffness-degradation function $\Phi_{ki}(\tau)$ and the load-deterioration function $\Phi_{li}(\tau)$ for the i-th spring are represented by the following expressions, respectively:

$$\Phi_{ki}(\tau) = \frac{1}{1 + \lambda_{ki}h_i(\tau)}$$

$$\Phi_{li}(\tau) = \frac{1}{1 + \lambda_{li}h_i(\tau)}$$

where $\lambda_{ki} \geq 0$ and $\lambda_{li} \geq 0$ are stiffness-degradation and load-deterioration factors for the the i-th spring, respectively.

Eqs. (3-17), (3-18) and (3-19) provide the $(2n-1)$ equations needed to completely define the behavior of a multilinear hysteretic system of n linear segments, with pinching, stiffness degradation and load deterioration, for given physical values for the system parameters. In fact, a Mostaghel's multilinear hysteretic model with n-lines segments involves $(7n-4)$ parameters represented by the following parameter vector θ:

$$\theta = \{\xi, \lambda_{pi}, \alpha_i, \alpha_{si}, \gamma_{si}, \lambda_{ki}, \lambda_{li}, \delta_i\} \tag{3-20}$$

In the same way, as in the bilinear formulation, the simultaneous solution of this set of equations allows calculating the response of a multilinear system; these equations can be solved using numerical methods for solving differential equations, for example, the Runge-Kutta method. Then, the dimensional response of the system is obtained applying Eqs. (3-16a-f). Fig. **3-14** illustrates two examples of four-linear hysteretic systems, which demonstrate that the analytical model proposed by Mostaghel (1999) provides realistic descriptions of the force-deformation behavior for general hysteretic systems. Thus, based on the presented examples, the Mostaghel's multilinear hysteretic formulation will be used in this study to simulate the hysteretic behavior and to assess the seismic performance of structural walls subjected to earthquake loads.

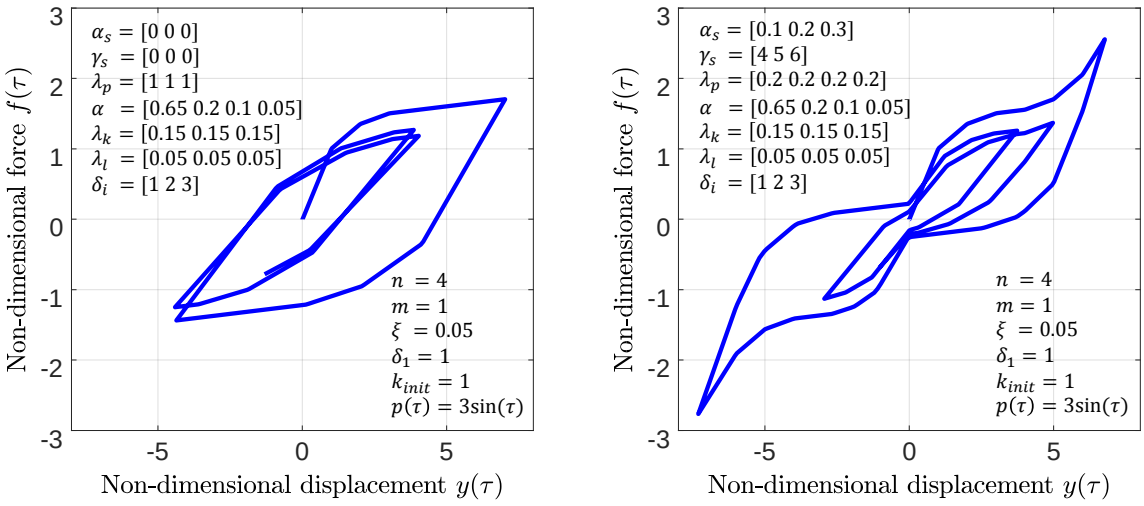

a) Response of a four - linear hysteretic system with stiffness degrading and load deterioration.

b) Response of a four - linear hysteretic system with stiffness degrading, load deterioration, pinching and stiffness hardening.

Figure 3-14: Two examples of four-linear hysteretic systems with different parameters values

3.6 Identification of hysteretic structural systems

Hysteretic mathematical models involve a certain number of parameters which must be previously identified to apply these models in the analysis of structural systems, in order to simulate accurately the response of them. By a process known as Identification of Systems which aims to evaluate the numerical values to be assigned to a Parameter Vector θ (Pelliciari et al., 2018), the model parameters are tuned using reliable data obtained from experimental tests so that the simulated response of the system matches as much as possible the experimental one. Consequently, an identification technique is usually utilized to obtain the set of optimal values of the model parameters; in fact, this problem has been widely tackled in the literature where several methodologies have been developed.

In general, the procedures suggested for the parameter identification of hysteretic models can be classified into two groups (Ortiz et al., 2013): 1) Techniques based on nonlinear filtering such as the Kalman filters (Zhang et al., 2002; Yang and Ma, 2003; Askari et al., 2012, 2016); and 2) Techniques based on the minimization of a objective function (or cost function) such as Gauss-Newton methods (Yar and Hammond, 1987; Kunnath et al., 1997), least squares (Sues et al., 1988; Garrido and Rivero-Angeles, 2006), genetic algorithms (GAs) (Zheng Xueliang et al., 1997; Giuclea et al., 2009; Sengupta and Li, 2014; Pelliciari et al., 2018), multi-objective optimization algorithms (Ortiz et al., 2013), bayesian model updating techniques (Ortiz et al., 2015), particle swarm optimization procedures (Ye and Wang, 2007; Tang et al., 2007; Xue et al., 2009; Tang et al., 2010; Charalampakis and Dimou, 2010; Tang et al., 2015), among others.

3.6.1 Particle Swarm Optimization (PSO)

Particle Swarm Optimization (PSO) is a population-based stochastic optimization method introduced by Kennedy and Eberhart (1995). This method mimics the social behavior of swarms of animals, such as flocks of birds or fish schooling, in which each individual (particle) adapts its behavior according to its own experience and to its neighbors' behavior, satisfying the five axioms of swarm intelligence: proximity, quality, diverse response, stability, and adaptability (Millonas, 1993; Charalampakis and Dimou, 2010). PSO is similar to the GAs in the sense that it starts with a set of random solutions, called the initial swarm, and then an optimal solution is reached by updating generations. Ever since PSO was proposed, a lot of variations and improvements on the method have been developed in order to obtain better algorithms and procedures that eliminate the possible deficiencies of the original method and allow expanding its applications. The reader is referred to (Imran et al., 2013) and (Marini and Walczak, 2015) for more information about this topic.

PSO has been widely applied in many fields, having success in the solution of many types of problems, such as mechanical, structural and multi-objective optimization, artificial neural network training, fuzzy system control, among others. In structural engineering, Fourie and Groenwold (2002) used PSO for the size and shape optimization problem in the design of structures and Perez and Behdinan (2007) presented in detail the background and implementation of the PSO algorithm for constraint structural optimization tasks, in which they showed the ability of PSO to find better optimal solutions for structural optimization tasks than other optimization algorithms. Particularly, PSO has been used for: topology, size and shape optimization and design of trusses (Schutte and Groenwold, 2003; Tang et al., 2009; Luh and Lin, 2011; Cao et al., 2017); reliability-based optimal design of truss structures (Dimou and Koumousis, 2009); optimum design of reinforced concrete structures (McCarthy and McCluskey, 2009; Kaveh and Sabzi, 2011); structural detection of damage (Sandesh and Krishnapillai, 2011; Wei et al., 2018); optimization of steel structures (Gholizadeh and Moghadas, 2014; Ye et al., 2016); optimal seismic design of structures (Salajegheh et al., 2008; Gholizadeh and Salajegheh, 2009; Esfandiari et al., 2018), among others.

Regarding the identification of systems, Tang et al. (2007) developed a method for this purpose using the PSO algorithm in order to find the optimal estimation of the parameters. In the same year, Ye and Wang (2007) used PSO to estimate the parameters of the Bouc-Wen hysteresis model with noisy data, showing that the proposed method was still effective even if the simulated data were corrupted by noise. Then, Xue et al. (2009) utilized the PSO algorithm for the parameter estimation of structural systems which could be formulated as a multi-modal numerical optimization problem with high dimension. Subsequently, Tang et al. (2010, 2015) developed a comprehensive learning particle swarm optimization method to estimate parameters of structural systems; this variant of PSO enabled the diversity of the swarm to be preserved to avoid premature convergence. Charalampakis and Dimou (2010) employed two variants of the PSO algorithm for the identification of a Bouc-Wen hysteretic system that represented a full-scale bolted-welded steel connection; the first variant was simple while the other was enhanced by the implementation of additional operators. In recent years, Zheng and Liao (2016) solved the parameter identification problem for nonlinear dynamic systems through a novel social-emotional particle swarm optimization.

3.6.1.1 The simple PSO algorithm

In the PSO algorithm, the set of potential solutions to the optimization problem is defined as a swarm of particles that represent a point in a D-dimensional parameter (or design) space in which D is the number of parameters to be optimized. In this sense, the position of the i-th particle is described by the following vector (see e.g. Marini and Walczak, 2015):

$$\theta_i = [\theta_{i1}\ \theta_{i2}\ \theta_{i3}\ ...\ \theta_{iD}]$$

which must meet the condition $\theta_L \leq \theta_i \leq \theta_U$, where θ_L and θ_U are the lower and upper values of the variables, respectively. The population of N_p particles that constitutes the swarm is defined as:

$$\Theta = \{\theta_1, \theta_2, \theta_3, ..., \theta_{N_p}\}$$

The particles are attracted towards better positions in the parameter space, according to the best local position and the best position of the swarm (i.e. the position of the swarm leader) by simple expressions related to the position and velocity of each particle, which change at each k-th iteration. The position of the i-th particle is given by:

$$\theta_i^{k+1} = \theta_i^k + \mathbf{v}_i^{k+1} \tag{3-21}$$

for $i = 1, 2, 3, ..., N_p$, where k and $k+1$ are two successive iterations. $\mathbf{v}_i^{k+1}$ is the velocity vector of the i-th particle at the $(k+1)$ iteration, which governs the way as the particle moves across the parameter space and is composed of three terms (Marini and Walczak, 2015): the first one, which is called the *inertia*, prevents that the particle changes drastically direction, by keeping track of the previous route direction; the second term is known as the *cognitive component* which represents the tendency of the particle to move to its own previously found best position; and the third one is the

social component which identifies the propensity of a particle to move towards the best position of the swarm. According to this, the velocity vector is then defined by the following equation (Charalampakis and Dimou, 2010):

$$\mathbf{v}_i^{k+1} = w\mathbf{v}_i^k + c_1\mathbf{r}_1 \cdot (\mathbf{p}_i^k - \theta_i^k) + c_2\mathbf{r}_2 \cdot (\mathbf{g}^k - \theta_i^k) \tag{3-22}$$

for $i = 1,2,3,...,N_p$, where w is the inertia factor; c_1 and c_2 are the cognitive and the social coefficient, respectively, which are usually in the range between 0 to 4; $\mathbf{r}_1$ and $\mathbf{r}_2$ are vectors of random numbers generated from a uniform distribution in the interval $[0,1]$; $\mathbf{p}_i^k$ is the best position of the particle i-th based on its travel history at the k-th iteration; and $\mathbf{g}^k$ is the best position among all particles of the swarm at the k-th iteration. Fig. **3-15** illustrates the position and velocity updates in PSO.

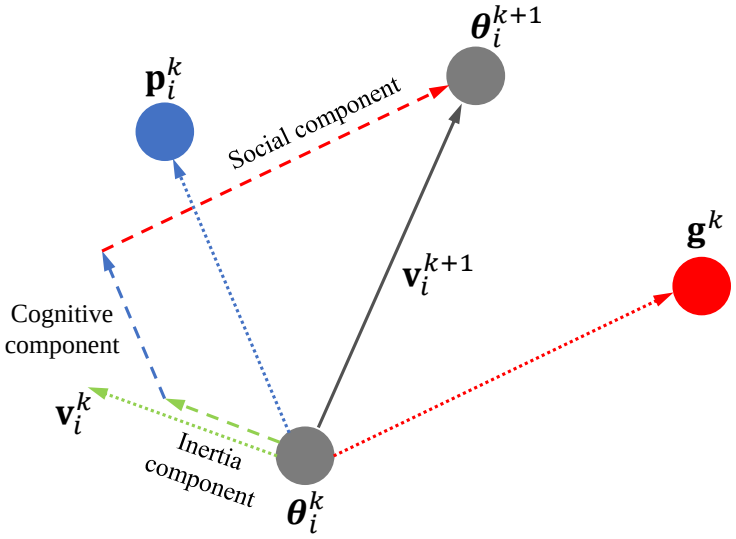

Figure 3-15: Scheme of the position and velocity updates in the iterative process of PSO

The process to implement the basic version of PSO can be summarized in the following steps (see also Arora, 2011):

1. Select the number of particles (N_p) of the initial swarm, the c_1 and c_2 coefficients, the w factor, the maximum number of iterations (k_{max}) and the cost function ($F(\theta)$) to be minimized.
2. Generate randomly N_p particles with their corresponding initial position vector (θ_i^0) and evaluate the cost function for these points ($F(\theta_i^0)$). Then, set the initial velocity vector of the particles ($\mathbf{v}_i^0$) as a zero vector.
3. Determine $\mathbf{g}^k$ as the particle with the smallest cost function value.
4. Generate the random vectors $\mathbf{r}_1$, $\mathbf{r}_2$ and calculate $\mathbf{v}_i^{k+1}$ by Eq. (3-22).
5. Compute θ_i^{k+1} using Eq. (3-21) to update the positions of each particle. Check that the particle positions are within the limit values, i.e. $\theta_L \leq \theta_i^{k+1} \leq \theta_U$.

6. Evaluate the cost function at all new positions ($F(\theta_i^{k+1})$). Then, perform the following checks for $i = 1,2,3,...,N_p$:

   Update the best local solutions: If $F(\theta_i^{k+1}) \leq F(\mathbf{p}_i^k)$, then $\mathbf{p}_i^{k+1} = \theta_i^{k+1}$; otherwise $\mathbf{p}_i^{k+1} = \mathbf{p}_i^k$

   Update the best global solution: If $F(\mathbf{p}_i^{k+1}) \leq F(\mathbf{g}^k)$, then $\mathbf{g}^{k+1} = \mathbf{p}_i^{k+1}$; otherwise $\mathbf{g}^{k+1} = \mathbf{g}^k$

7. Stop the iterative process if a stopping criterion is satisfied, for example if $k = k_{max}$ or if all the particles have converged to the best swarm solution. Otherwise, set $k = k+1$ and repeated the process from step 4.

3.6.2 Procedure for the parameter identification of hysteretic models using PSO

In general, the solution for the parameter identification problem is represented by an optimal parameter vector that is determined from an optimization, in such a way that minimizes only a cost function which is a measure of error between the experimental response and the estimated one, usually computed with the displacement response. However, a better solution can be obtained by the minimization of multiple cost functions, which is known as a multi-objective optimization. In fact, some studies have been carried out using this approach in order to identify the parameters of nonlinear dynamical model to simulate the behavior of structural walls. For instance, Ortiz et al. (2013, 2015) presented a novel identification methodology that simultaneously minimizes both the discrepancies between the estimated displacements and the experimental ones and the error between the experimental total dissipated energy and the estimated one using a nonlinear dynamical model. The results showed a good approximation of the estimated hysteresis cycles with respect to the shape of the experimental ones.

In this study, a procedure for the parameter identification of hysteretic systems using the simple PSO algorithm is proposed and is evaluated with the Mostaghel's multilinear hysteretic model in structural walls. Each particle of the PSO algorithm is related to a parameter vector of the mathematical model given by Eq. (3-20) and represents a point in the D-dimensional design space in which D is equal to the number of parameters that involves a Mostaghel's multilinear hysteretic model with n-lines segment, so that $D := 7n-4$. The proposal takes into account the multi-objective approach using the aforementioned cost functions, but keeps the single-objective PSO algorithm by a total cost function that is defined as a linear combination of those cost functions. The cost function for the displacement C_d is defined using the method of least squares between the experimental displacement measured from cyclic tests (x_{exp}) and the estimated displacements by the multilinear hysteretic model ($x_{mh}(\theta)$) for the parameter vector θ given by Eq. (3-20):

$$C_d = \sum_{j=1}^{q} \left[x_{exp}(t_j) - x_{mh}(t_j|\theta)\right]^2 \tag{3-23}$$

where q represents the number of records in the time series.

Similarly, the cost function for the total dissipated energy C_e is given by the following equation:

$$C_e = \sum_{j=1}^{q} \left[\varepsilon_{exp}(t_j) - \varepsilon_{mh}(t_j|\theta)\right]^2 \tag{3-24}$$

where ε_{exp} is the experimental total dissipated energy and $\varepsilon_{mh}(\theta)$ is the estimated one with the multilinear hysteretic model. Both expressions are a cumulative measure and represent the area enclosed by the hysteresis curves (Ortiz et al., 2013), so they are computed as a cumulative integral of this area using the trapezoidal method.

To construct the linear combination, the C_d and C_e functions are normalized to the maximum values $C_{d_{max}}$ and $C_{e_{max}}$ of the swarm at the first iteration of the identification process, respectively. Thus, the total cost function C is defined by:

$$C = A\left(\frac{C_d}{C_{d_{max}}}\right) + B\left(\frac{C_e}{C_{e_{max}}}\right) \tag{3-25}$$

where $0 < A < 1$ and $B := A - 1$ are the weighting parameters of the linear combination. A is included in the parameter vector θ given by Eq. (3-20) for the optimization process.

The proposed procedure is described by the following steps:

1. Select the number of particles (N_p) for swarms, the maximum number of iterations (k_{max}) for each simulation, and the c_1, c_2 and w coefficients. In the present study, the coefficients proposed by Clerc (2011) will be used: $c_1 = 1.193$, $c_2 = 1.193$ and $w = 0.721$.

2. Generate the initial swarm of N_p particles by random samples uniformly distributed in which each particle θ_i^0 must meet all the parameter constraints of the multilinear hysteretic model ($\theta_L \leq \theta_i^0 \leq \theta_U$).

3. Set the initial velocity vector ($\mathbf{v}_i^0$) as a zero vector and the initial best local solutions $\mathbf{p}_i^0 = \theta_i^0$. Subsequently, do the following routine for each initial particle θ_i^0:

   I. Run the Mostaghel's multilinear hysteretic model and obtain the estimated responses of displacement ($x_{mh}(\theta_i^0)$) and total dissipated energy ($\varepsilon_{mh}(\theta_i^0)$).

   II. Compute the cost functions of displacement ($C_{d_i}^0$) and total dissipated energy ($C_{e_i}^0$) using Eqs. (3-23) and (3-24), respectively.

   III. Select the $C_{d_{max}}^0$ and $C_{e_{max}}^0$ values. Then, extract the weighting parameter A_i from θ_i and determine the weighting parameter B_i.

   IV. Compute the total cost function C_i^0 using Eq. (3-25) and set $C_{\mathbf{p}_i}^0 = C_i^0$.

4. At each k-th iteration, repeat the following steps for each i-th particle:

I. Determine the best global solution ($\mathbf{g}^k$) as the particle with the smallest total cost function ($C_{\mathbf{g}}^k$).

II. Generate the random vectors $\mathbf{r}_1$, $\mathbf{r}_2$ and calculate $\mathbf{v}_i^{k+1}$ by Eq. (3-22).

III. Compute θ_i^{k+1} using Eq. (3-21) and check the parameter constraints of the multilinear hysteretic formulation:
If $\theta_L \leq \theta_i^{k+1} \leq \theta_U$, then continue with the following steps; otherwise return the particle to its previous position ($\theta_i^{k+1} = \theta_i^k$), set $k = k+1$ and continue from step 4.

   i. Run the Mostaghel's multilinear hysteretic model and obtain the estimated responses of displacement $x_{mh}(\theta_i^{k+1})$ and total dissipated energy $\varepsilon_{mh}(\theta_i^{k+1})$.

   ii. Compute the new cost functions $C_{d_i}^{k+1}$ and $C_{e_i}^{k+1}$ using Eqs. (3-23) and (3-24), respectively.

   iii. Extract the weighting parameter A_i from θ_i and determine the weighting parameter B_i. Subsequently, compute the new total cost function C_i^{k+1} using Eq. (3-25).

   iv. Update the best local solutions:
   If $C_i^{k+1} \leq C_{\mathbf{p}_i}^k$, then $C_{\mathbf{p}_i}^{k+1} = C_i^{k+1}$ and $\mathbf{p}_i^{k+1} = \theta_i^{k+1}$;

   otherwise $C_{\mathbf{p}_i}^{k+1} = C_{\mathbf{p}_i}^k$ and $\mathbf{p}_i^{k+1} = \mathbf{p}_i^k$

   v. Update the best global solutions:
   If $C_{\mathbf{p}_i}^{k+1} \leq C_{\mathbf{g}}^k$, then $C_{\mathbf{g}}^{k+1} = C_{\mathbf{p}_i}^{k+1}$, $\mathbf{g}^{k+1} = \theta_i^{k+1}$, and save $C_{d\mathbf{g}}^{k+1}$ and $C_{e\mathbf{g}}^{k+1}$;

   otherwise $C_{\mathbf{g}}^{k+1} = C_{\mathbf{g}}^k$ and $\mathbf{g}^{k+1} = \mathbf{g}^k$

IV. Stop the iterative process if $k = k_{max}$; otherwise, set $k = k+1$ and repeat the process from step 4.

5. Conduct N simulations of the above steps in order to find convergence. If this is reached, stop the identification process in which the $\mathbf{g}^{k_{max}}$ of the final simulation will be the optimal parameter vector for the Mostaghel's multilinear hysteretic model; otherwise, gather together the particles of the N simulations and create a new swarm. Subsequently, repeat the procedure from step 3 with the best N_p particles of that new swarm.

The above procedure is applied and tested in Chapter 4 in order to identify the parameters of the Mostaghel's multilinear hysteretic system for the structural walls.

4 Experimental and analytical hysteretic behavior of the structural walls

The development of new materials and structural systems requires experimental tests that allow a wide knowledge of their properties and their behavior under the load conditions for which they have been proposed. Then, mathematical models are calibrated with the experimental results to develop design criteria that facilitate and extend the use of the structural proposals.

This chapter focuses on both tasks, which begins with the descriptions of the cyclic tests. Then, brief literature reviews about each material and its applications in structural walls are presented. In the same section, the constitutive elements and the structural system of each wall are described in detail. Subsequently, Section 4.3 presents the experimental results for each structural wall, which include: hysteretic response curves, ductility levels, the estimation of structural parameters, the energy dissipation and the equivalent viscous damping, the estimation of the coefficient of energy dissipation capacity, and the damage states. On the other hand, the analytical modeling of the experimental hysteretic behavior for each wall is presented in Section 4.4 which includes the application of three variants of the Mostaghel's multilinear hysteretic model studied in Section 3.5.2, with the proposed procedure for the parameter identification, presented in Section 3.6.2. The chapter ends with the selection of the more adequate multilinear hysteretic model variant for each structural wall, which will be used in the following chapter to perform nonlinear dynamic analyses.

4.1 Test setup and load history

In order to provide lateral support, the structural walls were anchored to rigid concrete foundation beams. Then, each "wall-foundation beam" system was anchored to a strong reaction floor with steel stud bolts as illustrated in Fig. **4-1**. A lateral bracing was employed to constrain the structural walls to in-plane-displacements. The lateral displacement induced by the hydraulic actuator was measured using a LVDT placed at the top of the walls. Also, the structural walls were instrumented with LVDTs vertical and diagonally arranged. Each wall was subjected to the cyclic loading pattern shown in Fig. **4-2**, according to the ASTM Standard E2126-11 (2011), where Δ_m is the ultimate displacement corresponding to the failure limit state. All the structural wall specimens were tested at the Laboratory of Structures of the Universidad Nacional de Colombia at Manizales.

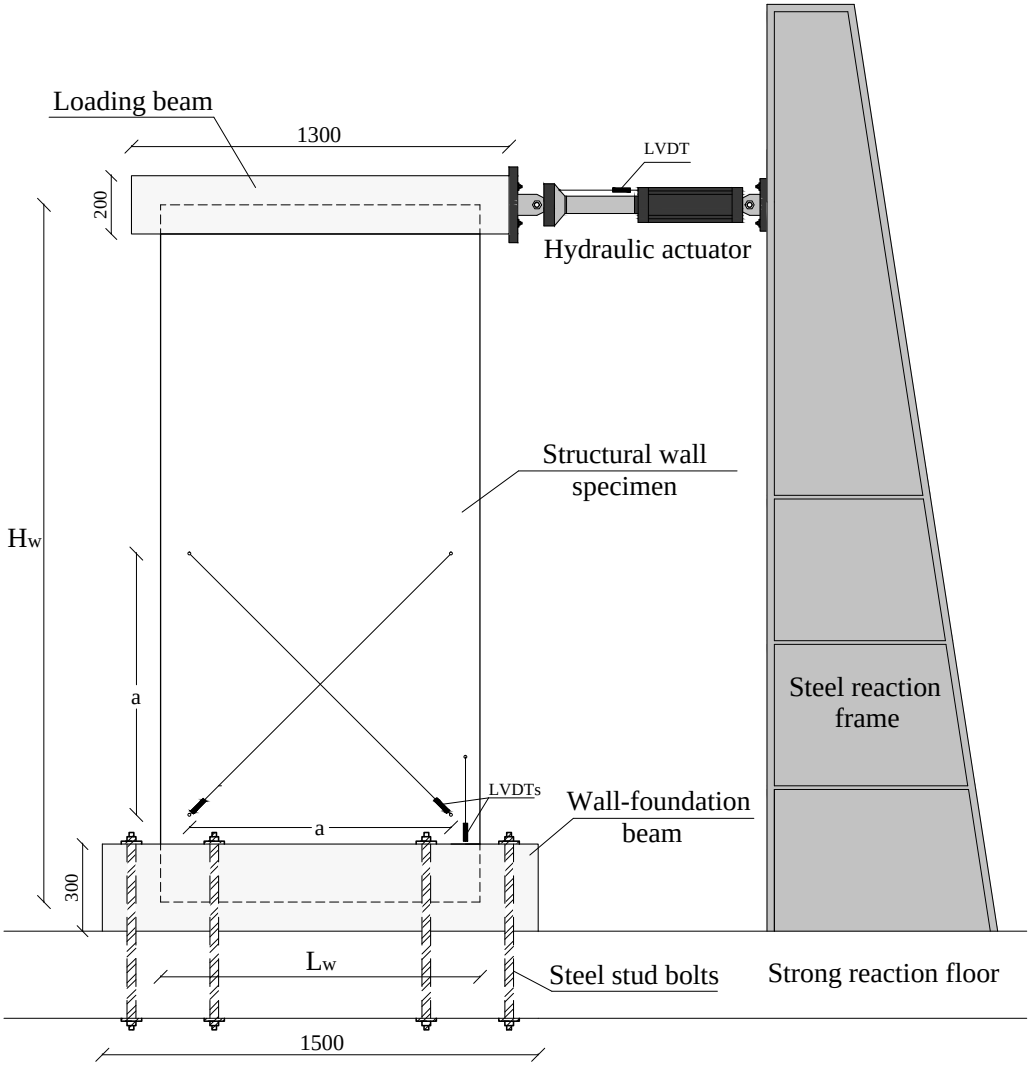

Figure 4-1: General test setup for the structural walls (mm)

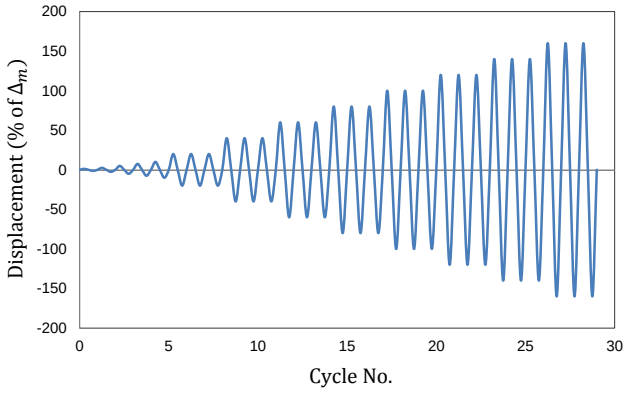

Figure 4-2: Cyclic loading pattern according to the ASTM Standard E2126-11 (2011)

4.2 Description of the structural walls

4.2.1 Recycled Plastic Lumber Wall (RPLW)

Recycled Plastic Lumber (RPL) is a wood-like material made from recycled plastic that aims to diminish the environmental pollution resulting from plastic wastes and that is used as a substitute for the raw materials in some structures made from concrete, metals, and wood. RPL needs a few chemical and industrial processes, and the current technology allows the correct separation and cleaning of its raw material. The manufacture of RPL allows making the most of the large quantities of plastic wastes and converting them into useful and durable products (Krishnaswamy and Lampo, 2001). To manufacture RPL, the raw materials are sorted, cleaned and ground into small flakes. Then, by an extrusion process, the flakes are homogenized and rapidly melt; finally, the molten mixture is discharged into a mold and cooled, shaping the finished product. This material has shown be rot resistant and not be susceptible to the corrosion or insect attacks, assuring the durability (Carroll et al., 2001).

Structural elements made of RPL have a non-homogeneous cross-section due to the cooling process during extrusion; this feature together with the nonlinear nature of the material makes different its tension and compression behavior, and some mechanical properties are difficult to determine (Macbain and Saadeghvaziri, 1999). As a consequence, in order to characterize this material and to enable the market acceptance of RPL in structural and building applications, ASTM International has developed specifications and test method standards (ASTM D6108-13, 2013; ASTM D6109-13, 2013; ASTM D6111-13a, 2013; ASTM D6112-13, 2013; ASTM D6117-16, 2016). Additionally, RPL has been studied from materials engineering to know its mechanical properties which are important for the structural design, such as density, elasticity modulus, compressive, flexural, shear and tensile strength (Carroll et al., 2001; Li et al., 1994; Macbain and Saadeghvaziri, 1999; Gulhane and Gulhane, 2017), creep behavior (Macbain and Saadeghvaziri, 1999; Chen et al., 2007), among others.

The first applications of RPL were in urban furniture and in low-stress or non-critical load outdoor structures, such as picnic tables, park benches, trash receptacle covers, among others. With the satisfactory performance of these applications, RPL gained popularity and it was seen as a novel material for others applications, such as docks, boardwalks, and decks (Krishnaswamy and Lampo, 2001). Gradually, RPL started to be used in several structural applications where concrete, steel or wood, were the traditional material, such as joists, marine pilings, bridges (for military tanks, railroads and vehicular traffic), one and two-story housing, among others. Recently, RPL has been investigated and implemented for the construction of housings of one and two-story (Gulhane and Gulhane, 2017; Econciencia S.A.S., 2018), looking to diminish the housing deficiency and the accumulations of plastic wastes in the natural environment; in fact, some building companies and researchers have developed housing systems based RPL structural walls that define the structural system of seismic resistance (Econciencia S.A.S., 2018).

Gulhane and Gulhane (2017) developed analytical studies of houses built with precast RPL elements, which allowed identifying some structural features, such as large horizontal displacements in the walls that formed the houses when they were subjected to seismic or wind loads. These displacements suggested doubling the thickness of the walls and using a hollow section in order to improve the structural behavior. Compression and flexural strength were not exceeded by the stress induced by seismic, wind or typical loads of use or occupancy of the housings, but care must be taken with the excessive lateral displacements respect to the height of the building. Moreover, they found that the RPL elements had a specific density of 2.2-2.8 times less than the masonry walls or concrete elements, and a compressive strength of 25-26 MPa, which is more than the compressive strength of the masonry wall (1.8-2.9 MPa) and similar to concrete compressive strength (17-28 MPa).

From seismic-resistant engineering, the use of light and resistant materials constitutes a natural seismic-resistant system for any kind of building (Bedoya-Ruiz et al., 2010). Houses built of RPL may have a better seismic performance given its low density than those built of usual materials, so it is necessary to assess the behavior of the structural systems based RPL walls under cyclic loads that simulate the strong phase of an earthquake, in order to determine structural parameters, such as stiffness, lateral resistance, ductility, energy dissipation capacity and damping, which allow a reliable design of the houses.

4.2.1.1 Test specimen

The type of RPL manufactured for the wall was a Commingled RPL (Econciencia S.A.S., 2018) which had a density of 821 kg/m^3 (ASTM D6111-13a, 2013), a compressive strength of 18.06 MPa (ASTM D6108-13, 2013), a flexural strength of 19.32 MPa (ASTM D6109-13, 2013) and a Young modulus of 1102.55 MPa (ASTM D6109-13, 2013).

The mass of the wall was 100 kg. Regarding the structural system, the RPLW was formed of: 1) RPL battens that had a rectangular cross-section 50 mm wide and 90 mm deep, and they are vertical, horizontally and diagonally arranged; and 2) rectangular RPL boards with 1100 mm length, 100 mm wide and 20 mm of thickness, horizontally arranged. These structural elements were assembled by drywall screws #8 x 2 in. located at the places where both structural elements converge to guarantee the structural integrity of the system. This type of screw has shown to be suitable for the thickness of the structural elements that form the RPL walls, and besides, it is typically used in the assembly of RPL elements that form others structural and nonstructural applications. Nevertheless, it is worth to emphasize that the type of connection, the type, the localization, and the number of screws change the structural response. Therefore, these features and the configuration of the connections could be modified according to a design or capacity requirements in particular. In this research, it was chosen the structural configuration and the connection type previously presented, which are typical in structural systems based RPL walls for one and two-story housing. The geometry of the RPLW is sketched in Fig. **4-3**

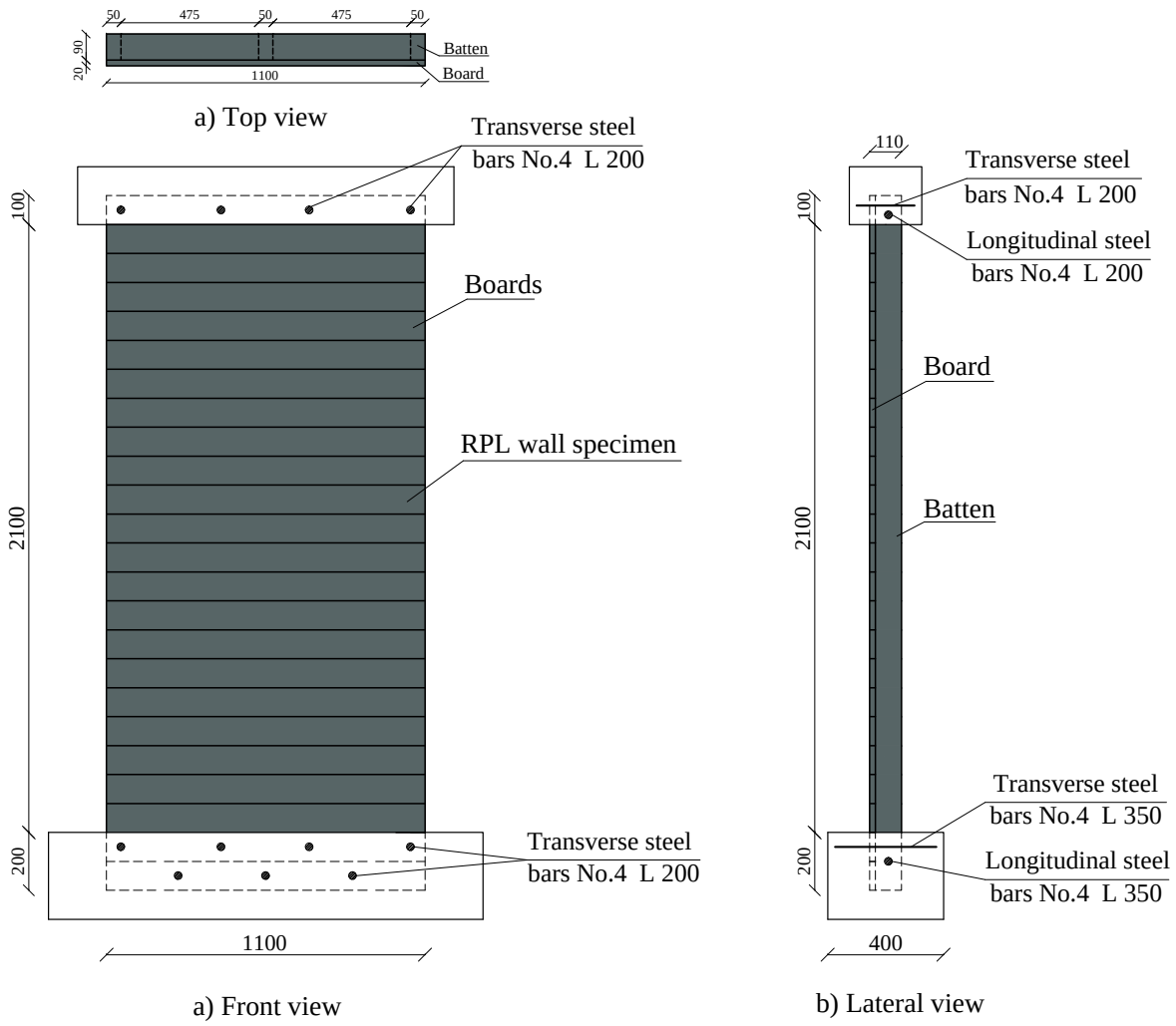

Figure 4-3: Detailing of the RPLW test specimen (mm)

4.2.2 Precast Ferrocement Wall (PFW)

Ferrocement is a structural material used commonly to build thin-wall sections, which is composed of a cement mortar of high strength reinforced with multiple layers of wire mesh. Sections built with ferrocement have a simple construction process which consists of using the multiple layers of wire mesh to give shape to the section and applying then the mortar to both sides of this reinforcement armature until achieving the required thickness. According to the American Concrete Institute (ACI), this material has a very high tensile strength-to-weight ratio and superior cracking behavior in comparison to conventional reinforced concrete. The strength of the ferrocement sections is provided by the multiple layers of mesh which are used to achieve the required density of steel and sometimes by steel reinforcing bars embedded in the high-strength mortar. Structural systems based ferrocement are usually formed of precast thin walls which are assembled in different configurations depending on the design and the constructive system of the housing (Cas-

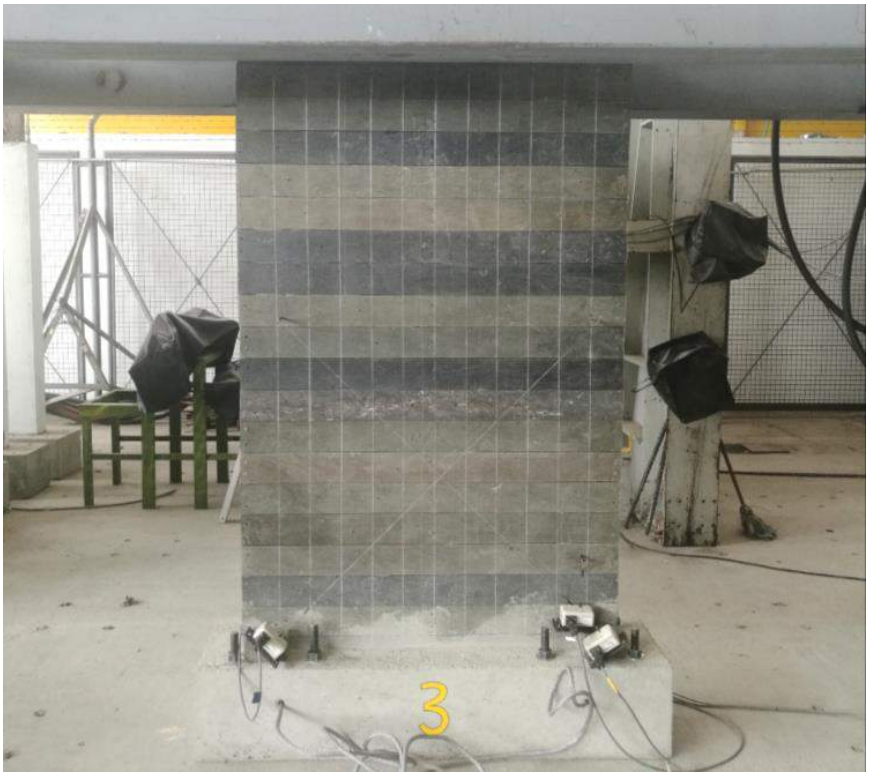

Figure 4-4: The RPLW test specimen

tro, 1979; Gokhale, 1983; Wainshtok-Rivas, 1994; Abdullah, 1995; Olvera, 1998; Machado, 1998; Naaman, 2000). Additionally, the use of hollow sections in the wall configurations has allowed reaching higher strength (Bedoya-Ruiz et al., 2015a). Typical dimensions of precast ferrocement walls range between 500 and 1000 mm in width, 2000 to 2400 mm in height and 10 to 50 mm in thickness (Bedoya-Ruiz et al., 2014). These systems have shown to have high resistance (Naaman, 2000; Bedoya-Ruiz, 2005) and low seismic fragility and vulnerability (Bedoya-Ruiz et al., 2010).

The first applications of ferrocement in the design and building of one and two-story housing were described by Castro (1979) and Olvera (1998). Naaman (2000) carried out investigations on ferrocement houses, in which he studied the advantages of ferrocement from an industrialized viewpoint in order to expound the benefits of the material and to encourage its mass production development. Later, Bedoya-Ruiz (2005) developed experimental and analytical researches on walls and ferrocement houses. Regarding to the methodologies for the earthquake resistant design of ferrocement structural systems, Bedoya-Ruiz et al. (2002) and Wainshtok-Rivas (2004) developed an approach to design ferrocement houses by the Method of Equivalent Horizontal Force for regions of moderate to high seismic hazard. In the recent years, Bedoya-Ruiz et al. (2014, 2015b) have applied a nonlinear dynamical model to evaluate the vulnerability of ferrocement houses, which was calibrated with the experimental behavior exhibited by the structures when subjected to cyclic loading conditions.

4.2.2.1 Test specimen

The proposed PFW was designed with the objective of allowing its wide use in the building sector in Colombia. In fact, this structural system was built using precast ferrocement elements made from common structural materials such as mortar, hexagonal wire meshes, and steel reinforcing bars (rebars), which facilitate its mass production via industrial processes and its implementation. All the materials met the requirements of the Colombian seismic building code (AIS, 2010). The mortar, which was a mix of Portland cement type I and sand without coarse aggregate, had a compressive strength of 44 MPa after 28 days. On the other hand, the hexagonal meshes had an opening of 31.75 mm and a yield resistance of 282 MPa, whereas the rebars had a yield strength of 420 MPa. The structural system was formed of two precast ferrocement boundary elements and two precast ferrocement panels. Both elements were built with several layers of thin reinforcement and designed in a such a way as would allow the assembly between them. The two precast boundary elements were designed as columns of 80 x 200 mm with 2 rebars No.3. The precast panels had a thickness of 25 mm and a reinforcement compound of 4 rebars No.2 and eight layers of hexagonal wire mesh that enclosed the rebars. These panels were located one per face between the columns which linked with the panels by the assembly system (see Fig. **4-5**). The PFW had two hollow sections which were designed with the purpose of being used as ducts for hydro-sanitary or electrical systems, or for the use of thermal or acoustic isolators. Furthermore, the mass of the PFW was 330 kg and its geometry is shown in Fig. **4-6**.

Figure 4-5: The PFW test specimen

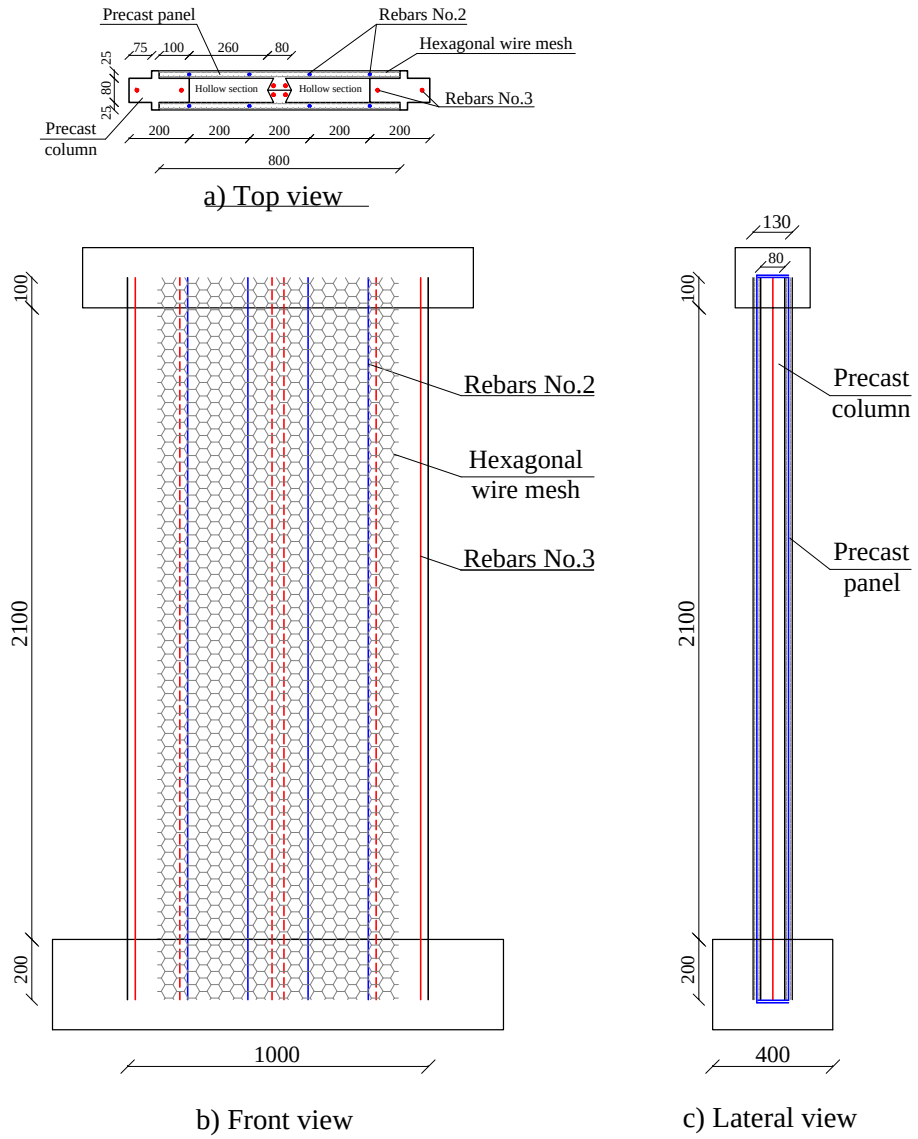

Figure 4-6: Detailing of the PFW test specimen (mm)

4.2.3 Hollow Reinforced Concrete Wall (HRCW)

Reinforced concrete (RC) walls have been used widely in the design and construction of different types of earthquake-resistant structural systems. In fact, many variants of these structural elements have been proposed in the literature and their behavior have been also widely researched, for example: Pilakoutas and Elnashai (1995) studied the cyclic behavior of RC Cantilever Walls, Hidalgo et al. (2002) developed an experimental program that included the test of 26 full-scale RC walls subjected to cyclic loads, Holden et al. (2003) studied the seismic performance of precast reinforced and prestressed concrete walls, Kuang and Ho (2008) researched the ductility of RC walls, Carrillo and Alcocer (2012) compared the seismic performance of six RC walls tested under

shaking table excitations, Quiroz et al. (2013) tested seven full-scale thin RC shear walls under cyclic loads, Sengupta and Li (2014) studied the hysteretic behavior of a database of reinforced concrete wall specimens tested under cyclic loading, among others. In this research, a Hollow Reinforced Concrete Wall (HRCW) is proposed for the earthquake-resistant structural system for one and two-story housing, and its seismic behavior is studied. This wall differs significantly in terms of geometry and reinforcement layout from the traditional designs of RC walls.

4.2.3.1 Test specimen

The HRCW was built using common structural materials, such as concrete, steel reinforcing bars, hexagonal wire meshes, and welded wire mesh. All these materials met the requirements of the Colombian seismic building code (AIS, 2010). For example, the compressive strength of the concrete was 22 MPa at the age of 28 days and the yield strength of the reinforcing bars was 420 MPa. The hexagonal wire meshes had an opening of 31.75 mm and a yield resistance of 282 MPa, whereas the welded wire mesh XX-131 had an opening of 150 mm in both directions and a yield strength of 485 MPa. Regarding the structural design, the HRCW had 2400 mm height, 1000 mm width and 120 mm thickness, with a hollow section of dimensions 40x920 mm which was designed with the purpose of being used as ducts for hydro-sanitary or electrical systems. Each face of the HRCW had 2 rebars No.3 at the ends and 4 rebars No.2 located over its length. A layer of welded wire mesh XX-131 surrounded the wall over the rebars No.3 and four layers of hexagonal wire mesh surrounded the layer of mesh XX-131. Also, four layers of hexagonal wire mesh enclosed the hollow section. The mass of the wall was 600 kg. Fig. **4-8** shows the detailing of the HRCW.

Figure 4-7: The HRCW test specimen

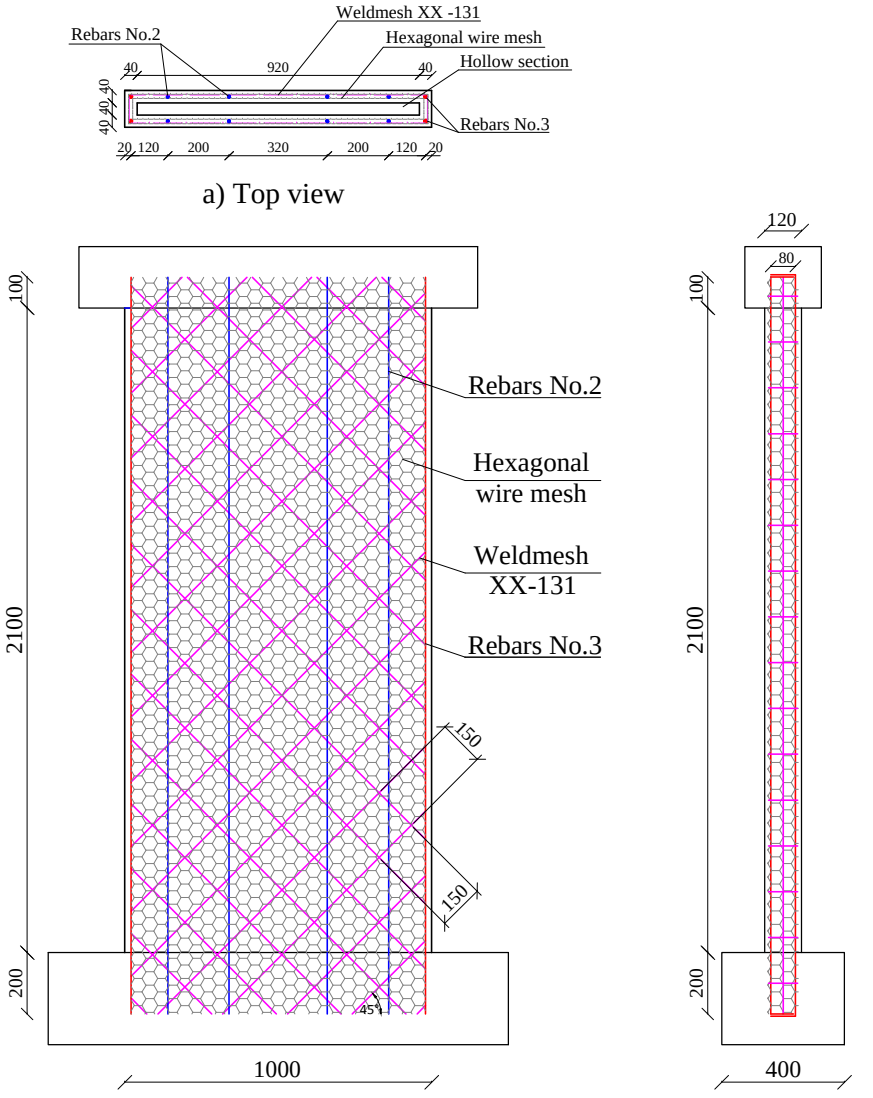

Figure 4-8: Detailing of the HRCW test specimen (mm)

4.3 Test results

4.3.1 Hysteretic behavior and strength

Hysteretic response curves were drawn from the cyclic load tests carried out on the three structural walls, in order to assess the performance, strength, and ductility of each system under seismic actions. The hysteretic behavior of the RPLW, PFW and HRCW can be observed in Figs. **4-9**, **4-11** and **4-13**, respectively. The RPLW exhibited stiffness degradation, scant strength deteriora-

tion in the last cyclic loading and pinching effect due to the type of connections and to the relative displacement between the boards. On the other hand, the PFW experienced scant stiffness degradation, cyclic strength deterioration in the last cycles, and moderate pinching effects as a result of the opening and closing cracks process, whereas the HRCW exhibited moderate stiffness degradation, high cyclic strength deterioration, and scant pinching effects. Additionally, both the PFW and the HRCW showed a higher stiffness and strength than the RPLW; however, the maximum top displacement reached in the RPLW was in the order of 160 mm (7% of drift ratio level), which shows its high deformation ability.

The ductility is computed for each peak values from hysteresis loops of each structural wall, as shown Figs. **4-9**, **4-11** and **4-13**. Every ductility level allows describing the behavior of the system and the ability of the system to maintain high levels of deformation without damage. According to the above, Table **4-1** shows the ductility levels in function of the drift ratio, together with the respective description of the behavior for each structural wall.

Table 4-1: Ductility levels associated with drift ratios for the structural walls

Wall	Completely elastic ($\mu < 1$)	Scant ductility ($1 \leq \mu < 3$)	Completely ductile ($\mu \geq 3$)
RPLW	drift ratio $< 2.0\%$	$2.0\% \leq$ drift ratio $< 6.0\%$	drift ratio $\geq 6.0\%$
PFW	drift ratio $< 0.5\%$	$0.5\% \leq$ drift ratio $< 1.8\%$	drift ratio $\geq 1.8\%$
HRCW	drift ratio $< 0.3\%$	$0.3\% \leq$ drift ratio $< 1.0\%$	drift ratio $\geq 1.0\%$

The positive and negative envelope curves corresponding to the peak values from hysteresis loops of each structural wall were computed and are depicted in Figs. **4-10**, **4-12** and **4-14**. It can be seen that both positive envelopes and negative envelopes of each structural wall show a similar behavior so that the average of these envelopes is used to estimate the structural parameters of each system.

Table **4-2** shows the experimental values of the structural parameters of each structural wall computed according to the ASTM Standard E2126-11 (2011) and using the average envelope.

Table 4-2: Parameters computed from the cyclic loading tests according to ASTM Standard E2126-11 (2011)

Wall	Elastic stiffness (K_e)	Elastic shear strength (v_{peak})	Yield load (P_{yield})	Maximum load (P_{peak})	Ultimate displacement (Δ_u)	Yield displacement (Δ_{yield})	Ductility ($\mu_{max} = \Delta_u/\Delta_{yield}$)
	kN/mm	kN/mm	kN	kN	mm	mm	
RPLW	0.149	0.006932	6.8835	7.625	159.45	46.201	3.451
PFW	8.960	0.13173	111.97	131.73	62.831	12.496	5.028
HRCW	14.143	0.12852	109.24	128.52	32.690	7.724	4.232

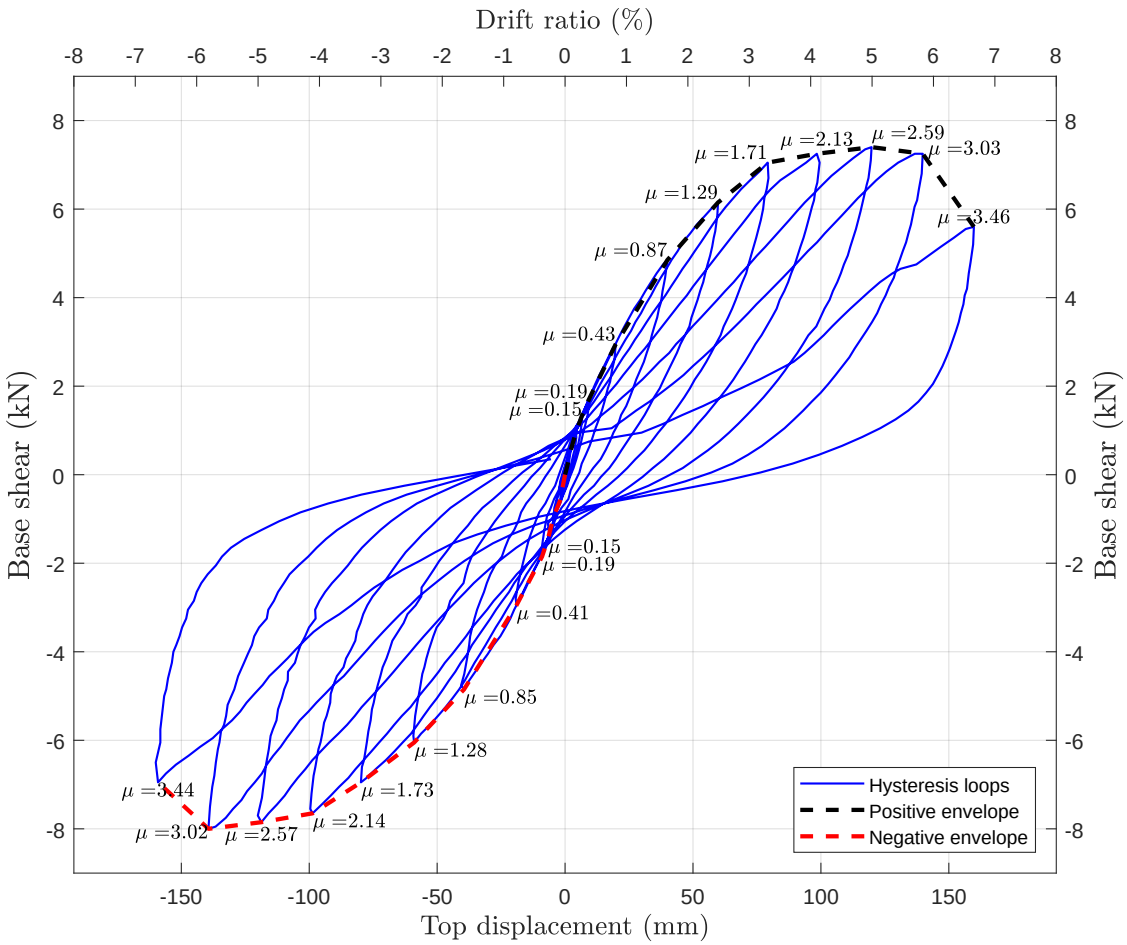

Figure 4-9: Hysteresis cycles of the RPLW

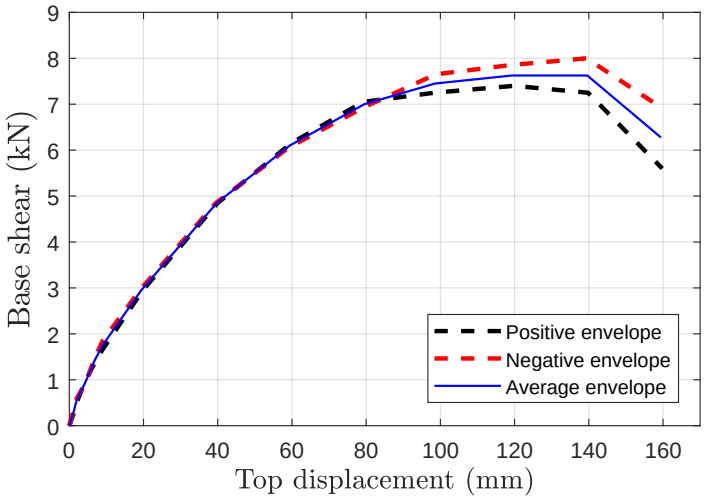

Figure 4-10: Positive, negative and average envelopes RPLW

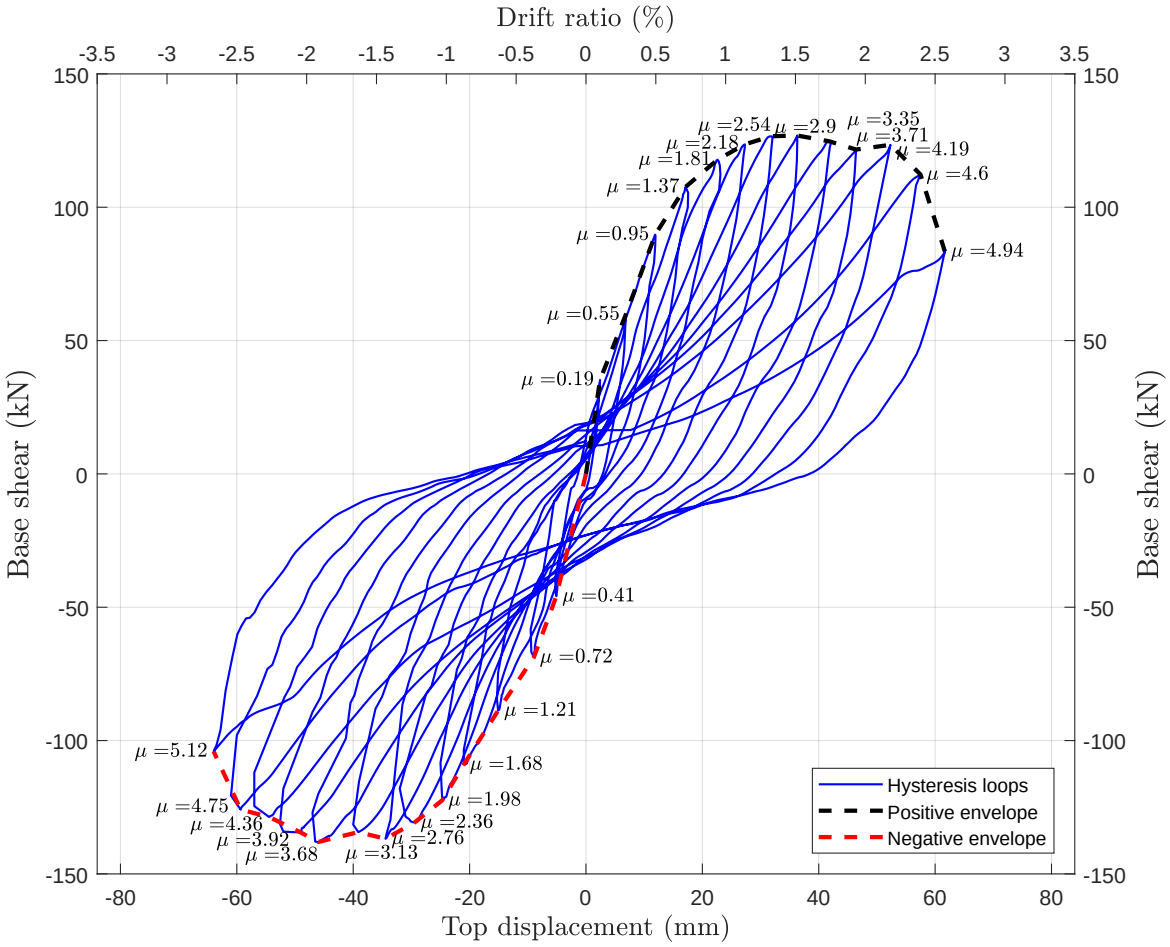

Figure 4-11: Hysteresis cycles of the PFW

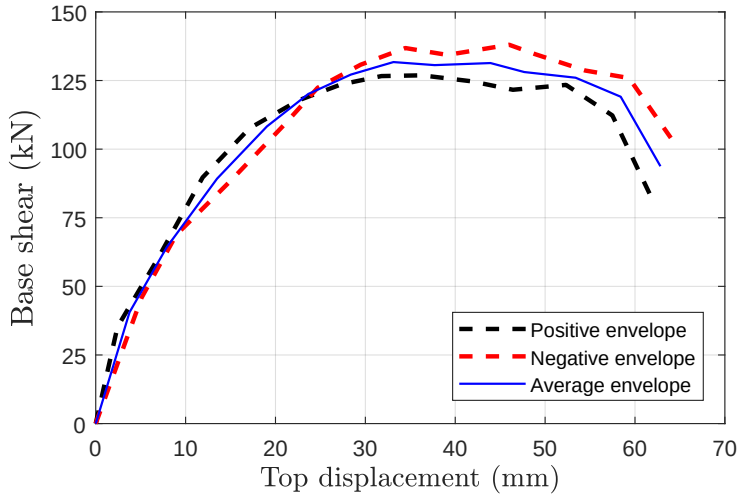

Figure 4-12: Positive, negative and average envelopes PFW

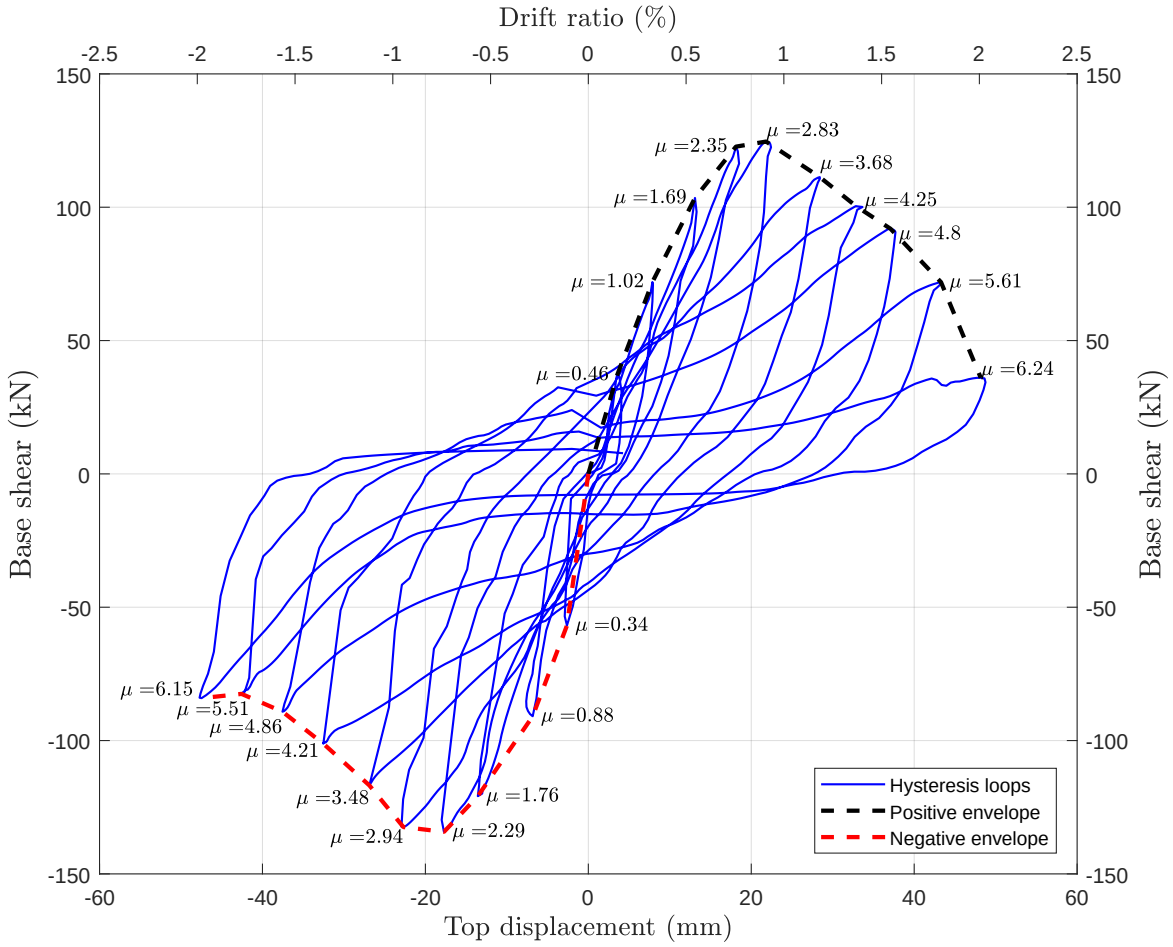

Figure 4-13: Hysteresis cycles of the HRCW

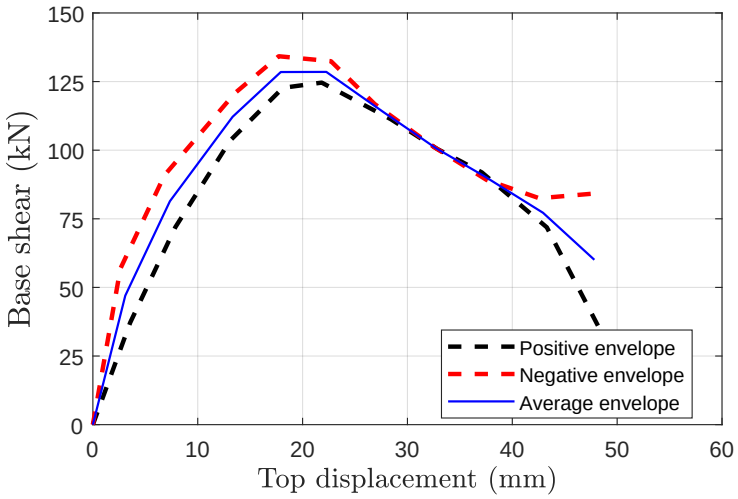

Figure 4-14: Positive, negative and average envelopes HRCW

4.3.2 Energy dissipation and damping

The structural designs based on fragility analyses aim at increasing the safety of structural elements and avoiding the sudden failure of the material, controlling the structure's damage when is subjected to severe loads due to earthquakes. The damage can be related to the ability of the structural system to dissipate the energy transmitted by external cyclic loads by means of hysteretic behavior. This dissipated energy can be computed by the area enclosed by the hysteresis loops (see Figs **4-9**, **4-11** and **4-13**).

The ability of the structural system in terms of energy dissipation can be quantified by means so-called equivalent viscous damping ratio (ξ_{eq}) (Priestley et al., 1996; Chopra, 2012) which is defined as:

$$\xi_{eq} = \frac{E_i}{4\pi (E_e)_i} \cdot 100\%,$$

where E_i is the energy dissipated by the structural element in the i-th loading cycle computed from the measured hysteresis loops and $(E_e)_i$ is the elastic strain energy stored by an equivalent linear elastic system when the maximum displacement in the i-th cycle is reached under static conditions; this energy is computed by the area under the Base shear vs. Top displacement curve obtained from the cyclic tests, which is a right triangle whose base equals the maximum positive displacement reached in the model $(\Delta_{\max})_i$ and whose height $(P_m)_i$ is the average peak load of the analyzed cycle, i.e.:

$$(P_m)_i = \frac{|(P_{\max})_i| + |(P_{\min})_i|}{2};$$

where $(P_{\max})_i$ and $(P_{\min})_i$ represent the maximum and minimum values that the load reaches in the i-th cycle. With these data, the energy $(E_e)_i$ can be computed as:

$$(E_e)_i = \frac{(P_m)_i (\Delta_{\max})_i}{2}.$$

The accumulated dissipated energy and the equivalent viscous damping of the structural walls as a function of the drift ratio are depicted in Fig. **4-15a** and Fig. **4-15b**, respectively. As can be seen, the structural systems develop high energy dissipation with an increase in the drift ratio level. The rounded shape of the hysteresis curves and the area enclosed by those loops suggest that the systems has good energy dissipation capacity, as this increases with the drift. The shape of the hysteresis loops effectively determines the ability of these walls to dissipate energy when they are subjected to loads beyond its linear range.

4.3.3 Coefficient of energy dissipation capacity

The coefficient of energy dissipation capacity (R_μ) is a designed-oriented concept which aims to approximate the nonlinear behavior of structural systems when subjected to seismic loads. It is

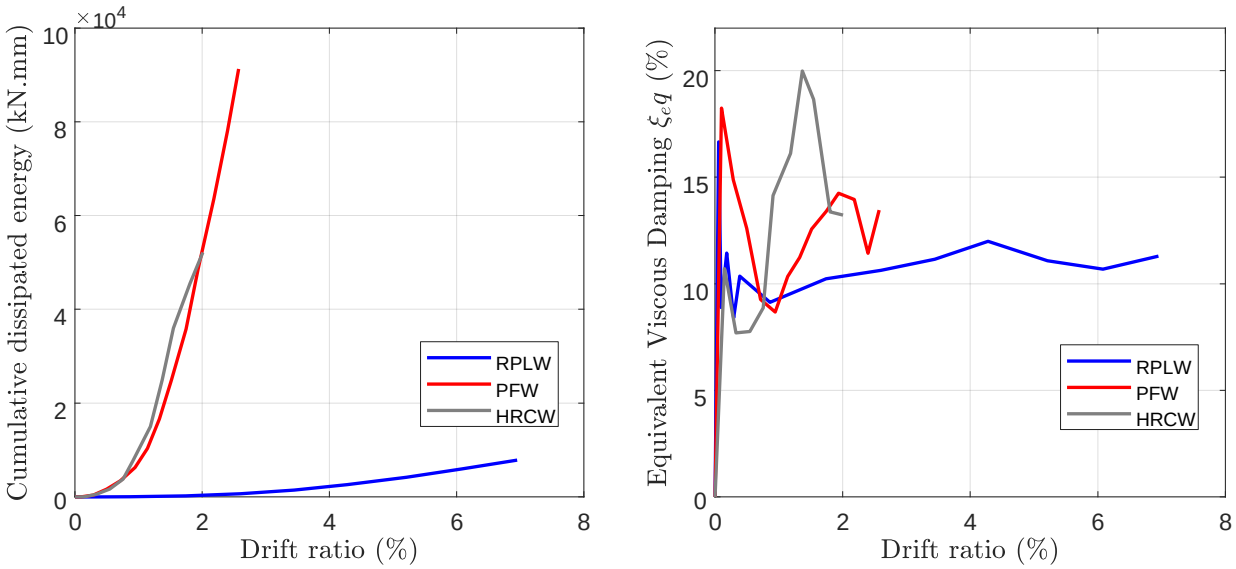

a) Cumulative dissipated energy b) Equivalent viscous damping ratio

Figure 4-15: Cumulative dissipated energy and equivalent viscous damping ratio for the walls

used in most of the earthquake resistant design codes, in order to reduce the magnitude of the loads assessed from an elastic viewpoint. The model proposed by Takada et al. (1988) to determine R_μ is used here, which is independent of the period of the structure:

$$R_\mu = \varepsilon\sqrt{2\mu - 1},$$

where ε is an adjustement factor which represents the degree of deviation of the R_μ vs. μ relation from the equal energy expression $\sqrt{2\mu-1}$. Results drawn from Monte-Carlo simulations indicate that the average value of ε is between 1.05 - 1.34 (Takada et al., 1988; Miranda and Bertero, 1994). Using the ductilities shown in Table **4-2** and taking the values of ε, the R_μ coefficient is given in Table **4-3** for each structural wall.

Table 4-3: Coefficient of energy dissipation capacity for the structural walls

Wall	R_μ	
	$(\varepsilon = 1.05)$	$(\varepsilon = 1.34)$
RPLW	2.550	3.255
PFW	3.160	4.032
HRCW	2.869	3.660

4.3.4 Damage limit states of the structural walls

The damage limit states (DS) are obtained from the experimental behavior exhibited by the structural walls during the cyclic loading test which simulated earthquake loading conditions. For each wall, four damage limit states are characterized by direct indicators of structural damage and related to an EDP, such as the story drift ratio which has been selected as the best indicator of potential damage.

4.3.4.1 Recycled Plastic Lumber Wall

Description of the damage limit State DS_1: Minor relative displacement of the boards; no failure in the battens connections or boards-battens connections; no failure in the drywall screws; the RPLW retains most of its initial strength and stiffness; light structural damage. The graphical representation of this damage limit state is shown in Fig. **4-16a**.

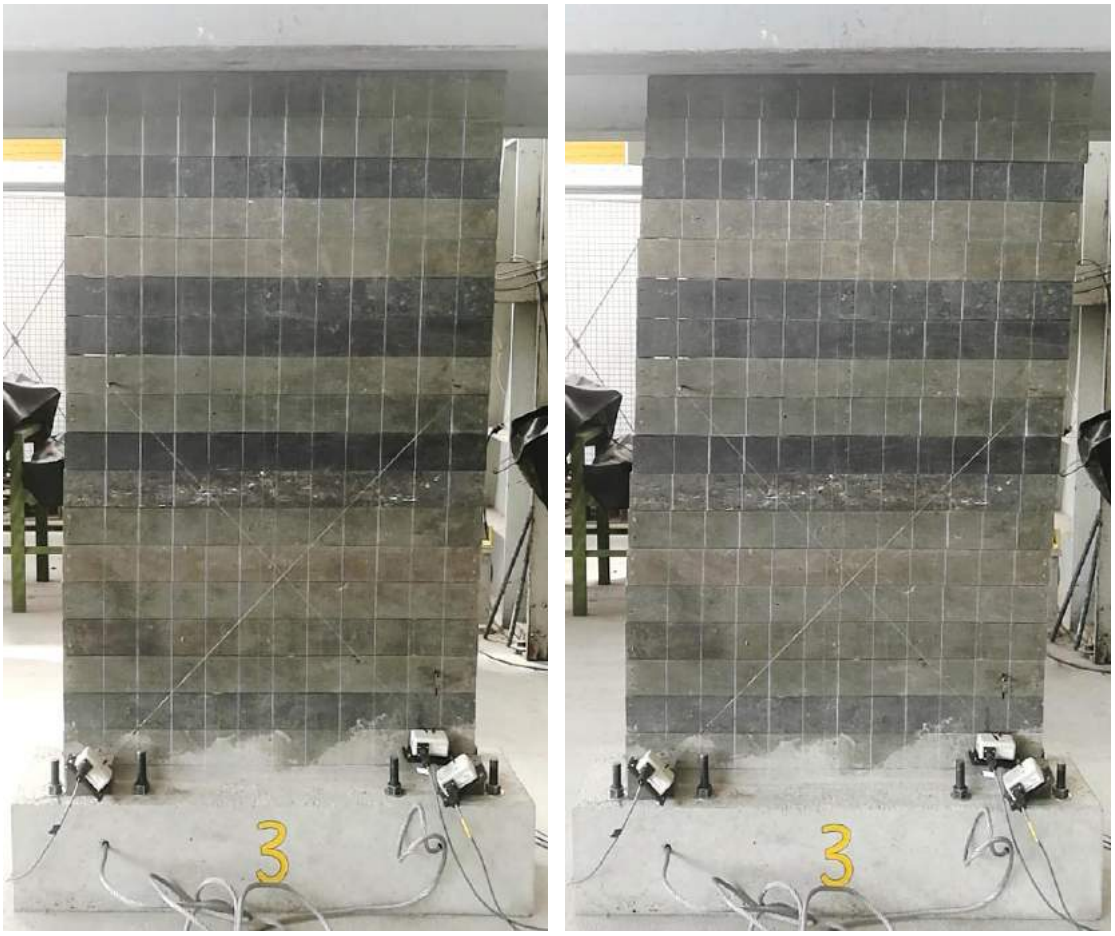

a) Damage state DS_1 b) Damage state DS_2

Figure 4-16: Graphical representation of the damage limit states **DS_1** and **DS_2** for the RPLW

Description of the damage limit state DS_2: Moderate relative displacement of the boards; no failure in the battens connections or boards-battens connections; no failure in the drywall screws; the RPLW behaves into the inelastic range; moderate structural damage. Fig. **4-16b** shows a graphical representation of this damage state.

Description of the damage limit State DS_3: Severe relative displacement of the boards; failure of a top connection between the diagonal, vertical and horizontal battens; bearing failure and tear-out failure in few boards-battens connections due to the fatigue produced by loading cyclic conditions; no single shear failure in the drywall screws; the RPLW has scant strength and stiffness to continue resisting lateral loads; severe structural damage. The graphical representation of this damage limit state can be seen in Fig. **4-17**.

a) Mode of failure of a top connection between the diagonal, vertical and horizontal battens

Figure 4-17: Graphical representation of the damage limit state DS_3 for the RPLW

Description of the damage limit state DS_4: Excessive relative displacement of the boards in the order of 15mm; failure of the two top connections between the diagonal, vertical and horizontal battens; bearing failure and tear-out failure in the boards-battens connections and single shear failure in the drywall screws due to the fatigue produced by loading cyclic conditions; the RPLW

has neither strength nor stiffness to resist lateral and vertical loads; complete structural damage. Fig. **4-18** presents the graphical representation of the $\mathbf{DS_4}$.

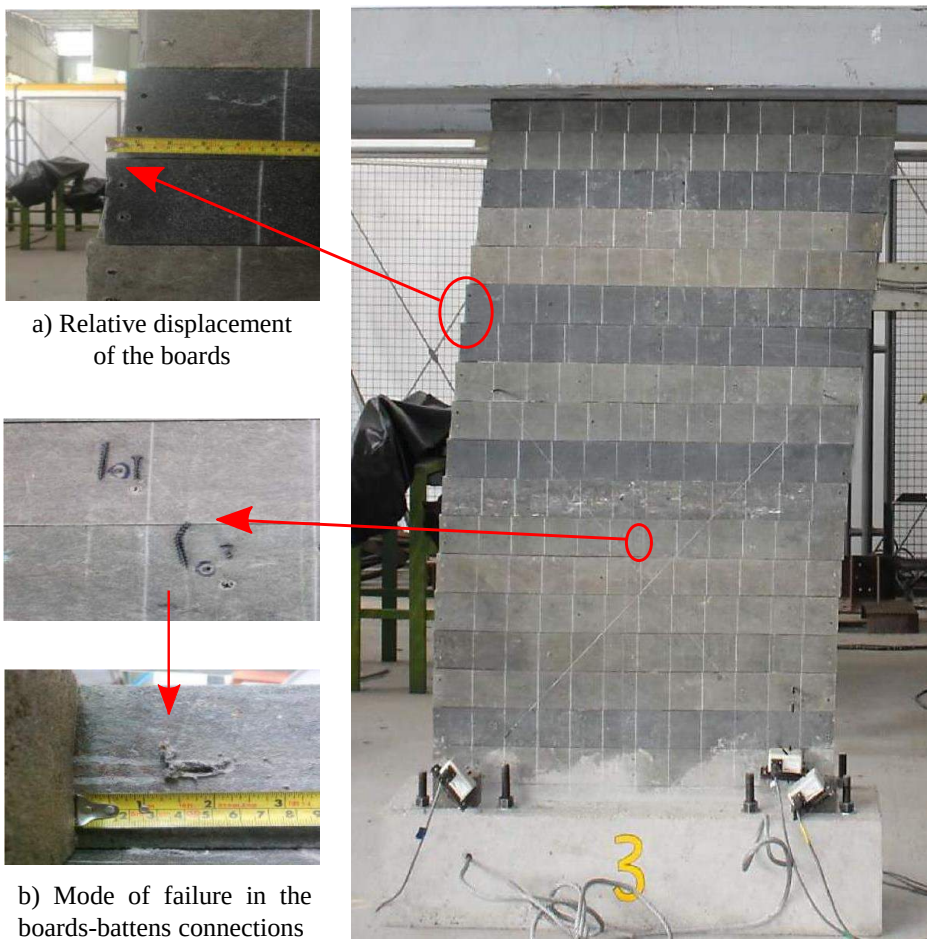

Figure 4-18: Graphical representation of the damage limit state $\mathbf{DS_4}$ for the RPLW

The above four damage limit states are related to the top lateral displacement and to the drift ratio levels in Table **4-4**. These values will be used in the following chapter to define the structural performance levels and to compute the fragility curves of the structural walls.

Table 4-4: Relation between the damage limit states and the drift ratio levels for the RPLW

Damage limit state	Structural damage	Top lateral displacement (mm)	Drift ratio (%)
$\mathbf{DS_1}$	Light	40	1.67
$\mathbf{DS_2}$	Moderate	100	4.17
$\mathbf{DS_3}$	Severe	140	5.83
$\mathbf{DS_4}$	Complete	160	6.67

4.3.4.2 Precast Ferrocement Wall

Description of the damage limit state DS_1: Minor flexural cracks; first diagonal tension cracks in the panels; no crushing or spalling of mortar; no fracture or buckling of reinforcement; no permanent drift; the PFW retains most of its initial strength and stiffness; light structural damage. The graphical representation of this damage state is shown in Fig. **4-19a**.

Description of the damage limit State DS_2: Spreading and widening of the flexural and diagonal tension cracks; appearance of numerous horizontal cracks in the boundary elements; no crushing or spalling of mortar; no fracture or buckling of reinforcement; small permanent drift; the PFW behaves into the inelastic range; moderate structural damage. Fig. **4-19b** shows a graphical representation of this damage limit state.

a) Damage state DS_1 b) Damage state DS_2

Figure 4-19: Graphical representation of the damage limit states **DS_1** and **DS_2** for the PFW

Description of the damage limit state DS_3: Severe flexural and diagonal tension crack patterns; flexural tension failure at the bottom of the boundary elements; crushing and some spalling of mortar; yielding of the reinforcement of the boundary elements; buckling of the rebars No.2 of the panels; fracture of some hexagonal meshes, but no fracture in rebars; significant permanent drift; the PFW has scant strength and stiffness to continue resisting lateral loads; severe structural damage. The graphical representation of this damage limit state can be seen in Fig. **4-20**.

a) Crack pattern

b) Crushing of mortar

c) Buckling of the rebars No.2

d) Flexural tension failure in the boundary elements

Figure 4-20: Graphical representation of the damage limit state DS_3 for the PFW

Description of the damage limit State DS_4: Severe crushing and spalling of mortar at the bottom of the boundary elements; fracture of the hexagonal meshes, rebars No.2 at the bottom of the panels, and rebars No.3 at the bottom of the boundary elements; sliding at base of the PFW; large permanent drifts; the PFW has neither strength nor stiffness to resist lateral and vertical loads; complete structural damage. Fig. **4-21** presents the graphical representation of the DS_4.

a) Crack pattern

b) Spalling of mortar in the boundary elements

c) Fracture of the rebar No.3 and the hexagonal mesh in the boundary elements

Figure 4-21: Graphical representation of the damage limit state **DS_4** for the PFW

The above four damage limit states are related to the top lateral displacement and to the drift ratio levels in Table **4-5**. These values will be used in the following chapter to define the structural performance levels and to compute the fragility curves of the structural walls.

Table 4-5: Relation between the damage states and the drift ratio levels for the PFW

Damage limit state	Structural damage	Top lateral displacement (mm)	Drift ratio (%)
DS_1	Light	8	0.33
DS_2	Moderate	24	1.0
DS_3	Severe	44	1.83
DS_4	Complete	63	2.63

4.3.4.3 Hollow Reinforced Concrete wall

Description of the damage limit state DS_1: Minor flexural and diagonal tension cracks; no crushing or spalling of concrete; no fracture or buckling of reinforcement; no permanent drift; the HRCW retains most of its initial strength and stiffness; light structural damage. The graphical representation of this damage limit state is shown in Fig. **4-22a**

Description of the damage limit state DS_2: Spreading and widening of the flexural and diagonal tension cracks; no crushing or spalling of concrete; no fracture or buckling of reinforcement; small permanent drift; the HRCW behaves into the inelastic range; moderate structural damage. Fig. **4-22b** shows a graphical representation of this damage limit state.

a) Damage state DS_1 b) Damage state DS_2

Figure 4-22: Graphical representation of the damage limit states **DS_1** and **DS_2** for the HRCW

Description of the damage limit state DS_3: Severe flexural and diagonal tension crack patterns; flexural compression failure at the bottom ends of the wall; crushing and some spalling of concrete; yielding of the reinforcement; fracture of some hexagonal meshes, but no fracture in rebars; moderate sliding at the base of the wall; significant permanent drift; the HRCW has scant strength and stiffness to continue resisting lateral loads; severe structural damage. The graphical representation of this damage limit state can be seen in Fig. **4-23**.

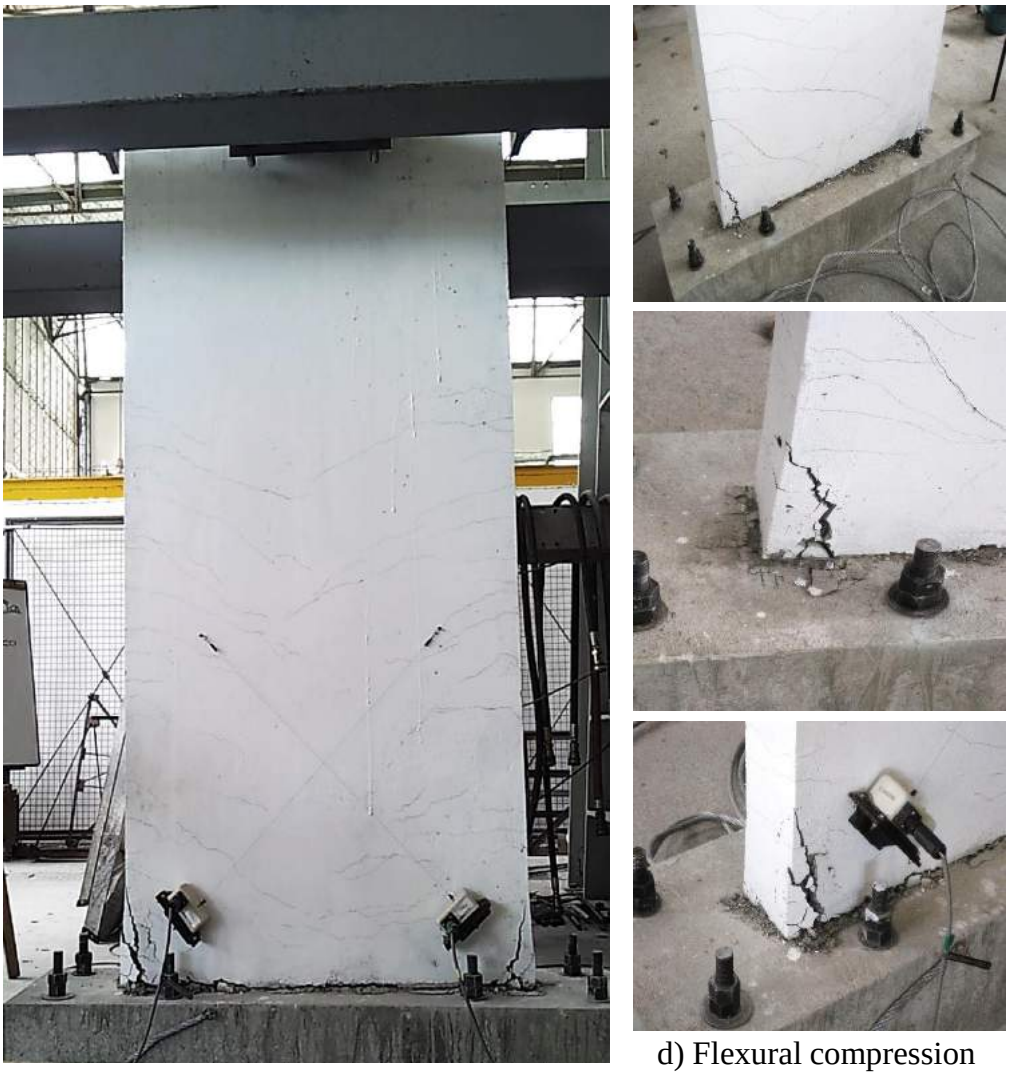

a) Crack pattern

d) Flexural compression failure and crushing

Figure 4-23: Graphical representation of the damage limit state $\mathbf{DS_3}$ for the HRCW

Description of the damage limit state DS_4: Severe crushing and spalling of concrete at the bottom ends of the wall; fracture of the hexagonal meshes and rebars No.3 at the bottom ends of the wall; severe sliding at the base of the wall; large permanent drifts; the HRCW has neither strength nor stiffness to resist lateral and vertical loads; complete structural damage. Fig. **4-24** presents the graphical representation of this damage limit state.

a) Crack pattern

b) Crushing and spalling of concrete

c) Fracture of the rebars No.3 at the base of the wall

Figure 4-24: Graphical representation of the damage limit state **DS_4** for the HRCW

The above four damage limit states are related to the top lateral displacement and to the drift ratio levels in Table **4-6**. These values will be used in the following chapter to define the structural performance levels and to compute the fragility curves of the structural walls.

Table 4-6: Relation between the damage states and the drift ratio levels for the HRCW

Damage limit state	Structural damage	Top lateral displacement (mm)	Drift ratio (%)
DS_1	Light	7.5	0.31
DS_2	Moderate	22.5	0.94
DS_3	Severe	33	1.38
DS_4	Complete	48	2.0

4.4 Application of the Mostaghel's multilinear hysteretic model for the structural walls

The Mostaghel's multilinear hysteretic model was employed to simulate the experimental cyclic behavior of the aforementioned structural walls. The efficiency of this model to carry out this task was tested using three variants for each wall: five-lines, six-lines, and seven-lines hysteretic models among which one variant will be chosen in order to asses subsequently the seismic performance of each structural wall. To obtain the parameters of each multilinear hysteretic model for each structural wall, the procedure proposed and described in Section 3.6.2 was applied with $N_p = 150$ and $k_{max} = 100$ for each simulation. Regarding the computational cost, the elapsed time in the iterative process was about 1.5 hrs to 1.8 hrs, therefore, the total elapsed time of the identification process of each model variant can be obtained multiplying that time by the N simulations carried out. Fig. **4-25** shows the typical evolution of each cost function during the iterative process of each simulation.

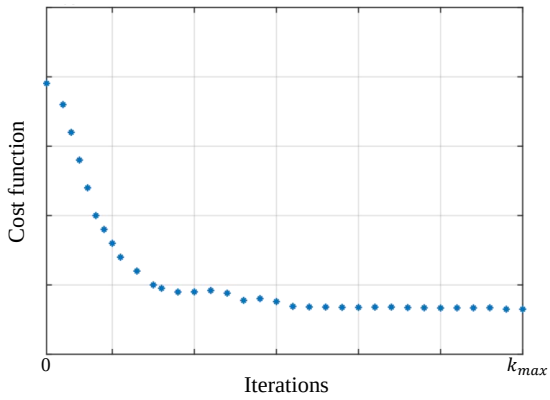

Figure 4-25: Typical evolution of the cost functions in each simulation of the proposed procedure

The results of the application of the Mostaghel's multilinear hysteretic model, with the proposed procedure for the parameter identification are presented in the following sections. For each structural wall, and for each variant of the multilinear model, these results include:

- A figure with the evolution of the cost functions in each simulation during the identification process, in which the shown points belong to the value of the cost function at the k_{max} iteration (see Fig. **4-25**) where the convergence was reached;
- A table with the identified parameters of the variant for the wall obtained from the proposed identification procedure, in which the parameters *mass*, k_{init} and δ_1 were obtained from experimental tests. It is important to emphasize that the parameter *mass* is the mass system which include the mass of the walls and the mass of the loading beam (approx. 190 kg).
- A figure with the comparison between the experimental and the estimated responses.

4.4.1 Recycled Plastic Lumber wall (RPLW)

4.4.1.1 Five-lines hysteretic model

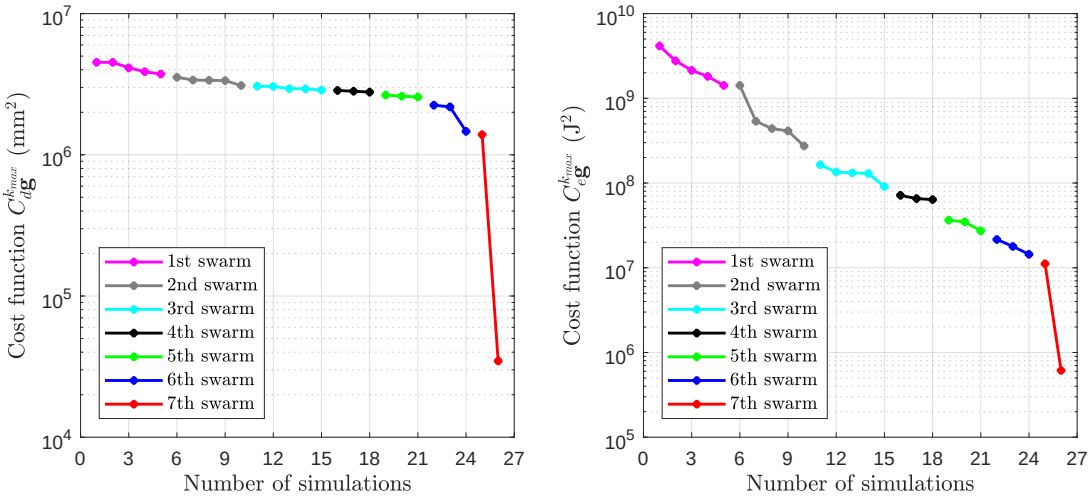

a) Displacement b) Total dissipated energy

Figure 4-26: Evolution of the cost functions in the identification process of a five-lines hysteretic model for the RPLW

Table 4-7: Identified parameters of a five-lines hysteretic model for the RPLW, obtained using the proposed identification procedure

Parameter	Values	Unit
n	5	
$mass$	290	kg
k_{init}	0.2053	kN/mm
ξ	16.659	%
λ_p	[0.96678, 0.33903, 0.47306, 0.60396, 0.98532]	
α	[0.47000, 0.30992, 0.10180, 0.10163, 0.01665]	
α_s	[0.12253, 0.05440, 0.01251, 0.00354]	
γ_s	[3.58830, 5.19740, 5.22130, 11.4360]	
λ_k	[0.00418, 0.12554, 0.22445, 0.16846]	
λ_l	[0.00407, 0.02707, 0.18911, 0.10437]	
δ	[8.95000, 35.2430, 35.7470, 82.2270]	
A	0.6	
B	0.4	
$C_{d\mathbf{g}}^{k_{max}}$	34661	mm^2
$C_{e\mathbf{g}}^{k_{max}}$	614144	J^2

Fig. **4-27** shows the comparison between the experimental and estimated responses. According to these graphs and taking into account the values of the displacement and total dissipated energy cost functions presented in the above table, it can conclude that the five-lines hysteretic model fitted in a satisfactory way the experimental hysteretic behavior exhibited by the RPLW under cyclic loads.

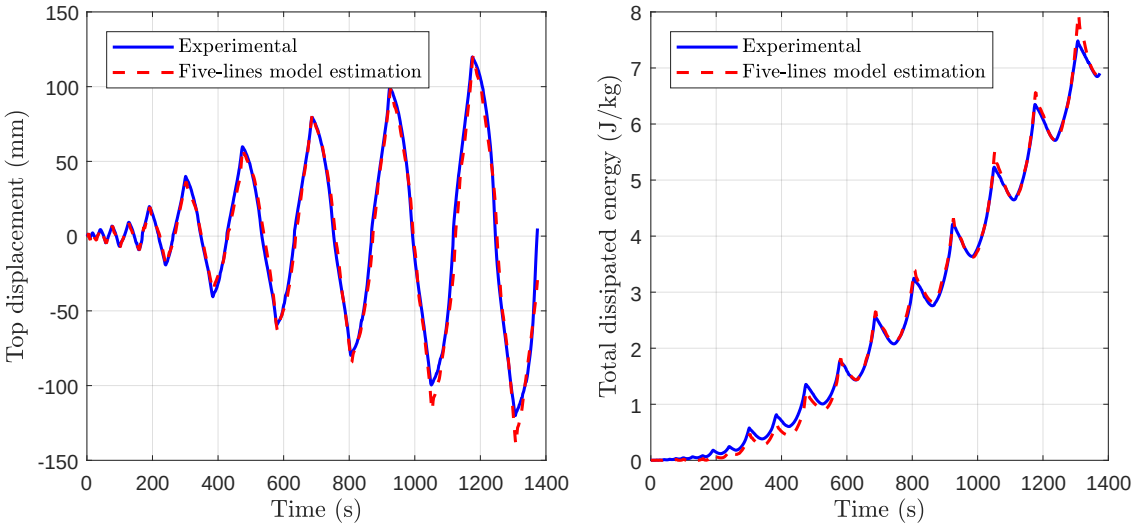

a) Displacement

b) Total dissipated energy per unit mass

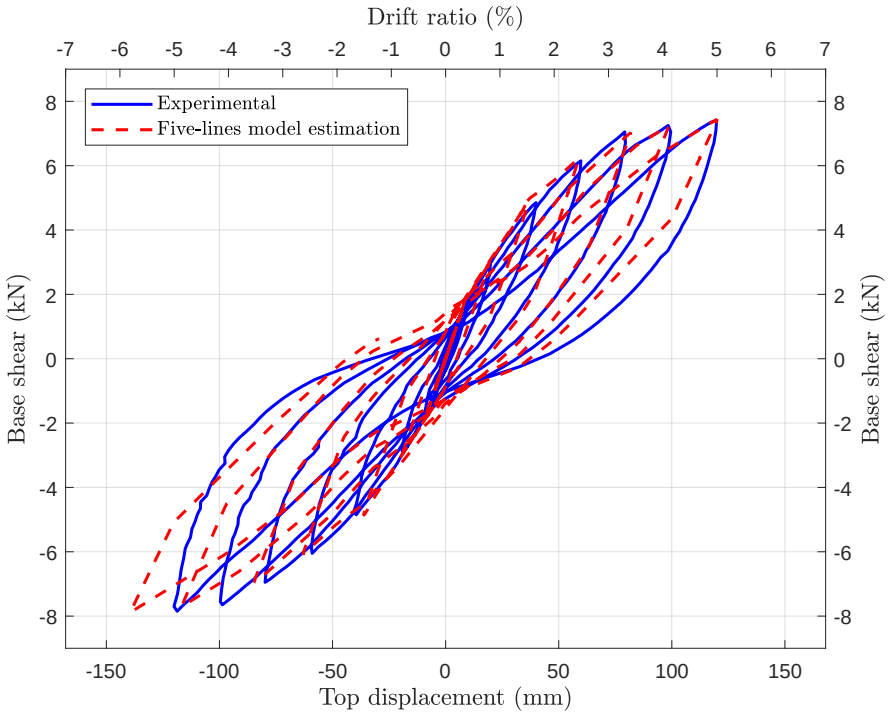

c) Hysteresis cycles

Figure 4-27: Comparison between the experimental and estimated response of the RPLW using a five-lines hysteretic model

4.4.1.2 Six-lines hysteretic model

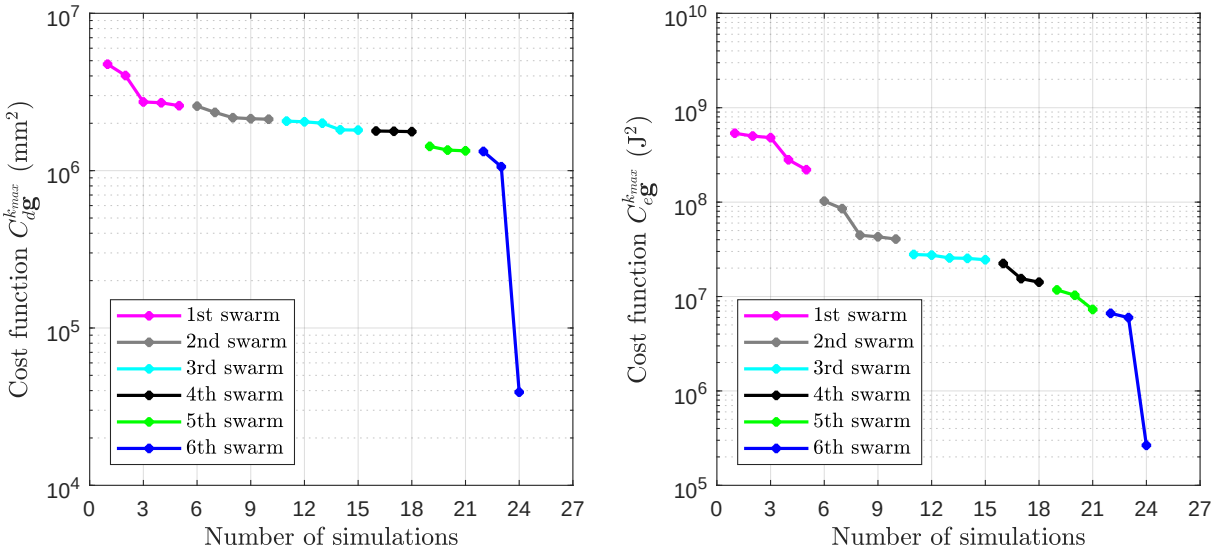

a) Displacement b) Total dissipated energy

Figure 4-28: Evolution of the cost functions in the identification process of a six-lines hysteretic model for the RPLW

Table 4-8: Identified parameters of a six-lines hysteretic model for the RPLW, obtained using the proposed identification procedure

Parameter	Values	Unit
n	6	
$mass$	290	kg
k_{init}	0.2053	kN/mm
ξ	12.544	%
λ_p	[0.49149, 0.42504, 0.03247, 0.52171, 0.00014, 0.19623]	
α	[0.51546, 0.15331, 0.12846, 0.10459, 0.09781, 0.00037]	
α_s	[0.04743, 0.02886, 0.05920, 0.09235, 0.04176]	
γ_s	[3.58690, 3.71320, 4.95360, 5.73630, 9.38250]	
λ_k	[0.00141, 0.17559, 0.08801, 0.30828, 0.01603]	
λ_l	[0.00960, 0.03828, 0.09992, 0.17463, 0.14005]	
δ	[8.95000, 32.9880, 33.6890, 68.9910, 72.6490]	
A	0.9	
B	0.1	
$C_{d\mathbf{g}}^{k_{max}}$	39088	mm^2
$C_{e\mathbf{g}}^{k_{max}}$	265185	J^2

Fig. **4-29** shows the comparison between the experimental and estimated responses. According to these graphs and taking into account the values of the displacement and total dissipated energy cost functions presented in the above table, it can conclude that the six-lines hysteretic model fitted in a good way the experimental hysteretic behavior exhibited by the RPLW under cyclic loads.

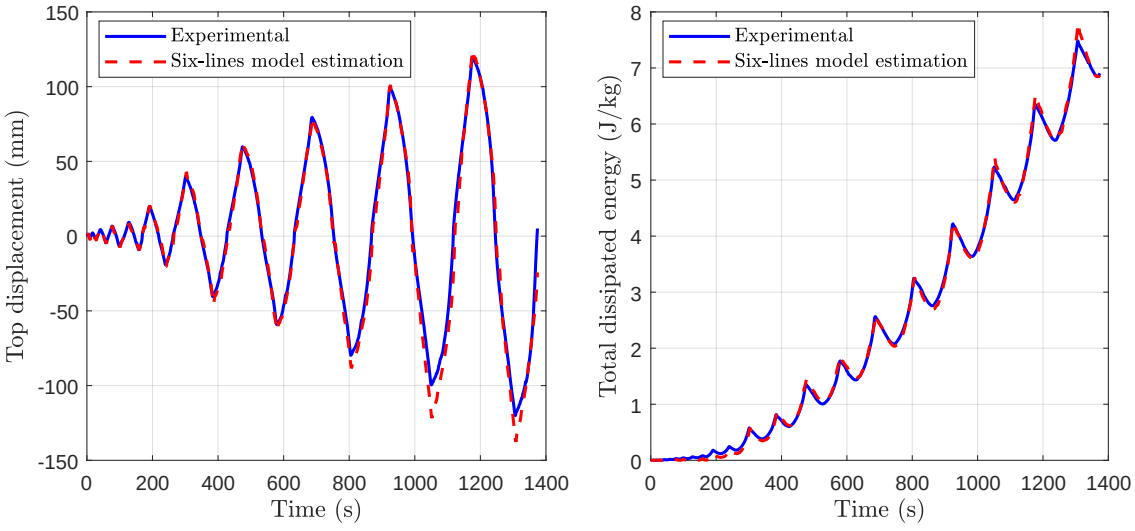

a) Displacement

b) Total dissipated energy per unit mass

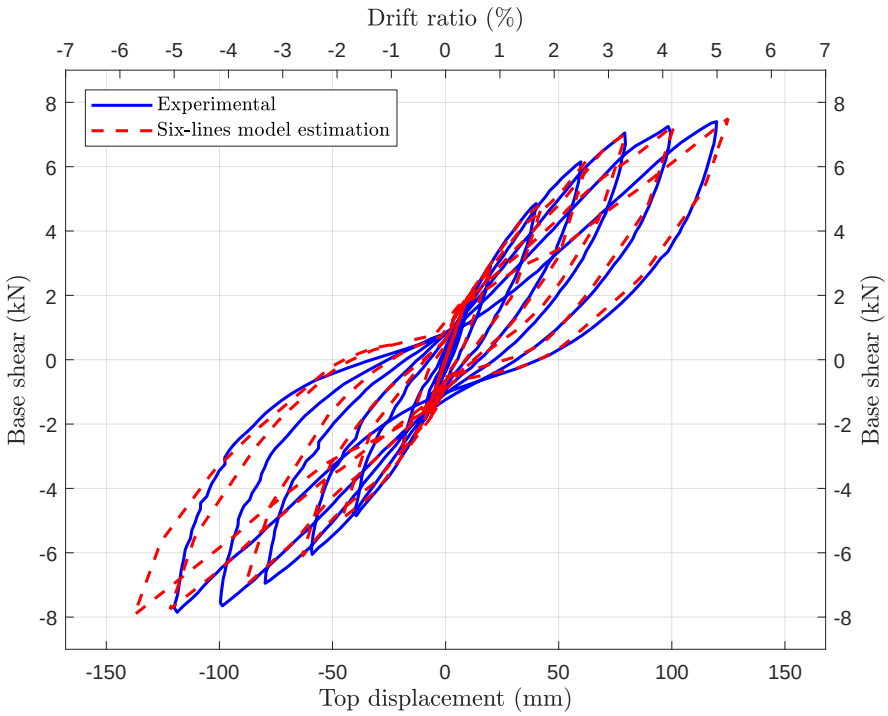

c) Hysteresis cycles

Figure 4-29: Comparison between the experimental and estimated response of the RPLW using a six-lines hysteretic model

4.4.1.3 Seven-lines hysteretic model

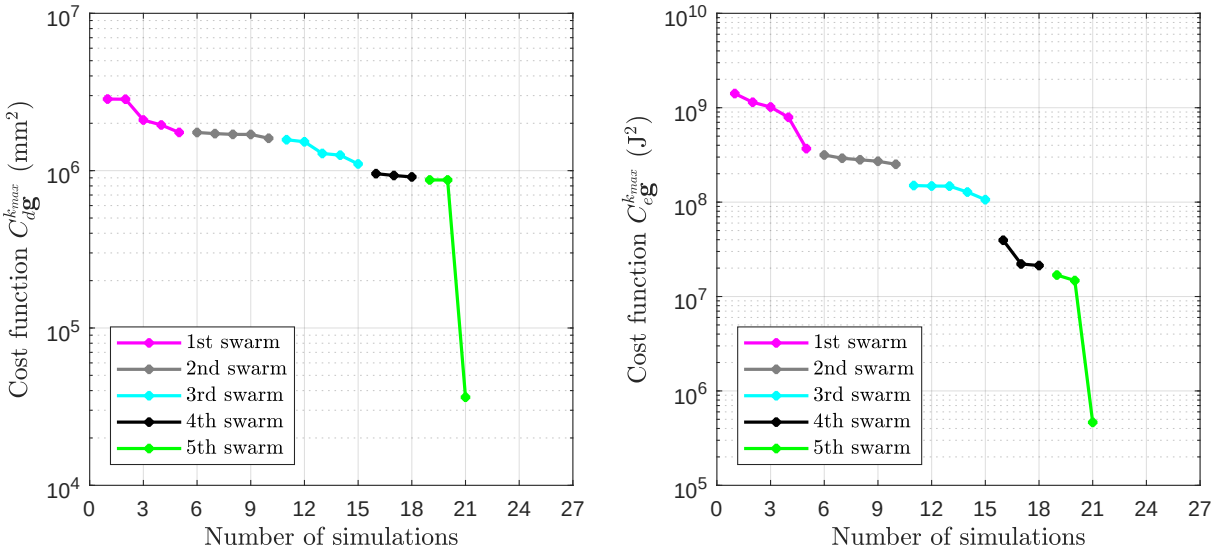

a) Displacement b) Total dissipated energy

Figure 4-30: Evolution of the cost functions in the identification process of a seven-lines hysteretic model for the RPLW

Table 4-9: Identified parameters of a seven-lines hysteretic model for the RPLW, obtained using the proposed identification procedure

Parameter	Values	Unit
n	7	
$mass$	290	kg
k_{init}	0.2053	kN/mm
ξ	8.9784	%
λ_p	[0.55360, 0.15451, 0.45999, 0.86228, 0.20622, 0.43415, 0.64593]	
α	[0.46154, 0.11694, 0.11386, 0.10051, 0.08528, 0.06979, 0.05209]	
α_s	[0.00700, 0.05703, 0.01216, 0.05517, 0.00151, 0.06681]	
γ_s	[3.28940, 5.36150, 5.91530, 5.91820, 6.37830, 8.96430]	
λ_k	[0.11902, 0.06681, 0.00302, 0.18346, 0.00006, 0.18902]	
λ_l	[0.05223, 0.00196, 0.02952, 0.05733, 0.12316, 0.76887]	
δ	[8.95000, 18.4180, 28.3170, 62.9670, 67.2570, 95.2480]	
A	0.6	
B	0.4	
$C_{d\mathbf{g}}^{k_{max}}$	36293	mm^2
$C_{e\mathbf{g}}^{k_{max}}$	464478	J^2

Fig. **4-31** shows the comparison between the experimental and estimated responses. According to these graphs and to the values of the displacement and total dissipated energy cost functions presented in the above table, it can conclude that the seven-lines hysteretic model fitted in an acceptable way the experimental hysteretic behavior exhibited by the RPLW under cyclic loads.

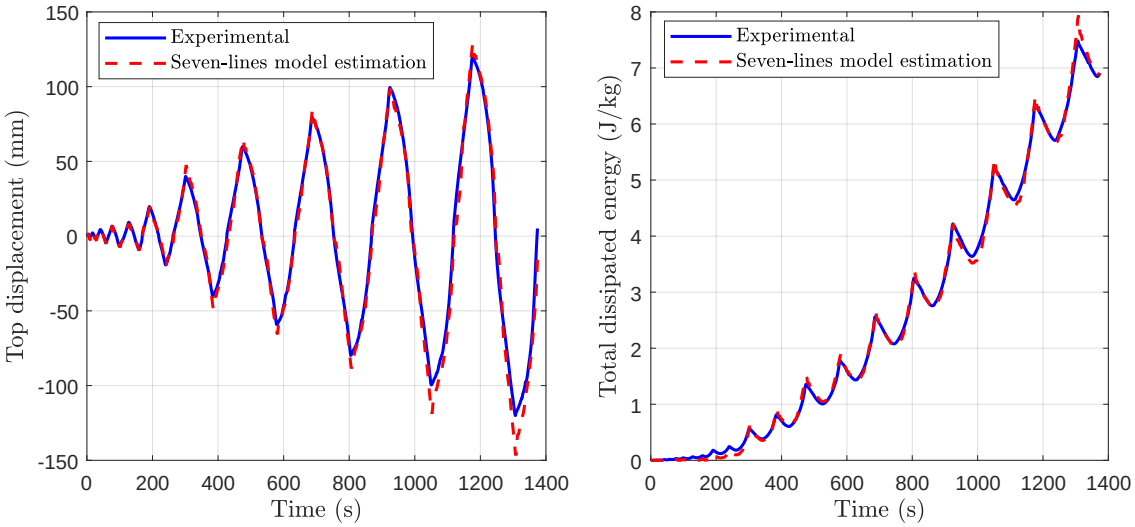

a) Displacement

b) Total dissipated energy per unit mass

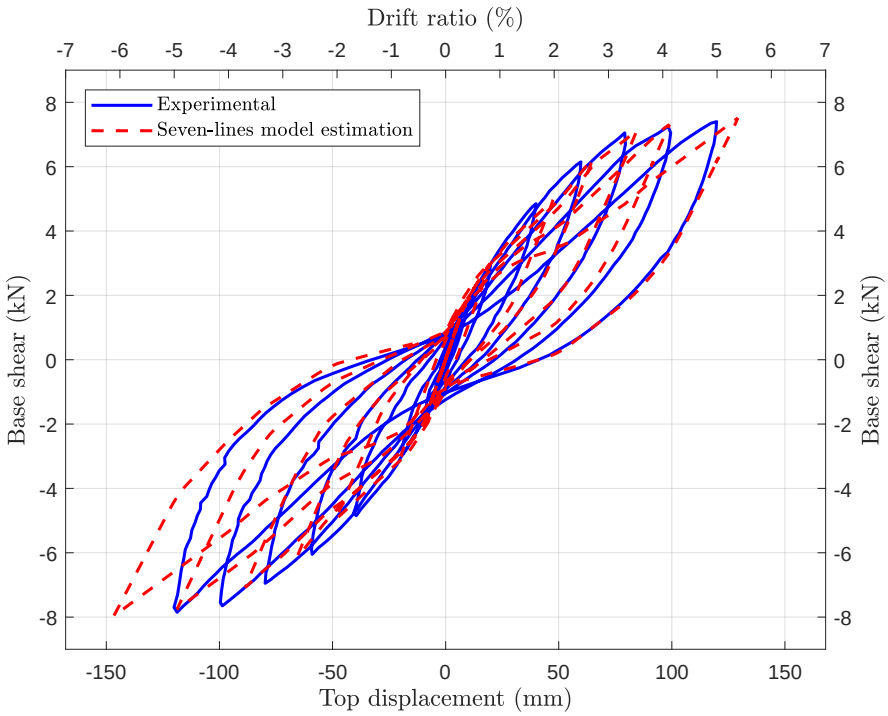

c) Hysteresis cycles

Figure 4-31: Comparison between the experimental and estimated response of the RPLW using a seven-lines hysteretic model

4.4.2 Precast Ferrocement wall (PFW)

4.4.2.1 Five-lines hysteretic model

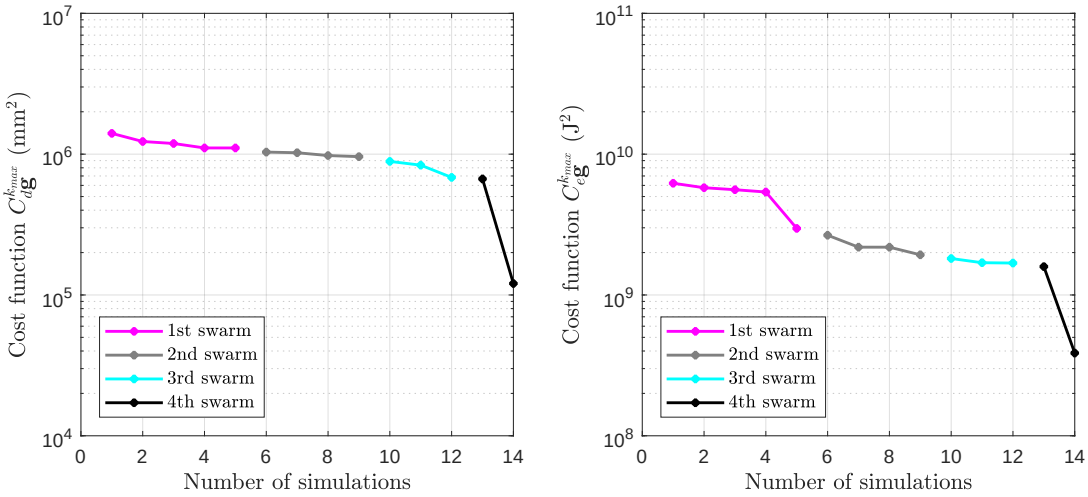

a) Displacement b) Total dissipated energy

Figure 4-32: Evolution of the cost functions in the identification process of a five-lines hysteretic model for the PFW

Table 4-10: Identified parameters of a five-lines hysteretic model for the PFW, obtained using the proposed identification procedure

Parameter	Values	Unit
n	5	
$mass$	522	kg
k_{init}	8.6895	kN/mm
ξ	15.619	%
λ_p	[0.60353, 0.96236, 0.26091, 0.26474, 0.19216]	
α	[0.54120, 0.23284, 0.11857, 0.06587, 0.04152]	
α_s	[0.08769, 0.12523, 0.12432, 0.11731]	
γ_s	[2.74080, 4.47370, 5.40360, 6.68300]	
λ_k	[0.01286, 0.15090, 0.17544, 0.12795]	
λ_l	[0.04749, 0.48543, 0.74661, 0.47684]	
δ	[7.83000, 24.5180, 37.4710, 44.1490]	
A	0.1	
B	0.9	
$C_{d\mathbf{g}}^{k_{max}}$	120584	mm^2
$C_{e\mathbf{g}}^{k_{max}}$	$1.127e+09$	J^2

Fig. **4-33** shows the comparison between the experimental and estimated responses. According to these graphs and to the values of the displacement and total dissipated energy cost functions presented in the above table, it can conclude that the five-lines hysteretic model fitted in an acceptable way the experimental hysteretic behavior exhibited by the PFW under cyclic loads.

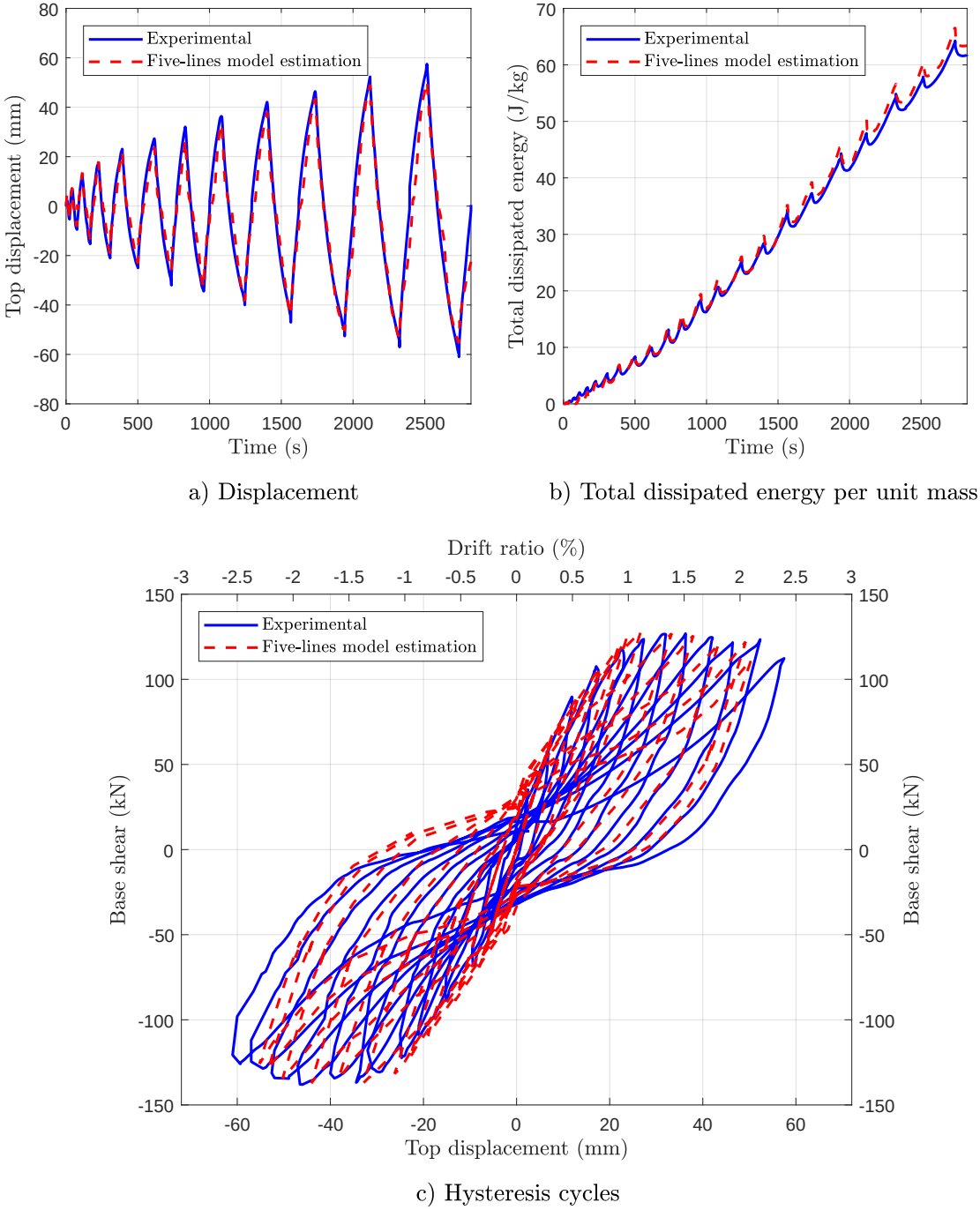

a) Displacement

b) Total dissipated energy per unit mass

c) Hysteresis cycles

Figure 4-33: Comparison between the experimental and estimated response of the PFW using a five-lines hysteretic model

4.4.2.2 Six-lines hysteretic model

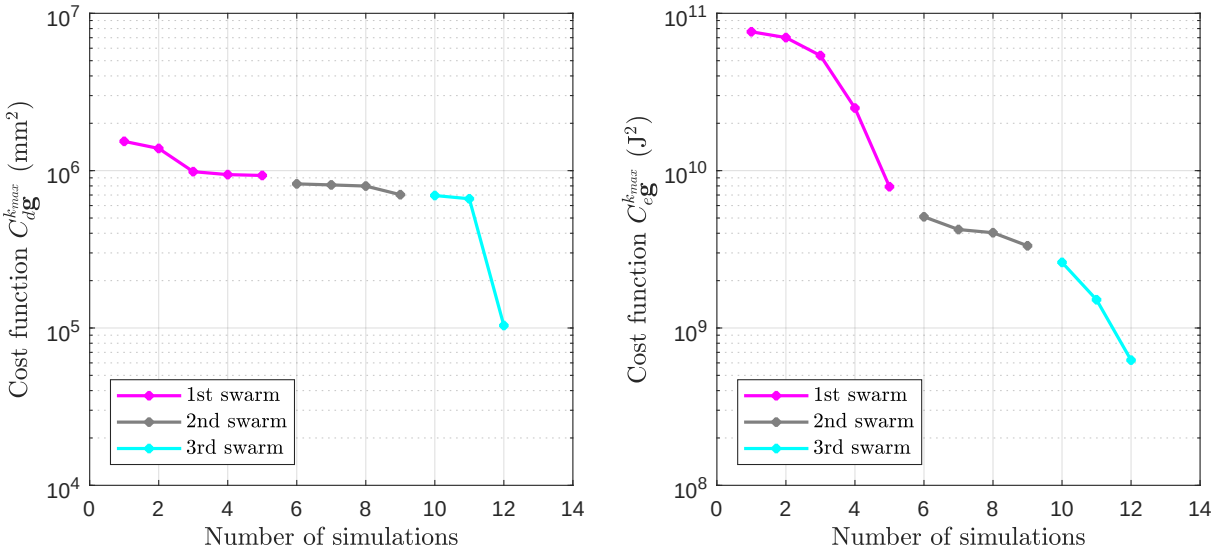

a) Displacement b) Total dissipated energy

Figure 4-34: Evolution of the cost functions in the identification process of a six-lines hysteretic model for the PFW

Table 4-11: Identified parameters of a six-lines hysteretic model for the PFW, obtained using the proposed identification procedure

Parameter	Values	Unit
n	6	
$mass$	522	kg
k_{init}	8.6895	kN/mm
ξ	9.6924	%
λ_p	[0.87249, 0.30063, 0.99262, 0.93824, 0.59796, 0.85505]	
α	[0.54248, 0.15300, 0.13500, 0.08000, 0.04624, 0.04328]	
α_s	[0.09592, 0.03824, 0.01617, 0.01151, 0.08956]	
γ_s	[2.84040, 4.06950, 6.04180, 6.21970, 8.18670]	
λ_k	[0.00043, 0.04902, 0.22379, 0.13145, 0.05572]	
λ_l	[0.10278, 0.19735, 0.78124, 1.67350, 2.12330]	
δ	[7.83000, 23.3450, 31.4720, 48.0960, 74.8240]	
A	0.5	
B	0.5	
$C_{d\mathbf{g}}^{k_{max}}$	103700	mm^2
$C_{e\mathbf{g}}^{k_{max}}$	$6.246e+08$	J^2

Fig. **4-35** shows the comparison between the experimental and estimated responses. According to these graphs and taking into account the values of the displacement and total dissipated energy cost functions presented in the above table, it can conclude that the six-lines hysteretic model fitted in a satisfactory way the experimental hysteretic behavior exhibited by the PFW under cyclic loads.

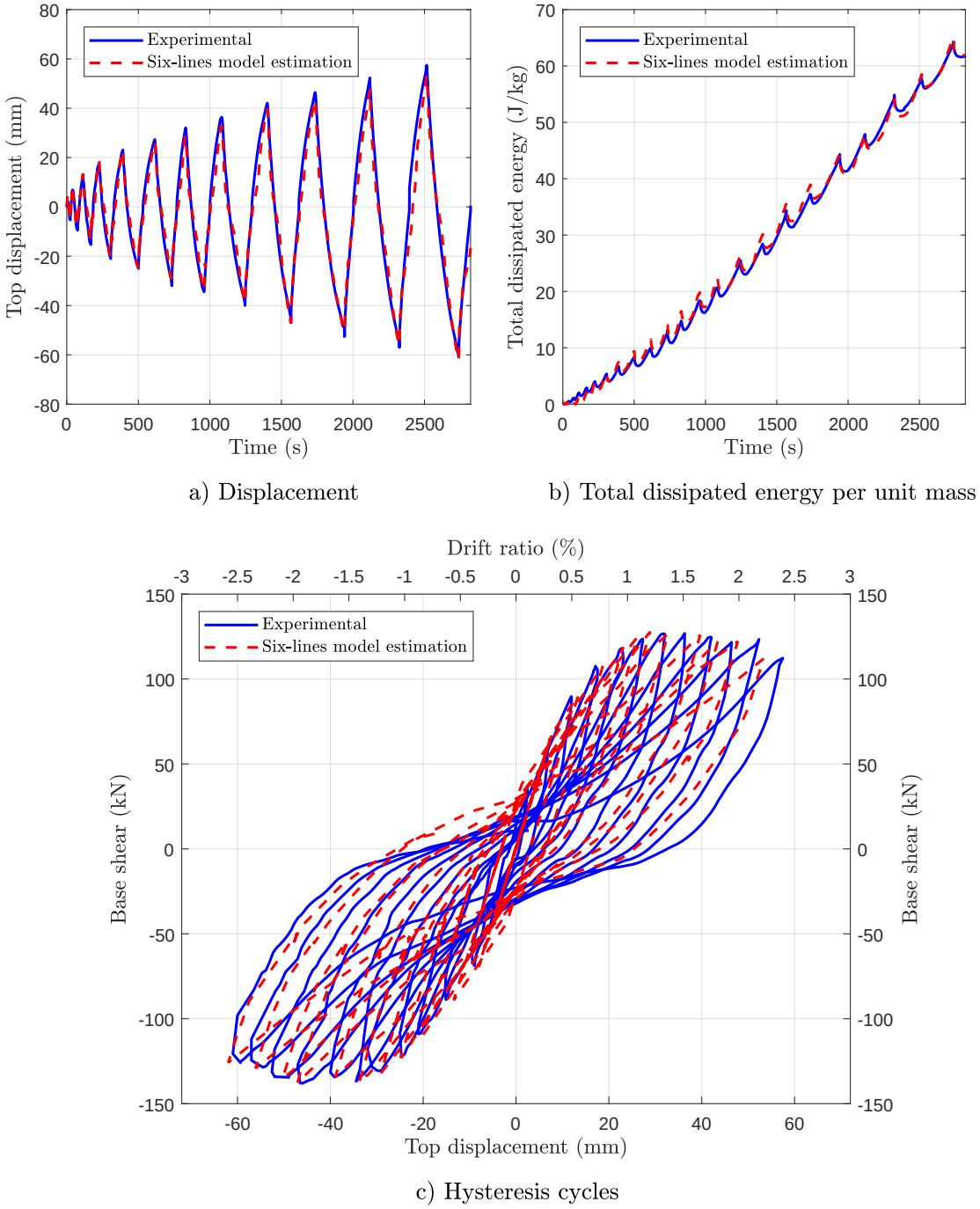

a) Displacement

b) Total dissipated energy per unit mass

c) Hysteresis cycles

Figure 4-35: Comparison between the experimental and estimated response of the PFW using a six-lines hysteretic model

4.4.2.3 Seven-lines hysteretic model

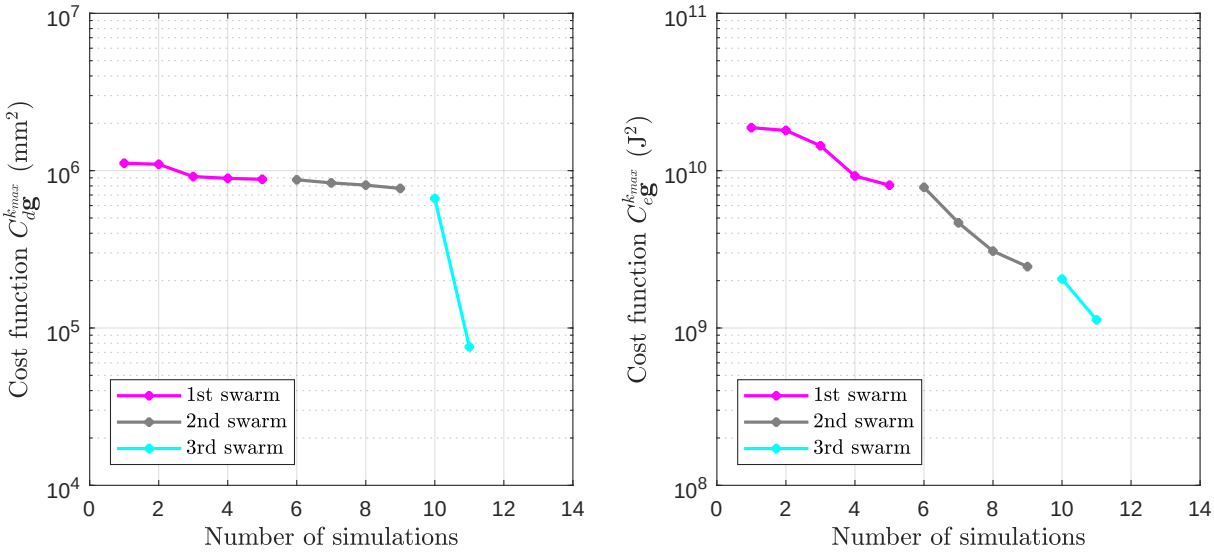

a) Displacement b) Total dissipated energy

Figure 4-36: Evolution of the cost functions in the identification process of a seven-lines hysteretic model for the PFW

Table 4-12: Identified parameters of a seven-lines hysteretic model for the PFW, obtained using the proposed identification procedure

Parameter	Values	Unit
n	7	
$mass$	522	kg
k_{init}	8.6895	kN/mm
ξ	13.589	%
λ_p	[0.80679, 0.44846, 0.99384, 0.11988, 0.56903, 0.27186, 0.49590]	
α	[0.52536, 0.17568, 0.14354, 0.08399, 0.03884, 0.01836, 0.01423]	
α_s	[0.07791, 0.08667, 0.01095, 0.00009, 0.00294, 0.01550]	
γ_s	[2.51230, 4.13520, 5.02880, 5.09740, 6.84130, 8.43890]	
λ_k	[0.00166, 0.13184, 0.22877, 0.21142, 0.24579, 0.18478]	
λ_l	[0.09886, 0.46446, 0.82403, 0.66468, 1.07510, 0.25942]	
δ	[7.83000, 22.4720, 33.3660, 46.0540, 62.6770, 78.8920]	
A	0.65	
B	0.35	
$C_{d\mathbf{g}}^{k_{max}}$	75830	mm^2
$C_{e\mathbf{g}}^{k_{max}}$	$3.869e+08$	J^2

Fig. **4-37** shows the comparison between the experimental and estimated responses. According to these graphs and to the values of the displacement and total dissipated energy cost functions presented in the above table, it can conclude that the seven-lines hysteretic model fitted in a good way the experimental hysteretic behavior exhibited by the PFW under cyclic loads.

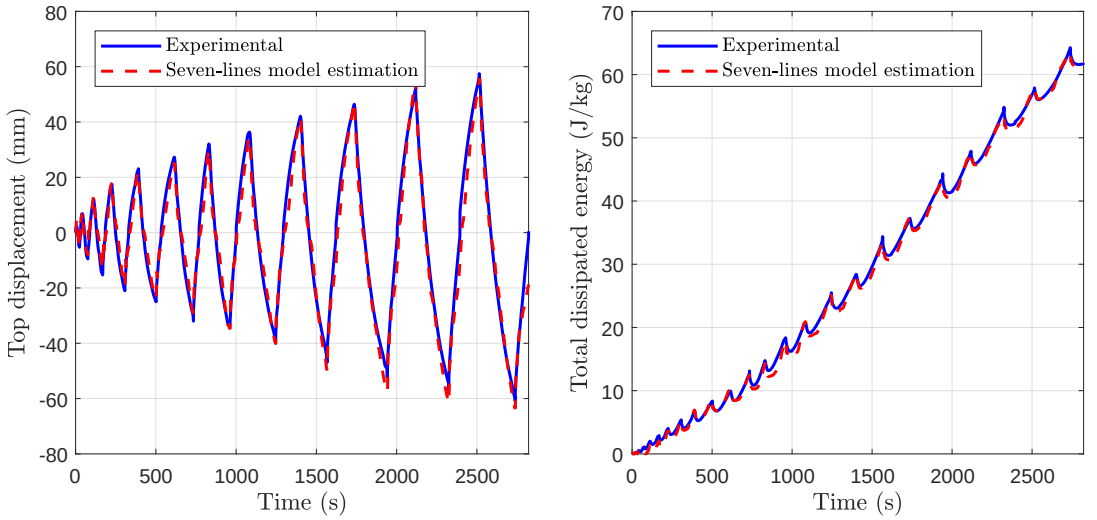

a) Displacement b) Total dissipated energy per unit mass

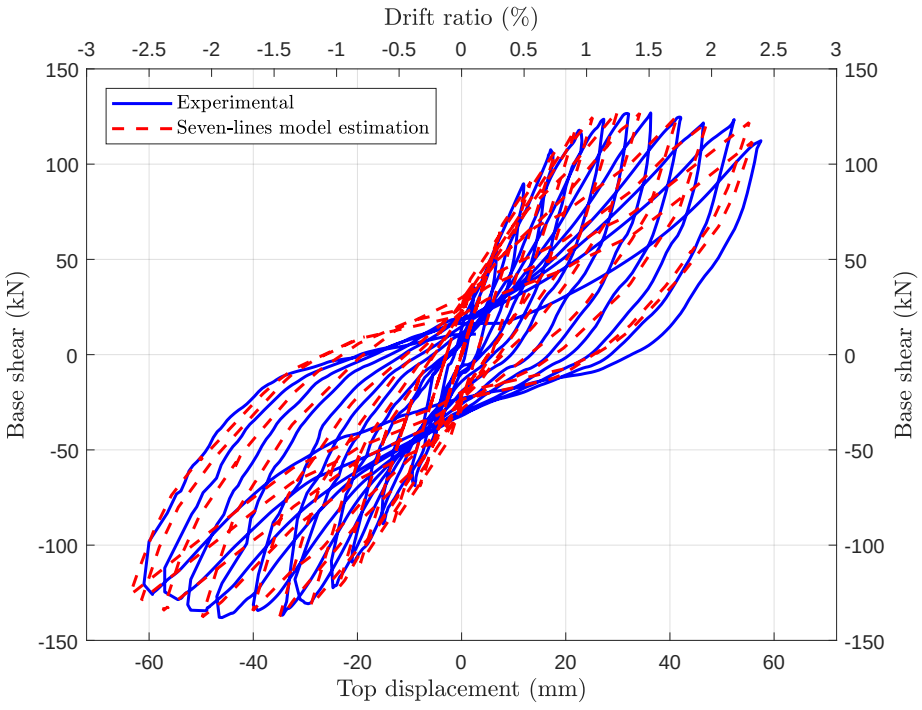

c) Hysteresis cycles

Figure 4-37: Comparison between the experimental and estimated response of the PFW using a seven-lines hysteretic model

4.4.3 Hollow Reinforced Concrete Wall (HRCW)

4.4.3.1 Five-lines hysteretic model

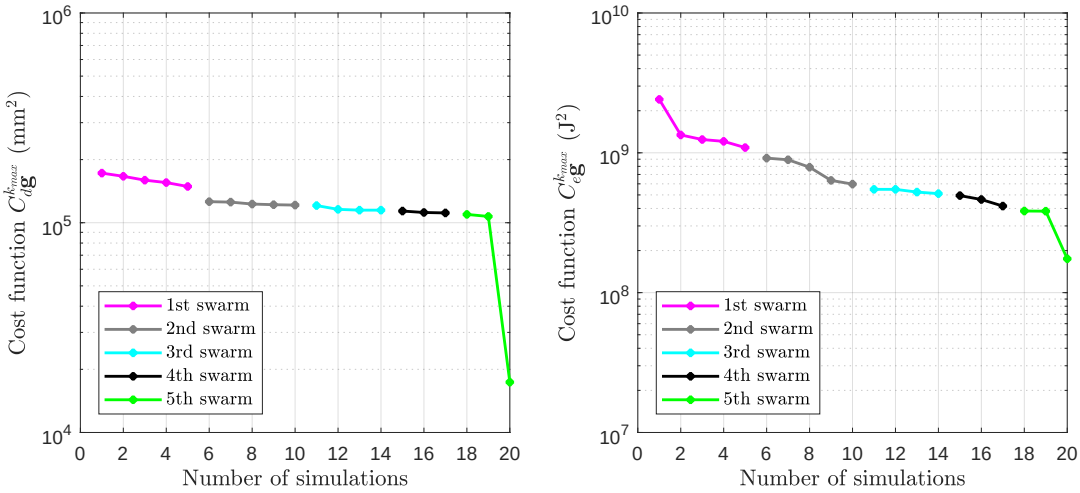

a) Displacement b) Total dissipated energy

Figure 4-38: Evolution of the cost functions in the identification process of a five-lines hysteretic model for the HRCW

Table 4-13: Identified parameters of a five-lines hysteretic model for the HRCW, obtained using the proposed identification procedure

Parameter	Values	Unit
n	5	
$mass$	787	kg
k_{init}	11.0798	kN/mm
ξ	16.116	%
λ_p	[1, 1, 1, 1, 1]	
α	[0.50223, 0.24813, 0.15589, 0.07040, 0.02335]	
α_s	[0.10173, 0.03149, 0.08413, 0.10180]	
γ_s	[3.44940, 3.72320, 5.32390, 6.10090]	
λ_k	[0.01602, 0.00236, 0.20183, 0.29486]	
λ_l	[0.49788, 0.79842, 1.27830, 0.80086]	
δ	[7.35000, 19.2550, 27.7920, 50.8130]	
A	0.9	
B	0.1	
$C_{d\mathbf{g}}^{k_{max}}$	17374	mm^2
$C_{e\mathbf{g}}^{k_{max}}$	$1.746e+08$	J^2

Fig. **4-39** shows the comparison between the experimental and estimated responses. According to these graphs and taking into account the values of the displacement and total dissipated energy cost functions presented in the above table, it can conclude that the five-lines hysteretic model fitted in a satisfactory way the experimental hysteretic behavior exhibited by the HRCW under cyclic loads.

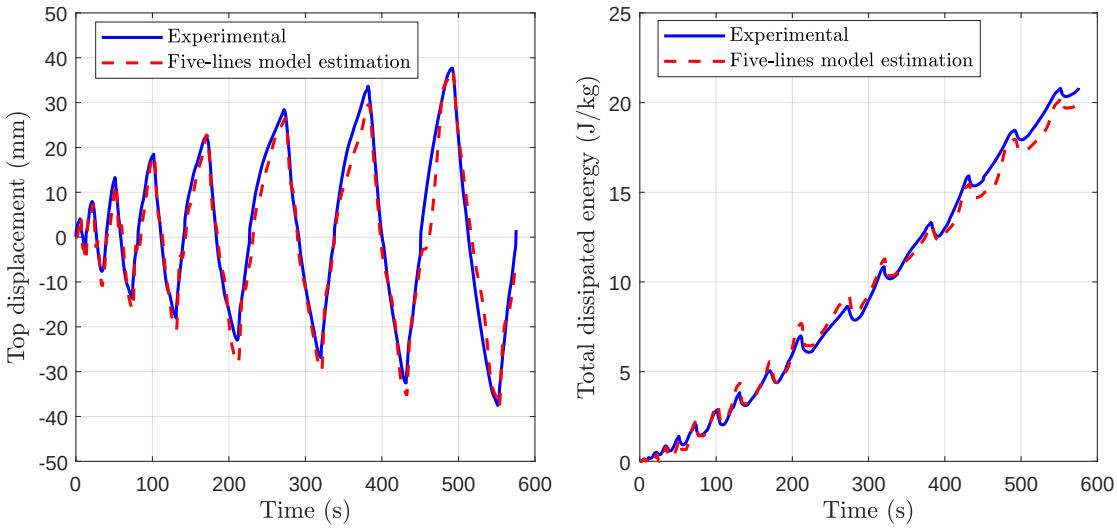

a) Displacement b) Total dissipated energy per unit mass

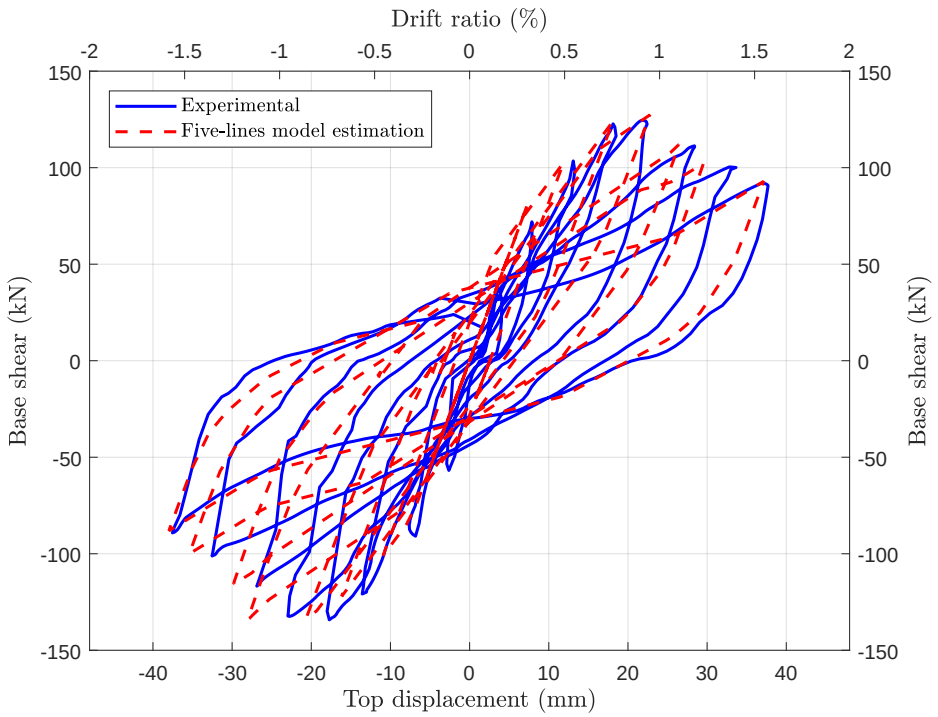

c) Hysteresis cycles

Figure 4-39: Comparison between the experimental and estimated response of the HRCW using a five-lines hysteretic model

4.4.3.2 Six-lines hysteretic model

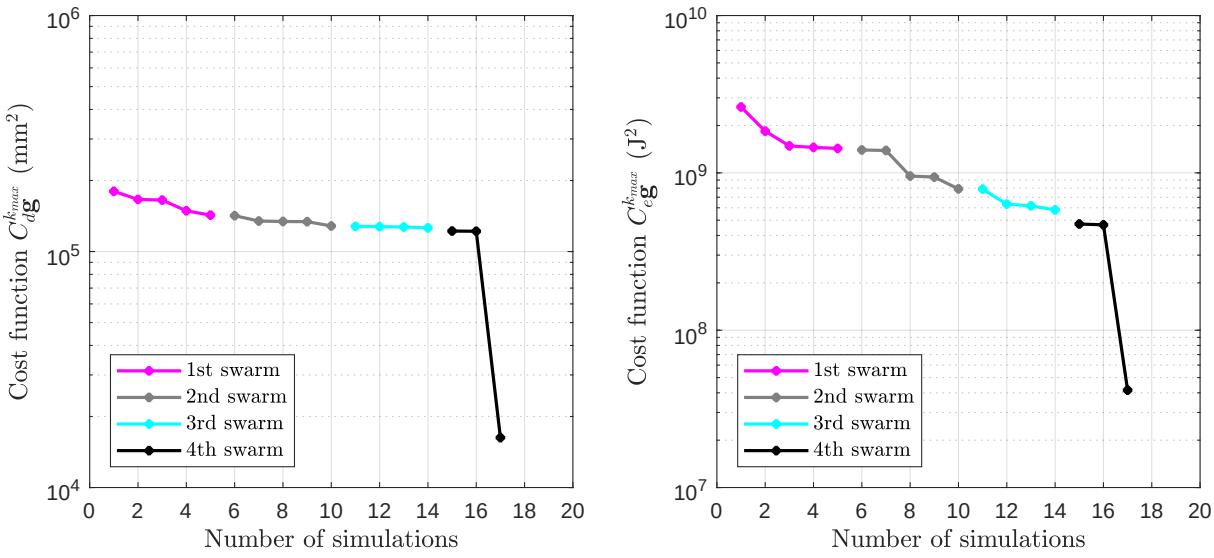

a) Displacement b) Total dissipated energy

Figure 4-40: Evolution of the cost functions in the identification process of a six-lines hysteretic model for the HRCW

Table 4-14: Identified parameters of a six-lines hysteretic model for the HRCW, obtained using the proposed identification procedure

Parameter	Values	Unit
n	6	
$mass$	787	kg
k_{init}	11.0798	kN/mm
ξ	19.028	%
λ_p	[1, 1, 1, 1, 1, 1]	
α	[0.51286, 0.24294, 0.13341, 0.04300, 0.03617, 0.03162]	
α_s	[0.04051, 0.02312, 0.15453, 0.07700, 0.38196]	
γ_s	[3.74390, 4.64140, 4.71480, 7.22730, 7.63430]	
λ_k	[0.01495, 0.10109, 0.16565, 0.06269, 0.28113]	
λ_l	[0.24237, 1.48440, 1.96340, 0.61416, 0.68420]	
δ	[7.35000, 19.1660, 27.8580, 52.8840, 54.6120]	
A	0.8	
B	0.1	
$C_{d\mathbf{g}}^{k_{max}}$	16275	mm^2
$C_{e\mathbf{g}}^{k_{max}}$	$4.159e+07$	J^2

Fig. **4-41** shows the comparison between the experimental and estimated responses. According to these graphs and taking into account the values of the displacement and total dissipated energy cost functions presented in the above table, it can conclude that the six-lines hysteretic model fitted in a good way the experimental hysteretic behavior exhibited by the HRCW under cyclic loads.

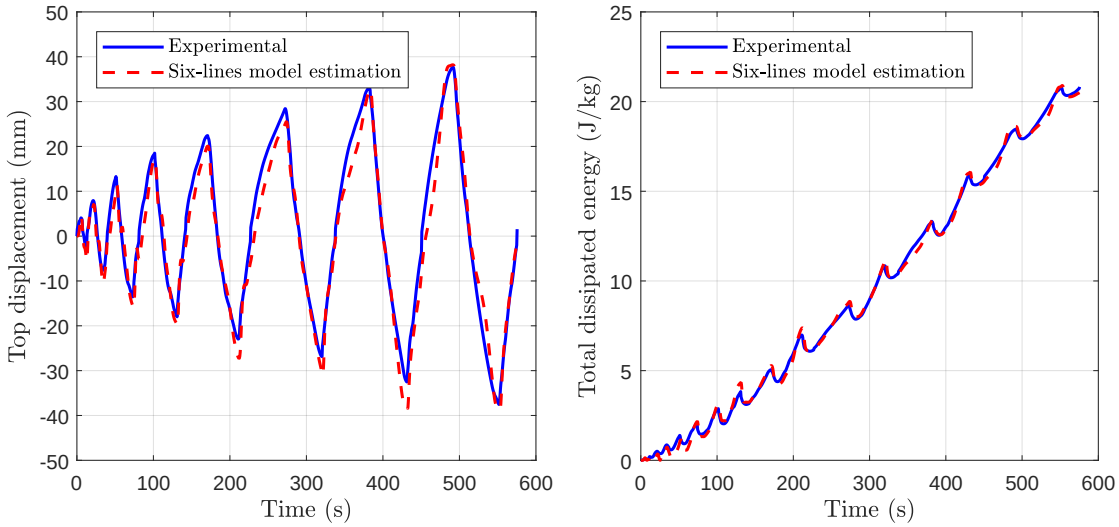

a) Displacement b) Total dissipated energy per unit mass

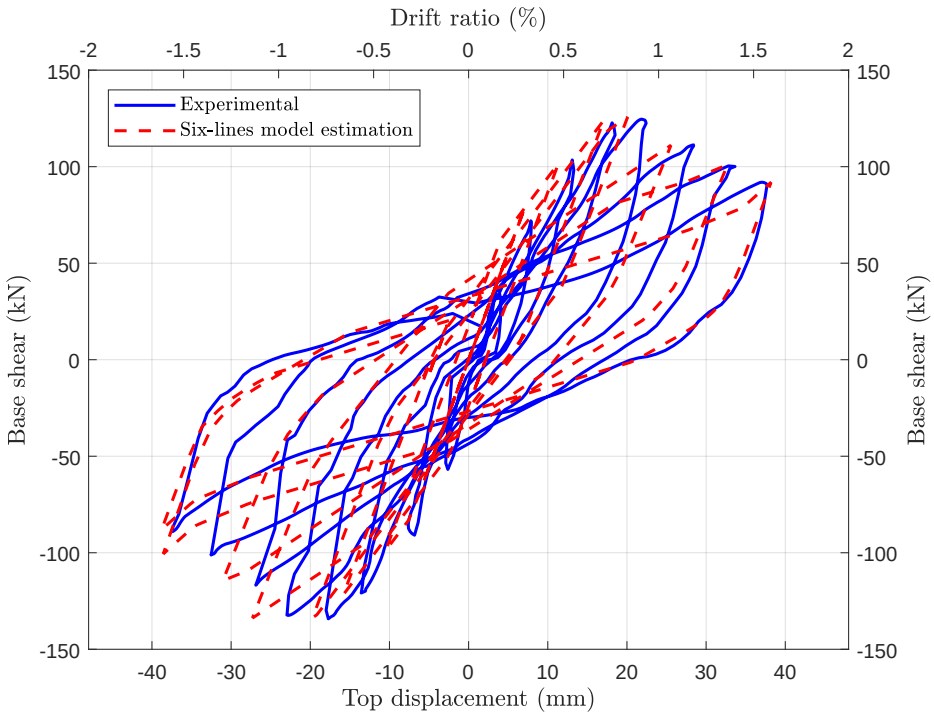

c) Hysteresis cycles

Figure 4-41: Comparison between the experimental and estimated response of the HRCW using a six-lines hysteretic model

4.4.3.3 Seven-lines hysteretic model

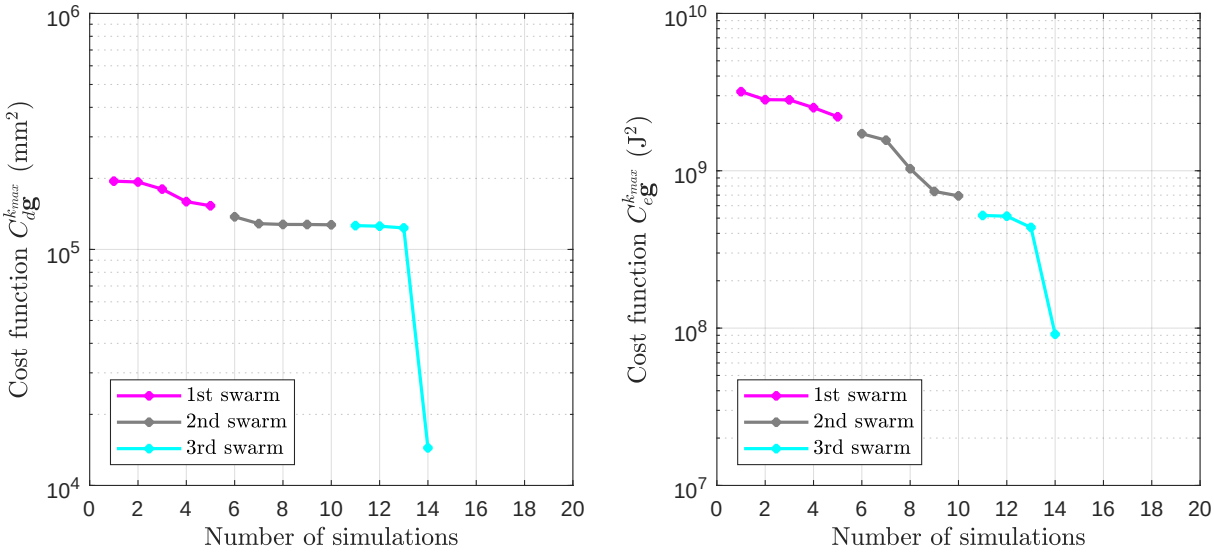

a) Displacement b) Total dissipated energy

Figure 4-42: Evolution of the cost functions in the identification process of a seven-lines hysteretic model for the HRCW

Table 4-15: Identified parameters of a seven-lines hysteretic model for the HRCW, obtained using the proposed identification procedure

Parameter	Values	Unit
n	7	
$mass$	787	kg
k_{init}	11.0798	kN/mm
ξ	14.855	%
λ_p	[1, 1, 1, 1, 1, 1, 1]	
α	[0.56366, 0.22485, 0.11080, 0.04772, 0.02132, 0.01735, 0.01430]	
α_s	[0.05640, 0.14420, 0.06509, 0.04058, 0.13096, 0.11219]	
γ_s	[2.96730, 5.45990, 5.47140, 5.69750, 6.00690, 8.14020]	
λ_k	[0.14707, 0.00564, 0.19101, 0.09240, 0.01500, 0.35554]	
λ_l	[0.37823, 0.85038, 1.66690, 1.18230, 0.98065, 0.12092]	
δ	[7.35000, 20.1570, 27.5250, 55.3340, 67.4750, 85.8000]	
A	0.6	
B	0.4	
$C_{d\mathbf{g}}^{k_{max}}$	14425	mm^2
$C_{e\mathbf{g}}^{k_{max}}$	$9.140e+07$	J^2

Fig. **4-43** shows the comparison between the experimental and estimated responses. According to these graphs and to the values of the displacement and total dissipated energy cost functions presented in the above table, it can conclude that the seven-lines hysteretic model fitted in an acceptable way the experimental hysteretic behavior exhibited by the HRCW under cyclic loads.

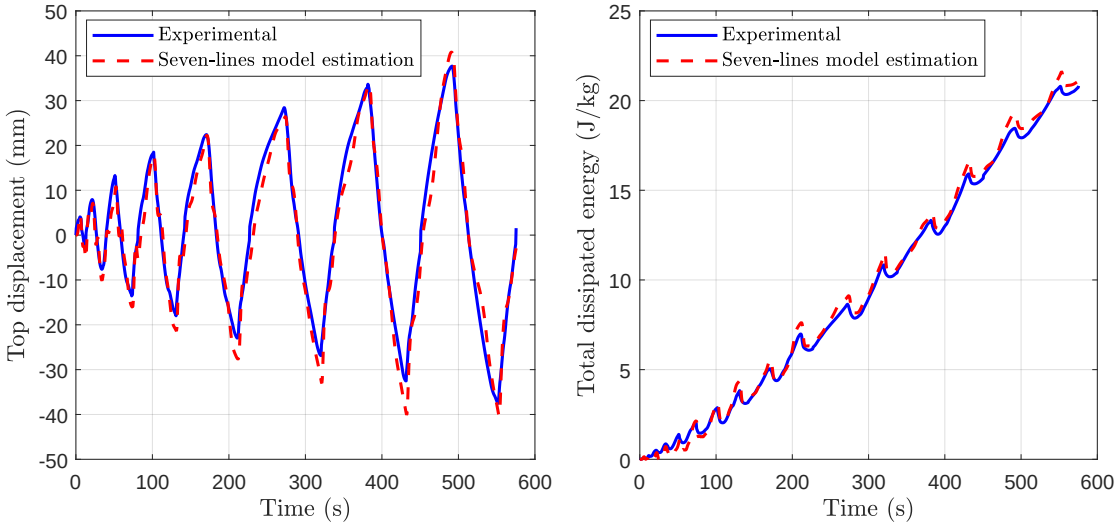

a) Displacement b) Total dissipated energy per unit mass

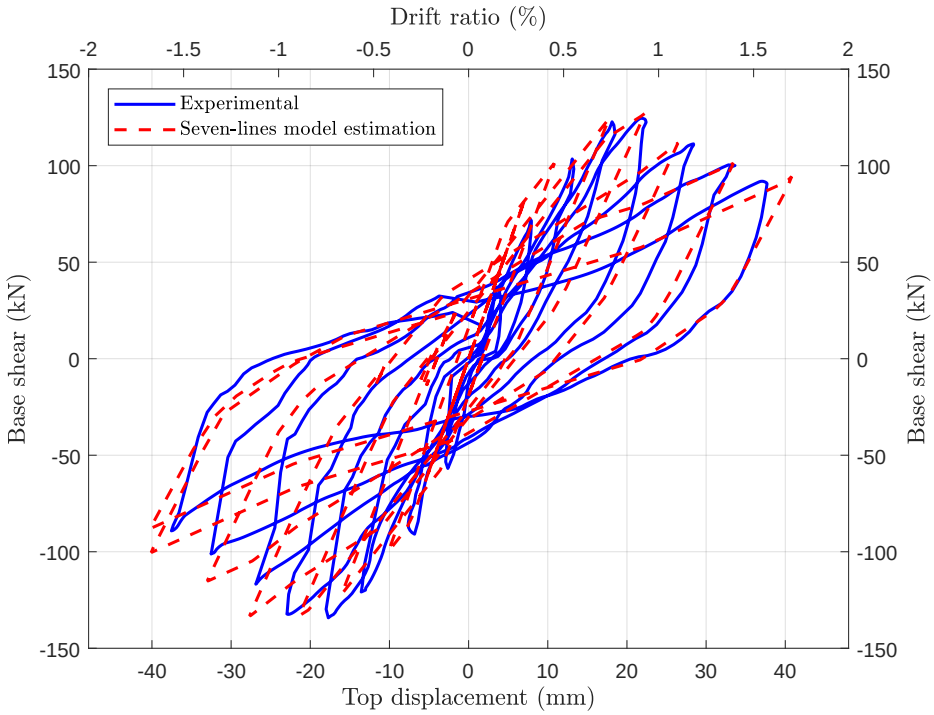

c) Hysteresis cycles

Figure 4-43: Comparison between the experimental and estimated response of the HRCW using a seven-lines hysteretic model

4.4.4 Selection of the Mostaghel's multilinear hysteretic models to perform nonlinear dynamic analyses

In general, the applied variants of the Mostaghel multilinear hysteretic model were in good agreement with the experimental hysteretic behavior of the structural walls. However, just a variant should be selected to perform the nonlinear dynamic analyses required to assess the seismic performance of the walls. On this matter, the selection task needs clearly defined decision variables which are determined depending on the formulation of the hysteretic model, its use purposes and its scope. For instance, in the simulation and identification of structural hysteretic systems, common decision variables include the fitting of the displacement, total dissipated energy or the shape of the hysteresis cycles; often, a combination of them are used.

Given that the structural walls experiences pinching, stiffness degradation and load deterioration (strength degradation) under cyclic loading conditions, and taking into account that these hysteretic phenomena in the Mostaghel's multilinear formulation are expressed in terms of the total hysteretic energy, the chosen decision variables for this research are mainly the fitting of the total dissipated energy and the shape of the hysteresis cycles (though the displacement is also considered but with less importance). The idea is selecting the variant that has the minor value of the total dissipated energy cost function and checking that the approximation of the estimated hysteresis cycles with respect to the shape of the experimental ones is good. To carry out this task, Table **4-16** summarizes the cost functions values obtained from each multilinear hysteretic variant applied for the structural walls, which were presented in the above section.

Table 4-16: Summary of the cost functions values obtained from the application of the multilinear hysteretic variants for the structural walls

Wall	Total dissipated energy cost function $\left(C_{e\mathbf{g}}^{k_{max}}\right)$			Displacement cost function $\left(C_{d\mathbf{g}}^{k_{max}}\right)$		
	Five-lines	Six-lines	Seven-lines	Five-lines	Six-lines	Seven-lines
RPLW	$6.141x10^5$	$\mathbf{2.651x10^5}$	$4.644x10^5$	$3.466x10^4$	$3.908x10^4$	$3.629x10^4$
PFW	$1.127x10^9$	$6.246x10^8$	$\mathbf{3.869x10^8}$	$1.205x10^5$	$1.037x10^5$	$7.583x10^4$
HRCW	$1.746x10^8$	$\mathbf{4.159x10^7}$	$9.140x10^7$	$1.737x10^4$	$1.627x10^4$	$1.442x10^4$

According to the above, the selected hysteretic model for the RPLW, PFW, and HRCW are the six-lines model, the seven-lines model, and the six-lines model, respectively, which besides fit in a good way the experimental hysteresis cycles, as shown Fig. **4-29**, Fig. **4-37**, and Fig. **4-41**, respectively. These models are good enough for simulation purposes.

5 Performance-based seismic assessment of the structural walls

This chapter starts with the definitions of the structural performance levels for each wall. Then, the typical tributary dead load that the structural walls would support is determined. After that, the earthquake hazard is presented and described with the definition of the target response spectrum, earthquake hazard levels, and the descriptions of the actual recorded and the artificial ground motions that are used in the IDA procedure. At the end of this chapter, Section 5.4 shows the results of the seismic performance assessment of each structural wall using both set of ground motions. In that section, the postprocessing of the IDA results, the determination of the performance points, and the seismic fragility assessment are presented.

5.1 Definition of the structural performance levels

The structural performance levels (SPLs) -Immediate Occupancy (IO), Life Safety (LS) and Collapse Prevention (CP))- are used in the present methodology for the performance seismic assessment of the structural walls. These performance levels are defined for each wall taking into the account the definitions of their damage limit states observed during the cyclic loading tests (see Section 4.3.4) and their corresponding limit value for the top lateral displacement and story drift ratio. Considering the explicit descriptions of each observed damage states, the IO, LS, and CP levels are related to the $\mathbf{DS}_1$, $\mathbf{DS}_2$ and $\mathbf{DS}_3$ damage limit states, respectively. Additionally, the Collapse level, which is not defined as a SPL, is related to the $\mathbf{DS}_4$ of each wall to assess later the probability of collapse via seismic fragility analyses. The following tables and figures show the proposed SPLs for each wall.

Table 5-1: Structural performance levels for the RPLW

SPL	Damage state associated	Top lateral displacement range (mm)	Drift ratio range (%)
IO	**No Damage** and $\mathbf{DS_1}$	$0-40$	$0-1.67$
LS	$\mathbf{DS_2}$	$40-100$	$1.67-4.17$
CP	$\mathbf{DS_3}$	$100-140$	$4.17-5.83$

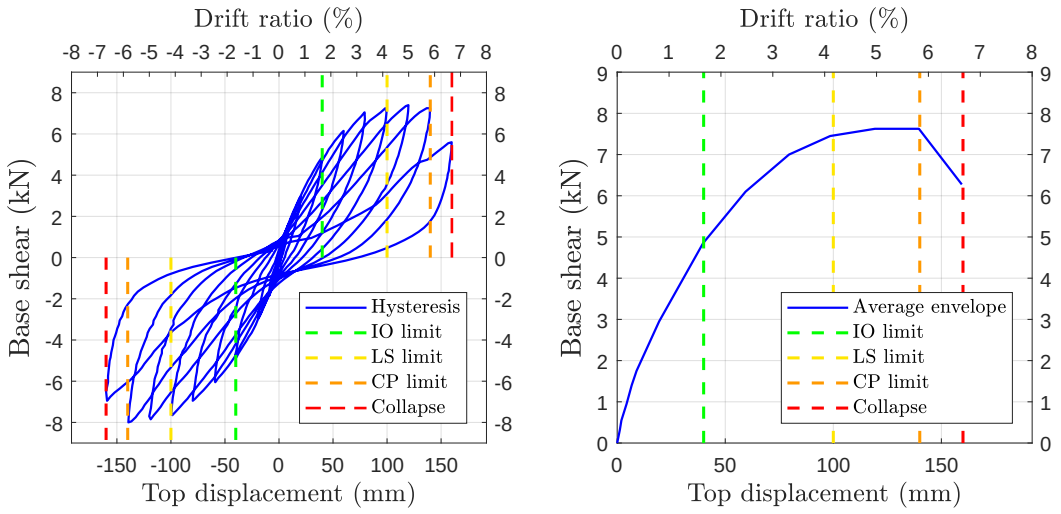

a) Hysteresis cycles b) Average envelope

Figure 5-1: Structural performance levels and collapse level on the hysteresis of the RPLW

Table 5-2: Structural performance levels for the PFW

SPL	Damage state associated	Top lateral displacement range (mm)	Drift ratio range (%)
IO	**No Damage** and $\mathbf{DS_1}$	$0-8$	$0-0.33$
LS	$\mathbf{DS_2}$	$8-24$	$0.33-1.0$
CP	$\mathbf{DS_3}$	$24-44$	$1.0-1.83$

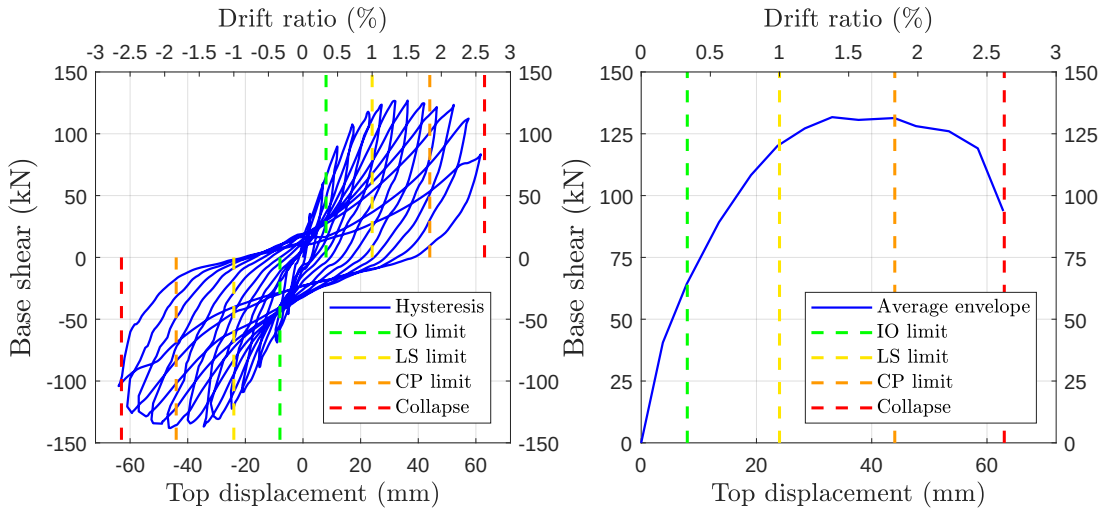

a) Hysteresis cycles b) Average envelope

Figure 5-2: Structural performance levels and collapse level on the hysteresis of the PFW

Table 5-3: Structural performance levels for the HRCW

SPL	Damage state associated	Top lateral displacement range (mm)	Drift ratio range (%)
IO	**No Damage** and $\mathbf{DS_1}$	0 – 7.5	0 – 0.31
LS	$\mathbf{DS_2}$	7.5 – 22.5	0.31 – 0.94
CP	$\mathbf{DS_3}$	22.5 – 33	0.94 – 1.38

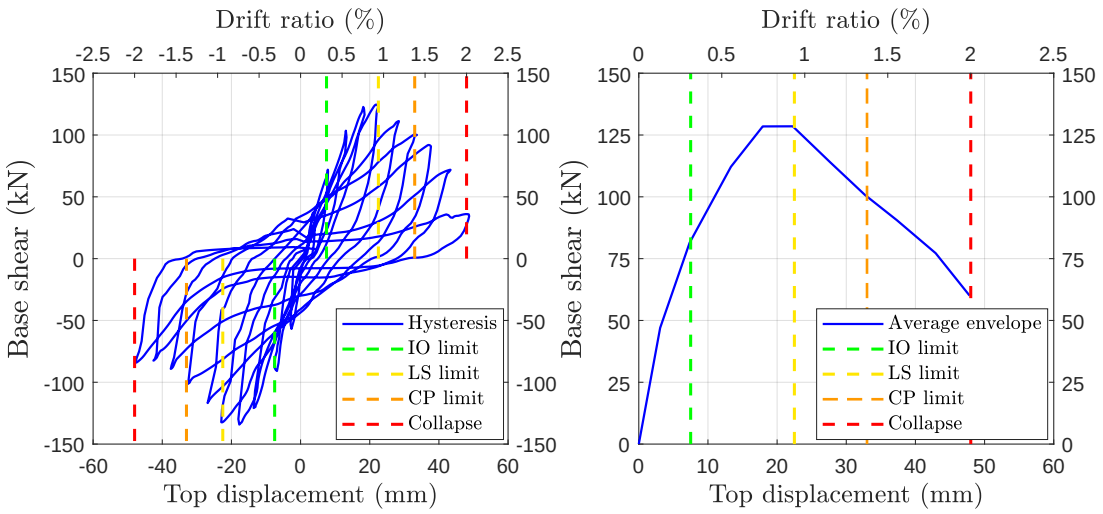

a) Hysteresis cycles b) Average envelope

Figure 5-3: Structural performance levels and collapse level on the hysteresis of the HRCW

5.2 Typical tributary dead load for the structural walls

Given that the structural walls have been proposed as structural systems for one and two-story housing, it is necessary to assess their seismic performance considering a typical tributary dead load which is defined as the load that a wall of the first story would support during a possible seismic event, i.e. the seismic weight.

For the case of this research, tributary dead loads of the walls have been assumed for two-story housing taking into account a typical design which includes a tributary width of 4 m, and definitions for the covering, the ceiling, and the floor fill, which are widely used in Colombia for these type of housing. These loads are composed of the superimposed dead loads, a 20% of the live load, and the dead loads of the structural walls. The analysis of loads is carried out in detail to compute the total tributary dead load of each story. Table **5-4** and Table **5-5** present these analysis for the second and the first story, respectively.

Table 5-4: Analysis of loads for the second story tributary dead load

Covering	
Corrugated asbestos-cement roofing $(\mathrm{kN/m^2})$	0.20
Ceiling	
Suspended metal lath and gypsum plaster $(\mathrm{kN/m^2})$	0.50
Total superimposed dead load per unit area $(\mathrm{kN/m^2})$	0.70
Tributary width (m)	4
Total superimposed dead load per unit length $(\mathrm{kN/m})$	2.80
Wall width (m)	1
Total superimposed dead load (kN)	2.80
Wall dead load (kN)	D_{wall}
Total second story tributary dead load (kN)	$2.80 + D_{wall}$

Table 5-5: Analysis of loads for the first story tributary dead load

Ceiling	
Suspended metal lath and gypsum plaster $(\mathrm{kN/m^2})$	0.50
Floor fill	
Ceramic or quarry tile (19 mm) on 25-mm mortar bed $(\mathrm{kN/m^2})$	1.00
Concrete slab of thickness 0.125 m $(\mathrm{kN/m^2})$	3.00
20% Live load	0.36
Total superimposed dead load per unit area $(\mathrm{kN/m^2})$	4.86
Tributary width (m)	4
Total superimposed dead load per unit length (kN/m)	19.44
Wall dead load (kN)	D_{wall}
Total first story tributary dead load (kN)	$19.44 + D_{wall}$

The total tributary dead load (D_{total}) is defined as the sum of the tributary loads of each story, which is described by the following expression in terms of the dead load of each wall (D_{wall}):

$$D_{total} = 22.24 + 2(D_{wall})$$

where D_{total} and D_{wall} are given in kN.

Table **5-6** summarizes the values of D_{total} for the structural walls. These values will be used as the mass source of the seismic weight for performing the nonlinear dynamic analyses required for the seismic performance and fragility assessments.

Table 5-6: Total tributary dead loads for the structural walls

Wall	Mass (kg)	D_{wall} (kN)	D_{total} (kN)
RPLW	100	0.98	24.20
PFW	330	3.26	28.76
HRCW	600	5.89	34.01

5.3 Definition of the earthquake hazard

According to the mentioned in Section 2.4.2.1, the definition of the earthquake hazard for Intensity-based assessment includes a target response spectrum and suites of ground motion records to represent accurately the specific seismic hazard of interest, which are presented in this section. For the case of this research, enough information about earthquakes and the database of actual acceleration records are not available to characterize the seismic hazard of Colombia. Therefore, actual recorded ground motions from the FEMA P695 report (FEMA, 2009b) and artificial ground motions generated by the SeismoArtif software (Seismosoft, 2016) are used in order to present and to validate the procedure for the seismic performance assessment of the structural walls.

5.3.1 NSR-10 target response spectrum

The target response spectrum for the structural walls is defined by the aforementioned NSR-10 response spectrum. In this study, the construction site for the structural walls is assumed in a high seismic hazard zone with a type of soil D which is characteristic of Colombia's Andean Region. The structural systems of this research are proposed for one and two-story housing so that the risk category is assumed to be in the Group I. With the above assumptions, all of the parameters required to define the spectrum are shown in Table **5-7**. Fig. **5-4** shows the NSR-10 target response spectrum.

Table 5-7: Parameters of the target NSR-10 response spectrum for the structural walls

Parameter	Value
A_a	0.25
A_v	0.25
Type of soil	D
F_a	1.3
F_v	1.9
I	1.0

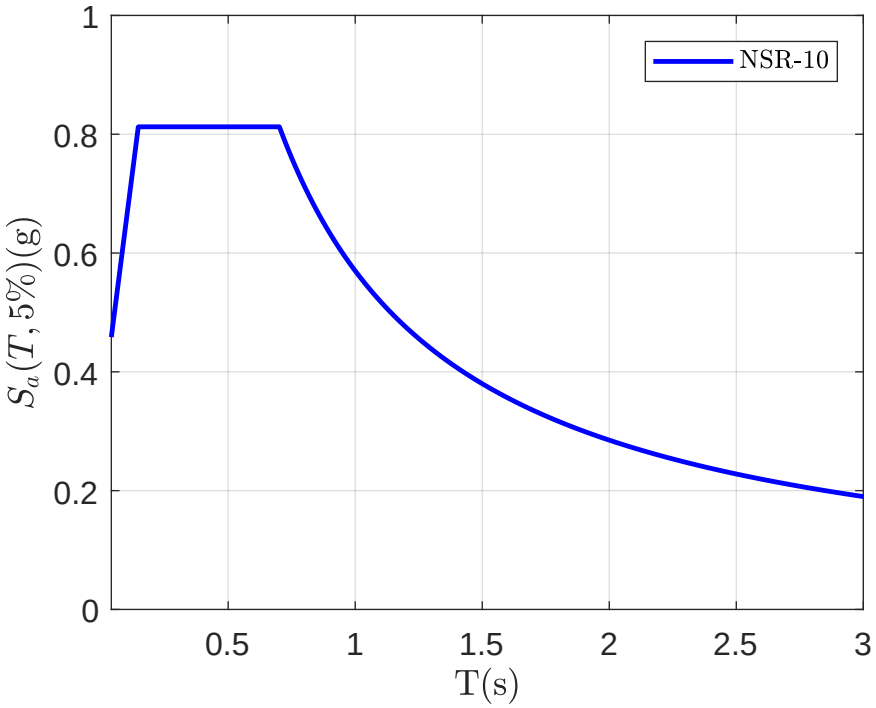

Figure 5-4: The target NSR-10 response spectrum for the structural walls

5.3.1.1 Earthquake hazard levels for the Intensity-based assessment

For the assessment of the structural walls, two earthquake hazard levels of the ASCE 41-13 standard are used: the Design Basic Earthquake (DBE) and the Maximum Considered Earthquake (MCE). Keeping in mind that the NSR-10 target response spectrum is defined as the DBE level of the earthquake hazard levels proposal in PBSD described in Table **2-5**, the MCE is taken as 1.5 times the DBE, according to the mentioned in Section 2.3.2.3.

Fig. **5-5** shows the DBE and the MCE spectra, whereas Table **5-8** presents the values of the earthquake hazard levels for the walls at their respective fundamental period T_o which were computed as the period of a SDoF system using the mass sources defined in the above section and the initial stiffnesses k_{init}.

Table 5-8: Earthquake hazard levels for the structural walls

Wall	T_o (s)	DBE (g)	MCE (g)
RPLW	0.6850	0.8125	1.2188
PFW	0.1148	0.7079	1.0618
HRCW	0.1107	0.6943	1.0414

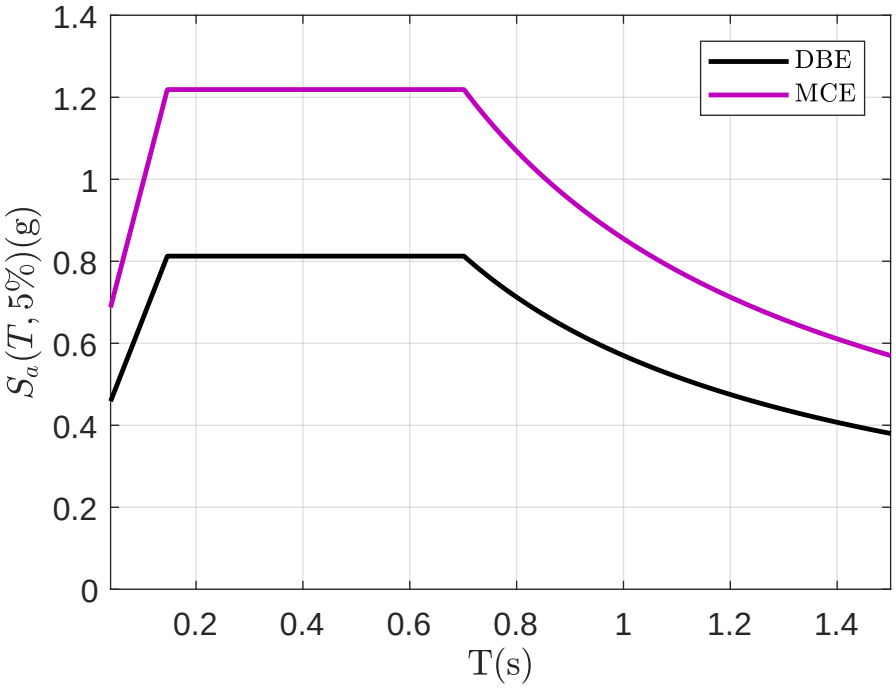

Figure 5-5: The DBE and MCE spectra for the structural walls

5.3.2 Actual recorded ground motions

The FEMA P695 report includes a set of ground motions recorded at sites located greater than or equal to 10 km from fault rupture, known as the ”Far-Field” record set, which meet some requirements, such as code consistent, very strong ground motions, large number of records, structure type independent, etc (FEMA, 2009b). Individual records were normalized by their respective PGV to remove unwarranted variability between records due to their inherent differences. The Far-Field record set includes 22 component pairs of horizontal ground motions (44 individual components) selected from the Pacific Earthquake Engineering Research Center (PEER) Next-Generation Attenuation (NGA) database (PEER, 2006) with a sufficient number of records that permit statistically describe the median value of the responses and the record-to-record variability. According to FEMA (2009b), to perform nonlinear dynamic analyses (e.g. IDA analyses) using all twenty-two pairs of records of the Far-Field record set for two-dimensional analyses, analytical models should be analyzed separately for each ground motion component in each pair, for a total of 44 analyses.

Table **5-9** summarizes key information for each record, where many of these records have been used in order to perform nonlinear dynamic analyses for PBSD and for fragility functions for different type of structural systems (see e.g. Filiatrault and Folz, 2002; Vamvatsikos et al., 2003; Vamvatsikos and Cornell, 2004; Mander et al., 2007; Asgarian et al., 2010; Li et al., 2014; Gaxiola-Camacho et al., 2017; Miano et al., 2018; Fattahi and Gholizadeh, 2018)

Table 5-9: Summary of the actual recorded ground motions

No.	Earthquake			Recording Station	Recorded motions		Normalized motions	
	M	Year	Name		PGA_{max} (g)	PGV_{max} (cm/s)	PGA_{max} (g)	PGV_{max} (cm/s)
1	6.7	1994	Northridge	Beverly Hills-Mulhol	0.52	63	0.34	41
2	6.7	1994	Northridge	Canyon Country-WLC	0.48	45	0.40	38
3	7.1	1999	Duzce, Turkey	Bolu	0.82	62	0.52	39
4	7.1	1999	Hector Mine	Hector	0.34	42	0.37	46
5	6.5	1979	Imperial Valley	Delta	0.35	33	0.46	43
6	6.5	1979	Imperial Valley	El Centro Array #11	0.38	42	0.39	43
7	6.9	1995	Kobe, Japan	Nishi-Akashi	0.51	37	0.53	39
8	6.9	1995	Kobe, Japan	Shin-Osaka	0.24	38	0.26	42
9	7.5	1999	Kocaeli, Turkey	Duzce	0.36	59	0.25	41
10	7.5	1999	Kocaeli, Turkey	Arcelik	0.22	40	0.30	54
11	7.3	1992	Landers	Yermo Fire Station	0.24	52	0.24	51
12	7.3	1992	Landers	Coolwater	0.42	42	0.48	49
13	6.9	1989	Loma Prieta	Capitola	0.53	35	0.58	38
14	6.9	1989	Loma Prieta	Gilroy Array #3	0.56	45	0.49	39
15	7.4	1990	Manjil, Iran	Abbar	0.51	54	0.40	43
16	6.5	1987	Superstition Hills	El Centro Imp. Co.	0.36	46	0.31	40
17	6.5	1987	Superstition Hills	Poe Road (temp)	0.45	36	0.53	42
18	7.0	1992	Cape Mendocino	Rio Dell Overpass	0.55	44	0.45	36
19	7.6	1999	Chi-Chi, Taiwan	CHY101	0.44	115	0.18	47
20	7.6	1999	Chi-Chi, Taiwan	TCU045	0.51	39	0.49	38
21	6.6	1971	San Fernando	LA - Hollywood Stor	0.21	19	0.44	40
22	6.5	1976	Friuli, Italy	Tolmezzo	0.35	31	0.50	44

5.3.2.1 Spectral scaling of the actual ground motions to match the target spectrum

The spectra of the actual recorded ground motions are computed and the median spectrum is determined, in order to compare it with the NSR-10 target spectrum at the fundamental period T_o for each wall. The determined median spectrum does not match the target spectrum at T_o for any structural wall, so it is necessary to scale the ground motions in such a way that the spectral matching is reached. The following figures show the unscaled and scaled spectra, with the matching between their median curves and the target spectrum at T_o for each wall.

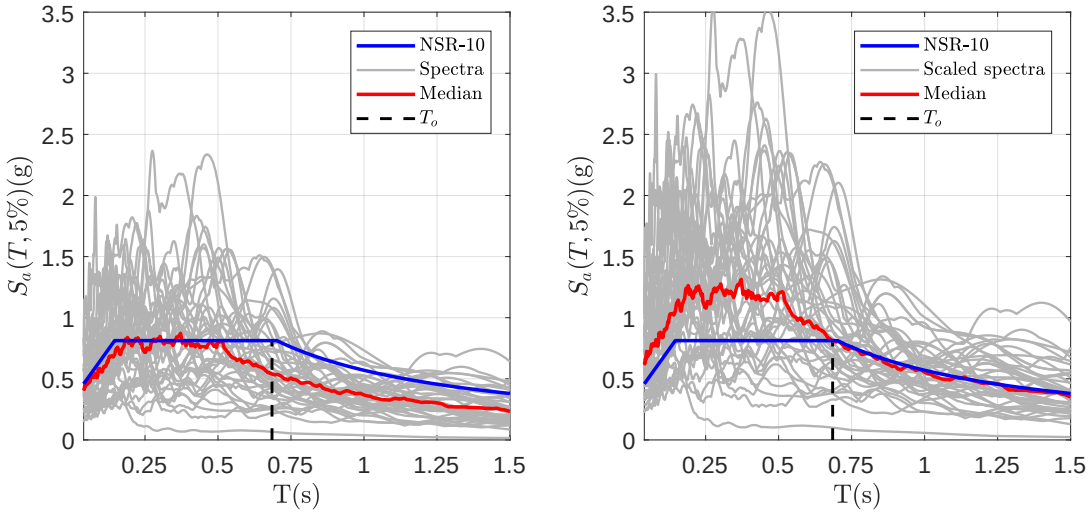

a) Unscaled spectra b) Scaled spectra

Figure 5-6: Spectral match of the actual recorded ground motions at the T_o of the RPLW

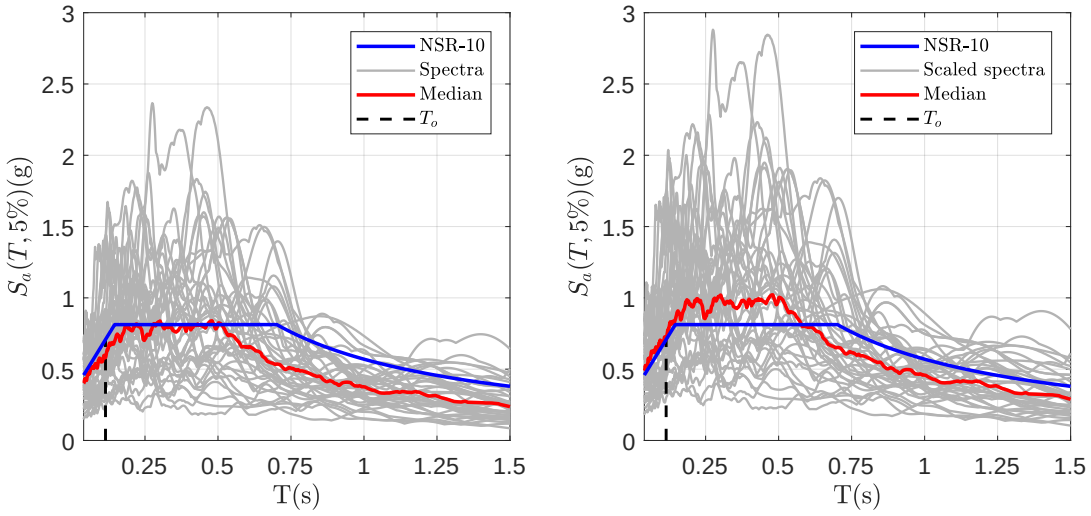

a) Unscaled spectra b) Scaled spectra

Figure 5-7: Spectral match of the actual recorded ground motions at the T_o of the PFW

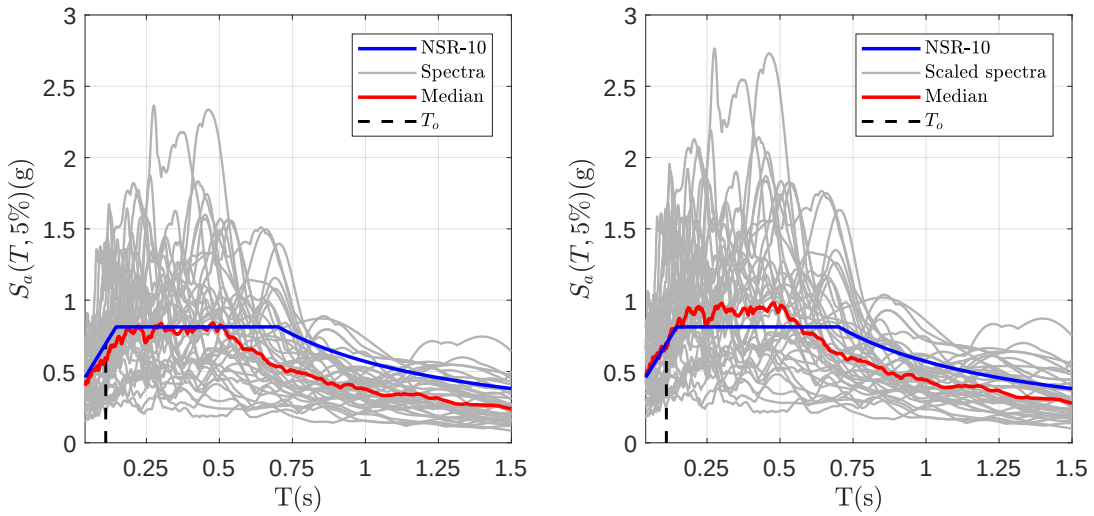

a) Unscaled spectra b) Scaled spectra

Figure 5-8: Spectral match of the actual recorded ground motions at the T_o of the HRCW

5.3.3 Artificial ground motions

The artificial ground motions are generated by the SeismoArtif software (Seismosoft, 2016) which is an application capable of generating artificial earthquake accelerograms matched to a specific target response spectrum, using different calculation methods and varied assumptions. It can thus be used to generate suites of accelerograms for nonlinear dynamic analysis of new or existing structures, in fact it has been widely employed in different researches with the same purpose (see e.g. Turk, 2013; Pozza et al., 2014; Yön, 2016; Khansefid and Bakhshi, 2017; Čada and Máca, 2017; Chomchuen and Boonyapinyo, 2017; Mase, 2018; Sagliyan and Yön, 2018).

SeismoArtif uses the well-known method proposed by Gasparini and Vanmarcke (1976) for the artificial accelerogram generation. This method is based on the fact that each periodic function can be expressed as a series of sinusoidal waves as given in the following equation:

$$X(t) = A_n \cdot sin(\omega_n t + \phi_n)$$

where A_n, ω_n and ϕ_n are the amplitude, the frequency and the phase angle of the nth sinusoidal wave, respectively. It is possible to obtain different processes with the same general aspect but with different characteristics by the definition of a vector of amplitudes and the simulation of different arrays of phase angles. These processes are stationary (or steady-state) and their characteristics are independent of time. The phase angles are generated in the interval $[0, 2\pi]$ following a uniform probability distribution, whereas the amplitudes are calculated using the Power Spectral Density Function (PSDF) by the following expression:

$$G(\omega)\Delta\omega = \frac{{A_n}^2}{2}$$

where $G(\omega)\Delta\omega$ represents the contribution to the total power of the motion from the sinusoid with frequency ω_n. If the number of sinusoidal waves considered in the motion is very large, the total power will become the area under the continuous curve $G(\omega)$.

To simulate the transient nature of the earthquakes, the steady state motions are multiplied by a deterministic envelope shape (or intensity function) $I(t)$. Fig. **5-9** illustrates the Constant, the Trapezoidal (Hou, 1968), the Exponential (Liu, 1969), and the Compound (Jennings et al., 1968) envelope shapes which are widely used in the generation and adjustment of artificial earthquakes. It is important to emphasize that the Exponential envelope shape can be limited to a maximum value equal to unity, which allows fitting the PGA of the artificial earthquake to any desired value (Vargas Alzate, 2013).

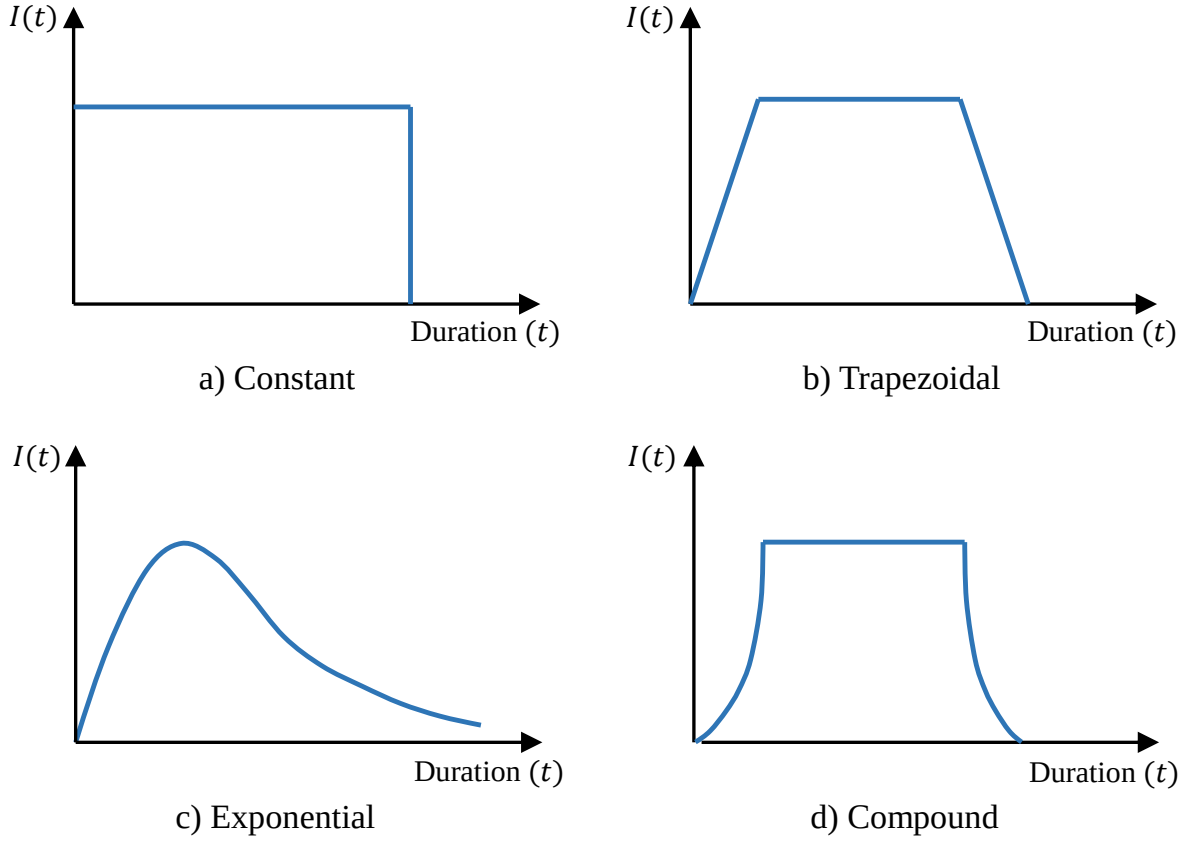

Figure 5-9: Different types of envelope shapes in the generation of artificial earthquakes. (Adapted from Seismosoft (2016))

Consequently, the artificial ground motion is then defined as:

$$Z(t) = I(t) \cdot A_n \cdot sin(\omega_n t + \phi_n)$$

The resulting ground motion is stationary in frequency content, with a peak acceleration close to the target one. This artificial accelerogram generation method is iterative so that the response spectrum of the ground motion generated is computed and then compared and matched against the selected target response spectrum (at a set of control frequencies) for each cycle. A schematic summary of this method is given in Fig. **5-10**.

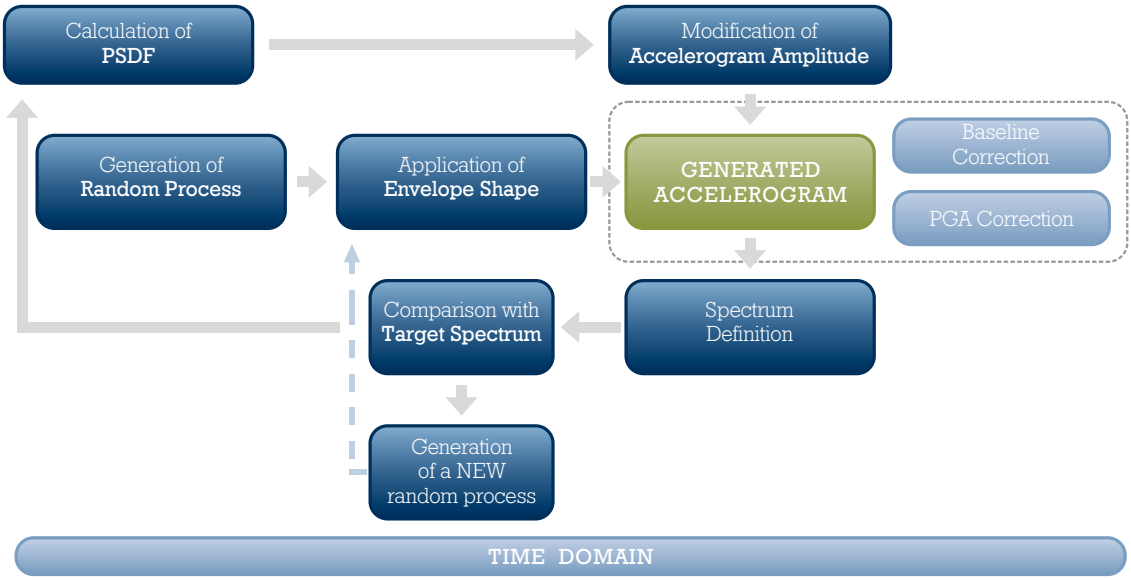

Figure 5-10: A schematic summary of the artificial accelerogram generation method of SeismoArtif (Seismosoft, 2016)

According to the recommendations of the ASCE/SEI 7-16 standard (ASCE, 2017a), a set of seven artificial ground motions are used. These ground motions are generated using the Exponential envelope shape with the parameters $\alpha = 0.1$, $\beta = 0.5$ for a duration of 30 seconds. Table **5-10** presents the information related with the PGA and the mean error of the matching of each artificial ground motion with the target response spectrum.

Table 5-10: Summary of the artificial ground motions

ID	PGA (g)	Mean error (%)
Artificial 1	0.32463	8.11
Artificial 2	0.32494	6.54
Artificial 3	0.32485	7.60
Artificial 4	0.32435	9.15
Artificial 5	0.32469	8.05
Artificial 6	0.32259	10.03
Artificial 7	0.32699	10.22

5.3.3.1 Spectral scaling of the artificial ground motions to match the target spectrum

The spectra of the artificial ground motions are computed and the median spectrum is determined, so as to compare it with the NSR-10 target spectrum at the fundamental period T_o for each wall. The determined median spectrum does not match the target spectrum at T_o for any structural wall, so it is necessary to scale the ground motions in such a way that the spectral matching is reached. The following figures show the unscaled and scaled spectra, with the matching between their median curves and the target spectrum at T_o for each wall.

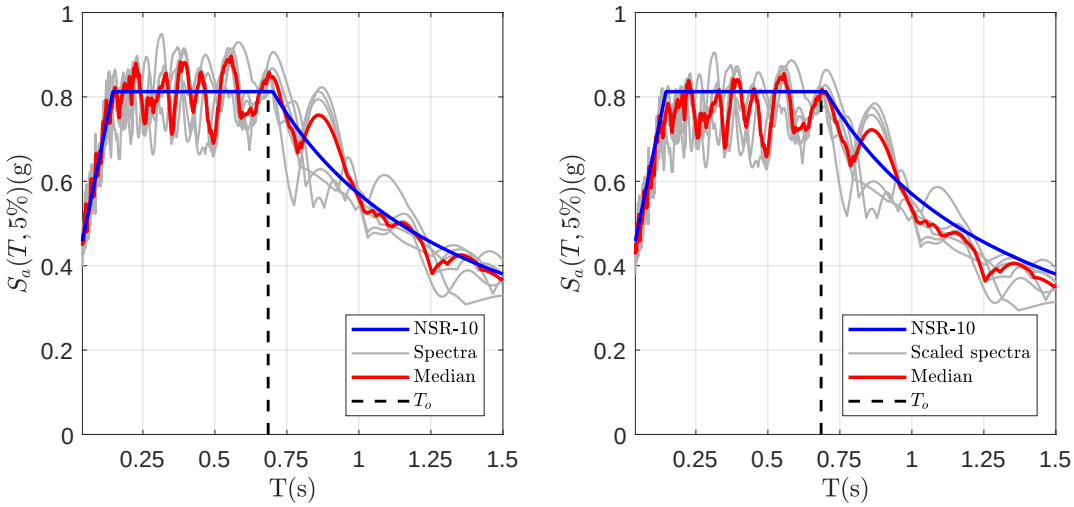

Figure 5-11: Spectral match of the artificial ground motions at the T_o of the RPLW

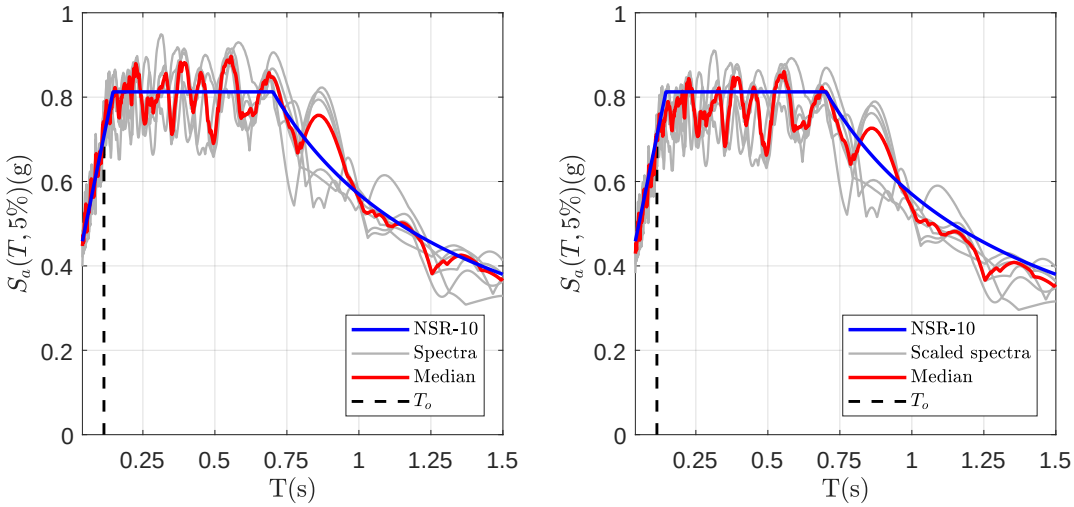

Figure 5-12: Spectral match of the artificial ground motions at the T_o of the PFW

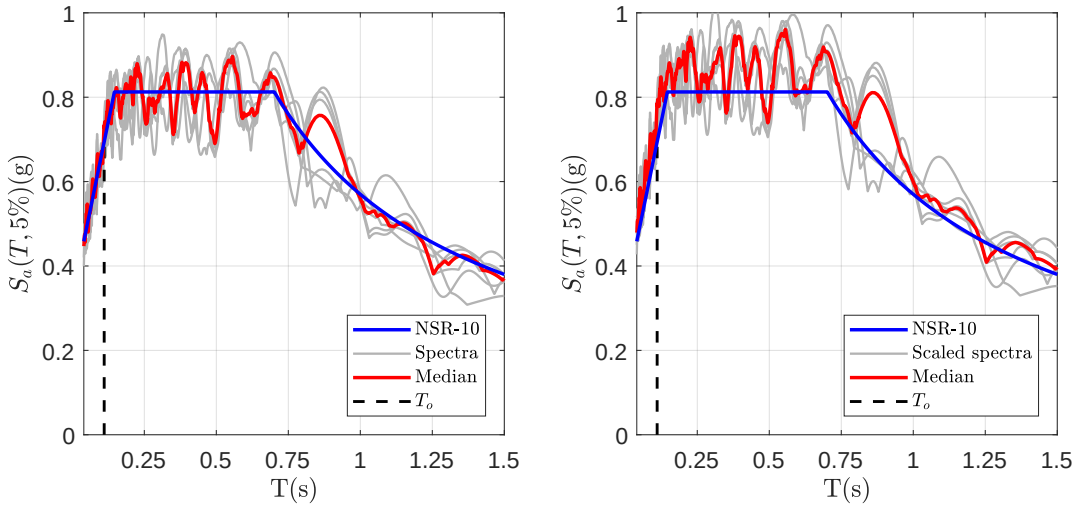

a) Unscaled spectra b) Scaled spectra

Figure 5-13: Spectral match of the artificial ground motions at the T_o of the HRCW

5.4 Seismic performance assessment of the structural walls

With the above definitions and employing the Mostaghel's multilinear hysteretic models selected in Section 4.4.4, nonlinear dynamic analyses were performed by the IDA technique explained in Section 2.4.2.2 with an IM step size of 0.1 g, using both actual recorded and artificial ground motions; the EDP and the IM used in IDA were the maximum interstory drift ratio and the 5%-damped spectral acceleration $Sa(T_o;5\%)$, respectively. Then, with the IDA results, seismic fragility functions were developed using the Baker's parametric approach presented in Section 2.4.3. The fragility parameters of the functions were estimated using an open-source Excel spreadsheet developed by Baker (2015a), which maximizes Eq. (2-8) using the Solver tool. Finally, the FEMA P695 sources of uncertainty were applied to correct the fitted fragility functions.

The results are presented in the following sections for each structural wall, which include:

- The postprocessing of IDA results, in which the IDA curves are generated by spline interpolation of the resulting points (EDP, IM) and summarized into the median, the 16th percentile and 84th percentile;
- The determination of the performance points by the intersection of the median IDA curve with the horizontal lines related to the earthquake hazard levels;
- The seismic fragility functions for the IDA results with the actual recorded and artificial ground motions for each damage limit state.

5.4.1 Recycled Plastic Lumber Wall (RPLW)

5.4.1.1 Postprocessing of IDA results

Figs. **5-14** and **5-15** show the IDA curves after the postprocessing for the actual recorded ground motions and for the artificial ones, respectively. In both cases, the IDA algorithm stopped when the collapse was reached and not due to numerical non-convergence. Regarding the computational cost, the elapsed time of the IDA procedure with the actual recorded ground motions was 0.90 hrs, whereas with the artificial ones was 0.15 hrs.

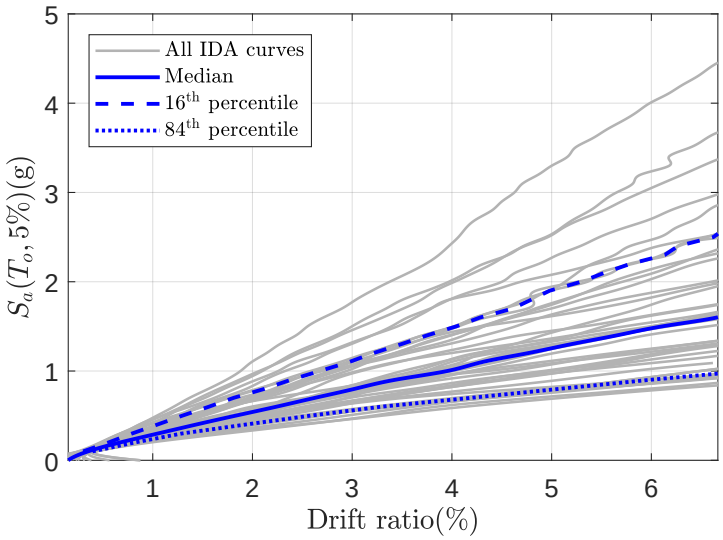

Figure 5-14: IDA curves for the RPLW using the actual recorded ground motions

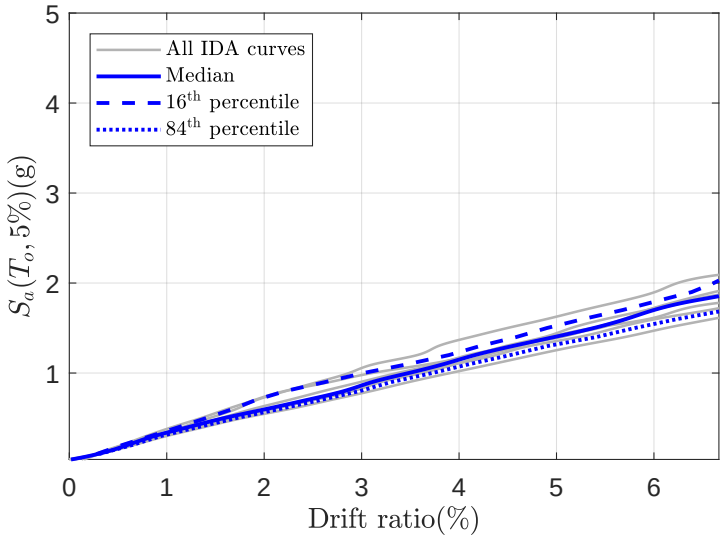

Figure 5-15: IDA curves for the RPLW using the artificial ground motions

5.4.1.2 Determination of the performance points

Figs. **5-16** and **5-17** illustrates the graphical determination of the RPLW's performance points using the actual recorded and artificial ground motions, respectively. The limit values of the SPLs are also plotted in order to determine the relationship between the SPLs and the performance points for DBE and MCE. Table **5-11** summarizes important information extracted from the figures.

Table 5-11: Performance points of the RPLW for the DBE and MCE levels

Earthquake hazard level	$Sa(T_o;5\%)$ (g)	Actual performance point			Artificial performance point		
		d_p (%)	d_p (mm)	SPL	d_p (%)	d_p (mm)	SPL
DBE	0.8125	3.069	73.66	LS	2.860	68.64	LS
MCE	1.2188	4.851	116.42	CP	4.230	101.52	CP

The results for DBE differ in a 7% and for MCE in a 13%, which is acceptable and validates the comparison. The performance points for DBE and MCE fall within the LS and CP ranges, respectively. This fact evidences that the RPLW meets exactly the basic safety performance objective established in the design philosophy of the NSR-10 building code.

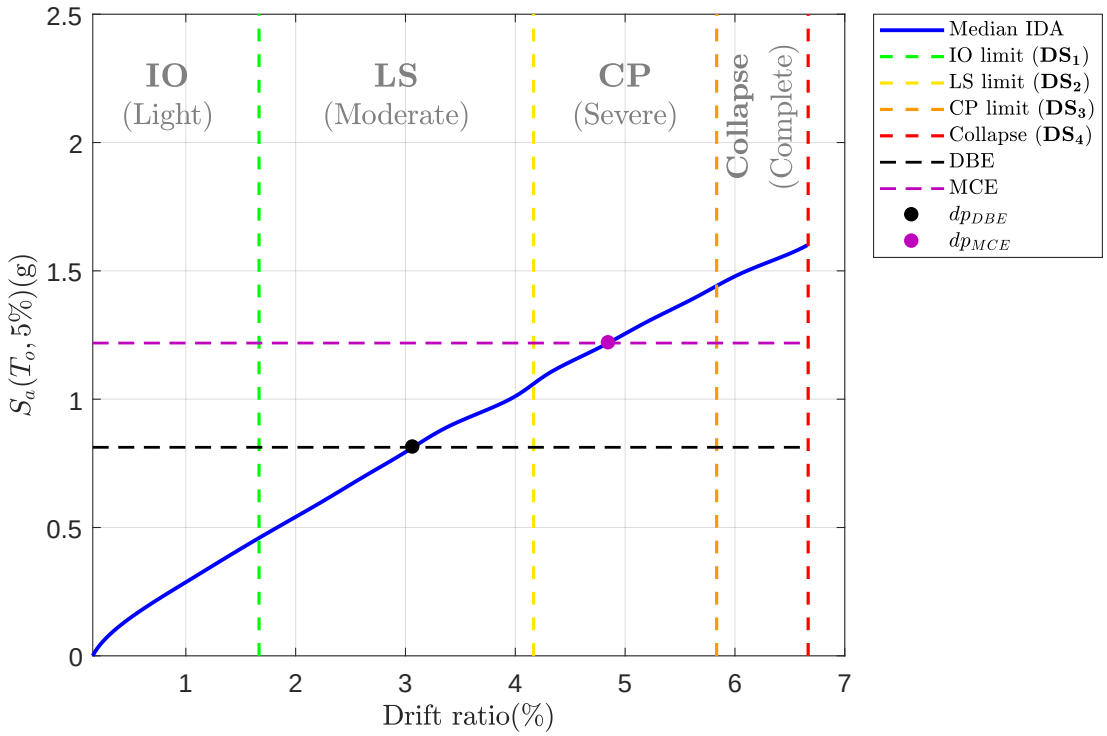

Figure 5-16: Determination of the RPLW's performance points for DBE and MCE using the median IDA curve from the IDA results with the actual recorded ground motions

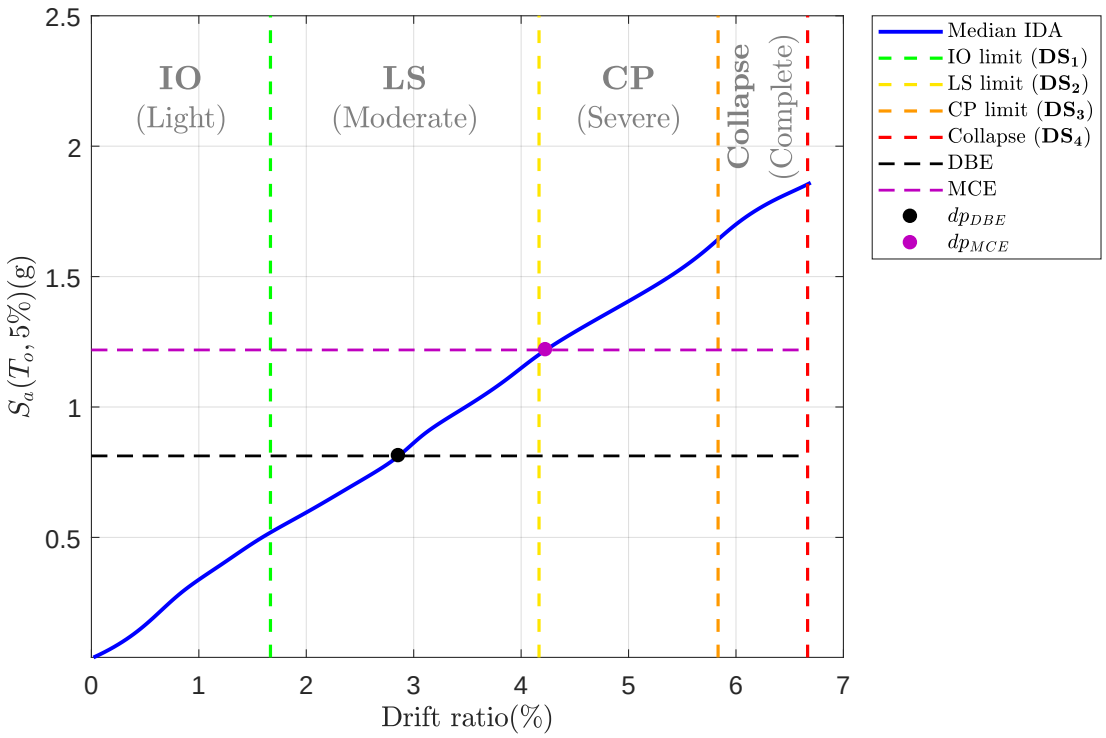

Figure 5-17: Determination of the RPLW's performance points for DBE and MCE using the median IDA curve from the IDA results with the artificial ground motions

5.4.1.3 Seismic fragility functions

The fragility functions of the RPLW were determined as lognormal CDFs (Eq. (2-7)) for the damage states defined in Table **4-4**, which are related to the structural performance levels by Table **5-1**. The estimation of the fragility parameters for these functions using the Excel spreadsheet tool (Baker, 2015a) was a simple process in which only the observed data were provided. Table **5-12** presents the parameters for the lognormal fragility functions fitted to the IDA results with the actual recorded and artificial ground motions.

Table 5-12: Estimated parameters of the lognormal fragility functions fitted to the IDA results with the actual recorded and artificial ground motions for the RPLW damage states

Ground motions	Fragility parameters	**DS$_1$** (Light)	**DS$_2$** (Moderate)	**DS$_3$** (Severe)	**DS$_4$** (Complete)
Actual recorded	θ	0.4814	1.0712	1.4261	1.5965
	β	0.25806	0.37549	0.42423	0.44278
Artificial	θ	0.5329	1.2181	1.6196	1.8331
	β	0.10317	0.09068	0.06848	0.06487

With the above parameters, the fragility curves are built and subsequently drawn together with the observed fractions of damages. Fig. **5-18** and Fig. **5-19** show both representations for the IDA results with the actual recorded and artificial ground motions, respectively. As can be seen, the fragility curves fitted in a good way the observed points, which validate the parametric approach and the software tool used. In spite of that, there are significant differences between the actual and artificial fragility curves. For instance, the β values for the artificial curves are much smaller than the actual ones, which suggests that there is not enough variability in the results. Due to that, it is necessary to correct the fragility functions to obtain more reliable results.

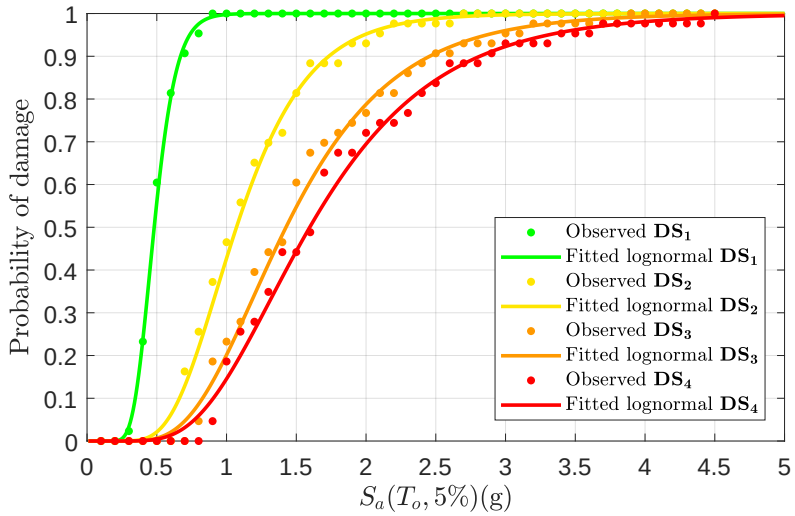

Figure 5-18: Observed fractions of damages and the lognormal fragility curves fitted to the IDA results with the actual recorded ground motions for the RPLW

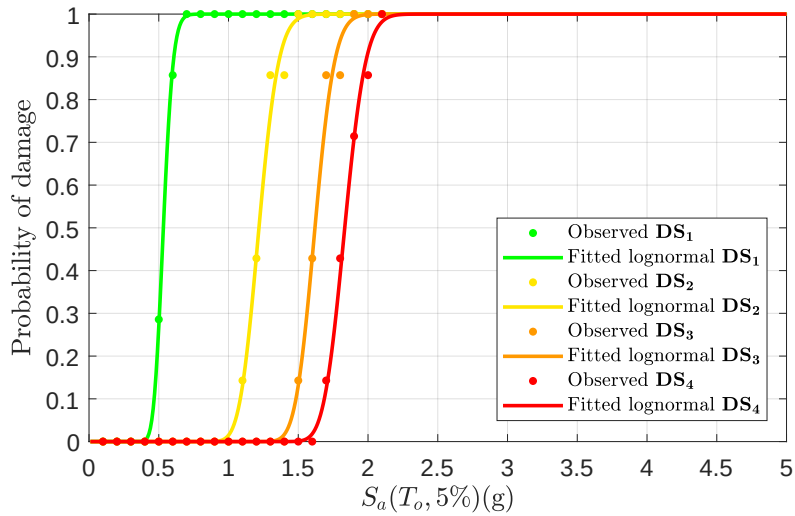

Figure 5-19: Observed fractions of damages and the lognormal fragility curves fitted to the IDA results with the artificial ground motions for the RPLW

Correction of the fragility functions

The values of the fragility parameter β are corrected following the FEMA P695 methodology presented in Section 2.4.3.3. This correction process is applied both the actual and the artificial fragility curves to consider the total system damage uncertainty. The definition and the selection of the uncertainty sources and their corresponding values for the RPLW are presented as follows:

- Design Requirements (β_{DR}): The structural design for the RPLW was developed to afford reasonable safeguards against unexpected failure modes and to establish a suggested hierarchy of component yielding and failure. However, the NSR-10 building code does not have specific criteria or requirements for structural systems made of RPL. In addition, there are not enough evidence in the literature to validate and to compare the proposal structural design. According to these reasons, $\beta_{DR} = 0.35$ $(Fair)$.
- Test Data (β_{TD}): Given that the cyclic loading tests were performed according to the ASTM Standard E2126-11 (2011), all measuring devices were properly calibrated, and some experimental issues were addressed adequately, the experimental data are reliable. Additionally, the cyclic loading tests were led until severe strength deterioration and damage, which afforded a complete understanding of the hysteretic behavior of the wall as well as of the possible failure mechanisms. On the other hand, individual tests of connections, assemblies, and components were not performed. However, the experimental behavior of these elements is implicitly contained in the hysteretic results. Hence, $\beta_{TD} = 0.20$ $(Good)$.
- Modeling (β_{MDL}): All the nonlinear behaviors, including the yielding, pinching, stiffness and strength degradation were simulated by the Mostaghel's six-lines hysteretic model. In fact, it can conclude that this hysteretic model was sufficiently suitable and accurate to predict the structural response until collapse without convergence issues. On the other hand, the structural model used in the analysis was assumed with some simplifications such as SDoF systems, 2D-models, etc. Therefore, $\beta_{MDL} = 0.20$ $(Good)$.

The corrected parameters β_{Tot} of the fragility functions for the RPLW are presented in Table **5-13**. As shown in Fig. **5-20**, the correction methodology improved significantly the fragility curves.

Table 5-13: Corrected parameters of the lognormal fragility functions fitted to the IDA results with the actual recorded and artificial ground motions for the RPLW damage states

Ground motions	Fragility parameters	**DS_1** (Light)	**DS_2** (Moderate)	**DS_3** (Severe)	**DS_4** (Complete)
Actual recorded	θ	0.4814	1.0712	1.4261	1.5965
	β_{Tot}	0.51874	0.58609	0.61844	0.63131
Artificial	θ	0.5329	1.2181	1.6196	1.8331
	β_{Tot}	0.46168	0.45905	0.45518	0.45465

The corrected fragility curves fitted to the actual and artificial IDA results are similar. This fact proves the use of both sets of earthquakes in the seismic performance assessment of the RPLW.

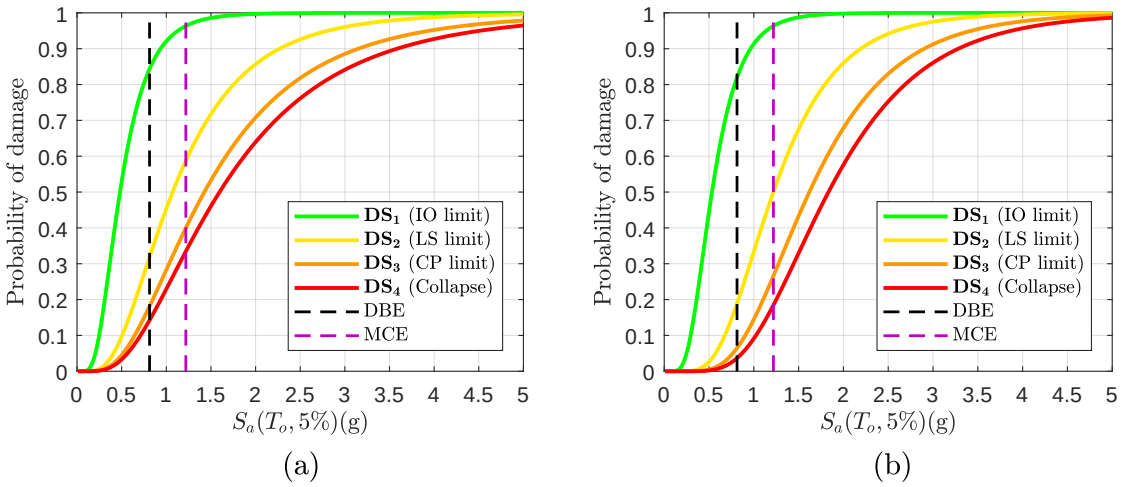

Figure 5-20: Corrected fragility curves for the RPLW: (a) Fitted to the IDA results with actual recorded ground motions; (b) Fitted to the IDA results with artificial ground motions

At the DBE level, the probability of falling into the IO performance level is 68% using the actual recorded ground motions and 80% using the artificial ones, whereas the probability of collapse is 14% and 3%, respectively; for the case of MCE level, the probability of falling into the IO performance level is 42% using the actual recorded ground motions and 50% using the artificial ones, whereas the probability of collapse is 33% and 18%, respectively. These results show the satisfactory seismic performance of the RPLW for one and two-story housing subjected to those earthquake hazard levels. Fig. **5-21** shows the cumulative probability of damage of the RPLW.

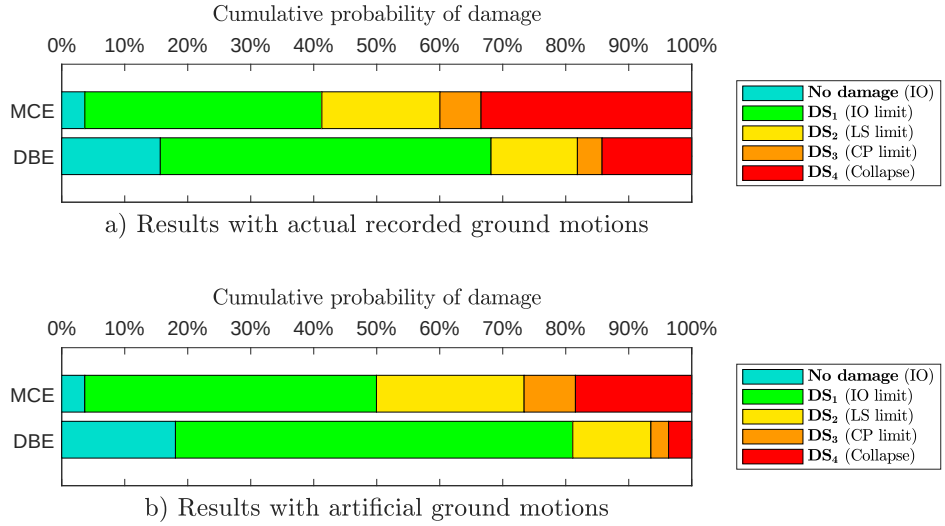

Figure 5-21: Cumulative probability of damage of the RPLW for each earthquake hazard level

5.4.2 Precast Ferrocement Wall (PFW)

5.4.2.1 Postprocessing of IDA results

The IDA curves after the postprocessing for the actual recorded ground motions and for the artificial ones are shown in Figs. **5-22** and **5-23**, respectively. In both cases, the IDA algorithm stopped when the collapse was reached and not due to numerical non-convergence. In regard to the computational cost, the elapsed time of the IDA procedure with the actual recorded ground motions was 5.15 hrs, whereas with the artificial ones was 0.9 hrs.

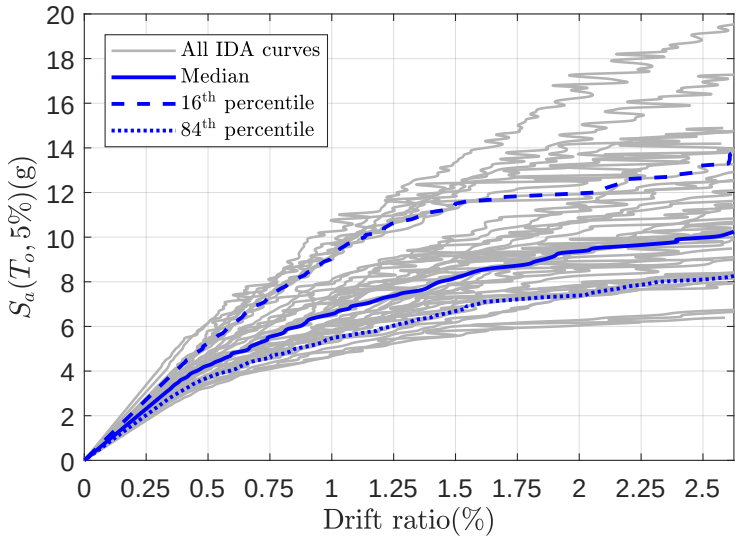

Figure 5-22: IDA curves for the PFW using the actual recorded ground motions

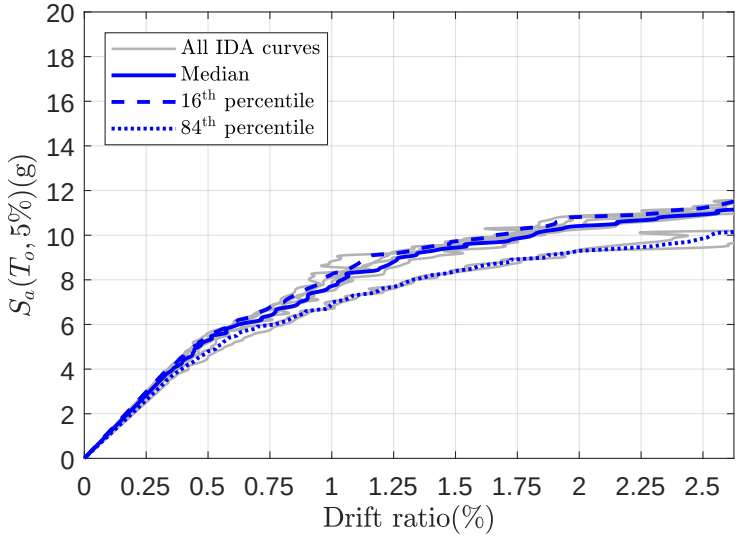

Figure 5-23: IDA curves for the PFW using the artificial ground motions

5.4.2.2 Determination of the performance points

The graphical determination of the PFW's performance points using the actual recorded and artificial ground motions is illustrated in Figs. **5-24** and **5-25**, respectively. The limit values of the SPLs are plotted in order to determine the relationship between the SPLs and the performance points for DBE and MCE. Table **5-14** summarizes important information extracted from the figures.

Table 5-14: Performance points of the PFW for the DBE and MCE levels

Earthquake hazard level	$Sa(T_o;5\%)$ (g)	Actual performance point			Artificial performance point		
		d_p (%)	d_p (mm)	SPL	d_p (%)	d_p (mm)	SPL
DBE	0.7079	0.0765	1.84	IO	0.0620	1.49	IO
MCE	1.0618	0.1150	2.76	IO	0.0932	2.24	IO

The results for DBE and MCE differ in a 19%, which can be considered as acceptable. The performance points for DBE and MCE fall within the IO range, which evidences the very good seismic performance of the PFW under the seismic conditions defined by the NSR-10 building code.

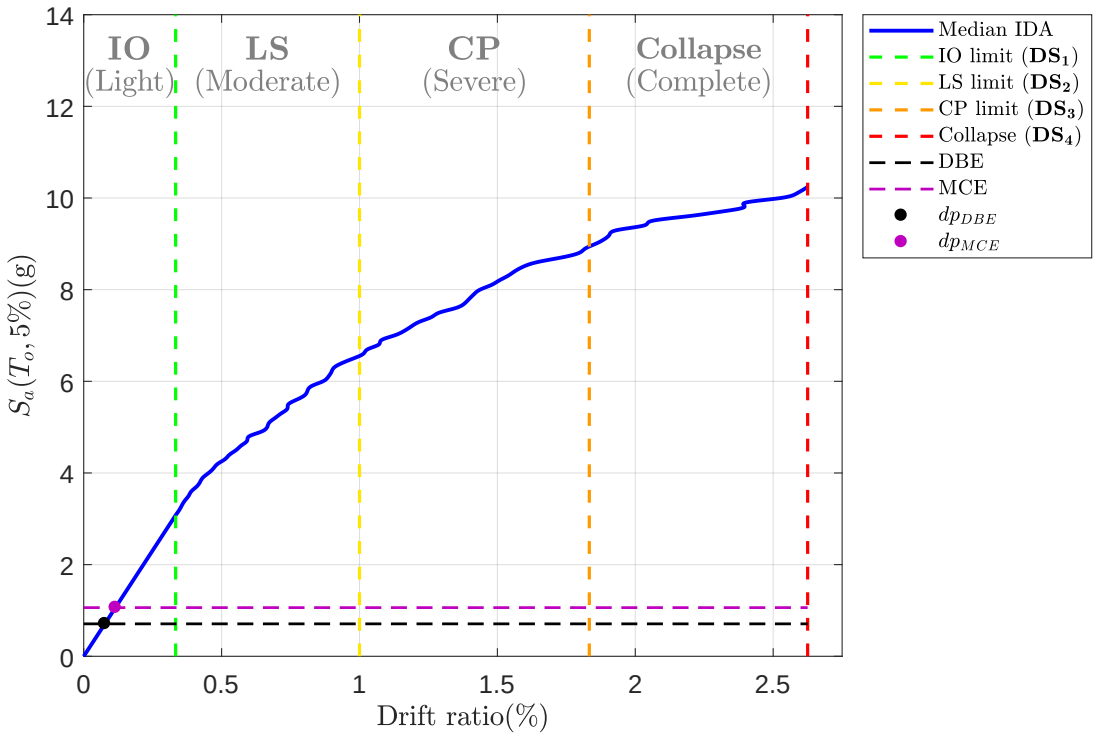

Figure 5-24: Determination of the PFW's performance points for DBE and MCE using the median IDA curve from the IDA results with the actual recorded ground motions

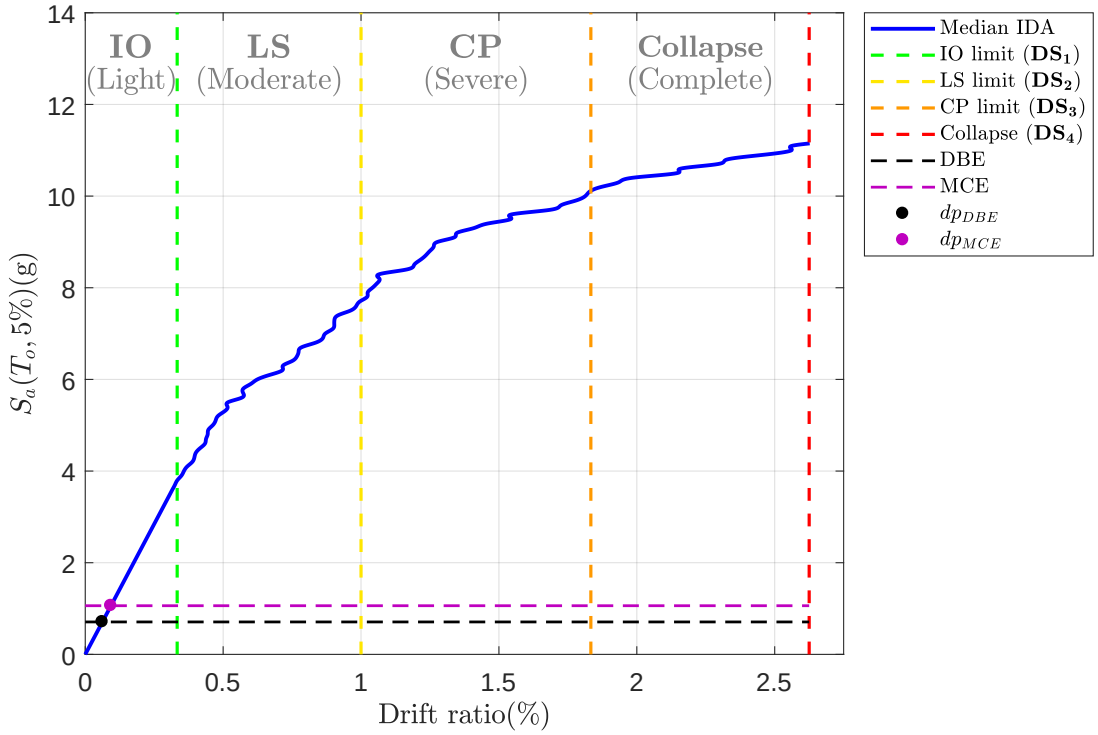

Figure 5-25: Determination of the PFW's performance points for DBE and MCE using the median IDA curve from the IDA results with the artificial ground motions

5.4.2.3 Seismic fragility functions

The fragility functions of the PFW were determined as lognormal CDFs (Eq. (2-7)) for the damage states defined in Table **4-5**, which are related to the structural performance levels by Table **5-2**. The estimation of the fragility parameters for these functions using the Excel spreadsheet tool (Baker, 2015a) was a simple process in which only the observed data were provided. The parameters for the lognormal fragility functions fitted to the IDA results with the actual recorded and artificial ground motions are summarized in Table **5-15**

Table 5-15: Estimated parameters of the lognormal fragility functions fitted to the IDA results with the actual recorded and artificial ground motions for the PFW damage states

Ground motions	Fragility parameters	**DS$_1$** (Light)	**DS$_2$** (Moderate)	**DS$_3$** (Severe)	**DS$_4$** (Complete)
Actual recorded	θ	3.1042	6.7076	9.1045	10.277
	β	0.14312	0.21314	0.23478	0.26395
Artificial	θ	3.7108	7.655	9.8426	10.996
	β	0.05368	0.07837	0.05709	0.07806

The fragility curves and the observed fractions of damages are shown in Fig. **5-26** and Fig. **5-27** for the IDA results with the actual recorded and artificial ground motions, respectively. It is evident that the fragility curves matched in a good agreement the observed points, which validates the parametric approach and the software tool used. However, there are significant differences between the actual and artificial fragility curves. As in the RPLW, the β values for the artificial curves are much smaller than the actual ones, which suggests that it is necessary to correct the fragility functions to take into account uncertainty sources, in order to obtain more reliable results.

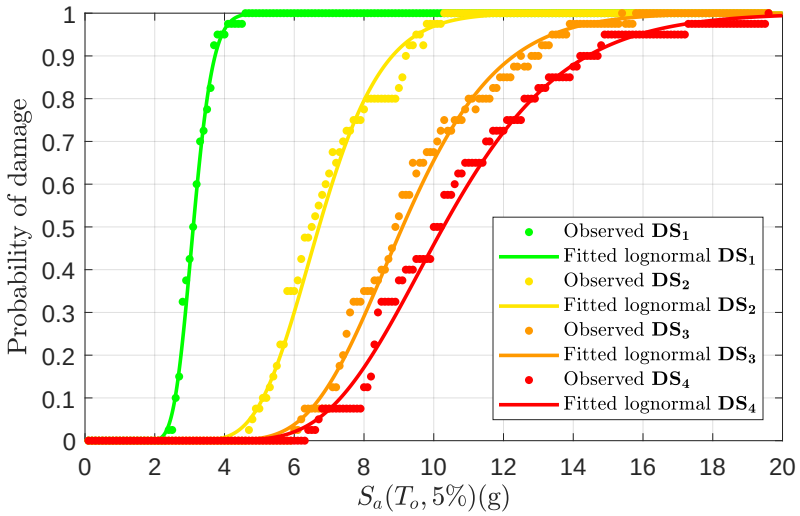

Figure 5-26: Observed fractions of damages and the lognormal fragility curves fitted to the IDA results with the actual recorded ground motions for the PFW

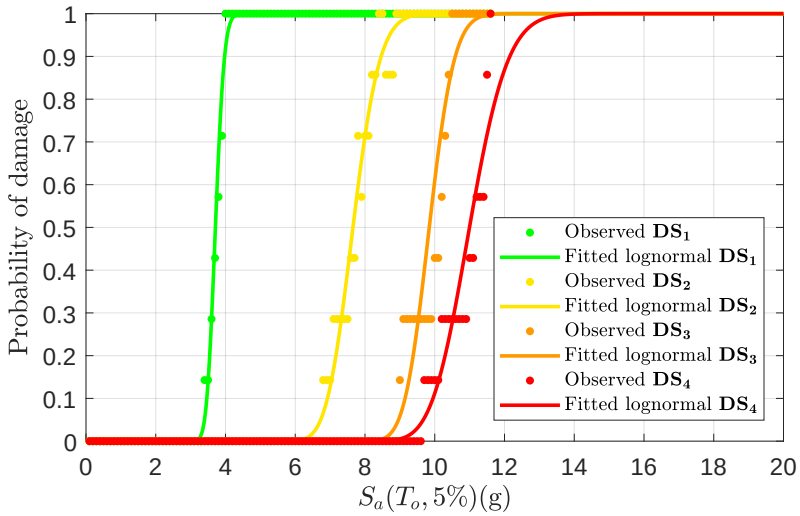

Figure 5-27: Observed fractions of damages and the lognormal fragility curves fitted to the IDA results with the artificial ground motions for the PFW

Correction of the fragility functions

Following the FEMA P695 correction methodology presented in Section 2.4.3.3, the values of the fragility parameter β are corrected both for the actual and the artificial fragility curves. The definitions of the sources of uncertainty for the PFW are presented as follows:

- Design Requirements (β_{DR}): The structural design followed the requirements of the ACI and NSR-10 building codes in which the design equations and criteria have been widely vetted and validated by experimental evidence, therefore a high level of confidence is considered. On the other hand, given that the PFW is a new structural system, there is not a specific set of design requirements for its structural design. However, this structural design was developed to afford reasonable safeguards against unexpected failure modes and to establish a suggested hierarchy of component yielding and failure. Given the above, $\beta_{DR} = 0.20$ $(Good)$.
- Test Data (β_{TD}): The information obtained from the experimental campaign is reliable because of the cyclic loading tests were carried out following the criteria of the ASTM Standard E2126-11 (2011), all measuring devices were properly calibrated, and several general testing issues were addressed adequately. Additionally, the cyclic loading tests were led until severe strength deterioration and damage, which afforded a complete understanding of the hysteretic behavior of the wall as well as of the possible failure modes. On the other hand, the tests of connections, assemblies, and components were not carried out individually. However, the experimental information of these elements is implicitly contained in the hysteretic results. Therefore, $\beta_{TD} = 0.20$ $(Good)$.
- Modeling (β_{MDL}): The Mostaghel's seven-lines hysteretic model simulated all the nonlinear behaviors, including the yielding, pinching, stiffness and strength degradation. This hysteretic model was sufficiently suitable and accurate to predict the structural response until collapse without convergence issues. On the other hand, the structural model used in the analysis was assumed with some simplifications such as SDoF systems, 2D-models, etc. According to these reasons, $\beta_{MDL} = 0.20$ $(Good)$.

The corrected standard deviation β_{Tot} of the fragility functions for the PFW is shown in Table **5-16**.

Table 5-16: Corrected parameters of the lognormal fragility functions fitted to the IDA results with the actual recorded and artificial ground motions for the PFW damage states

Ground motions	Fragility parameters	**DS$_1$** (Light)	**DS$_2$** (Moderate)	**DS$_3$** (Severe)	**DS$_4$** (Complete)
Actual recorded	θ	3.1042	6.7076	9.1045	10.277
	β_{Tot}	0.37481	0.40673	0.41847	0.43551
Artificial	θ	3.7108	7.655	9.8426	10.996
	β_{Tot}	0.35055	0.35516	0.35108	0.35510

The corrected fragility curves fitted to the actual and artificial IDA results are shown in Fig. **5-28**, which have a better similarity that validates the use of both sets of earthquakes for the seismic performance assessment of the PFW. Furthermore, the corrected probability distribution function of any **DS** has a better variability and the results are more reliable.

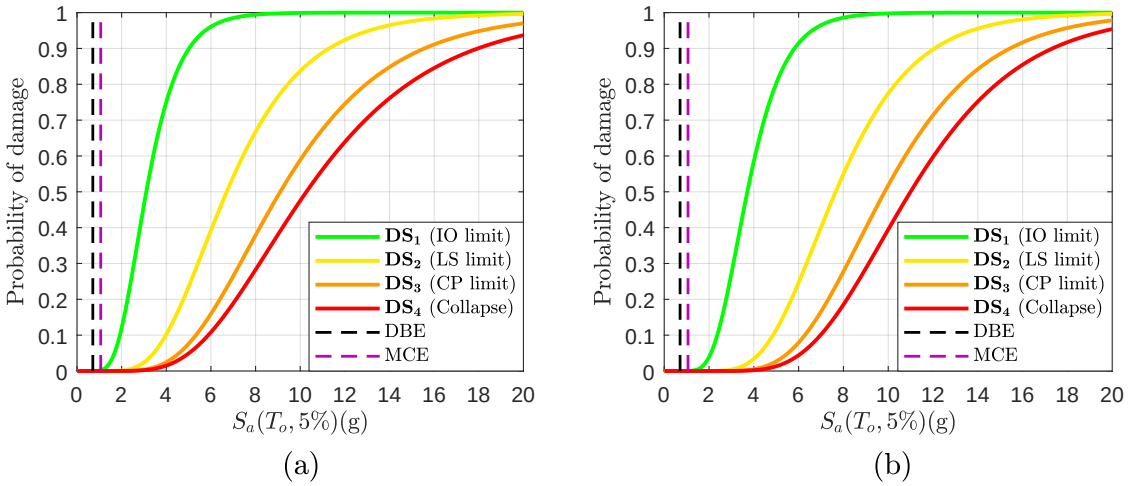

Figure 5-28: Corrected fragility curves for the PFW: (a) Fitted to the IDA results with actual recorded ground motions; (b) Fitted to the IDA results with artificial ground motions

As can be seen in Fig. **5-29**, there is a 0% probability of incurring any **DS** for both earthquake hazard levels. In other words, the probability of no structural damage is 100%. As the **DS**s and the SPLs were previously related, it can be concluded that the PFW has a 100% probability of falling into the IO performance level, which demonstrates the very good seismic performance of this structural wall for one and two-story housing subjected to the DBE and the MCE levels.

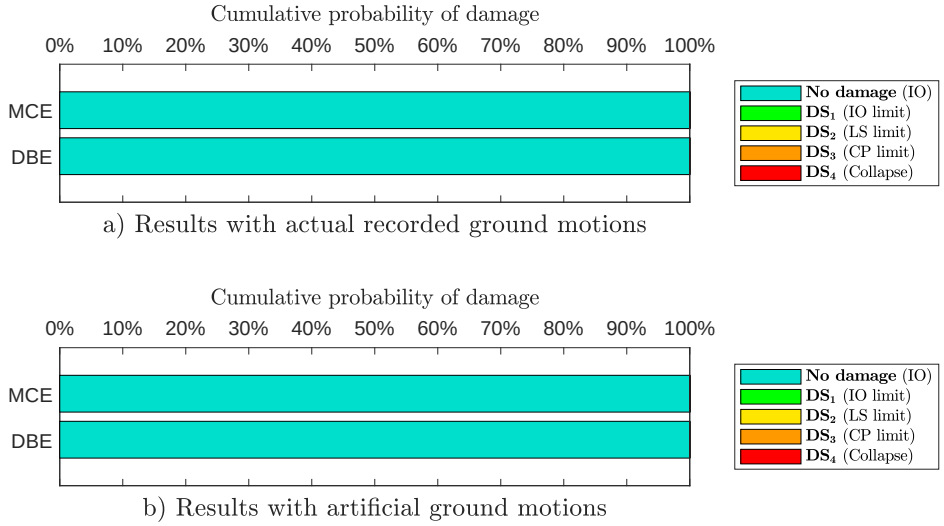

Figure 5-29: Cumulative probability of damage of the PFW for each earthquake hazard level

5.4.3 Hollow Reinforced Concrete Wall (HRCW)

5.4.3.1 Postprocessing of IDA results

Figs. **5-30** and **5-31** show the IDA curves after the postprocessing for the actual recorded ground motions and for the artificial ones, respectively. In both cases, the IDA algorithm stopped when the collapse was reached and not due to numerical non-convergence. Regarding the computational cost, the elapsed time of the IDA procedure with the actual recorded ground motions was 3.4 hrs, whereas with the artificial ones was 0.35 hrs.

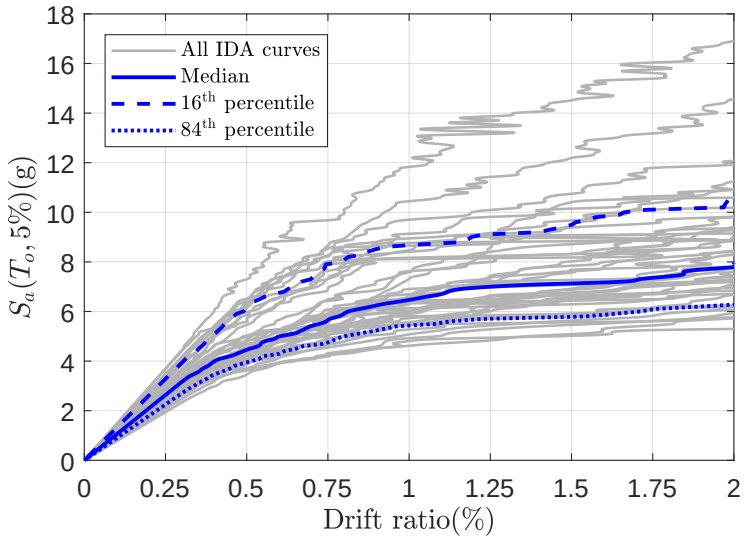

Figure 5-30: IDA curves for the HRCW using the actual recorded ground motions

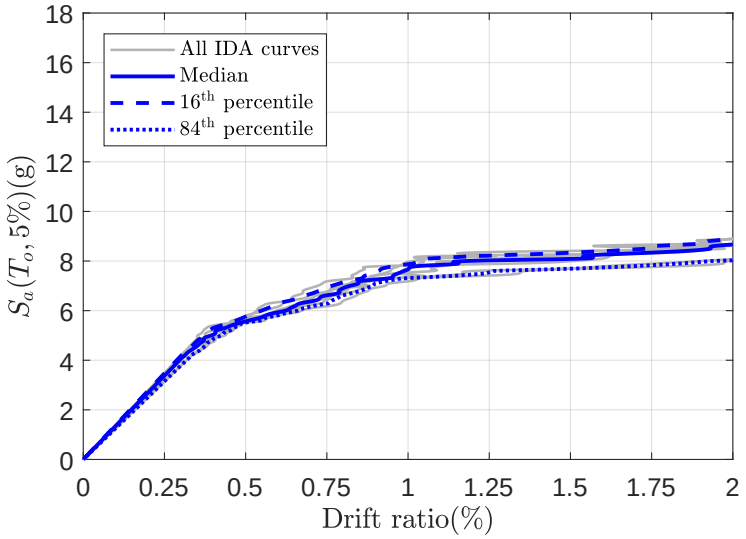

Figure 5-31: IDA curves for the HRCW using the artificial ground motions

5.4.3.2 Determination of the performance points

Figs. **5-32** and **5-33** shows the graphical determination of the HRCW's performance points using the actual and artificial ground motions, respectively. Additionally, the limit values of the SPLs are plotted in order to determine the relationship between the SPLs and the performance points for DBE and MCE. Important information extracted from the figures is presented in Table **5-17**.

Table 5-17: Performance points of the HRCW for the DBE and MCE levels

Earthquake	$Sa(T_o;5\%)$	Actual performance point			Artificial performance point		
hazard level	(g)	d_p (%)	d_p (mm)	SPL	d_p (%)	d_p (mm)	SPL
DBE	0.6943	0.0659	1.581	IO	0.0515	1.236	IO
MCE	1.0414	0.0987	2.369	IO	0.0771	1.850	IO

The results for DBE and MCE differ in a 22% between the IDA results with actual and artificial ground motions. In spite of that, the performance points for DBE and MCE fall within the IO range, which demonstrates the very good seismic performance of the HRCW under seismic loads.

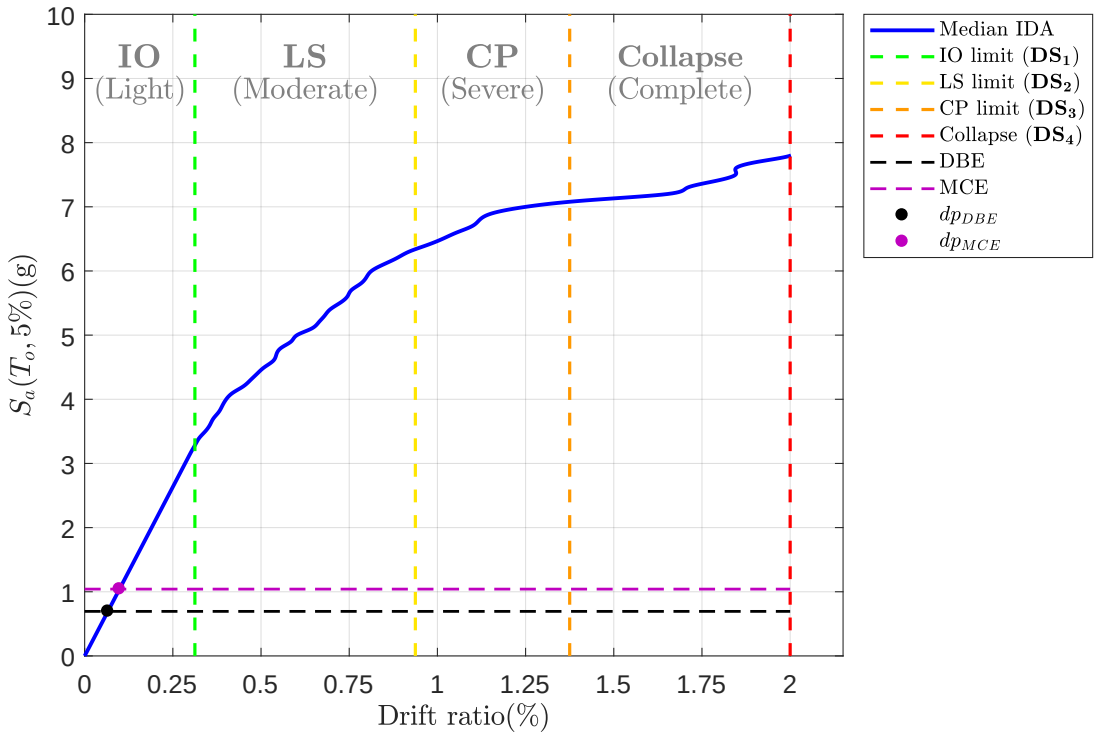

Figure 5-32: Determination of the HRCW's performance points for DBE and MCE using the median IDA curve from the IDA results with the actual recorded ground motions

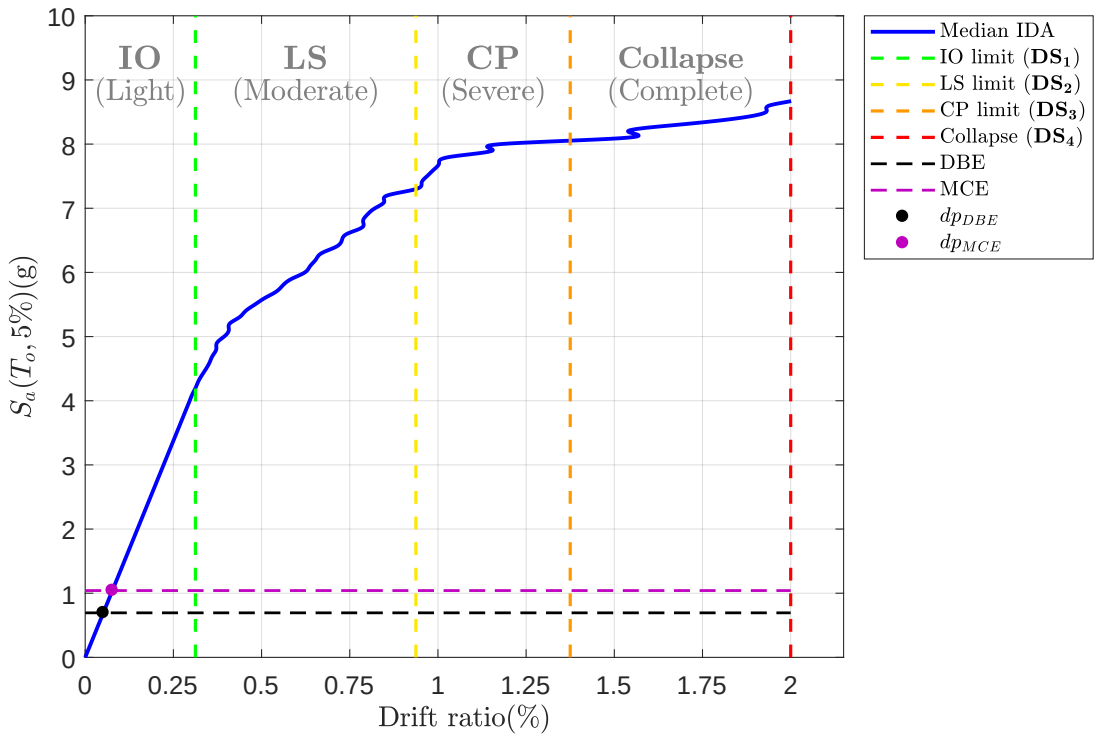

Figure 5-33: Determination of the HRCW's performance points for DBE and MCE using the median IDA curve from the IDA results with the artificial ground motions

5.4.3.3 Seismic fragility functions

The fragility functions of the HRCW were determined as lognormal CDFs (Eq. (2-7)) for the damage states defined in Table **4-6**, which are related to the structural performance levels by Table **5-3**. The estimation of the fragility parameters for these functions using the Excel spreadsheet tool (Baker, 2015a) was a simple process in which only the observed data were provided. Table **5-18** presents the parameters for the lognormal fragility functions fitted to the IDA results with the actual recorded and artificial ground motions.

Table 5-18: Estimated parameters of the lognormal fragility functions fitted to the IDA results with the actual recorded and artificial ground motions for the HRCW damage states

Ground motions	Fragility parameters	**DS$_1$** (Light)	**DS$_2$** (Moderate)	**DS$_3$** (Severe)	**DS$_4$** (Complete)
Actual recorded	θ	3.3348	6.5995	7.3403	8.1639
	β	0.16386	0.22858	0.24379	0.27318
Artificial	θ	4.1597	7.3807	7.9996	8.5542
	β	0.03536	0.03220	0.03072	0.04176

The fragility curves are built using the above parameters. Subsequently, they are drawn together with the observed fractions of damages. Fig. **5-34** and Fig. **5-35** show both representations for the IDA results with the actual recorded and artificial ground motions, respectively. As can be seen, the fragility curves fitted in a good way the observed points, which validate the parametric approach and the software tool used. However, there are significant differences between the actual and artificial fragility curves. In fact, the β values for the artificial curves are much smaller than the actual ones, which suggests that there is not enough variability in the results. Therefore, it is necessary to correct the fragility functions to obtain more reliable results.

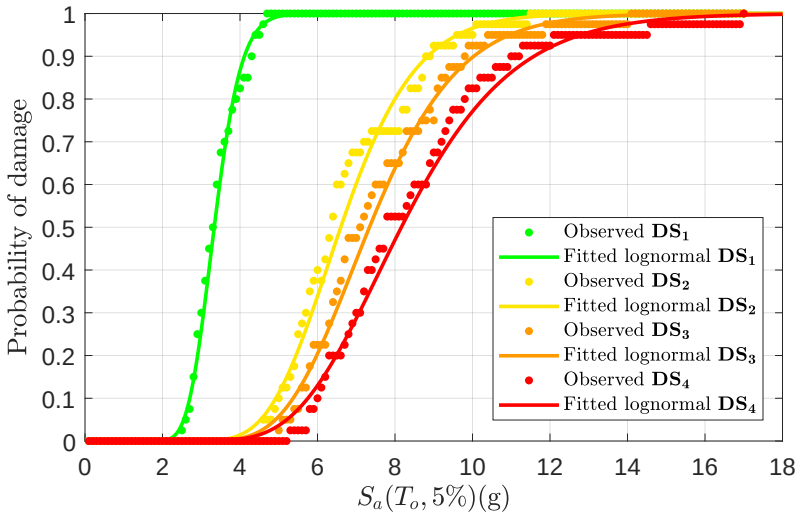

Figure 5-34: Observed fractions of damages and the lognormal fragility curves fitted to the IDA results with the actual recorded ground motions for the HRCW

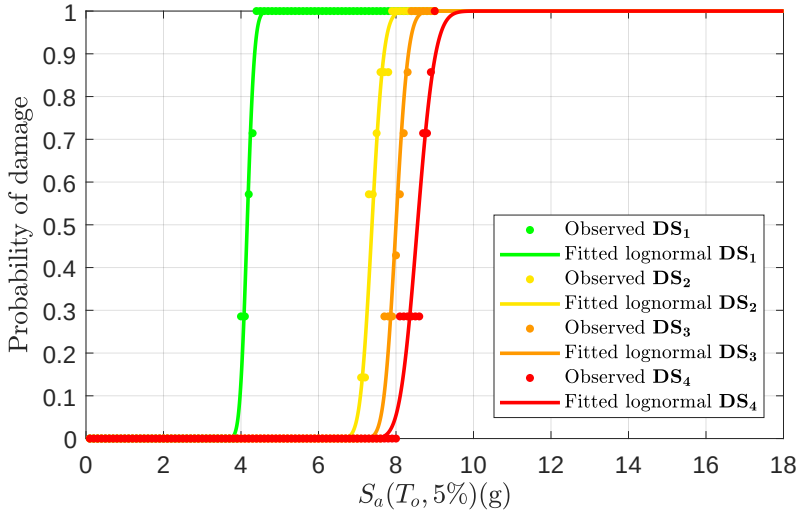

Figure 5-35: Observed fractions of damages and the lognormal fragility curves fitted to the IDA results with the artificial ground motions for the HRCW

Correction of the fragility functions

The values of the fragility parameter β are corrected following the FEMA P695 methodology presented in Section 2.4.3.3. This correction process is applied both the actual and the artificial fragility curves in order to consider the total system damage uncertainty. The definition and the selection of the uncertainty sources and their values for the HRCW are presented as follows:

- Design Requirements (β_{DR}): The structural design has a high level of confidence because of it followed the criteria and design equations of the ACI and NSR-10 building codes which have been widely vetted and validated by experimental evidence. The specific set of design requirements of RC walls were extended and applied to the HRCW structural system. Additionally, the structural design was developed to afford reasonable safeguards against unexpected failure modes and to establish a suggested hierarchy of component yielding and failure. Given the above, $\beta_{DR} = 0.10$ $(Superior)$.
- Test Data (β_{TD}): The experimental results are reliable due to the cyclic loading tests were performed according to the ASTM Standard E2126-11 (2011), all measuring devices were properly calibrated, and several experimental issues were addressed adequately. Additionally, the cyclic loading tests were led until severe strength deterioration and damage, which afforded a complete understanding of the hysteretic behavior of the wall as well as of the possible failure modes. In spite that the tests of connections, assemblies, and components were not carried out individually, the experimental behavior of these elements is implicitly contained in the hysteretic results. Therefore, $\beta_{TD} = 0.20$ $(Good)$.
- Modeling (β_{MDL}): The Mostaghel's six-lines hysteretic model captured all the nonlinear behaviors, including the yielding, pinching, stiffness and strength degradation. This hysteretic model was sufficiently suitable and accurate to predict the structural response until collapse without convergence issues. On the other hand, the structural model used in the analysis was assumed with some simplifications such as SDoF systems, 2D-models, etc. According to these reasons, $\beta_{MDL} = 0.20$ $(Good)$.

The corrected parameter β_{Tot} of the fragility functions for the HRCW is presented in Table **5-19**.

Table 5-19: Corrected parameters of the lognormal fragility functions fitted to the IDA results with the actual recorded and artificial ground motions for the HRCW damage states

Ground motions	Fragility parameters	**DS_1** (Light)	**DS_2** (Moderate)	**DS_3** (Severe)	**DS_4** (Complete)
Actual recorded	θ	3.3348	6.5995	7.3403	8.1639
	β_{Tot}	0.34183	0.37716	0.38656	0.40581
Artificial	θ	4.1597	7.3807	7.9996	8.5542
	β_{Tot}	0.30208	0.30172	0.30157	0.30289

Fig. **5-36** presents the corrected fragility curves fitted to the actual and artificial IDA results. The differences between the actual and artificial fragility curves were diminished to the point that they are similar, which validates the use of both sets of earthquakes in the assessment of the seismic performance of the HRCW.

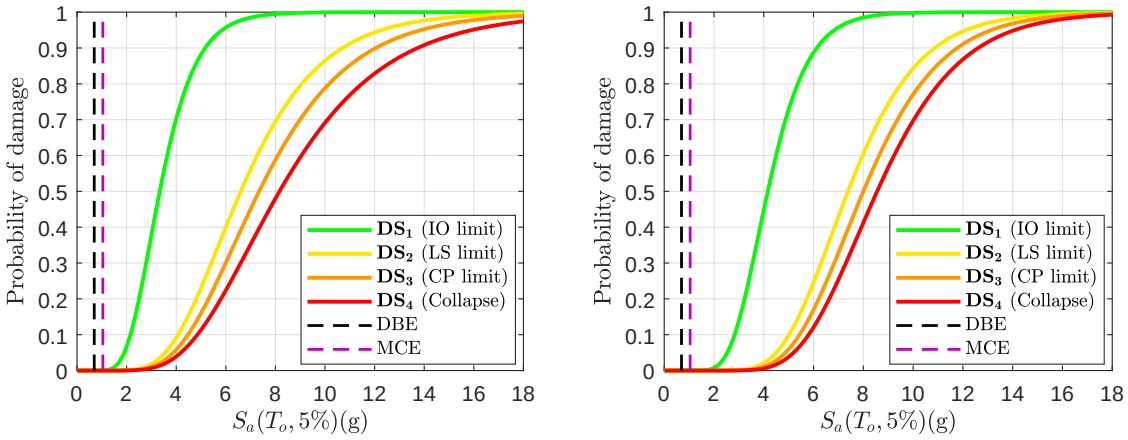

Figure 5-36: Corrected fragility curves for the HRCW: (a) Fitted to the IDA results with actual recorded ground motions; (b) Fitted to the IDA results with artificial ground motions

From the above figures, it can see that the probability of incurring any **DS** is 0% for DBE and MCE. In other words, there is a 100% probability of no structural damage. Therefore, and considering that the **DS**s and the SPLs were previously related, this fact also demonstrates the HRCW has a 100% probability of falling into the IO performance level, which reveals the very good seismic performance of this structural wall for one and two-story housing.

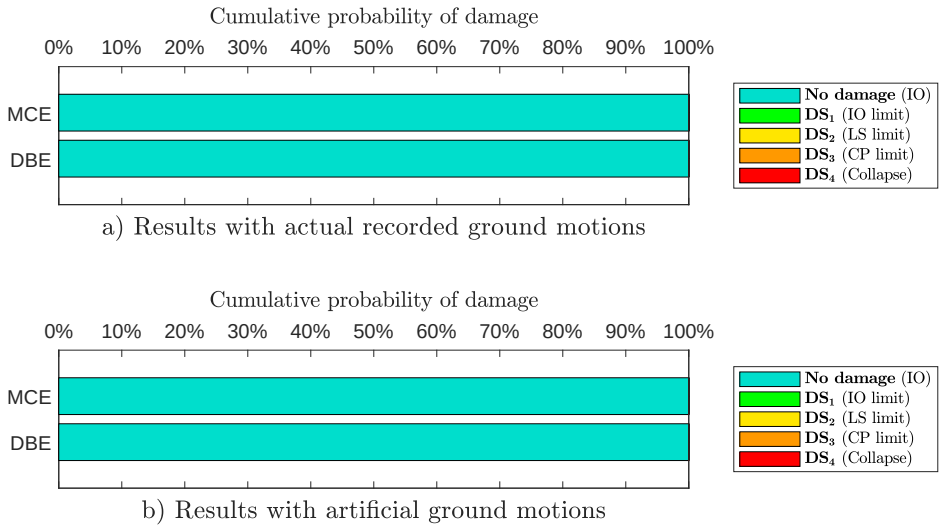

Figure 5-37: Cumulative probability of damage of the HRCW for each earthquake hazard level

6 Conclusions

6.1 Literature review of the state of development of PBSD

With the purpose to reach the main objectives of this dissertation, the fundamentals of PBSD were studied in detail in Chapter 2. The basic concepts about this emerging design philosophy allowed understanding completely the importance of all the definitions and the key steps required to apply it, in this case, in structural systems such as structural walls made of RPL, ferrocement, and reinforced concrete, which have been proposed for one and two-story housing. Some advantages and possible applications of PBSD in structural and earthquake engineering were expounded for making a comparison of this design approach with the traditional one and, besides, for supporting its application in this study.

A whole literature review of the state of development of PBSD was presented for contextualizing the reader with the roots, the evolution, the advances and the current outlook of this design philosophy. This review also included a summary of the proposals that have been used for the performance objectives, performance levels, and earthquake hazard levels, which later helped to define these concepts for the application of PBSD in the structural walls.

Due to that the performance-based seismic assessment is an indispensable step for predicting the structural performance and the likely amount of damage, the descriptions of the NSP and NDA procedures commonly used for this task were also presented rigorously. Some concluding remarks about the predominant procedures of NSPs are listed below:

- The first CSM (ATC, 1996) was based on equivalent linearization in which a nonlinear system is replaced by an equivalent linear system that has a larger equivalent period and equivalent damping ratio. The ATC 40 also provided three graphical procedures that simplify the iterative process of the determination of the performance point, among which the Procedure A is the most straightforward application.
- The FEMA 440 report presented an improved CSM in which the estimations of the equivalent period and the equivalent damping ratio were determined on an optimization process that minimized the differences between the displacements predicted using the equivalent linear system and the nonlinear response history analysis. However, this method estimates deformation demands that are very sensitive to ductility levels.

- These CSMs based on equivalent linearization do not have any physical principle that justify the relationship between the hysteretic energy dissipation and equivalent viscous damping. In fact, this damping is approximated in order to avoid dynamic analysis of the inelastic system. Additionally, the period of the equivalent linear system associated with the performance point does not represent accurately the dynamic response of inelastic systems.

- In order to eliminate those deficiencies, an approach of CSM based on inelastic spectra was developed by some authors and was extended as a simple nonlinear method known as the N2 method. This method combines the visual representation both the capacity spectrum and the inelastic demand spectra in the performance point estimation, with the superior physical basis of inelastic demand spectra. All steps that the N2 method involves can be performed numerically.

- The previous DCM employs empirical modification coefficients that are used to modify the elastic response of the SDOF system for estimating the nonlinear behavior, which is more accurate than an elastic spectra with equivalent viscous damping.

- The current DCM includes improvements of the coefficients used to calculate the target displacement, in order to expound the actual understanding of building behavior during seismic events. Also, this methodology eliminates the coefficient related to the amplification in deformations due to the dynamic P-Δ effects. Instead, it suggests a limit on the minimum strength required to avoid dynamic instability.

For its part, the main features and the advantages of NDA were explained, which differ to a certain extent with those of the NSPs. Both types of analyses have been applied in many studies, building codes, and standards for performing the seismic design and assessment of structures. However, it can be concluded that NDA is more accurate and reliable because it considers appropriate definitions both the input ground motion records and the hysteretic behavior of elements and, besides, NSPs imply a greater uncertainty due to the empirical procedures used to estimate the seismic response. Given these reasons, NDA was selected as the preferential type of analysis for estimating and assessing the seismic performance of the structural walls.

The IDA algorithm was studied and described in detail in Chapter 2, with the purpose of performing multiple NDA for sets of ground motions records so as to obtain statistically robust values of the demand parameters. This algorithm has been adopted in many researches as the predominant method to perform NDA, so it was used for the NDA required in the seismic performance assessment and in the development of the fragility functions for the structural walls in this research. On the other hand, a brief review of the seismic fragility analysis was made to illustrate to the reader the approaches used in the estimation of the fragility functions and probabilities of damage.

6.2 Hysteretic systems

In Chapter 3, all the necessary theory and concepts of structural dynamics related to linear and nonlinear SDoF systems subjected to external dynamic loading were studied. The concept of hysteresis was explained in detail as well as the stiffness degradation, strength deterioration, and pinching effect. Additionally, a brief review of the types of hysteretic models (SHM and PHM) and their features was presented, in order to illustrate the mathematical methods that have been developed for simulating the hysteretic responses of structural systems.

The PHM proposed by Mostaghel (1999) and corrected by Zeynalian et al. (2012) was selected with the same aim for the structural walls. The criteria for this selection were based on two main facts: first, this is a model capable of describing effectively the behavior of SDoF hysteretic systems that experience stiffness degradation, strength or load deterioration, and pinching effect; second, all of its parameters are in terms of definite physical quantities which can be measured through tests. The mathematical formulation of this model for both bilinear and multilinear hysteretic systems was also explained in detail.

The application of the Mostaghel multilinear model requires to determine a certain number of parameters to simulate correctly the experimental hysteretic behavior of the structural walls. In this sense, a novel procedure for the parameter identification of the Mostaghel's multilinear hysteretic model using the simple PSO algorithm was developed. In this procedure, particles of the PSO algorithm are related to parameter vectors of the mathematical model, which are determined from an optimization. This proposal is based on the multi-objective optimization approach proposed by Ortiz et al. (2013, 2015), which minimizes at the same time both the error between the experimental displacements and the estimated ones and the error between the experimental total dissipated energy and the estimated one. However, the proposed procedure keeps the single-objective PSO algorithm by a total cost function which is defined as a linear combination of the aforementioned cost functions. The simple PSO algorithm was employed in the development of the parameter identification procedure given its simplicity and practicality, and besides, because it has been widely and successfully applied for the solution of this kind of problems.

6.3 Experimental and analytical study

The experimental campaign and the descriptions of the structural walls were reported in detail in Chapter 4 where the experimental results allowed obtaining the hysteretic behavior of the structural walls under cyclic loading conditions. The following comments are highlighted:

- The RPLW exhibited stiffness degradation, scant strength deterioration in the last cyclic loading and pinching effect due to the type of connections and to the relative displacement between the boards. On the other hand, the PFW experienced scant stiffness degradation,

cyclic strength deterioration in the last cycles, and moderate pinching effects as a result of the opening and closing cracks process, whereas the HRCW exhibited moderate stiffness degradation, high cyclic strength deterioration, and scant pinching effects.

- Both the PFW and the HRCW showed a higher stiffness and strength than the RPLW; however, the maximum top displacement reached in the RPLW was in the order of 160 mm (7% of drift ratio level), which shows its high deformation ability.

- Structural parameters of the walls such as elastic stiffness, elastic shear strength, ultimate strength, ductility, energy dissipation, equivalent viscous damping, and coefficient of energy dissipation capacity were computed according to the ASTM Standard E2126-11 (2011) and using the experimental average envelope curve of each system. These parameters are indispensable to design the housing systems following the criteria of seismic design codes.

- The structural walls developed high energy dissipation with an increase in the drift ratio level. In fact, the rounded shape of the hysteresis curves and the area enclosed by those loops suggest that the systems have good energy dissipation capacity when they are subjected to loads beyond its linear range.

- Four damage limit states were determined from the experimental behavior exhibited by each structural wall in the cyclic tests, which were described by direct indicators of structural damage and related to the story drift ratio that is usually selected as a suitable indicator of damage. For the case of the RPLW, the damage states were defined in terms of the relative displacement of the boards and of the failure in the battens' connections, whereas for the PFW and HRCW were defined in terms of cracking, crushing and spalling of concrete and mortar, and buckling and fracture of the rebars.

The appropriateness and the efficiency of the Mostaghel's multilinear hysteretic model to estimate the experimental hysteretic behavior of each structural wall were tested employing three variants: five-lines, six-lines, and seven-lines hysteretic models. The parameters of each variant were estimated by the proposed parameter identification procedure. In general, these multilinear models were in good agreement with the experimental hysteretic behavior of each wall so that only one variant was selected to perform subsequently nonlinear dynamic analyses.

The decision variables for the selection process were the fitting of the total dissipated energy and the shape of the hysteresis cycles because the hysteretic phenomena experienced by the walls (i.e. pinching, stiffness degradation, and load deterioration) are formulated in the Mostaghel's model in terms of those quantities. Therefore, the selected hysteretic models for the RPLW, PFW, and HRCW were the six-lines model, the seven-lines model, and the six-lines model, respectively. These models are good enough for simulation purposes.

6.4 Performance-based seismic assessment methodology

Chapter 5 expounded all the definitions needed to execute the performance-based seismic assessment of the structural walls as well as the results obtained. There, the structural performance levels IO, LS, and CP, were related to the damage limit states $\mathbf{DS}_1$, $\mathbf{DS}_2$ and $\mathbf{DS}_3$, respectively, of each wall. This relationship was made with the aim to express the performance levels in terms of the interstory drift ratio. Furthermore, it was associated Collapse with the $\mathbf{DS}_4$ level, which would allow later assessing the probability of collapse of the walls.

With the purpose of accomplishing performance-based seismic assessments as realistic as possible, several assumptions were made for the construction site and the type of soil, which represented in a good way the real ones where one and two-story housing with these structural systems have been built. Additionally, the seismic weight of the walls was assumed as the tributary dead load that each one would support in a typical two-story housing design which considered definitions widely used in Colombia for the covering, the ceiling, and the floor fill. These loads were composed of the superimposed dead loads, 20% of the live load, and the self-weight of the structural walls. This assumption allowed for simulating the actual performance of these structural systems.

Regarding the earthquake hazard, Intensity-based assessment was used in the performance-based seismic assessment procedure of the structural walls. The following remark summarize the corresponding definitions:

- The NSR-10 response spectrum was selected as the target spectrum, and the DBE and MCE earthquake hazard levels of the ASCE 41-13 standard were considered.
- Given that enough information about past earthquakes and the database of actual acceleration records were not available to characterize the seismic hazard in question, two sets of ground motion records were used to represent the specific seismic hazard and to validate the procedure.
- The first set of ground motions was the Far-Field record set of actual recorded ground motions of the FEMA P695 report, which includes 22 component pairs of horizontal ground motions (44 analyses in total) that have been widely used to perform NDA for PBSD and seismic fragility analysis of many structural systems. The second one was defined following the criterion of the ASCE/SEI 7-16 standard of seven artificial ground motions which were generated by the SeismoArtif software that has been also employed in many researches with the same purpose.
- For each set, the spectra of the ground motions were computed and their median spectrum was determined and compared to the NSR-10 target spectrum at the fundamental period T_o of each wall. As expected, the median spectra did not match the target spectrum at T_o for any structural wall, therefore, the ground motions of each set were scaled to achieve that spectral matching. The results obtained from this task were good.

Chapter 5 also presented the results of the seismic performance assessment of the walls. The IDA algorithm was applied using the actual recorded and the artificial ground motions; in all cases, the algorithm stopped when the collapse level was reached and not due to numerical non-convergence.

The determination of the performance points was carried out by the intersection of the median IDA curves with the horizontal lines related to the earthquake hazard levels. In general, the differences between the performance points for the DBE and the MCE of each type of ground motions are acceptable, which validates the use of both sets for this purpose. It is worth mentioning the following concluding remarks about the performance points of each structural wall:

- The interstory drift ratios of the RPLW for the DBE level were 3.07% using the IDA results of the actual recorded ground motions and 2.86% using the IDA results of the artificial ones, whereas for the MCE level were 4.85% and 4.23%, respectively. These performance points fall within the LS and CP ranges for the DBE and the MCE, respectively. This fact evidences that the RPLW meets exactly the basic safety performance objective established in the design philosophy of the NSR-10 building code.

- For the PFW, the interstory drift ratio using the IDA results of the actual recorded ground motions and the artificial ones for the DBE level were 0.076% and 0.062%, respectively; on the other hand, for the MCE level were 0.115% and 0.093%, respectively. These performance points fall within the IO range, which demonstrates the very good performance of the PFW under seismic loading conditions.

- The interstory drift ratio of the HRCW using the IDA results of the actual recorded ground motions and the artificial ones for the DBE level were 0.066% and 0.051%, respectively; and for the MCE level were 0.098% and 0.077%, respectively. Similarly, as in the PFW, these performance points fall within the IO range, which proves the very good performance of the HRCW under seismic loading conditions.

The seismic fragility functions for the IDA results with the actual recorded and artificial ground motions for each damage limit state were developed as lognormal CDFs by the Baker's parametric approach. The fragility parameters of the functions were estimated using an open-source Excel spreadsheet developed by that same author (Baker, 2015a). In general, the fragility curves fitted in a good way the observed points, which validates the parametric approach and the software tool used. However, the values of the standard deviation were too small, which suggested that it was essential to correct the fragility functions so as to consider the total system damage uncertainty.

The FEMA P695 sources of uncertainty associated with Design Requirements, Test Data and Modeling, were defined in detail for each wall and employed to correct their fitted fragility functions. This correction process was successfully applied to the fragility functions of the IDA results with the actual recorded and artificial ground motions to obtain more reliable results and to diminish the differences between them. Consequently, it is important to present the following concluding remarks about the seismic fragility results of each structural wall:

- At the DBE level, the RPLW's probability of falling into the IO performance level ranges from 68% to 80%, whereas the probability of collapse is less than 15%. On the other hand, at the MCE level, the probability of falling into the IO performance level ranges from 42% to 50% and the probability of collapse ranges from 18% to 33%. In conclusion, these results illustrate the satisfactory seismic performance of the RPLW for one and two-story housing subjected to those earthquake hazard levels. Nevertheless, this structural system could be improved to diminish the probability of collapse, specially for the MCE level.
- Regarding the PFW and HRCW, there is a 0% probability of incurring any damage limit state for both earthquake hazard levels. In other words, the probability of no structural damage is 100%. For this reason, it can be concluded that they have a 100% probability of falling into the IO performance level, which demonstrates and ratifies the very good seismic performance of these structural walls for one and two-story housing subjected to the DBE and the MCE earthquake hazard levels. The PFW and the HRCW could be used for more than two-story buildings.

The obtained results approve the use of these structural systems for one and two-story housing. The expectation is that the use of them increases together with the effective efforts in investigation and development of more innovative structural materials and systems.

6.5 Directions for future research

Based on the conclusions and the results obtained in this study, some ideas for future research are proposed below:

- The structural walls were anchored to a strong reaction floor by rigid concrete foundation beams, in order to provide the lateral support needed to test effectively the cyclic behavior of the walls. In fact, the structural walls reached their damage states at high levels of Sa. However, some damage in another element of the housing systems, e.g. in the actual foundation system of the walls, could occur at these levels of Sa. Because of this, special interest is generated in studying the experimental behavior of full-scale housing systems under earthquake shaking table tests.
- Different structural configurations of the RPLW could be studied to extend the use of this materials for more than two-story buildings. Regarding the PFW and HRCW, studies could be performed to know up to what number of stories these systems are appropriate.
- The Mostaghel's multilinear hysteretic model demonstrated to be a versatile and useful model to simulate the nonlinear behavior of different types of structural walls. Therefore, this model together with the proposed parameter identification technique could be applied in other structural elements and systems.

- Although this hysteretic model has been only applied to SDoF systems, future studies could be carried out on MDoF systems on the basis of the formulation proposed by Mostaghel and Byrd (2000).
- The proposed methodology for the performance-based seismic assessment can be extended to study other structural elements and systems. For instance, it could be applied to know the performance of structural systems based on prestressed concrete walls which also have been proposed in recent years for one and two-story housing.
- Additionally, the methodology and the obtained fragility curves could be used for the seismic performance assessment approach presented in the FEMA P58 report (FEMA, 2012) in which the performance is expressed as the probable consequences, in terms of human losses (deaths and serious injuries), direct economic losses (building repair or replacement costs), and indirect losses (repair time and unsafe placarding) resulting from building damage due to strong ground motions.

Appendix A. Research products

Articles in high impact journals

- Herrera, J.P., Bedoya-Ruiz, D., & Hurtado, J. E. (2018). "Seismic behavior of recycled plastic lumber walls: An experimental and analytical research". *Engineering Structures*, 177, 566-578. https://doi.org/10.1016/j.engstruct.2018.10.006
- Herrera, J.P., Bedoya-Ruiz, D., & Hurtado, J. E. (2019). "Performance-based seismic assessment of precast ferrocement walls for one and two-story housing". *Engineering Structures*. Article submitted for publication.

References

Abdullah, A. A. (1995). Applications of ferrocement as a low cost construction material in Malaysia. *Journal of ferrocement*, 25(2):123–128.

AIS (2010). Normas Colombianas de Diseño y Construcción Sismo Resistente, NSR-10. Technical report, AIS. Asociación Colombiana de Ingeniería Sísmica, Bogotá.

Arora, J. S. (2011). *Introduction to optimum design*. Academic Press.

ASCE (2007). Seismic rehabilitation of existing buildings. Technical report, ASCE 41-06. American Society of Civil Engineers, Reston, Virginia.

ASCE (2014). Seismic Evaluation and Retrofit of Existing Buildings. Technical report, ASCE 41-13. American Society of Civil Engineers, Reston, Virginia.

ASCE (2017a). Minimum design loads and associated criteria for buildings and other structures. Technical report, ASCE/SEI 7-16. American Society of Civil Engineers, Reston, Virginia.

ASCE (2017b). Seismic Evaluation and Retrofit of Existing Buildings. Technical report, ASCE 41-17. American Society of Civil Engineers, Reston, Virginia.

Asgarian, B., Khazaee, H., and Mirtaheri, M. (2012). Performance evaluation of different types of steel moment resisting frames subjected to strong ground motion through Incremental dynamic analysis. *International Journal of Steel Structures*, 12(3):363–379.

Asgarian, B., Sadrinezhad, A., and Alanjari, P. (2010). Seismic performance evaluation of steel moment resisting frames through incremental dynamic analysis. *Journal of Constructional Steel Research*, 66(2):178–190.

Askari, M., Li, J., and Samali, B. (2012). Application of extended, unscented, iterated extended and iterated unscented Kalman Filter for real-time structural identification. In *Advances in Applied Mechanics Research, Conference Proceedings - 7th Australasian Congress on Applied Mechanics, ACAM 2012*.

Askari, M., Li, J., and Samali, B. (2016). Application of Kalman Filtering Methods to Online Real-Time Structural Identification: A Comparison Study. *International Journal of Structural Stability and Dynamics*, 16(06):1550016.

ASTM D6108-13 (2013). Standard Test Method for Compressive Properties of Plastic Lumber and Shapes. Technical report, ASTM International, West Conshohocken, PA.

ASTM D6109-13 (2013). Standard Test Methods for Flexural Properties of Unreinforced and Reinforced Plastic Lumber and Related Products. Technical report, ASTM International, West Conshohocken, PA.

ASTM D6111-13a (2013). Standard Test Method for Bulk Density And Specific Gravity of Plastic Lumber and Shapes by Displacement. Technical report, ASTM International, West Conshohocken, PA.

ASTM D6112-13 (2013). Standard Test Methods for Compressive and Flexural Creep and Creep-Rupture of Plastic Lumber and Shapes. Technical report, ASTM International, West Conshohocken, PA.

ASTM D6117-16 (2016). Standard Test Methods for Mechanical Fasteners in Plastic Lumber and Shapes, ASTM International, West Conshohocken, PA, 2016. Technical report, ASTM International, West Conshohocken, PA.

ASTM Standard E2126-11 (2011). Standard Test Methods for Cyclic (Reversed) Load Test for Shear Resistance of Vertical Elements of the Lateral Force Resisting Systems for Buildings. Technical report, ASTM International, West Conshohocken, PA.

ATC (1996). Seismic Evaluation and retrofit of concrete buildings. Technical report, ATC 40. Applied Technology council, Redwood City, California.

ATC (2003). Preliminary evaluation of methods for defining performance. Technical report, ATC 58. Applied Technology council, Redwood City, California.

Baber, B. T. T., Asce, A. M., and Noori, M. N. (1986). Random Vibration Hysteretic, Degrading Systems. I(8):1010–1026.

Baber, T. T. and Noori, M. N. (1985). Random Vibration of Degrading, Pinching Systems. *Journal of Engineering Mechanics*, 111(8):1010–1026.

Baber, T. T. and Wen, Y.-K. (1981). Random Vibration Hysteretic, Degrading Systems. *Journal of the Engineering Mechanics Division*, 107(6):1069–1087.

Baker, J. W. (2015a). Code supplement to "Efficient analytical fragility function fitting using dynamic structural analysis.".

Baker, J. W. (2015b). Efficient Analytical Fragility Function Fitting Using Dynamic Structural Analysis. *Earthquake Spectra*, 31(1):579–599.

Bedoya-Ruiz, D., Chalarca, B., Alvarez, D. A., and Hurtado, J. E. (2015a). Behavior of precast ferrocement walls under cyclic loading.

Bedoya-Ruiz, D., Farbiaz, D., Hurtado, J. E., and Pujades, L. (2002). Ferrocemento: Un acercamiento al diseño sismo-resistente.

Bedoya-Ruiz, D., Hurtado, J. E., and Pujades, L. (2010). Experimental and analytical research on seismic vulnerability of low-cost ferrocement dwelling houses. *Structure and Infrastructure Engineering*, 6(1-2):55–62.

Bedoya-Ruiz, D., Ortiz, G., Álvarez, D., and Hurtado, J. (2015b). Modelo dinámico no lineal para evaluar el comportamiento sísmico de viviendas de ferrocemento. *Revista Internacional de Métodos Numéricos para Cálculo y Diseño en Ingeniería*, 31(3):139–145.

Bedoya-Ruiz, D., Ortiz García, G. A., and Alvarez, D. A. (2014). Behavior of precast ferrocement thin walls under cyclic loading: an experimental and analytical study. *Ingeniería e Investigación*, 34(1):29–35.

Bedoya-Ruiz, D. A. (2005). *Estudio de resistencia y vulnerabilidad sísmicas de viviendas de bajo costo estructuradas con ferrocemento*. Ph.d. dissertation, Universidad Politécnica de Catalunya.

Bermúdez, C., Barbat, A. H., and Pujades, L. G. (2008). Vulnerabilidad y fragilidad sísmicas de un edificio de acero localizado en Manizales, Colombia. *Hormigón y acero*, 59:77–94.

Bertero, R. D. and Bertero, V. V. (2002). Performance-based seismic engineering: The need for a reliable conceptual comprehensive approach. *Earthquake Engineering & Structural Dynamics*, 31(3):627–652.

Bouc, R. (1967). Forced vibration of mechanical systems with hysteresis. In Djadkov, S., editor, *Proceedings of the Fourth International Conference on Nonlinear Oscillation*, page p. 315, rague, Czechoslovakia.

Bougioukos, A. (2017). *Effects of strength hardening , stiffness degradation , strength deterioration and pinching on the seismic response of SDoF systems*. PhD thesis, Delft University of Technology.

Brunesi, E., Nascimbene, R., Parisi, F., and Augenti, N. (2015). Progressive collapse fragility of reinforced concrete framed structures through incremental dynamic analysis. *Engineering Structures*, 104:65–79.

Čada, P. and Máca, J. (2017). Comparison of methods used for seismic analysis of structures. *Acta Polytechnica CTU Proceedings*, 13(0):20.

Cao, H., Qian, X., Chen, Z., and Zhu, H. (2017). Enhanced particle swarm optimization for size and shape optimization of truss structures. *Engineering Optimization*, 49(11):1939–1956.

Carrillo, J. and Alcocer, S. M. (2012). Seismic performance of concrete walls for housing subjected to shaking table excitations. *Engineering Structures*, 41:98–107.

Carroll, D. R., Stone, R. B., Sirignano, A. M., Saindon, R. M., Gose, S. C., and Friedman, M. A.

(2001). Structural properties of recycled plastic/sawdust lumber decking planks. *Resources, Conservation and Recycling*, 31(3):241–251.

Castro, J. (1979). Applications of Ferrocement in Low-Cost Housing in Mexico. *Special Publication. American Concrete Institute*, 61:143–156.

Charalampakis, A. (2009). *Inelastic dynamic analysis of structures using Bouc-Wen hysteretic models*. Phd thesis, National Technical University of Athens.

Charalampakis, A. E. and Dimou, C. K. (2010). Identification of Bouc-Wen hysteretic systems using particle swarm optimization. *Computers and Structures*, 88(21-22):1197–1205.

Chen, C.-W., Salim, H., Bowders, J. J., Loehr, J. E., and Owen, J. (2007). Creep Behavior of Recycled Plastic Lumber in Slope Stabilization Applications. *Journal of Materials in Civil Engineering*, February(February):130.

Chomchuen, P. and Boonyapinyo, V. (2017). Incremental dynamic analysis with multi-modes for seismic performance evaluation of RC bridges. *Engineering Structures*, 132:29–43.

Chopra, A. K. (2012). *Dynamics of structures : theory and applications to earthquake engineering*. Prentice Hall.

Chopra, A. K. and Goel, R. K. (1999a). Capacity-Demand-Diagram Methods Based on Inelastic Design Spectrum. *Earthquake Spectra*, 15(4):637–656.

Chopra, A. K. and Goel, R. K. (1999b). Capacity-Demand-Diagram Methods for Estimating Seismic Deformation of Inelastic Structures. Technical report, PEER 1999/02. Pacific Earthquake Engineering Research Center, University of California, Berkeley.

Christovasilis, I. P., Filiatrault, A., Constantinou, M. C., and Wanitkorkul, A. (2009). Incremental dynamic analysis of woodframe buildings. *Earthquake Engineering and Structural Dynamics*, 38(4):477–496.

Clerc, M. (2011). From Theory to Practice in Particle Swarm Optimization. In *Handbook of Swarm Intelligence: Concepts, Principles and Applications*, pages 3–36.

Clough, R. W. and Johnston, S. B. (1966). Effect of stiffness degradation on earthquake ductility requirements. In *Second Japan National Conference on Earthquake Engineering*, pages 227–232.

Clough, R. W. and Penzien, J. (1975). *Dynamics of structures*. McGraw-Hill Companies.

Dimou, C. K. and Koumousis, V. K. (2009). Reliability-Based Optimal Design of Truss Structures Using Particle Swarm Optimization. *Journal of Computing in Civil Engineering*, 23(2):100–109.

Econciencia S.A.S. (2018). Econciencia - Construcción sostenible.

Esfandiari, M. J., Urgessa, G. S., Sheikholarefin, S., and Dehghan Manshadi, S. H. (2018). Optimization of reinforced concrete frames subjected to historical time-history loadings using DMPSO algorithm. *Structural and Multidisciplinary Optimization*, 58(5):2119–2134.

Fajfar, P. (1999). Capacity spectrum method based on inelastic demand spectra. *Earthquake Engineering & Structural Dynamics*, 28(9):979–993.

Fajfar, P. (2000). A Nonlinear Analysis Method for Performance-Based Seismic Design. *Earthquake Spectra*, 16(3):573–592.

Fattahi, F. and Gholizadeh, S. (2018). Seismic fragility assessment of optimally designed steel moment frames. *Engineering Structures*, 179:37–51.

FEMA (1997). NEHRP guidelines for the seismic rehabilitation of buildings. Technical report, FEMA 273. Federal Emergency Management Agency, Washington, D.C.

FEMA (2000). Prestandard and Commentary for the Seismic Rehabilitation of Buildings. Technical report, FEMA 356. Federal Emergency Management Agency, Washington, D.C.

FEMA (2006). Next-Generation Performance-Based Seismic Design Guidelines, Program Plan for New and Existing Buildings. Technical report, FEMA 445. Federal Emergency Management Agency, Washington, D.C.

FEMA (2009a). Effects of Strength and Stiffness Degradation on Seismic Response. Technical report, FEMA P440A. Federal Emergency Management Agency Agency, Washington, D.C.

FEMA (2009b). Quantification of Building Seismic Performance Factors. Technical report, FEMA P695. Federal Emergency Management Agency, Washington, D.C.

FEMA (2012). Seismic Performance Assessment of Buildings. Technical report, FEMA P58. Federal Emergency Management Agency, Washington, D.C.

Filiatrault, A. and Folz, B. (2002). Performance-Based Seismic Design of Wood Framed Buildings. *Journal of Structural Engineering*, 128(1):39–47.

Foliente, G. C. (1995). Hysteresis Modeling of Wood Joints and Structural Systems. *Journal of Structural Engineering*, 121(6):1013–1022.

Foliente, G. C., Singh, M. P., and Noori, M. N. (1996). Equivalent linearization of generally pinching hysteretic, degrading systems. *Earthquake Engineering and Structural Dynamics*, 25(6):611–629.

Fourie, P. C. and Groenwold, A. A. (2002). The particle swarm optimization algorithm in size and shape optimization. *Structural and Multidisciplinary Optimization*, 23(4):259–267.

Freeman, S., Nicoletti, J., and Tyrell, J. (1975). Evaluation of Existing Buildings for Seismic Risk-A Case Study of Puget Sound Naval Shipyard, Bremerton, Washington. In EERI, editor,

Proceedings of U.S. National Conference on Earthquake Engineering, pages 113–122, Berkeley. EERI.

Freeman, S. A. (1978). Prediction of Response of Concrete Buildings to Severe Earthquake Motion. *Special Publication*, 55:589–606.

Garrido, R. and Rivero-Angeles, F. J. (2006). Hysteresis and Parameter Estimation of Mdof Systems By a Continuous-Time Least Squares Method. *Journal of Earthquake Engineering*, 10(2):237–264.

Gasparini, D. and Vanmarcke, E. (1976). Simulated Earthquake Motions Compatible with Prescribed Response Spectra. Technical report, Massachusetts Institute of Technology, Department of Civil Engineering.

Gaxiola-Camacho, J. R., Azizsoltani, H., Villegas-Mercado, F. J., and Haldar, A. (2017). A novel reliability technique for implementation of Performance-Based Seismic Design of structures. *Engineering Structures*, 142:137–147.

Ghobarah, A. (2001). Performance-based design in earthquake engineering: State of development. *Engineering Structures*, 23(8):878–884.

Gholizadeh, S. and Moghadas, R. K. (2014). Performance-Based Optimum Design of Steel Frames by an Improved Quantum Particle Swarm Optimization. *Advances in Structural Engineering*, 17(2):143–156.

Gholizadeh, S. and Salajegheh, E. (2009). Optimal design of structures subjected to time history loading by swarm intelligence and an advanced metamodel. *Computer Methods in Applied Mechanics and Engineering*, 198(37-40):2936–2949.

Ghosh, S., Ghosh, S., and Chakraborty, S. (2017). Seismic fragility analysis in the probabilistic performance-based earthquake engineering framework: an overview. *International Journal of Advances in Engineering Sciences and Applied Mathematics*, pages 1–14.

Giuclea, M., Sireteanu, T., and Mitu, a. M. (2009). Use of Genetic Algorithms for Fitting the Bouc-Wen Model To Experimental Hysteretic Curves. (January 2015):3–10.

Goda, K. and Yoshikawa, H. (2013). Incremental dynamic analysis of wood-frame houses in Canada: Effects of dominant earthquake scenarios on seismic fragility. *Soil Dynamics and Earthquake Engineering*, 48:1–14.

Gokhale, V. (1983). System built ferrocement housing. *Journal ferrocement*, 13:37–42.

Gulec, K. and Whittaker, A. (2009). Damage states and fragility curves for low aspect ratio reinforced concrete walls.

Gulhane, S. and Gulhane, S. (2017). Analysis of Housing Structures Made From Recycled Plas-

tic. In *Proceedings of the International Conference on Science & Engineering for Sustainable Development (2017)*, volume 7, pages 45–55.

Hamburger, R., Rojahn, C., Moehle, J., Bachman, R., Comartin, C., and Whittaker, A. (2004). The ATC-58 Project : Development of next-generation Performance-Based Earthquake Engineering Design criteria for buildings. In *13 th World Conference on Earthquake Engineering*, number 1819.

Hariri-Ardebili, M., Zarringhalam, Y., Estekanchi, H., and Yahyai, M. (2013). Nonlinear seismic assessment of steel moment frames using time-history, incremental dynamic, and endurance time analysis methods. *Scientia Iranica*, 20(3):431–444.

Hidalgo, P. A., Ledezma, C. A., and Jordan, R. M. (2002). Seismic Behavior of Squat Reinforced Concrete Shear Walls. *Earthquake Spectra*, 18(2):287–308.

Holden, T., Restrepo, J., and Mander, J. B. (2003). Seismic Performance of Precast Reinforced and Prestressed Concrete Walls. *Journal of Structural Engineering*, 129(3):286–296.

Hou, S. (1968). Earthquake simulation models and their applications. Technical report, Massachusetts Institute of Technology, Department of Civil Engineering.

Ibarra, L. F., Medina, R. A., and Krawinkler, H. (2005). Hysteretic models that incorporate strength and stiffness deterioration. *Earthquake Engineering and Structural Dynamics*, 34(12):1489–1511.

Ikhouane, F. and Rodellar, J. (2007). *Systems with Hysteresis*. John Wiley & Sons, Ltd, Chichester, UK.

Imran, M., Hashim, R., and Khalid, N. E. A. (2013). An overview of particle swarm optimization variants. *Procedia Engineering*, 53(1):491–496.

Iwan, W. D. (1966). A Distributed-Element Model for Hysteresis and Its Steady-State Dynamic Response. *Journal of Applied Mechanics*, 33(4):893.

Iwan, W. D. and Cifuentes, A. O. (1986). A model for system identification of degrading structures. *Earthquake Engineering & Structural Dynamics*, 14(6):877–890.

Jennings, P. C., Housner, G. W., and Tsai, N. C. (1968). Simulated earthquake motions. Technical report, California Institute of Technology, Pasadena, California.

Kafali, C. and Grigoriu, M. (2007). Seismic fragility analysis: Application to simple linear and nonlinear systems. *Earthquake Engineering & Structural Dynamics*, 36(13):1885–1900.

Kaveh, A. and Sabzi, O. (2011). Optimum Design of Reinforced Concrete Frames using a Heuristic Particle Swarm-Ant Colony Optimization. *Civil Engineering*, pages 1–18.

Kennedy, J. and Eberhart, R. (1995). Particle swarm optimization. *Neural Networks, 1995. Proceedings., IEEE International Conference on*, 4:1942–1948 vol.4.

Khansefid, A. and Bakhshi, A. (2017). Strengthening an existing industrial building by optimally designed passive dampers under seismic and service loads. In *SMAR 2017, the fourth International Conference on Smart Monitoring, Assessment and Rehabilitation of Civil Structures*, Zurich, Switzerland.

Kostinakis, K. and Athanatopoulou, A. (2016). Incremental dynamic analysis applied to assessment of structure-specific earthquake IMs in 3D R/C buildings. *Engineering Structures*, 125:300–312.

Krawinkler, H. (1994). New trends in seismic design methodology. In *10th European conference, Earthquake engineering*, volume 2, pages 821–830, Vienna. A.A. Balkema.

Krishnaswamy, B. P. and Lampo, R. (2001). Recycled-Plastic Lumber Standards : From Waste Plastics to Markets for Plastic Lumber Bridges. *World Standards Day: 2001 Paper Competition*, pages 1–12.

Kuang, J. S. and Ho, Y. B. (2008). Seismic Behavior and Ductility of Squat Reinforced Concrete Shear Walls with Nonseismic Detailing. *ACI Structural Journal*, 105(2):225–231.

Kunnath, S. K., Mander, J. B., and Fang, L. (1997). Parameter identification for degrading and pinched hysteretic structural concrete systems. *Engineering Structures*, 19(3):224–232.

Li, T., Silverstein, M. S., Hiltner, A., and Baer, E. (1994). Mechanical properties of commingled plastic from recycled polyethylene and polystyrene. *Journal of Applied Polymer Science*, 52(2):315–327.

Li, Z., He, M., Li, M., and Lam, F. (2014). Damage assessment and performance-based seismic design of timber-steel hybrid shear wall systems. *Earthquakes and Structures*, 7(1):101–117.

Liu, B.-q., Liu, M., and Li, Y.-b. (2004). Research and development of performance-based seismic design theory. In *Proceedings of the 13th World Conference on Earthquake Engineering*, number 417, Vancouver.

Liu, S.-C. (1969). Autocorrelation and power spectral density functions of the Parkfield earthquake of June 27, 1966. *Bulletin of the Seismological Society of America*, 59(4):1475–1493.

Luco, N. and Cornell, C. A. (1998). Effects of Random Connection Fractures on the Demands and Reliability for a 3-Storey Pre-Northridge SMRF Structure. In *Proceedings of the 6th U.S. National Conference on Earthquake Engineering*, pages 1–12, Seattle, Washington. EERI, Earthquake Engineering Research Institute.

Luh, G. C. and Lin, C. Y. (2011). Optimal design of truss-structures using particle swarm optimization. *Computers and Structures*, 89(23-24):2221–2232.

Macbain, K. and Saadeghvaziri, M. A. (1999). Analytical Modeling of the Mechanical Properties of Recycled Plastics. 8(June):339–346.

Machado, E. F. (1998). Building system for low-cost ferrocement housing. In Naaman, A. E., editor, *Memoirs from Ferrocement 6: Lambot symposium, Proceedings of the sixth international on ferrocement.*, pages 129–138.

Mander, J. B., Dhakal, R. P., Mashiko, N., and Solberg, K. M. (2007). Incremental dynamic analysis applied to seismic financial risk assessment of bridges. *Engineering Structures*, 29(10):2662–2672.

Marini, F. and Walczak, B. (2015). Particle swarm optimization (PSO). A tutorial. *Chemometrics and Intelligent Laboratory Systems*, 149:153–165.

Mase, L. Z. (2018). Seismic Response Analysis along the Coastal Area of Bengkulu during the September 2007 Earthquake. *Makara Journal of Technology*, 22(1):37.

McCarthy, T. and McCluskey, S. (2009). A Particle Swarm Optimisation Approach to Reinforced Concrete Beam Design according to AS3600. In *Proceedings of the First International Conference on Soft Computing Technology in Civil, Structural and Environmental Engineering*, pages 1–14, Madeira, Portugal.

Miano, A., Jalayer, F., Ebrahimian, H., and Prota, A. (2018). Cloud to IDA: Efficient fragility assessment with limited scaling. *Earthquake Engineering and Structural Dynamics*, 47(5):1124–1147.

Millonas, M. M. (1993). Swarms, Phase Transitions, and Collective Intelligence.

Miranda, E. and Bertero, V. V. (1994). Evaluation of Strength Reduction Factors for Earthquake-Resistant Design. *Earthquake Spectra*, 10(2):357–379.

Moradi, S., Alam, M. S., and Asgarian, B. (2014). Incremental dynamic analysis of steel frames equipped with NiTi shape memory alloy braces. *Structural Design of Tall and Special Buildings*, 23(18):1406–1425.

Mostaghel, N. (1999). Analytical Description of Pinching, Degrading Hysteretic Systems. *Journal of Engineering Mechanics*, 125(2):216–224.

Mostaghel, N. and Byrd, R. A. (2000). Analytical Description of Multidegree Bilinear Hysteretic System. *Journal of Engineering Mechanics*, 126(6):588–598.

Naaman, A. E. (2000). *Ferrocement and laminated cementitious composites*. Techno Press, Michigan, 1st edition.

Nazri, F. M. and Ken, P. Y. (2014). Seismic performance of moment resisting steel frame subjected to earthquake excitations. *Frontiers of Structural and Civil Engineering*, 8(1):19–25.

NIST (2010). Nonlinear Structural Analysis for Seismic Design: A guide for Practicing Engineers. Technical report, NIST GCR 10-917-5, prepared by the NEHRP Consultants Joint Venture, a partnership of the Applied Technology Council and the Consortium for Universities for

Research in Earthquake Engineering, for the National Institute of Standards and Technology, Gaithersburg, Maryland.

NIST (2017a). Guidelines for Nonlinear Structural Analysis for Design of Buildings, Part I-General. Technical report, NIST GCR 17-917-46v1, prepared by the Applied Technology Council for the National Institute of Standards and Technology, Gaithersburg, Maryland.

NIST (2017b). Recommended Modeling Parameters and Acceptance Criteria for Nonlinear Analysis in Support of Seismic Evaluation, Retrofit, and Design. Technical report, NIST GCR 17-917-45, prepared by the Applied Technology Council for the National Institute of Standards and Technology, Gaithersburg, Maryland.

Olvera, A. (1998). Applications of prefabricated ferrocement housing in Mexico. In Naaman, A. E., editor, *Memoirs from Ferrocement 6: Lambot symposium, Proceedings of the sixth international on ferrocement*, pages 95–108.

Ortiz, G. A., Alvarez, D. A., and Bedoya-Ruíz, D. (2013). Identification of Bouc-Wen type models using multi-objective optimization algorithms. *Computers & Structures*, 114-115:121–132.

Ortiz, G. A., Alvarez, D. A., and Bedoya-Ruíz, D. (2015). Identification of Bouc-Wen type models using the Transitional Markov Chain Monte Carlo method. *Computers & Structures*, 146:252–269.

Park, Y. J., Reinhorn, A. M., and Kunnath, S. K. (1987). IDARC: Inelastic Damage Analysis of Reinforced Concrete Frame - Shear-Wall Structures. NCEER-87-0008. Technical report, University at Buffalo, State University of New York, New York.

PEER (2006). PEER NGA Database. Technical report, University of California, Berkeley.

Pelliciari, M., Marano, G. C., Cuoghi, T., Briseghella, B., Lavorato, D., and Tarantino, A. M. (2018). Parameter identification of degrading and pinched hysteretic systems using a modified Bouc-Wen model. *Structure and Infrastructure Engineering*, pages 1–13.

Perez, R. and Behdinan, K. (2007). Particle swarm approach for structural design optimization. *Computers & Structures*, 85(19-20):1579–1588.

Pilakoutas, K. and Elnashai, A. (1995). Cyclic Behavior of RC Cantilever Walls, Part I: Experimental Results. *ACI Structural Journal*, 92(3):271–281.

Porter, K., Kennedy, R., and Bachman, R. (2007). Creating Fragility Functions for Performance-Based Earthquake Engineering. *Earthquake Spectra*, 23(2):471–489.

Pozza, L., Scotta, R., Trutalli, D., Pinna, M., Polastri, A., and Bertoni, P. (2014). Experimental and Numerical Analyses of New Massive Wooden Shear-Wall Systems. *Buildings*, 4(3):355–374.

Priestley, M. J. N., Seible, F. F., and Calvi, G. M. G. M. (1996). *Seismic design and retrofit of bridges*. Wiley.

Quiroz, L. G., Maruyama, Y., and Zavala, C. (2013). Cyclic behavior of thin RC Peruvian shear walls: Full-scale experimental investigation and numerical simulation. *Engineering Structures*, 52:153–167.

Ray, T. and Reinhorn, A. M. (2014). Enhanced Smooth Hysteretic Model with Degrading Properties. *Journal of Structural Engineering*, 140(1):04013028.

Reinhorn, A. M. (1997). Inelastic analysis techniques in seismic evaluations. In *International workshop, Seismic design methodologies for the next generation of codes*, pages 277–288, Bled, Slovenia. A A Balkema.

Rodgers, G. W., Mander, J. B., and Geoffrey Chase, J. (2012). Modeling cyclic loading behavior of jointed precast concrete connections including effects of friction, tendon yielding and dampers. *Earthquake Engineering & Structural Dynamics*, 41(15):n/a–n/a.

Sagliyan, S. and Yön, B. (2018). Assessment of Earthquake Behavior of Reinforced Concrete Buildings with Slab Discontinuity. *Firat University Turkish Journal Of Science and Technology*, 13(1):87–92.

Salajegheh, E., Gholizadeh, S., and Khatibinia, M. (2008). Optimal design of structures for earthquake loads by a hybrid RBF-BPSO method. *Earthquake Engineering and Engineering Vibration*, 7(1):13–24.

Sandesh, S. and Krishnapillai, S. (2011). Structural damage detection using a hybrid particle swarm algorithm. *World Journal of Modelling and Simulation*, 7(4):290–298.

Schutte, J. F. and Groenwold, A. A. (2003). Sizing design of truss structures using particle swarms. *Structural and Multidisciplinary Optimization*, 25(4):261–269.

SEAOC (1995). *Vision 2000, Performance based seismic engineering of buildings, vols I and II: conceptual framework*. Sacramento, California.

Seismosoft (2016). SeismoArtif 2016 - A computer program for generating artificial earthquake accelerograms matched to a specific target response spectrum.

Sengupta, P. and Li, B. (2014). Hysteresis Behavior of Reinforced Concrete Walls. *Journal of Structural Engineering*, 140(7):04014030.

Sengupta, P. and Li, B. (2016). Seismic Fragility Assessment of Lightly Reinforced Concrete Structural Walls. *Journal of Earthquake Engineering*, 20(5):809–840.

Shinozuka, M., Feng, M. Q., Lee, J., and Naganuma, T. (2000). Statistical Analysis of Fragility Curves. *Journal of Engineering Mechanics*, 126(12):1224–1231.

Silwal, B., Ozbulut, O. E., and Michael, R. J. (2016). Incremental dynamic analyses of steel moment resisting frames with superelastic viscous dampers. In *Conference Proceedings of the Society for Experimental Mechanics Series*, volume 6, pages 165–174.

Sivaselvan, M. V. and Reinhorn, A. M. (1999). Hysteretic Models for Cyclic Behavior of Deteriorating Inelastic Structures. MCEER-99-0018. Technical report, University at Buffalo, State University of New York, New York.

Sivaselvan, M. V. and Reinhorn, A. M. (2000). Hysteretic Models for Deteriorating Inelastic Structures. *Journal of Engineering Mechanics*, 126(6):633–640.

Sues, R. H., Mau, S. T., and Wen, Y. (1988). Systems Identification of Degrading Hysteretic Restoring Forces. *Journal of Engineering Mechanics*, 114(5):833–846.

Takada, T., Hwang, H. H. M., and Shinozuka, M. (1988). Response modification factor for multiple-degree-of-freedom systems. *Proceedings of the 9th World conference on Earthquake Engineering*, 5:129–134.

Takeda, T., Sozen, M. A., and Nielsen, N. N. (1970). Reinforced Concrete Response to Simulated Earthquakes. *Journal of the Structural Division*, 96(12):2557–2573.

Tang, H., Fukuda, M., and Xue, S. (2007). Particle swarm optimization for structural system identification. In *STRUCTURAL HEALTH MONITORING 2007: QUANTIFICATION, VALIDATION, AND IMPLEMENTATION, VOLS 1 AND 2*, pages 483–492.

Tang, H., Xie, L., and Xue, S. (2015). Usage of Comprehensive Learning Particle Swarm Optimization for Parameter Identification of Structural System. *International Journal of Natural Computing Research*, 5(2):1–15.

Tang, H., Xu, R., Xue, S., and Zhang, W. (2010). Structural system identification using comprehensive learning particle swarm optimization algorithm. *Zhendong Ceshi Yu Zhenduan/Journal of Vibration, Measurement and Diagnosis*, 30(6).

Tang, H.-S., Li, F., Wang, Y., Xue, S.-T., and Chen, R. (2009). Particle swarm optimization algorithm for shape optimization of truss structures. *Harbin Gongye Daxue Xuebao/Journal of Harbin Institute of Technology*, 41(12).

Tehrani, P. and Mitchell, D. (2013). Incremental dynamic analysis (IDA) applied to seismic risk assessment of bridges. In *Handbook of Seismic Risk Analysis and Management of Civil Infrastructure Systems*, pages 561–596.

Thyagarajan, R. S. (1989). *Modeling and analysis of hysteretic structural behavior*. Phd thesis, California Institute of Technology.

Turk, A. M. (2013). Seismic Response Analysis of Masonry Minaret and Possible Strengthening by Fiber Reinforced Cementitious Matrix (FRCM) Materials. *Advances in Materials Science and Engineering*, 2013:1–14.

Uribe, F., A. Ortiz, G., Alvarez, D., and Bedoya-Ruíz, D. (2014). Nonlinear modeling and fragility

analysis of ferrocement structures. In *7th International Conference on Computational Stochastic Mechanics (CSM7)*, Santorini, Greece.

Vamvatsikos, D. (2015). *Incremental Dynamic Analysis*, pages 1165–1171. Springer Berlin Heidelberg, Berlin, Heidelberg.

Vamvatsikos, D. and Cornell, C. A. (2002a). Incremental Dynamic Analysis. *Earthquake Engineering & Structural Dynamics*, 31(3):491–514.

Vamvatsikos, D. and Cornell, C. A. (2002b). The incremental dynamic analysis and its application to performance-based earthquake engineering. In *The 12th European Conference on Earthquake Engineering*, London, UK. Elsevier Science Ltd.

Vamvatsikos, D. and Cornell, C. A. (2004). Applied Incremental Dynamic Analysis. *Earthquake Spectra*, 20(2):523–553.

Vamvatsikos, D., Jalayer, F., and Cornell, C. (2003). Application of incremental dynamic analysis to an RC-structure. *Proceedings of the FIB Symposium on Concrete Structures in Seismic Regions, Athens*, (Figure 1):1–12.

Vargas, Y., Pujades, L., Barbat, A., and Hurtado, J. (2013). Evaluación probabilista de la capacidad, fragilidad y daño sísmico de edificios de hormigón armado. *Revista Internacional de Métodos Numéricos para Cálculo y Diseño en Ingeniería*, 29(2):63–78.

Vargas, Y. F., Barbat, A. H., Pujades, L. G., and Hurtado, J. E. (2014). Probabilistic seismic risk evaluation of reinforced concrete buildings. *Proceedings of the Institution of Civil Engineers - Structures and Buildings*, 167(6):327–336.

Vargas Alzate, Y. F. (2013). *Análisis estructural estático y dinámico probabilista de edificios de hormigón armado. Aspectos metodológicos y aplicaciones a la evaluación del daño.* Doctoral thesis, Universitat Politècnica de Catalunya.

Vidic, T., Fajfar, P., and Fischinger, M. (1994). Consistent inelastic design spectra: Strength and displacement. *Earthquake Engineering & Structural Dynamics*, 23(5):507–521.

Wainshtok-Rivas, H. (1994). Low-cost housing built with ferrocement precast elements. *Journal of ferrocement*, 24(1):29–34.

Wainshtok-Rivas, H. (2004). Model seismic resistant ferrocement houses. *Journal of ferrocement*, 34(2):363–371.

Wang, Q. W., Shi, Q. X., and Men, J. J. (2010). Seismic Performance Evaluation of SRC Frames Based on Incremental Dynamic Analysis. *Advanced Materials Research*, 163-167:4331–4335.

Wei, Z., Liu, J., and Lu, Z. (2018). Structural damage detection using improved particle swarm optimization. *Inverse Problems in Science and Engineering*, 26(6):792–810.

Wen, Y.-K. (1976). Method for Random Vibration of Hysteretic Systems. *Journal of the Engineering Mechanics Division*, 102(2):249–263.

Whitworth, H. (1997). A stiffness degradation model for composite laminates under fatigue loading. *Composite Structures*, 40(2):95–101.

Xue, S., Tang, H., and Zhou, J. (2009). Identification of Structural Systems Using Particle Swarm Optimization. *Journal of Asian Architecture and Building Engineering*, 1(November):517–524.

Yang, Y. and Ma, F. (2003). Constrained Kalman Filter for Nonlinear Structural Identification. *Modal Analysis*, 9(12):1343–1357.

Yar, M. and Hammond, J. (1987). Parameter estimation for hysteretic systems. *Journal of Sound and Vibration*, 117(1):161–172.

Ye, J., Hajirasouliha, I., Becque, J., and Eslami, A. (2016). Optimum design of cold-formed steel beams using Particle Swarm Optimisation method. *Journal of Constructional Steel Research*, 122:80–93.

Ye, M. and Wang, X. (2007). Parameter estimation of the Bouc-Wen hysteresis model using particle swarm optimization. *Smart Materials and Structures*, 16(6):2341–2349.

Yön, B. (2016). An evaluation of the seismic response of symmetric steel space buildings. *Steel and Composite Structures*, 20(2):399–412.

Zameeruddin, M. and Sangle, K. K. (2016). Review on Recent developments in the performance-based seismic design of reinforced concrete structures. *Structures*, 6:119–133.

Zarfam, P. and Mofid, M. (2011). On the modal incremental dynamic analysis of reinforced concrete structures, using a trilinear idealization model. *Engineering Structures*, 33(4):1117–1122.

Zeynalian, M. and Mokhtari, M. (2017a). A New Displacement-Control Analytical Hysteresis Model for Structural Systems. *International Journal of Civil Engineering*, 16(6):671–680.

Zeynalian, M. and Mokhtari, M. (2017b). Displacement Control Based Analytical Description of Pinching , Sliding and Degrading Hysteretic System. *Journal of Ferdowsi Civil Engineering*, 28(2):2–3.

Zeynalian, M., Ronagh, H. R., and Dux, P. (2012). Analytical Description of Pinching, Degrading, and Sliding in a Bilinear Hysteretic System. *Journal of Engineering Mechanics*, 138(11):1381–1387.

Zhang, H., Foliente, G. C., Yang, Y., and Ma, F. (2002). Parameter identification of inelastic structures under dynamic loads. *Earthquake Engineering and Structural Dynamics*, 31(5):1113–1130.

Zheng, Y. X. and Liao, Y. (2016). Parameter identification of nonlinear dynamic systems using an improved particle swarm optimization. *Optik*, 127(19):7865–7874.

Zheng Xueliang, Huang Yumei, Liu Yongchao, Wang Xiaoyue, and Gao Feng (1997). A method identifying the parameters of Bouc-Wen hysteretic nonlinear model based on genetic algorithm. In *1997 IEEE International Conference on Intelligent Processing Systems (Cat. No.97TH8335)*, volume 1, pages 602–605. IEEE.

Declaración

Me permito afirmar que he realizado la presente tesis de manera autónoma y con la única ayuda de los medios permitidos y no diferentes a los mencionados en la propia tesis. Todos los pasajes que se han tomado de manera textual o figurativa de textos publicados y no publicados, los he reconocido en el presente trabajo. Ninguna parte del presente trabajo se ha empleado en ningún otro tipo de tesis.

Manizales, 05 de abril de 2019

_____

Juan Pablo Herrera Castaño
CC 1.053.833.454